Effects of Lower Atmospheric and Solar Forcings on Daytime Upper Atmospheric Dynamics

A thesis submitted in partial fulfilment of

the requirements for the degree of

Doctor of Philosophy

by

Fazlul Islam Laskar

(Roll No. 11330004)

Under the guidance of

Prof. Duggirala Pallamraju

Space and Atmospheric Sciences Division

Physical Research Laboratory, Ahmedabad, India.

DISCIPLINE OF PHYSICS

INDIAN INSTITUTE OF TECHNOLOGY GANDHINAGAR

2014 - 2015

to

my family

Declaration

I declare that this written submission represents my ideas in my own words and where others' ideas or words have been included, I have adequately cited and referenced the original sources. I also declare that I have adhered to all principles of academic honesty and integrity and have not misrepresented or fabricated or falsified any idea/data/fact/source in my submission. I understand that any violation of the above can cause disciplinary action by the Institute and can also evoke penal action from the sources which have thus not been properly cited or from whom proper permission has not been taken when needed.

(Signature)

(Name: Fazlul Islam Laskar)

(Roll No: 11330004)

Date: February 25, 2015

Thesis Approval

The thesis entitled

Effects of Lower Atmospheric and Solar Forcings on Daytime Upper Atmospheric Dynamics

by

Fazlul Islam Laskar
(Roll No. 11330004)

is approved for the degree of

Doctor of Philosophy

Examiner	Examiner
Supervisor	Chairman

Date: ____________________

Place: ____________________

Acknowledgments

This thesis is the result of research work carried out during 2009 to 2014 at Physical Research Laboratory (PRL), Ahmedabad. It gives me a great pleasure to acknowledge all those who supported me directly or indirectly and made this thesis possible.

First and foremost, I express my sincere gratitude to my advisor, Prof. Duggirala Pallamraju for his guidance, patience, and instructions in the journey of this thesis. He not only provided me the freedom and confidence but also encouraged me to explore the world of new ideas. Whenever I felt that I have no other way to proceed, discussions with him opened up myriads of ways/ideas for further steps. I am indebted to him for providing me countless opportunities, unending support, and freedom of independent thinking in all these five years.

I thank Prof. J. N. Goswami, the Director; Mr. Y. M. Trivedi, the Registrar; Prof. A. Joshipura, former Dean; and Prof. U. Sarkar, present Dean for providing necessary facilities to carry out my research work.

I am highly obliged to Prof. R. Sekar for his suggestions and critical comments which helped me to improve scientific outcomes. The fruitful discussions with him always helped me to improve the quality of the scientific results and manuscripts. I would like to thank Dr. Varun Sheel who has evaluated reports and suggested improvements as a member of the Doctoral Studies Committee (DSC) along with Prof. R. Sekar.

I am grateful to Dr. D. Chakrabarty for our scientific discussions during tea, lunch, and at anytime whenever I went to his office with any problem. I also would like to thank Dr. Smitha Thampi for discussions.

I feel very happy to acknowledge Prof. R. Sridharan for the scientific discussions. Particularly, his encouraging comments and critical questions during seminars were very helpful during my research.

I thank Dr. J. S. Ray, Dr. D. Angom, Dr. D. Banerjee, Dr. N. Mahajan, Dr. R. Rangarajan, Dr. S. Naik, Dr. Varun Sheel, Prof. R. Ramachandran, Dr. D. Chakrabarty, Mr. T. Sarvaiya, Dr. H. Mishra and Prof. K. P. Subramanian for teaching the courses during my course work at PRL which turned out to be very useful in my research work. My sincere thanks to Prof. J Banerji for teaching me communications skill. I thank all the staff members of PRL computer center for providing excellent computational and internet facilities. In addition, I express my appreciation for the co-operation and help extended by the library and its staff members, in general, and Mrs. Nistha Anilkumar, in particular.

I am thankful to all my laboratory/group colleagues, R. P. Singh, Kedar, R.

Narayanan, and Deepak for their company, being friendly and co-operative during this research journey. I will always remain grateful to them for the discussions. In particular, I am very grateful to R. P. Singh and Kedar for their patience in listening to my practices and reading some of my first drafts of papers and thesis chapters. Our academic and non-academic discussions have made my stay enjoyable in lab. I have learned a lot about different fields in which my peers are working. I would like to thank some of the seasonal colleagues, Parshv Shah, Suneel Krishna, Keval Patel for their company and help.

I thank my seniors/colleagues, Uma Das, Sumanta Sarkel, and Amitava Guharay, for their help and discussions. I would like to acknowledge the help of Mala for introducing to me the GPS-based TEC, RINEX data and for many scientific and non-scientific discussions. She has always been there with me during my good and sad days of PhD life and encouraged me like a true friend.

I express my sincere thanks to all the faculty and staff members of Space and Atmospheric Sciences Division: Prof. Harish Chandra, Prof. H.S.S. Sinha, Prof, S.P. Gupta, Prof. Shyam Lal, Prof. S.A. Haider, Prof. S. Ramachandran, Dr. Varun Sheel, Dr. Lokesh Sahu, Prof. K. P. Subramanium, Dr. Bhas Bapat, Dr. Som Kumar Sharma, Dr. Y. B. Acharya, Dr. B. Sivaraman, Dr. S. B. Banerjee, Mr. M. B. Dadhania, Mr. S. Venkataramani, Mr. T. A. Rajesh, Mr. Atul Manke, and Mr. Prashant Kumar for their valuable comments and suggestions. I also thank Mr. Mitesh Bhavsar, Mr. T. K. Sunil Kumar, Raza, and Sneha for their help. I thank Dr. R. D. Deshpande for his encouragements.

I am also thankful to Arvind, Amrendra, Chinmay, Kaushik, Naveen, Ashim, Dipti, Sneha, Lijo, and Kuldeep for their help and support. I also would like to thank Dr. S. Sunda of Airport Authority of India for his help and discussions.

My special thanks and gratitude goes to my batchmates Shashi, Tanushree, Devagnik, and Kabitri. Their company is unforgettable. Special thanks to Shashi for his continued help. In particular, his help during course work and many computer related issues from software to hardware is immense. In fact, I learned 'abc' to 'xxx' of linux, LaTeX, etc., from him. He has been a constant source of information for me, both in physics and in daily life.

I am thankful to the Vice Chancellor, Jawaharalal Nehru Technological University, Hyderabad (JNTUH) and all supporting staff members of JNTUH during the installation and maintenance of the Optical Aeronomy Laboratory in JNTUH. I thank Prof. M. Anji Reddy, Dr. T.V. Lakshmi, Srikanth, Hema, Sambha, Vijay for their help.

I would like to keep on record my sincere gratitude to (late) Prof. R. Raghavarao for initiating the PRL-JNTUH collaborative work. I was fortunate to be a part of *discussions with him and Prof. P. B. Rao on many occasions. I also would like to acknowledge the discussions with Prof. K. Shiokawa (Japan), Prof. Fuller-Rowell (USA), Prof. S. Chakrabarti (USA), Prof. L. Goncharenko (USA), and Prof. D. Pancheva (Bulgaria). The foreign travel support on three occasions from SCOSTEP is also duly acknowledged.*

I would like to thank Prof. Sudhir Jain, the Director; Prof. Amit Prashant, the Dean; Prof. B. Datta, the associate Dean; and the academic section of Indian Institute of Technology, Gandhinagar for the support and help. Special thanks to Mr. Piyush for his prompt response and help during registration.

This acknowledgment section remains incomplete if there is no mention of my wonderful seniors and friends who were always there to support and help during my stay in PRL hostel. Seniors Arun, Amrendra, Abhishek, Sunil, Siddharth, Koushik, Chinmay, Sushant, Yogita and Vema have helped me to keep my loneliness away from me. In particular the 'adda' with Arun, Kaushik, Amrendra, Sunil, Chinmay, Sushant is unforgettable. I am also thankful to Waliur Rahman, Ashwini Jha, Ritesh, Arvind Singh, Pankaj, Vineet, Neeraj, Prashant, Bhaswar, Sandeep, Vimal, Ketan, Sudhanwa, Suman, Srikant, Naveen Chauhan, Naveen Gandhi, Sumita, Suchita, Satinder, Rohit for making my stay comfortable. In addition, I express my sincere thanks to my dear juniors Avdhesh, Damu, Gangi, Lekshmy, Midhun, Anjali, Arko, Bhavya, Dillip, Gaurav, Girish C., Girish K., Gulab, Monojit, Priyanka, Tanmoy C., Tanmay M., Yashpal, Dinesh, Upendra, Wageesh, Arun, Gaurava, Abhaya, Anirban, Guru, Ikshu, Kuldeep, Manu, Shraddha, Alok, Sanjay, Bivin, Apurv, Dipti, Jinia, Lalit, Rahul, Chandana, Newton, Pankaj, Venky, Chandan, Hemant, Venkata, Navpreet, Prahlad, Satish, Rukmani, Rupa, Yasir, Ali, Jabir, Komal, Manish, Vaidehi, Sneha, Upasana and several others who made my stay in PRL pleasant wonderful experience.

I also would like to acknowledge "Google" for help in various types of web searching. I also would like to acknowledge open-source packages like Ubuntu, Firefox, TexStudio, GIMP, InkScape, etc., which had made my work simpler.

I am grateful to NOAA/OAR/ESRL PSD, Boulder, CO, USA, for the NCEP/NCAR Reanalysis data. The RINEX format GPS observational and navigational data are obtained from the International GNSS Service (IGS) network.

My sincere thanks to my teachers Prof. R. Bhattacharjee, Prof. A. K. Sen, Dr. A. Deshmukhya, Dr. B. I. Sharma, and Dr. H. S. Das of Assam University for their excellent teaching. Specially, I am grateful to Dr. A. Deshmukhiya for her encouragement and friendly advices. I also would like to thank my college teacher Abhijit Nath and high school teacher Abdul Odud for their help, support, and encouradgements. Special thanks to my friends Nazmul, Suhail, Boloki, *Moumita, Golam, Atiqur and others for their constant support and encouragements.*

I take this opportunity to express my gratitude to my cousin Amzad for teaching me first lesson of physics and his constant support and encouragement throughout my career. I express my gratitude to my maternal uncles Kabir and Saleh for their encouragements.

Last, but not the least, I express my indebtedness, love, and gratitude to my parents and family. Words cannot express my gratitude for my parents, my maternal aunt, my cousins and my family members.

Fazlul Laskar

Abstract

The upper atmosphere of the Earth is influenced by incoming solar radiation (UV, EUV, and X-rays) and by secondary effects like waves from the lower atmosphere. The EUV radiation is absorbed above about 100 km altitude of the Earth's surface by atomic and molecular constituents resulting in their excitation to higher energy states. These excited species while returning to their respective ground states give rise to radiations, which are called dayglow (or daytime airglow). Chemically excited atmospheric species can also contribute to dayglow emissions. The intensity of these dayglow emissions depends on the number densities of the reactants and on the temperature. The distribution in densities of the reactants can be affected by the waves, thereby leading to the variations in the intensities of the dayglow emissions. Thus, the dayglow measurements provide an effective means to investigate the upper atmospheric dynamics, which are influenced by both solar flux variations and lower atmospheric processes.

Solar activity changes due to its internal dynamics giving rise to variations of different periods ranging from hours to years. The lower atmospheric waves are excited by topography, convection, etc., and in the presence of stable atmosphere they can propagate to the upper atmospheric altitudes. In this study we characterize various types of coupling processes in the atmosphere and their variations with waves and solar activity. The main data set that has been used in this work has been retrieved using Multiwavelength Imaging Spectrograph using Echelle-grating (MISE). MISE is a unique instrument capable of obtaining daytime sky spectra at high-spectral resolutions over a large field-of-view. From such spectra of MISE oxygen dayglow emission intensities at 557.7 nm, 630.0 nm, and 777.4 nm wavelengths have been obtained. In addition to oxygen dayglow emission intensities, data sets of ionospheric total electron content (TEC), zonal mean winds and temperatures from the stratosphere to the lower thermosphere, and the equatorial electrojet (EEJ) strengths have been used.

In this thesis, it has been shown that the lower atmospheric influence on the upper atmosphere through waves is affected by solar activity. This is because the latter is responsible for the alteration of the atmospheric background condi-

tions on which wave propagation and dissipation depend. From an investigation of the oscillations of planetary wave regime in dayglow and other atmospheric parameters at three different levels of solar activity, it has been shown that the vertical coupling of atmospheres through these waves is solar activity dependent. It is proposed that: (i) the effect on upper atmospheric dynamics due to lower atmosphere exists at least until the average sunspot number (SSN) is ≤ 35, (ii) there is a transition from the lower atmospheric forcing to mixed behavior between average SSNs of 35 to 52, and (iii) another transition from mixed effects to those of purely solar origin occurs between SSN values of 52 to 123. Further, in this thesis it has also been shown that even during high solar activity period if a sudden stratospheric warming (SSW) event occurs then the vertical coupling is enhanced, as the SSW related processes provide additional energy to enable this coupling.

A statistical study of gravity waves present in the thermospheric altitudes is made using the three dayglow emissions and the EEJ strength data obtained during the years 2011 to 2013. The gravity waves are found to be present in higher numbers in the thermosphere during higher solar activity of 2013 compared to 2011, which is attributed to a reduction in dissipation in the lower thermosphere during higher solar activity epoch.

Investigations using long-term data sets of EEJ and TEC revealed that the vertical coupling during SSW events depends on the strength of the SSW. Also, the interaction between quasi-16-day planetary waves and semi-diurnal tides has been found to be very strong for the strong major SSW events. In an another result, using both ground- and satellite-based optical remote sensing measurements, a new circulation cell in the mesosphere-thermosphere system has been shown to exist during SSW events, which has been alluded to in previous modeling studies.

Keywords: Atmospheric coupling, Dayglow, Ionosphere, Upper atmosphere, Sudden stratospheric warming, Sun-Earth interaction, Gravity waves, Planetary waves.

Contents

Acknowledgements **i**

Abstract **v**

Contents **vii**

List of Figures **xi**

List of Tables **xv**

1 Introduction **1**

1.1 Background 1

1.2 Atmospheric Structure and Nomenclature 2

1.3 Atmospheric Waves 3

1.3.1 Gravity Waves 5

1.3.2 Planetary Waves 12

1.3.3 Tidal Waves 15

1.4 Sudden Stratospheric Warming 18

1.5 Atmospheric Coupling 23

1.5.1 Vertical Coupling 23

1.5.2 Ionospheric E- and F-Region Coupling 25

1.5.3 Thermosphere Ionosphere Coupling 28

1.5.4 Latitudinal Coupling 30

1.6 Solar Influence on the Upper Atmosphere 30

1.7 Summary 32

1.8 Aim of the Thesis 33

1.9 Overview of the Thesis 33

2 Experimental Techniques and Data 35

2.1 Introduction 35

2.2 Brief Background on Dayglow Measurements 36

2.3 Production Mechanisms of Dayglow 39

2.3.1 OI 557.7 nm or Oxygen Green Line 40

2.3.2 OI 630.0 nm or Oxygen Red Line 43

2.3.3 OI 777.4 nm Line 45

2.4 Multiwavelengh Imaging Spectrograph using Echelle grating (MISE) 46

2.4.1 Components of MISE 46

2.4.2 Commissioning of MISE at Field Station 53

2.4.3 Calibration of MISE 54

2.4.4 Dayglow Emission Intensity Extraction 58

2.4.5 Error Estimation in Dayglow Signals 62

2.4.6 Validation of Emission Intensities Obtained by MISE . . . 64

2.5 Other Datasets 66

2.5.1 Equatorial Electrojet (EEJ) 66

2.5.2 Total Electron Content (TEC) 67

2.5.3 TIDI Wind and SABER Temperature 71

2.6 Summary 73

3 Time Series Analysis Methods 75

3.1 Introduction 75

3.2 Time Series Analysis 76

3.2.1 Fourier Analysis 76

3.2.2 Lomb-Scargle Analysis 78

3.2.3 Wavelet Analysis 83

3.3 General Discussion 91

3.4 Summary 93

4 Dependence of Vertical Coupling on Solar Activity 95

4.1 Background 95

4.2 Longer Period Waves (Planetary-Scale) 96
4.2.1 Introduction 96
4.2.2 Data Set 98
4.2.3 Results and Discussion 100
4.2.4 Conclusion: Longer Period Waves 111
4.3 Shorter Period Waves (Gravity Waves) 112
4.3.1 Introduction 112
4.3.2 Data Description 115
4.3.3 Results and Discussion 117
4.3.4 Conclusion: Shorter Period Waves 124
4.4 Summary 125

5 Dependence of Vertical Coupling on Strength of SSW 127
5.1 Background 127
5.2 Data Set 132
5.3 Analysis Methodology 133
5.4 Results and Discussion 135
5.5 Summary 141

6 Mesosphere-Thermosphere Circulation During SSW 143
6.1 Background 143
6.2 SSW Events in 2010, 2011, 2012, and 2013 145
6.3 Measurements and Observations 146
6.4 Results and Discussion 150
6.5 Summary 158

7 Summary and Future Scope 159
7.1 Summary 159
7.2 Future Scope 162

Bibliography 165

List of Publications 189

Publications Attached with Thesis **193**

List of Figures

1.1 Classifications of the atmosphere 3

1.2 Types of waves in the atmosphere 4

1.3 Dispersion diagram of gravity waves 8

1.4 Stability conditions in terms of temperature distribution. 10

1.5 The non-linear wave breaking scheme 11

1.6 Perturbation vorticity field and induced velocity field 13

1.7 Laboratory simulation of Rossby waves 14

1.8 Schematic of the atmospheric/oceanic lunar-tide 16

1.9 Barometric variation at equatorial- and mid-latitudes 16

1.10 Hough functions for semi-diurnal and diurnal tides 19

1.11 NCEP/NCAR reanalysis arctic temperature & wind at 10 hPa . . 21

1.12 Seasonal variation of arctic stratospheric temperatures at 10 hPa . 21

1.13 Occurrence time of SSW events as a function of DOY 22

1.14 Schematic of wave dynamics in the atmosphere 24

1.15 Zonally averaged temperature anomalies 25

1.16 Schematic of coupling between E and F regions 26

1.17 Simulated electron density contours 27

1.18 Ionogram with spread-F 29

1.19 Sunspot number variation during solar cycle 23 and 24 31

1.20 Ionospheric and thermospheric parameters w.r.t. solar activity . . 32

2.1 Oxygen energy level diagram 40

2.2 OI 557.7 nm volume emission rate observed by WINDII 43

2.3 Schematic of MISE 47

2.4 Chromatic aberration in lenses 49
2.5 Description of echelle grating 49
2.6 Simulation of diffraction orders w.r.t. wavelength 51
2.7 Ray-trace simulation of relative positions of different wavelengths 52
2.8 Observational locations over Indian longitudes 53
2.9 Viewing arrangement for MISE at JNTUH 54
2.10 Sample spectral image formed by MISE 55
2.11 Flat field correction 56
2.12 Spatial/view angle calibration 57
2.13 Viewing geometry of MISE 57
2.14 Details of dayglow emission extraction method 60
2.15 The scattered sky background from MISE 63
2.16 Comparison of measured dayglow emission intensity with empirical and GLOW model estimates 65

3.1 Fourier spectrum of hourly values of EEJ 77
3.2 Lomb-Scargle periodogram of EEJ with data gaps 82
3.3 Box representation of time and frequency resolution of STFT . . . 84
3.4 Description of Morlet wavelet 86
3.5 Morlet daughter wavelets with different scales and translations . . 86
3.6 Box representation of time and frequency resolutions for Fourier, STFT, and wavelet transforms 87
3.7 An example of wavelet power spectrum 91
3.8 An example of frequency aliasing 92

4.1 Standard score of TEC from southern and northern crest 100
4.2 The daily dayglow emission intensities at three wavelengths 101
4.3 Daily values of dayglow, peak-EEJ, TEC, SSN, and SZA 102
4.4 Daily-averaged OI 630.0 nm dayglow emissions obtained from Chile 103
4.5 Periodograms of atmospheric parameters obtained at different altitudes and of SSN 105
4.6 Wavelet spectra of the parameters seen in Figure 4.5 108

4.7 Dayglow emission intensities during the winters of 2011 to 2013 . 116
4.8 SSN and DST index during the winters of 2011 to 2013 116
4.9 An example of data analysis methods used 118
4.10 Statistics of periodicities obtained for all wavelengths 119
4.11 Modeled gravity wave drag 120
4.12 Statistics of periodicities in EEJ 121

5.1 ΔH variations over Trivandrum 129
5.2 Daytime vertical **E**×**B** drifts measured over Jicamarca 130
5.3 Hourly-binned daily values of EEJ & its periodograms 134
5.4 Contour plot of Lomb-Scargle periodograms of EEJ & TEC . . . 136
5.5 Inter-relationship of ΔT, SSN, and power of quasi-16-day periods in EEJ and TEC 138
5.6 Amplitudes of semidiurnal tides and quasi-16-day waves in EEJ . 140

6.1 Variations of F10.7 index and arctic winds & temperatures at 10 hPa 145
6.2 Oxygen dayglow emission intensity variations during SSW events 147
6.3 Enhancements in low-latitude OI dayglow during SSW events . . 148
6.4 Variations in daily averaged dayglow and lower thermospheric temperature & wind 150
6.5 Zonal mean TIDI measured meridional wind 154
6.6 Model simulation showing enhancement in oxygen density over low-latitudes during SSW 156
6.7 Schematic of the proposed meridional circulation in mesosphere-thermosphere during SSW 157

List of Tables

1.1 Some of the important waves present in the atmosphere of the Earth. 5

2.1 Characteristics of MISE. 48

4.1 The total number of occurrences of gravity waves with frequencies (or periods) greater than 0.33 hr^{-1} (less than 3 hrs.) and less than that of Brunt-Väisälä frequency at that altitude. 122

4.2 Percentage occurrences per bin in the given frequency ranges . . . 123

5.1 Some of the atmospheric and solar parameters during the years 2005-2013 132

Chapter 1

Introduction

1.1 Background

The sun acts as the primary source of energy for the solar system bodies. The solar influence on the upper atmosphere (region above 60 km altitude) occurs through the energy inputs from the incoming electromagnetic (mainly extreme ultraviolet, X-rays) and corpuscular (particle precipitation) radiations. The corpuscular radiation is essentially restricted to the high-latitude upper atmosphere but, on occasions, during geomagnetic storms their effects can be of appreciable magnitudes over the equatorial latitudes [*Paulikas*, 1975]. At altitudes above 100 km, the solar Extreme Ultraviolet (EUV) radiation is absorbed primarily by oxygen. Between 30 and 70 km altitudes the solar ultraviolet (UV) radiation is absorbed by ozone [*Rishbeth and Garriott*, 1969]. The visible radiation is absorbed by the land and sea surfaces which then re-emit them in longer wavelength like a black body. The water vapor and the carbon dioxide absorb the re-radiated longer wavelength radiation and keep the atmosphere of the Earth warm. Due to non-uniform coverage of the land and sea and due to the inhomogeneities in the land surfaces, there occur various kinds of instabilities which act as perturbation for the generation of waves [*Beer*, 1974]. Depending on the stability of the ambient atmosphere these waves can propagate towards higher altitudes. In this chapter we will discuss the different terminologies and nomenclature of the atmosphere, various types of waves, and related processes in the whole atmosphere.

1.2 Atmospheric Structure and Nomenclature

On average, the dry atmosphere of the Earth contains approximately 78% nitrogen, 21% oxygen, and the rest 1% is other constituents. Based on the temperature structure, composition, ionization, etc., the atmosphere has been classified into different 'spheres' as shown schematically in Figure 1.1. The black-body radiation emitted by the earth decays radially away from the surface and hence the temperature decreases. The atmosphere from surface up to about 12 km height region is called the *troposphere*. The region around 12 to 17 km altitude, where the temperature decrease with height pauses, is called the *tropopause*. Above the tropopause, temperature starts increasing due to absorption of UV radiation by ozone up to around 50 km altitude. This altitude region between tropopause and ~50 km is known as the *stratosphere*, and the height at which the temperature increase with height pauses is called the *stratopause*. Above the stratopause, there are no in-situ sources of heating up to around 85 km and this region is known as the *mesosphere*. The temperature at this region is governed by chemical and dynamical processes. The top of the mesosphere, which is called the *mesopause*, is the coldest region in the Earth's atmosphere. Above the mesopause, the temperature of the air increases with height due to absorption of solar EUV radiation by the neutral species and this region is called the *thermospere* [*Hargreaves*, 1992].

The region below 100 km is well mixed due to eddy diffusion and is called the *homosphere* or *turbosphere*. The region above 100 km, where molecular diffusion is dominant and different species are distributed according to their masses, is called the *heterosphere*. The boundary between homosphere and heterosphere is called the *turbopause*. There is a region within the heterosphere where hydrogen and helium are the main constituents and this region is called *protonosphere*.

Due to the influence of incoming solar EUV radiation, some of the neutral species of the upper atmosphere get ionized. This ionized portion of the upper atmosphere (60 km to about 1000 km) is called the *ionosphere*. Depending on the production sources, photochemical properties, and other considerations, there occur layers in the altitude profile of electron number density. Based on these layers, the ionosphere is subdivided into D-region (50-60 km to 90-95 km), E-region (90-95 km to 140-160 km), and F-region (140-160 km to about 1000 km). Sometimes, during daytime, the F-region splits up into two different layers called F1 ($\sim$ 170 km) and F2 ($\sim$ 250 km) layers. This splitting happens due to the competing effects of production and loss mechanisms [*Hargreaves*, 1992]. Since the thermosphere and the ionosphere share the same region of space many coupled dynamical processes occur in this region.

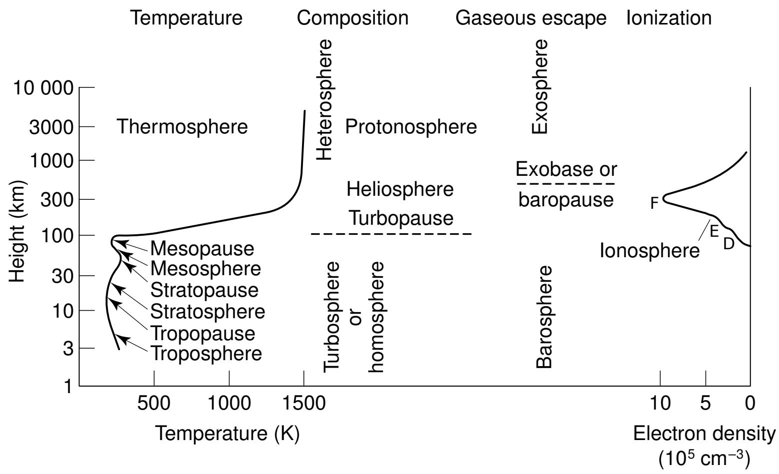

Figure 1.1: Classifications of the atmosphere based on temperature, composition, ionization etc. (After *Hargreaves* [1992])

1.3 Atmospheric Waves

Waves in the atmosphere are produced by the action of restoring forces on a displaced air parcel. If, somehow, an air-parcel is displaced (in altitude or latitude) from its equilibrium position, then it will be acted upon by inertia and restoring forces. The balance between these two forces gives rise to wave motions [*Beer*, 1974; *Salby*, 1996; *Andrews*, 2010]. The wave influence can be from the lower atmosphere or from the lower-thermosphere at high-latitudes (auroral disturbances). The lower-atmospheric wave sources are convective activities, wind-shears, natural events such as earth quake, tsunami, and volcanic eruption, or manmade explosions, etc. Whereas, in additions to these sources, the high-latitude wave sources include those due to interaction of particles of solar wind origin with those of Earth's magnetic field. The high-energetic particles from solar wind enter the high-latitude ionosphere via the highly conducting magnetic field lines and produce ionization and currents. The Joule heating due to these currents produces waves with periods of the order of hours [*Hocke and Schlegel*, 1996].

The atmosphere of the Earth is capable of sustaining various kinds of wave motions. These wave motions can be classified in various ways. Based on the direction of oscillation of the medium in response to the wave disturbance, the atmospheric waves are broadly classified into three categories: longitudinal, vertical transverse, and horizontal transverse, as depicted in Figure 1.2. All the possible waves in the atmosphere can be considered as combination of these three types [*Beer*, 1974].

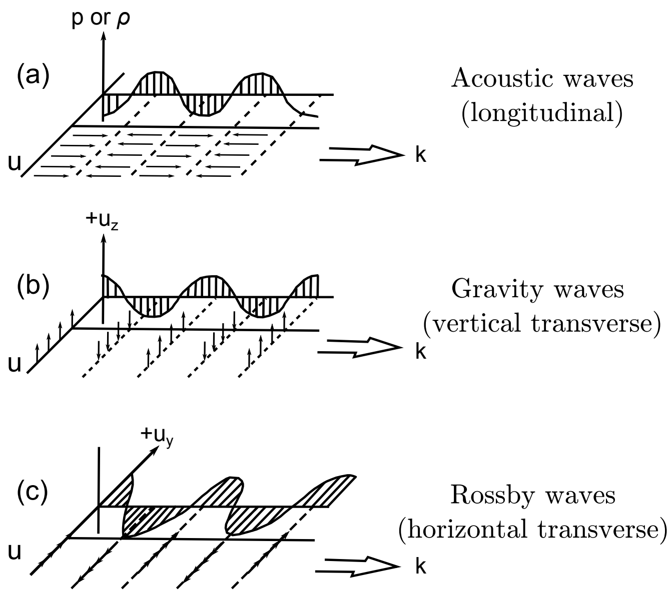

Figure 1.2: The three possible dimensions in which wave vibrations can occur in the atmosphere. The wavelengths or oscillation amplitudes are not to scale. (After *Beer* [1974])

Based on the excitation and restoring mechanisms, horizontal scale sizes, and periodicities of oscillations the atmospheric waves are categorized into various types as given in Table 1.1 along with their period of oscillation and their importance [*Beer*, 1974]. All these waves have very different excitation mechanisms and restoring forces. For completeness, here we have listed many wave types, but in this study we will restrict our discussion only to the gravity waves, tides,

Waves	Period	Importance
Acoustic	< 270 sec	Speech
Gravity	BV to 3 Hrs.	Ionosphere, UA
Atmospheric tides	24/m, m=1, 2,	Ionosphere, GM, UA
Planetary	$\sim$ days	Meteorology, UA
Semi annual	$\sim$6 months	Meteorology
Annual	$\sim$1 year	Meteorology
Quasi biennial	$\sim$2 years	Meteorology

Table 1.1: Some of the important waves present in the atmosphere of the Earth. Those in bold fonts are of interest in this study and are discussed in the text. Where BV, UA, and GM stands for Brunt-Väisälä period (the natural period of oscillation of an air-parcel in the atmosphere), upper atmosphere, and geomagnetism. (Adapted from *Beer* [1974].)

and planetary waves, which are of importance to the upper atmosphere (UA), ionosphere, and geomagnetism (GM).

Other classifications include: free (e.g., global normal modes) and forced (e.g., thermal tides which are continually maintained by an excitation source); stationary (phase is fixed with observer on Earth) and traveling (whose phase surfaces move); steady (no variation of amplitude with time) and transient (amplitude varies with time) [*Andrews et al.*, 1987]. The details of the waves that are of important to this study are described below.

1.3.1 Gravity Waves

The most well-known wave in the atmosphere is the sound (acoustic) waves through which we communicate directly with others. These longitudinally vibrating waves arise due to the balance between inertia (resistance to change in velocity) and compressibility (resistance to change in volume). These waves have timescales short enough to ignore rotation, heat transfer, friction, and buoyancy. In a homogeneous force-free medium (absence of gravitational, electromagnetic, etc., forces) these acoustic waves are the only possible waves. The atmosphere of the Earth is under the influence of its gravity and thus there occurs density gradients which decreases exponentially with altitude. This density gradient provides a static stability that is completely absent in a homogeneous medium. For waves with characteristic sizes greater than 100 km the effect of buoyancy or gravity force (ρg; ρ=number density and g=acceleration due to gravity) cannot be neglected in comparison to the pressure gradient (Δp) forces. When the restoring forces due to gravity and the compressibility forces on an air-parcel become comparable, the waves formed are called Acoustic Gravity Waves (AGW). Very often the term AGW is also used for atmospheric gravity waves. Sound waves are a class of AGW having very high frequency. When the restoring force for the dominant motion in the atmosphere is due to gravity (which is the cause of density gradient) the resulting waves are called gravity waves. As most of the gravity waves propagate in slanted path, the oscillation of an air-parcel experiencing gravity waves will not be longitudinal as that of sound waves as gravity acts in the vertical direction. Only for the vertically propagating gravity waves the wave oscillations will be longitudinal.

1.3.1.1 Propagation of Gravity Waves

As the atmosphere of the Earth is inhomogeneous (due to the existences of density gradient) the waves propagating through it would be expected to be both anisotropic (properties not same in all directions) and dispersive (wave velocity depends on wavelength). The anisotropy is due to dissimilar pulls in the horizontal and vertical directions. For example, the gravitational and Coriolis forces affect the waves in the vertical and horizontal directions, respectively. Gravity or buoyancy waves have time-scales short enough to ignore rotation, heat transfer, and friction. Also, they involve motions transverse to the direction of propagation and hence can be described using only two coordinates (x for horizontal and z for vertical). For a basic state of the atmosphere that is isothermal, in uniform motion, and assuming sinusoidal variations for the perturbed quantities in the equation of motion, continuity equation, and equation of state, the dispersion relation can be shown to be of the form [*Beer*, 1974; *Salby*, 1996; *Kelley*, 2009]:

$$\omega^4 - \omega^2 s^2(k^2 + m^2) + (\gamma - 1)g^2k^2 - \gamma^2 g^2 \omega^2/(4s^2) = 0 \tag{1.1}$$

where, γ is the ratio of specific heats at constant pressure (c_p) to constant volume (c_v) and ω, k, and m, are the angular frequency, horizontal wave number, and vertical wave number, respectively, s is the speed of sound, and g is the acceleration due to gravity. The contribution of Coriolis effect has not been considered here as these waves are of very short periods compared to the rotation period of the Earth.

Eq. (1.1) can be simplified to give

$$m^2 = \left(1 - \frac{\omega_a^2}{\omega^2}\right)\frac{\omega^2}{s^2} - k^2\left(1 - \frac{\omega_b^2}{\omega^2}\right) \tag{1.2}$$

where, $\omega_a = \gamma g/(2s)$ is the acoustic cut-off frequency, which is the resonance frequency of a column of air extending through the whole atmosphere. $\omega_b = (\gamma - 1)^{1/2} g/s$ is the buoyancy or Brunt-Väisälä frequency and is the natural frequency of oscillation of a displaced air-parcel with buoyancy as the restoring force. Figure 1.3 shows the dispersion diagram corresponding to Eq. (1.2). The waves whose frequencies are greater than ω_a are called acoustic waves and those with frequency less than ω_b are called internal atmospheric gravity waves. For waves with $\omega^2 \gg \omega_b^2$, Eq. (1.2) becomes:

$$k^2 + m^2 = \left(1 - \frac{\omega_a^2}{\omega^2}\right)\frac{\omega^2}{s^2} \tag{1.3}$$

This represents the acoustic regime where buoyancy forces are negligible. Again, for waves with $\omega^2 \gg \omega_a^2$, Eq. (1.3) becomes:

$$s = \omega/\sqrt{(k^2 + m^2)} \tag{1.4}$$

This gives the dispersion relation for a pure sound wave for which the phase speed is independent of direction. Now for lower-frequency waves, putting $\omega^2 \ll s^2k^2$ in Eq. (1.2), which removes the compressibility effects, we get,

$$m^2 \equiv k^2\left(\frac{\omega_b^2}{\omega^2} - 1\right) \tag{1.5}$$

which represents a pure gravity wave. For a propagating wave, both k and m

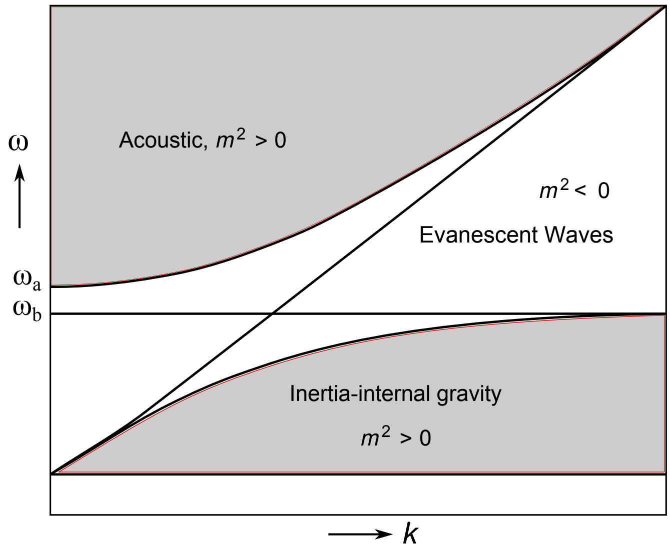

Figure 1.3: The dispersion diagram of gravity waves. (Adapted from *Kelley* [2009])

must be positive and thus the frequency ω must be larger than ω_a or smaller than ω_b (from Eqs. (1.3) and (1.5)). These acoustic and gravity wave regimes (where $m^2 > 0$) are shown in Figure 1.3 with grey shadows. The angle of propagation (θ) is given by $\tan^{-1}(m/k)$. In between these two regimes $m^2 < 0$ and the waves are external. Acoustic-gravity waves then propagate horizontally, with energy that decreases exponentially above the forcing and no net influence in the vertical direction, so the waves are evanescent and do not propagate vertically [*Salby*, 1996].

The group velocity and phase velocity derived from the dispersion relation can be shown to be of opposite sign, which means that if the wave propagates upward, then the phase velocity will be in the downward direction. This peculiarity follows from the dispersive nature of gravity waves and applies to all waves whose vertical restoring force is buoyancy. The energy propagates along the direction of group velocity. The particle motion under the action of AGW is elliptic, that is, they experience the longitudinal displacement of a sound wave and the transverse displacement of a gravity wave.

For an inhomogeneous, non-isothermal atmosphere in which the air is in motion with mean speed $\bar{u}$ and the basic state of the system varies with height, the dispersion relation can be shown to be as [*Salby*, 1996]:

$$m^2 = \frac{\omega_b^2}{(s-\bar{u})^2} - k^2 - \frac{1}{4H^2} \tag{1.6}$$

where $H(= k_B T/Mg$, with M, k_B, T, and g are mean molecular mass, Boltzman constant, temperature, and acceleration due to gravity, respectively) is the scale height. The greater the ω_b^2 (which is a measure static stability), the shorter the vertical wavelength, the more vertical propagation is favored. Since increase in k^2 reduces m^2, short horizontal wavelength (large k) are less able to propagate vertically than the long horizontal wavelength (small k). For a particular value of k, if m^2 is zero (i.e., the vertical wavelength infinite), then the propagation is forbidden and wave activity is fully reflected. The height where this occurs is called the turning level, above which wave structure is external ($m^2 < 0$). The vertical propagation is also controlled by mean flow, decreasing $s - \bar{u}$ favors vertical propagation by increasing m^2. If $s - \bar{u}$ decreases to zero, then Eq. (1.6) becomes singular and the vertical wavelength collapses to zero. The height where this occurs is called the critical level. Contrary to a turning level, which leads to reflection, the condition $m^2 \to \infty$ leads to absorption of wave activity. This is the reason why, if the phase velocity of wave and mean wind velocity are in the same direction then the wave dissipation is higher.

1.3.1.2 Dissipation of Gravity Waves

As stated above, the gravity waves are produced due to the combined action of disturbance and the buoyancy forces. The more stable the atmosphere is, the higher will be the possibility of gravity waves as in stable atmosphere gravity waves dissipate less. In the atmosphere the stability is controlled by the temperature distribution. The meteorologists derive a parameter called potential temperature (denoted by θ) to define the stability of the atmosphere. It is the temperature that a parcel of air would attain if brought adiabatically to a reference pressure (1000 mb). An atmosphere in adiabatic equilibrium has a constant potential temperature throughout. Figure 1.4(a) represents an atmosphere for which the vertical temperature gradient (α) exceeds the adiabatic temperature gradient (α^*). In such a situation an air parcel displaced (which follow adiabatic path) upward from the equilibrium will find itself in lower temperature than the surrounding (i.e., it feels heavier) and thus sinks back toward the original position. Such situations are stable and sustain wave motions. While for situations as shown in Figure 1.4(b) is unstable and a packet displaced in either direction will keep moving and thus will not sustain wave motions. The Brunt-Väisälä frequency ($\omega_b = gd(ln\theta)/(dz)$) is also a measure of stability. Greater the ω_b, higher is the stability.

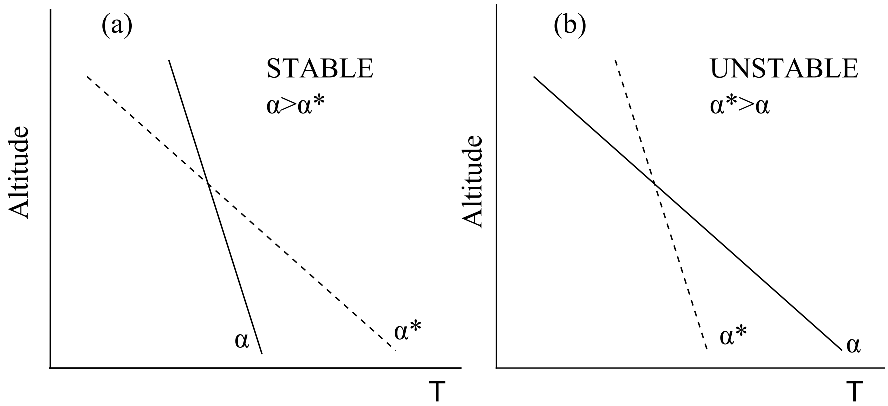

Figure 1.4: Temperature distribution for (a) stable and (b) unstable atmosphere. (After *Beer* [1974])

The stability of the atmosphere may be disturbed by waves and turbulences. It is not simple to differentiate between turbulence and waves. If turbulence exists for a stratified fluid, some of the energy of the turbulence is transformed into waves. The other possibility is, turbulence can grow at the expense of the energy present in waves, either by wave breaking phenomena, or by taking wave energy from the compressions and rarefactions. The energy of the turbulence is continually passed from larger to smaller scale motions. At the lower limit, a stage reaches where fluctuations are too small to form smaller eddies and then the energy of turbulence is ultimately converted into the kinetic energy of the molecules by viscosity. Thus, the viscous effect arises both from the diffusion of energetic molecules or from turbulence. Wave dissipation through thermal conduction is also comparable to viscosity. Viscosity is a measure of momentum diffusion, whereas, thermal conductivity is a measure of energy (i.e., heat) diffusion. Greater the thermal conductivity, the energy of the waves will be dissipated rapidly. Wave dissipation by kinematic viscosity and thermal conductivity are related as both are molecular diffusion phenomena.

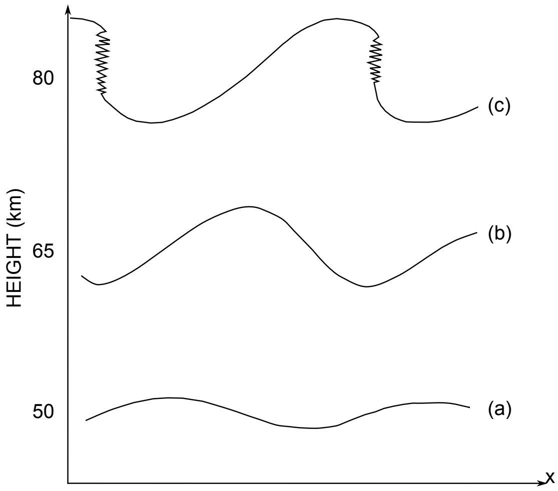

Figure 1.5: The non-linear wave breaking scheme. At mesospheric altitudes the amplitudes are very large and non-linear processes lead to the wave breaking. (After *Salby* [1996])

The kinetic energy of the waves is given by $\rho A^2/2$, where A is the amplitude of the waves. As the wave propagates upwards its amplitude increases to conserve the kinetic energy. At lower heights the wave amplitudes are too small to interact with other waves or with itself, but at higher altitudes the amplitudes becomes very large and non-linear effects start to arise as shown in Figure 1.5. At some altitude the wave amplitude becomes so large that the disturbance at one side loses interaction with the other side and thus the waves break down. In another situation, if a wave disturbance with higher energy air-parcel reaches lower energy region then the radiative heat transfer will help in damping the wave disturbance, in such cases, the wave's energy is dissipated as heat energy to the medium. This radiative energy transfer is most effective for long period waves, like planetary waves.

In section 1.3.1 it is mentioned that wind-shears can generate gravity waves. But they can also contribute to the dissipation of waves. In the presence of large wind-shear, waves become unstable [*Bretherton*, 1969]. Under the action of this instability (called Kelvin-Helmholtz instability) the amplified gravity waves break down and form patches of turbulence. A simplistic illustration of the wave breaking is given in Figure 1.5(c). Say, the wind is stronger at the upper part of the wave and opposite to the direction of propagation of the wave, then the upper part will deform faster compared to the lower part and thus non-linear process develops leading to wave breaking [*Beer*, 1974; *Fritts and Alexander*, 2003; *Holton*, 2004]. We will discuss more about the wave dissipation in Chapter 4 while discussing results on gravity waves.

1.3.2 Planetary Waves

While discussing gravity waves we have neglected the effect of rotation of the Earth or the Coriolis force on air parcels as their effects on the short period waves are very feeble. But for waves that have periods larger than days, these effects must be considered.

The planetary or Rossby waves are atmospheric waves with planetary scale size and have periods of the order of planetary rotation. For these waves the effect of rotation of the Earth cannot be neglected. Under barotropic (pressure balanced) condition of the atmosphere, the planetary waves are absolute vorticity (a measure of rotation in a fluid) conserving motions. The curl of absolute and relative velocity are known as absolute (η) and relative (ζ) vorticity. In large scale dynamical motions the vertical components of η and ζ are important quantities. The difference between absolute and relative vorticity is planetary vorticity (f), which is just the local vertical component of the vorticity of the Earth due to its rotation; $f \equiv 2\Omega sin\varphi$ is also called Coriolis parameter, Ω being the angular velocity of Earth and φ is the geographic latitude. Theoretical understanding of Rossby waves are given below.

Consider a closed chain of fluid parcels initially aligned along a circle of latitude as shown in Figure 1.6. As stated above, the absolute vorticity η is given by $\eta = \zeta + f$. Assume that $\zeta = 0$ at time t_0. Now suppose that at time t_1, δy is a small meridional displacement of the fluid parcel from the original latitude. Then by the conservation of absolute vorticity, we have,

$$(\zeta + f)_{t1} = f_{t0} \tag{1.7}$$

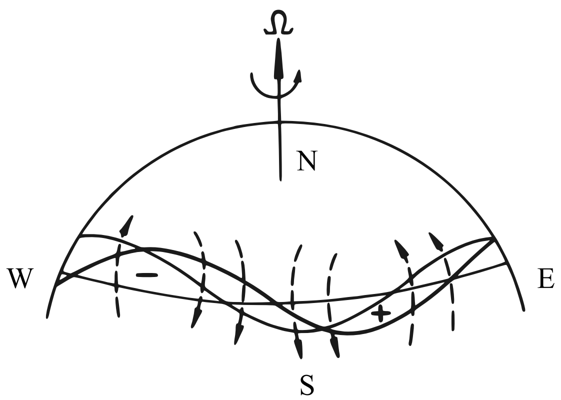

Figure 1.6: Perturbation vorticity field and induced velocity field (dashed arrows) for a meridionally displaced chain of fluid parcels. Thicker line shows original perturbation position; light line shows westward displacement of the pattern due to advection by the induced velocity. (Adapted from *Holton* [2004]).

Or

$$\zeta_{t1} = f_{t0} - f_{t1} = \beta \delta y \tag{1.8}$$

where $\beta \equiv df/dy$ is the planetary vorticity gradient at the original latitude.

From Eq. (1.8), it is evident that if the chain of parcels is subject to a sinusoidal meridional displacement, the resulting perturbation vorticity will be positive for a southward displacement and negative for a northward displacement. Since vorticity is the curl of velocity, these alternate vorticity perturbations induce meridional velocity field that advects the chain of fluid parcels southward in the west of the vorticity maximum and northward in the west of the vorticity minimum as shown in Figure 1.6. In this way the fluid parcels oscillate back and forth about their equilibrium latitude, and the pattern of vorticity maxima and minima propagates to the west. These westward propagating vorticity fields constitute the Rossby (planetary) waves. The meridional gradient of planetary vorticity acts as restoring force for Rossby waves which is just like buoyancy for gravity waves.

The speed of westward propagation, c, can be computed by letting $\delta y = a \sin[k(x - ct)]$, where a is the maximum northward displacement and x is the longitudinal distance. Then,

$$v = D(\delta y)/Dt = -kca \cos[k(x - ct)],$$

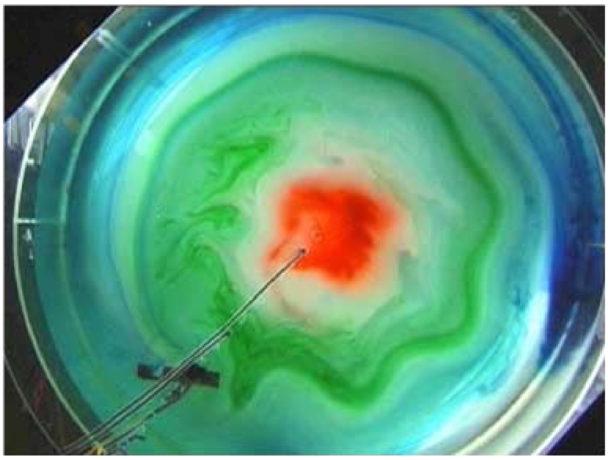

Figure 1.7: Laboratory simulation of Rossby waves in a rotating cylinder containing dye and water (as if viewed from a satellite over the north-pole of the Earth). The perturbation source is a stationary oscillator fitted at the bottom left corner. If we consider radial distance as latitude then we can see analogy of Rossby waves (Figure Courtesy: Geophysical Fluid Dynamics Laboratory, University of Washington).

and as ζ is the curl of relative velocity, we have,

$$\zeta = \partial v/\partial x = k^2 ca \sin[k(x - ct)]$$

Substituting the values of δy and ζ in Eq. 1.8, we get $c = -\beta/k^2$. Thus, the phase speed is westward relative to the mean flow and is inversely proportional to the square of the zonal wave number. A laboratory simulation of the Rossby wave formation in a cylindrical bowl is shown in Figure 1.7. One can see sinusoidal type perturbation generated in this system along the radial direction.

The dispersion relation for the planetary waves can be obtained by solving the quasi-geostropic planetary vorticity equation and can be shown to be [see, *Holton*, 1980, 2004],

$$m^2 \equiv \frac{\omega_b^2}{f^2}\left[\frac{\beta}{\bar{u} - c} - k^2\right] \tag{1.9}$$

We know that for vertical propagation, $m^2 > 0$. The gradient of planetary vorticity β, that provides the restoring force for horizontal displacements, is recognized as the essential positive contribution to m^2 – analogous to the role played by ω_b^2 for gravity waves (Eq. (1.6)). Then the Charney-Drazin criteria [*Charney and Drazin*, 1961] states that the planetary waves forced from below will propagate vertically only if,

$$0 < \bar{u} - c < \frac{\beta}{k^2} \equiv U_c \tag{1.10}$$

where U_c is called Rossby critical velocity. Planetary waves (PWs) can propagate vertically only if they have westward phase velocity relative to the mean wind and have magnitude less than U_c. For stationary waves ($c = 0$), the vertical propagation can occur only when the mean wind is eastward and weaker than the critical velocity which depends on the horizontal scale of the waves. This propagation condition explains why large amplitude stationary waves are found only in the winter hemispheric stratosphere (where velocity is eastward in the winter) and why only the longest wavelength (small k) planetary wave modes (zonal wavenumbers 1 and 2) have significant amplitude in the stratosphere. This is a simplistic model and may not illustrate the real atmosphere accurately, but it does provide a window for the zonal velocity (greater than 0 and less than U_c) for vertical propagation.

1.3.3 Tidal Waves

Tides are global scale daily oscillations of the atmosphere that are generated due to the differential gravitational or thermal influence of the celestial bodies on the atmosphere of the Earth. Atmospheric tides are simply rotationally modified gravity waves [*Beer*, 1974]. Secondary sources of tides are the non-linear interaction between tides and planetary waves and due to latent heat release from the deep convection in the tropics [*Teitelbaum and Vial*, 1991; *Hagan et al.*, 2001]. The heating due to absorption of UV radiation from the sun and the gravitational pull of the moon generates these tides in the atmosphere. Unlike ocean tides, which are excited by lunar gravitational attraction, the largest amplitude atmospheric tides are generated due to solar influence. The gravitational tide due to sun and the thermal tide due to moon are negligible, since they have periods of sub-multiples of the solar or lunar day.

According to the gravitational tidal theory for ocean, semi-diurnal tide is the strongest lunar tidal component, i.e., there occur two maxima and two minima

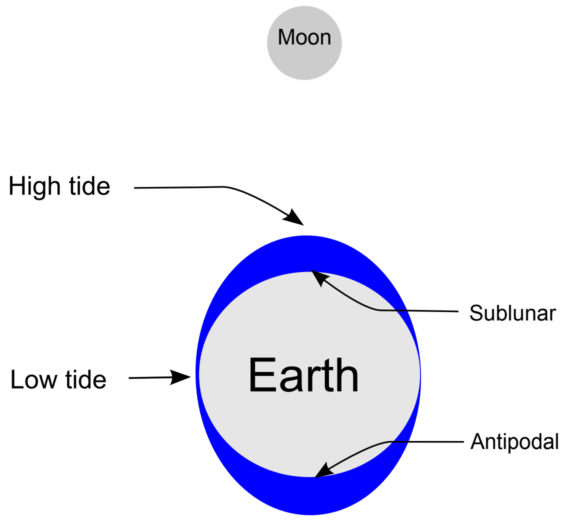

Figure 1.8: Schematic of the atmospheric/oceanic lunar gravitational tide, where blue bulged regions represents the atmosphere/ocean. It can be noted that there occurs two bulges, one each at sublunar and antipodal points. (Figure not to scale. Courtesy: https://en.wikipedia.org/wiki/Tide).

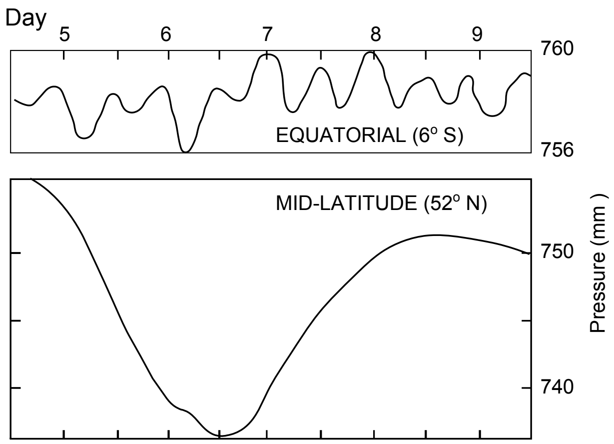

Figure 1.9: Ground based barometric pressure measurement during November 1919. Equatorial results show semi-diurnal tidal effects whereas planetary wave variations can be seen at mid-latitudes. (After *Beer* [1974])

each day at a particular location on the Earth. One maximum is at the time when moon is right overhead (sublunar) and the other is when the moon is on the opposite side (antipodal) of the observation point on the Earth as depicted in Figure 1.8. For the atmosphere, the solar thermal tides are of much large amplitudes compared to the lunar gravitational tides. Earth gets energy from the sun only during daytime (on an average for 12 hours, with a peak around local noon), so, one may expect the diurnal component to be the strongest. But observations show (see e.g., Figure 1.9) that the semidiurnal tide is of strongest amplitude at the ground level. The reason for this is that the vertical wavelength (greater than 100 km) of semi-diurnal tide is much greater than the diurnal tides (20-30 km) and thus they are excited more efficiently by deep ozone heating region and then reach the ground level altitudes. Also, the diurnal tide has more complex behavior and is trapped in the vertical close to its forcing regions [*Beer*, 1974; *Andrews et al.*, 1987]. Figure 1.9 shows the ground-based barometric measurement of atmospheric pressure which is a signature of tidal variation. One can note that the dominant variations at equatorial latitudes are the semidiurnal tide and at mid-latitudes they are planetary waves. But at heights above stratopause both diurnal and semidiurnal tides are of equal strength. The other tides with periods of around 8 hours (terdiurnal tide), 6 hours also do occur, albeit with smaller amplitudes, which are just the sub-harmonics of the solar day.

Based on their propagation direction tides are classified as migrating, non-migrating, and stationary. Migrating tides are sun-synchronous and thus, they propagate westward as viewed by a stationary observer on the Earth. Non-migrating tides do not follow the sun and they can be both eastward and westward propagating.

Laplace's tidal equation: The latitudinal and temporal structures of the tides are described by a standard equation called Laplace's tidal equation [*Longuet-Higgins*, 1968; *Andrews et al.*, 1987]:

$$L\Theta_{mn} + \varepsilon_{mn}\Theta_{mn} = 0 \tag{1.11}$$

where L is Laplace operator and is given by,

$$L = \frac{\partial}{\partial \mu}\left[\frac{(1-\mu^2)}{(\xi^2-\mu^2)}\frac{\partial}{\partial \mu}\right] - \frac{1}{\eta^2-\mu^2}\left[-\frac{k}{\xi}\frac{(\xi^2+\mu^2)}{(\xi^2-\mu^2)} + \frac{k^2}{1-\mu^2}\right] \tag{1.12}$$

where, k=zonal wavenumber, σ=frequency, $\mu = \sin\varphi$, $\xi = \sigma/(2\Omega)$, and eigenvalue

$$\varepsilon_{mn} = (2\Omega a)^2/gh_{mn}$$

with a as radius of Earth, g as the acceleration due to gravity, φ=geographic latitude, and h_{mn} is a constant called equivalent depth that relates the latitude structure of tide with vertical structure.

The atmospheric tides are eigen oscillations of Earth's atmosphere with eigenfunctions Θ_{mn}, called Hough functions, and with eigenvalues ε_{mn}. The Hough functions are labeled by (m, n), with m for longitude and n for latitude dependence. Hough functions for the semidiurnal ($m = 2$) and diurnal ($m = 1$) tides for different n are shown in Figure 1.10. Even and odd values of n represent the symmetric and anti-symmetric components about the equator. The negative values of n correspond to non-propagating modes [*Forbes and Garrett*, 1979].

From the discussions in this section, one can anticipate that depending on their scale sizes, background wind direction, ambient density, stability of the atmosphere these waves (gravity, tidal, and planetary) can influence the dynamics of the atmosphere-thermosphere system locally or globally. The influence of these waves on the upper atmosphere at varying solar and geophysical conditions are investigated in this thesis work.

1.4 Sudden Stratospheric Warming

The Sudden Stratospheric Warming (SSW) also knows as stratospheric sudden warming, is a dynamical process which occurs in the winter season of northern-hemispheric high-latitude stratosphere. These are very dramatic events and are believed to be caused by the interaction of the wintertime enhanced planetary waves with the zonal mean flow [*Matsuno*, 1971]. In this section we will summarize the current understanding of SSW events in brief. Extensive treatment of the

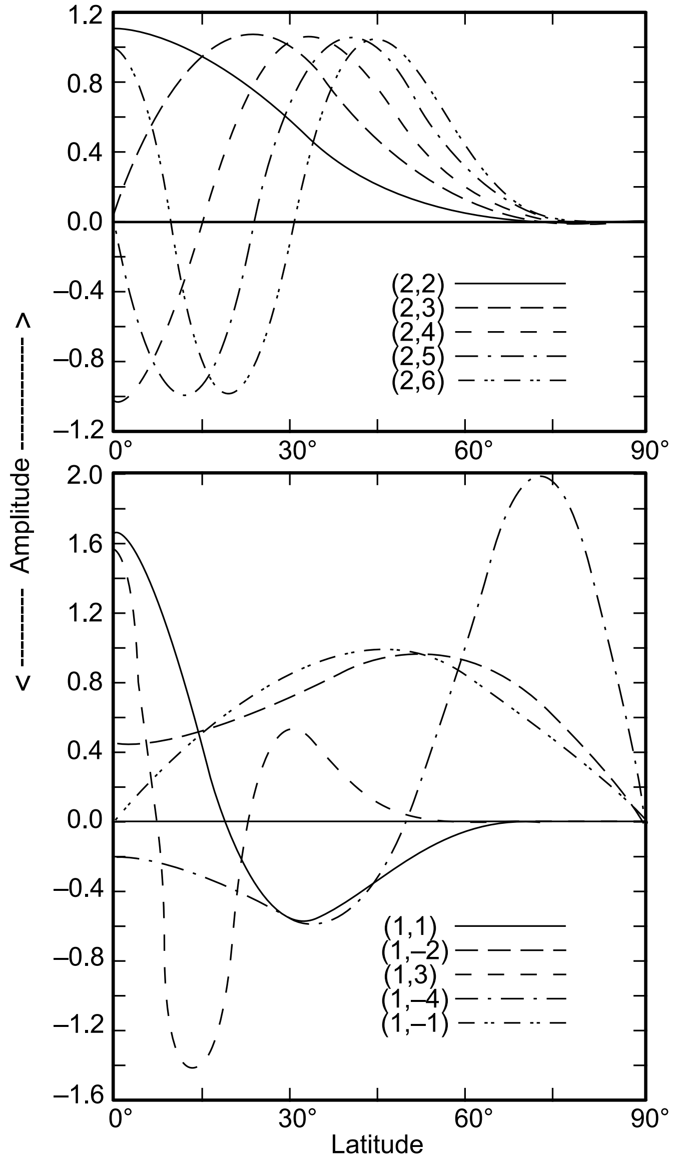

Figure 1.10: Semidiurnal (top) and diurnal (bottom) Hough functions for latitudes between 0° and 90°. (Adapted from *Forbes and Garrett* [1979])

SSW events have been reported in several review articles [*Matsuno*, 1971; *Holton*, 1980; *Chau et al.*, 2012]. The books by *Andrews et al.* [1987], and by *Holton* [2004] also provide very nice introductions on SSW along with the background theory and experimental observations.

According to World Meteorological Organization, if the stratospheric temperature at 10 hPa pressure level and poleward of 60° N increases by more than 25 K within a week then it is termed as SSW [*Labitzke*, 1977]. Due to the interaction of the PWs with the mean flow and consequent heat deposition, the usual winter-time stratospheric eastward wind becomes weak or reverses its direction. If the zonal mean zonal wind at 60° N and 10 hPa pressure level becomes westward then the SSW event is characterized as major. If with the increase in temperature the zonal mean wind becomes weak but does not reverse its direction then it is called a minor event [*Charlton and Polvani*, 2007; *Kuttippurath and Nikulin*, 2012; *Chau et al.*, 2012]. Figure 1.11 shows the zonal mean temperature at 90° N and zonal mean zonal wind at 60° N and at 10 hPa pressure level for the January-February months of the year 2013. One can note that there is an enhancement in temperature by more than 40 K and the zonal wind reversed during that time, signifying that the event was a major SSW. Figure 1.12 shows the 10 hPa stratospheric temperature over high-latitudes (60° - 90° N) for the years 2011/2012, 2012/2013, and the average values with range and percentage deviations for 1978-2012. It is very clearly noticeable that there occurs enhancement in the stratospheric temperatures in the winter months. On averages there occurs 6.2 SSW events per decade [*Charlton and Polvani*, 2007]. Figure 1.13 shows the occurrence time of major SSW events as a function of day of the years (DOY) from 1958-2013. It can be noted that most of the events have occurred during the months of January-February.

The first exhaustive theoretical explanation of SSW event was given by *Matsuno* [1971], and until today it is considered to be the best explanation of this meteorological event. Matsuno's heuristic model of SSW event consists of the following sequence,

1) Quasi-stationary planetary waves of zonal wavenumbers 1 or 2 become anoma-

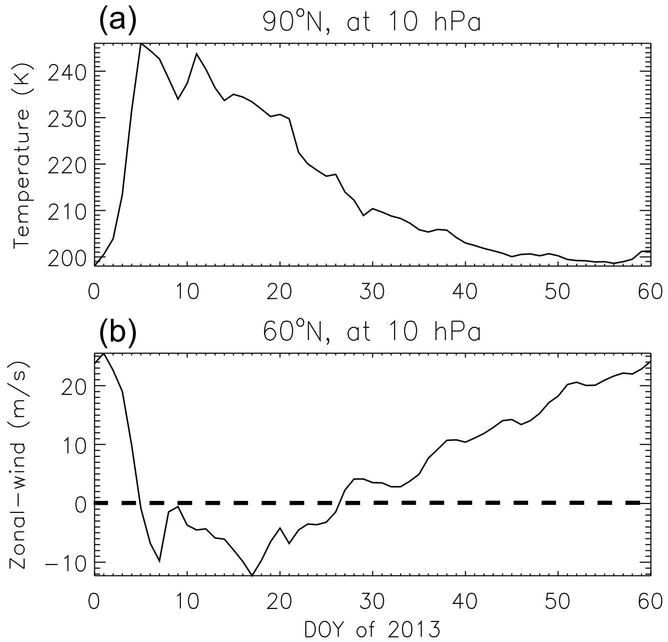

Figure 1.11: (a) The temperature at 90° N and (b) zonal mean wind at 60° N at stratospheric level (10 hPa) are shown. (Temperature and wind data are obtained from the NCEP/NCAR reanalysis project of National Oceanic & Atmospheric Administration (NOAA).)

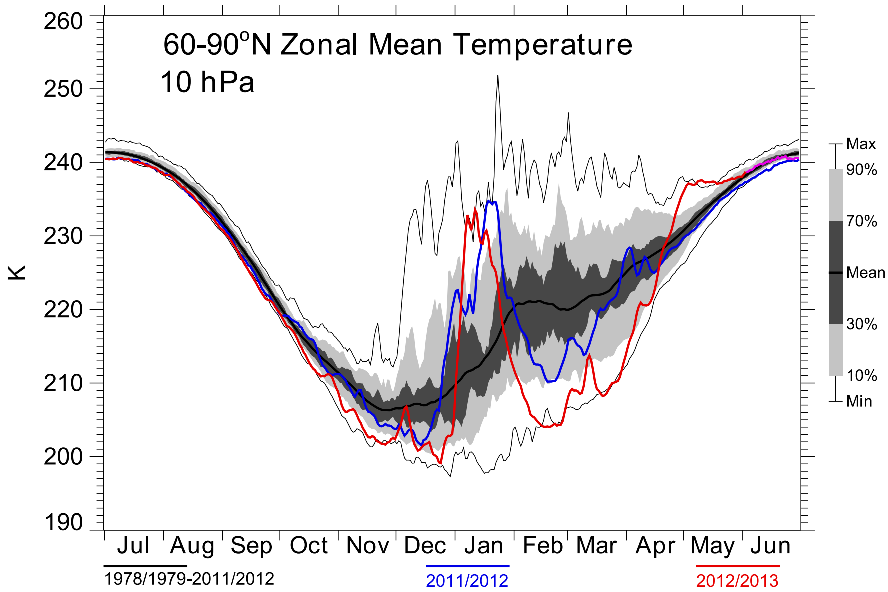

Figure 1.12: Stratospheric temperatures at 10 hPa pressure and 60-90° N obtained from the MERRA reanalysis project. One can clearly see the enhancement of the stratospheric temperature in the winter season. (Figure courtesy: MERRA project of NASA)

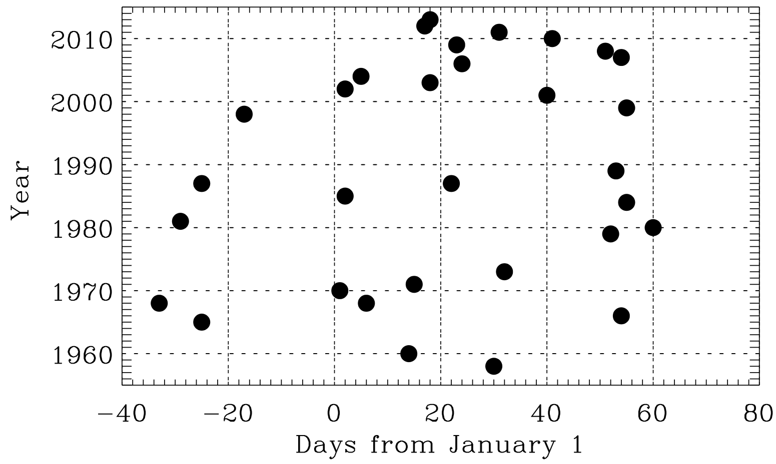

Figure 1.13: Occurrence time of SSW events as a function of day of the years from 1958-2013 (adapted from [*Chau et al.*, 2012]).

lously large in the winter-troposphere;

2) The growing waves propagate into the stratosphere under the favorable condition of winter-time eastward wind;

3) Interaction of the waves with mean flow decelerate the mean winds causing the polar night jet to weaken and become distorted by the growing waves;

4) If the waves are sufficiently strong then the mean flow may decelerate sufficiently so that a critical level (westward phase velocity of planetary wave equals the eastward wind velocity) is formed;

5) Further, upward transfer of wave energy is then blocked and a very rapid westward acceleration and polar warming occurs as the critical level moves downward.

Since the cause of the SSW events is the planetary waves which themselves are very large-scale events, low-spatial and temporal resolution measurements are sufficient for their investigation. This is the reason why the prediction of SSW events are possible as per *Lorenz* [1963] explanations of deterministic non-periodic flow, which states that the prediction of a non-linear system is possible only when the present conditions are known with sufficient accuracy. As the planetary waves have higher amplitudes in the northern hemisphere and the wind is favorable (eastward) during northern winter, the SSW events are mainly observed in the Northern hemisphere.

1.5 Atmospheric Coupling

The coupling of the atmospheres means that two different regions/geo-locations of the atmosphere are somehow connected to each other. Atmospheric coupling can be of two types: physical and chemical, which are very often inter-related. Physical transport can be in the form of radiative, wave dynamical, and electrodynamical, whereas, the chemical coupling happens through compositional transport. These couplings can happen in both horizontal and vertical direction. In this thesis work some of the coupling processes mentioned above have been studied. With regard to coupling between lower and the upper atmosphere, by lower atmosphere we mean atmosphere below turbopause. Below, we describe a variety of classes of these couplings which have been referred in various chapters in this thesis.

1.5.1 Vertical Coupling

Traditionally troposphere and stratosphere-mesosphere are defined as lower and middle atmosphere, respectively. As all these spheres (troposphere, stratosphere, and mesosphere) are below turbopause, in this thesis, however, they are jointly referred to as the lower atmosphere and the effects/developments in this combined (lower atmosphere) region are investigated in the upper atmosphere. Troposphere is the region where majority of the convective activities (thunderstorm, hurricane, cyclone, tornado, latent heat release, etc.) take place. These convective activities can lead to various kinds of wave motions. This happens because the temperature gradient in this region is negative and also satisfies the stability condition as discussed in section 1.3.1 (Figure 1.4). As discussed in section 1.3, lower atmospheric waves can propagate to the higher altitudes and influence the energetics and dynamics of the upper atmosphere. Figure 1.14 represents a schematic of the formation of gravity waves in the troposphere and their propagation towards mesosphere. Many of these waves are dissipated around the mesopause region where the non-linear effects are very prominent and deposit their energy there. The energy accumulated in this way may accelerate the mean flow and can also form secondary waves [*Fritts and Vadas*, 2008; *Vadas and Liu*, 2009].

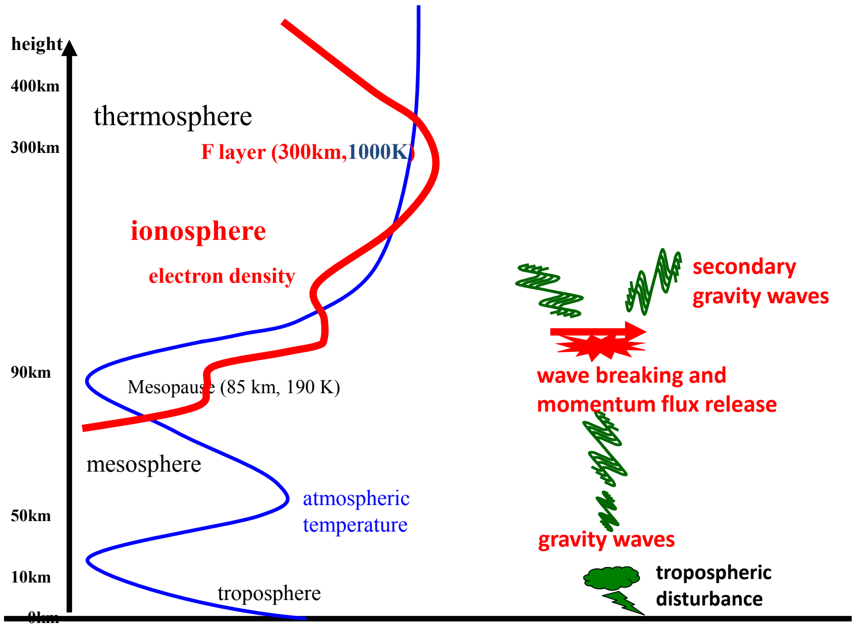

Figure 1.14: A schematic (not to scale) of the atmosphere ionosphere system with waves. (After Prof. K. Shiokawa, Lecture series in United Nations Centre for Space Science and Technology Education in Asia and the Pacific (CSSTEAP) course, 2011).

An example of lower and upper atmosphere coupling through large scale motions is the formation of SSW as discussed above. During an SSW event, not only does the dynamics at high-latitude stratosphere get affected, but also there occur alternate layers of heating, cooling, and heating in the stratosphere, mesosphere, and lower-thermosphere, respectively. These heating and cooling phenomena during SSW events occur due to altered circulation pattern and wave dynamics during SSW events. Figure 1.15 shows an example of the temperature measurement from the Michelson Interferometer for Passive Atmospheric Sounding (MIPAS) on board ESA's Envisat satellite. One can note clear signatures of heating, cooling, and heating in the stratosphere, mesosphere, and lower-thermosphere in this figure.

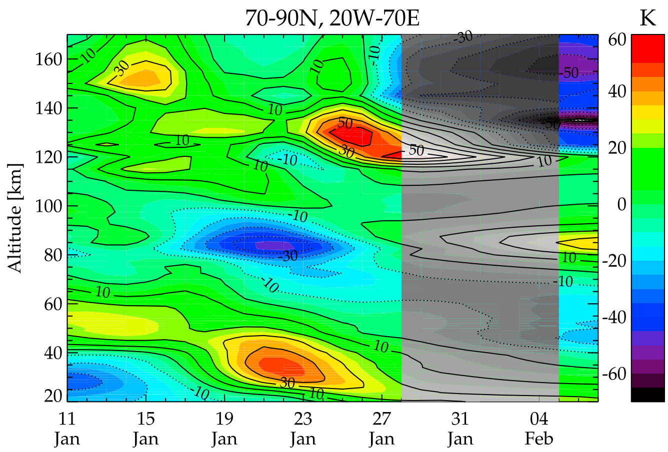

Figure 1.15: Zonally averaged temperature anomalies as obtained by MIPAS instrument onboard ESA's Envisat satellite for the SSW event in 2009. One can see clear enhancements of temperature in stratosphere and lower thermospheric altitudes and a depleting at the mesospheric altitudes. The grey portion represents data missing. (After *Funke et al.* [2010])

1.5.2 Ionospheric E- and F-Region Coupling

Ion-neutral collision frequency decreases with the decrease in atmospheric density as a function of altitude. At E-region altitudes the ion gyro-frequency (qB/m, q is charge, B is magnetic field, and m is mass) is less than the ion-neutral collision frequency, but the electron gyro-frequency is greater than its collision frequency with neutrals. Due to this, the ions in the E-region move with the neutral wind but not the electrons. Thus, there occurs charge separation and a net east-west electric field is produced in the lower E-region of the ionosphere. However, in the F-region altitudes (greater than about 170 km) as the ratios of ion and electron gyro-frequencies to their neutral collision frequencies are larger, both ions and electrons gyrate around magnetic field lines and hence no east-west electric fields are produced. The phenomenon of creation of electric field by mechanical forces such as that from wind is called dynamo action and is the reason why the lower E-region is also called dynamo region [*Farley*, 1960; *Heelis et al.*, 1974].

The east-west electric field ($\mathbf{E}$) in the dynamo region crosses with the magnetic field to produce an upward $\mathbf{E} \times \mathbf{B}$ drift. Even though this drift is independent of charge and mass only electrons respond to it as ions-are tied to the neutrals thereby producing an upward electric field. This vertical electric field again crosses with the northward magnetic field to produce a surge of westward movement of electrons resulting in an enhanced jet of current in the equatorial region, called the equatorial Electrojet (EEJ) [*Chandra and Rastogi*, 1974; *Rishbeth*, 1979; *Anandarao and Raghavarao*, 1987; *Raghavarao et al.*, 1988a].

The geometry of the magnetic field lines at low-latitudes is such that the off-equatorial E-region magnetic field passes through the lower F-region altitudes over the dip-equator as shown schematically in Figure 1.16. Since, magnetic field lines acts as equipotential lines, the electric field so produced in the off-equatorial E-region are mapped to the equatorial lower F-region. In this way the E- and F-regions in the low-latitude ionosphere are coupled. Since the electric field in the E-region is created by prevailing winds in these altitudes, the variations in winds in E-region by waves are communicated to the F-region through this coupling.

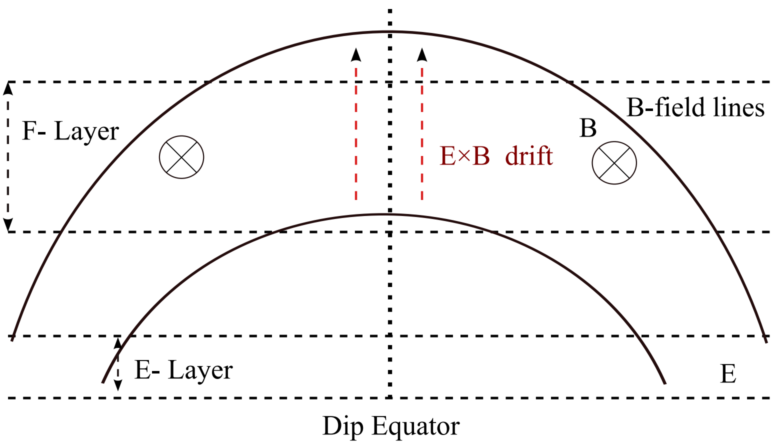

Figure 1.16: Ionospheric E-region winds generate dynamo electric fields (E) as the ions are dragged across magnetic field B. The dynamo fields are transmitted along the dipole magnetic field lines to the F region. (Adapted from *Rishbeth* [1997])

Under the action of the Earth's magnetic field and the electric field in the F-region arising from the mapping of E-region, the ions and electrons are drifted upward due to $\mathbf{E} \times \mathbf{B}$ drift as explained schematically in Figure 1.16. In the F-region, both electrons and ions are affected by the $\mathbf{E} \times \mathbf{B}$ drift. This plasma so drifted upwards moves along the magnetic field lines and away from the equator due to ambipolar diffusion. This diffused plasma then accumulates at around $\pm 15°$ degree latitudes at F-region altitudes. Due to this process there occur regions of reduced plasma densities over the dip-equatorial F-region and regions of

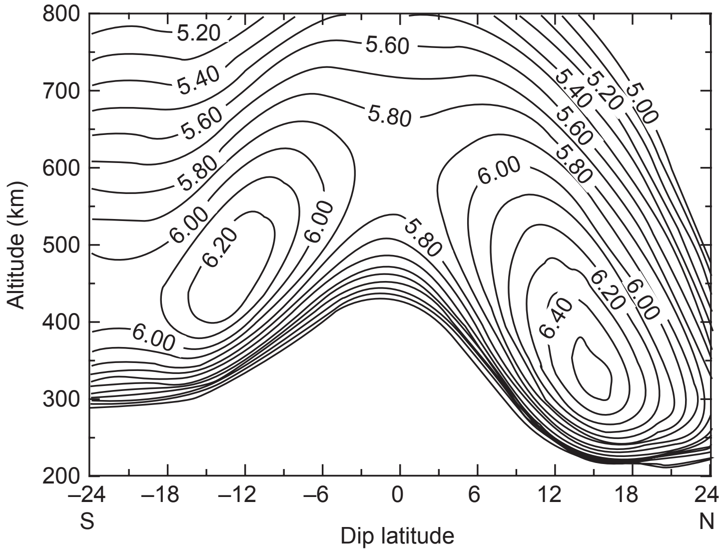

Figure 1.17: Calculated electron density contours ($\log_{10}n_e$) as a function of altitude and dip latitude at 2000 LT for December solstice conditions. Due to the meridional wind from south (summer) hemisphere to north (winter) hemisphere the electron density contours are asymmetric about the dip-equator. (After [*Anderson*, 1973])

comparatively higher plasma density at approximately ±15° latitudes. This phenomenon is known as the Equatorial Ionization Anomaly (EIA) and the regions of higher densities are called "crests" of the EIA and region over the dip-equator where plasma density is less is called "trough" of the EIA [e.g., *Farley*, 1960; *Anderson*, 1973; *Heelis et al.*, 1974; *Moffett*, 1979; *Raghavarao et al.*, 1988b; *Pallam Raju et al.*, 1996; *Heelis et al.*, 2012]. *Appleton* [1946] first reported it as an unusual or anomalous behavior but later it has been found that it is an obvious feature in the equatorial ionosphere. The EIA is also known as the Appleton anomaly or equatorial anomaly. Figure 1.17 shows modeling result of the electron density contours showing the EIA structure. The asymmetry about the equator is due to the north south (summer to winter) seasonal meridional wind. The development and variations of EIA have both day-to-day and solar activity dependence [*Rao and Malhotra*, 1964; *Sivaraman et al.*, 1976; *Rastogi and Klobuchar*, 1990; *Walker et al.*, 1994; *Pallamraju*, 1996]. The solar activity dependence of vertical coupling in the EIA region physical parameters will be discussed in Chapters 4 and 5.

1.5.3 Thermosphere Ionosphere Coupling

The neutral part of the atmosphere above about 100 km is known as the thermosphere. A brief introduction on thermosphere and ionosphere has been given in section 1.2. One can note that both thermosphere and ionosphere share the same volume in space and thus they are coupled to each other, as interaction between ions and neutrals is appreciable. Charged particles and neutrals have different mobilities and thus show differential motion. The ions in the F-region are strongly coupled to the magnetic fields and thus they exert a force on the neutrals. The drag force is given by $\nu_{ni}(\mathbf{u} - \mathbf{v_i})$, where, ν_{ni} is the neutral ion collision frequency, $\mathbf{u}$ is the neutral wind velocity, and $\mathbf{v_i}$ is the ion drift velocity. This ion drag is the reason why daytime zonal wind at F2-region is much lower than that during nighttime.

The enhanced plasma density over the crest of the EIA provides higher drag force on the neutrals compared to the trough region of EIA. Due to higher densities there will be more collisions, chemical heating, and ion-drag and thus the temperature of EIA crest region will be higher compared to that at the trough region. Also, the kinetic energies of the neutrals are lost due to these collisions which result in slowing down of the usual zonal wind at the crest regions. For the same reasons, the neutral temperature over the trough of the EIA is lower and the zonal winds are stronger than those at the EIA crest. This phenomenon of slowing down of the neutral zonal wind and rise of neutral temperature at the crest regions compared to that of trough is known as the Equatorial Temperature and Wind Anomaly (ETWA) [*Raghavarao et al.*, 1991, 1993]. Some authors call this process of higher wind over the magnetic equator compared to crest region as wind jet and the higher density over the crests is called as equatorial mass anomaly.

After the E-region sunset, the electrons and ions in this region recombine rapidly due to their higher collision frequency at these altitudes. But the F-region collision frequency is low and thus the recombination is very slow. Due to these reasons there occurs a sharp gradient in plasma density in the lower F-region. This situation is unstable and a slight perturbation in the lower F-region can lead to

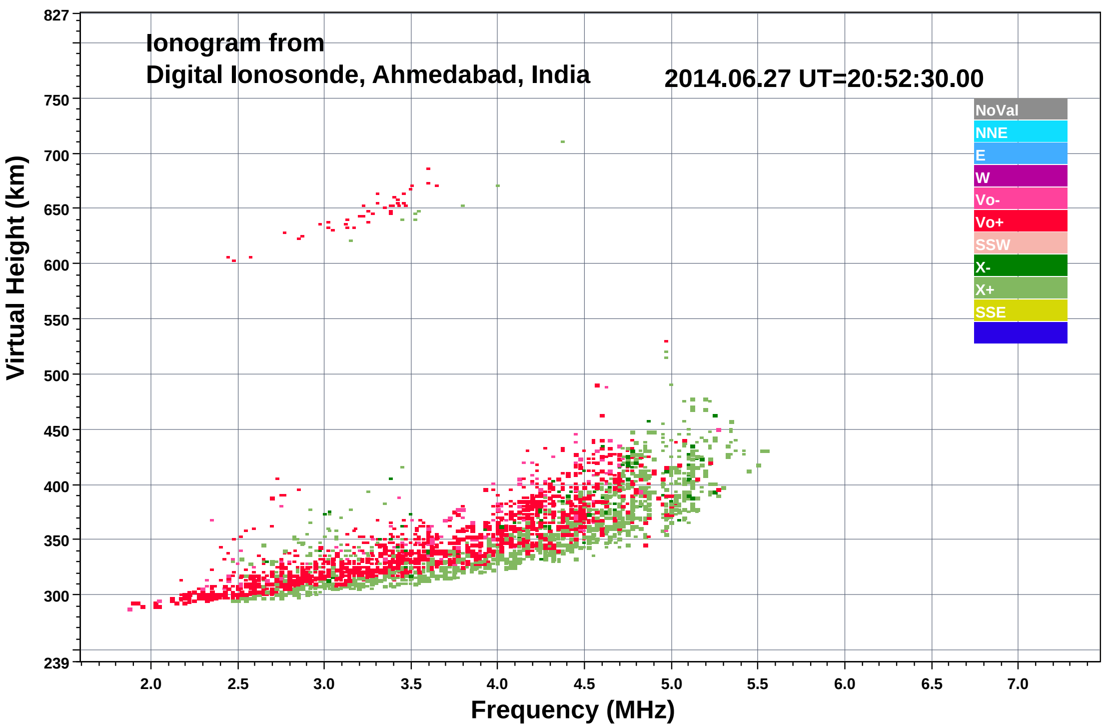

Figure 1.18: An example of spread-F as observed by the digital ionosonde (digisonde) station in Ahmedabad, India. Here one can see signatures of both range and frequency spread.

Rayleigh-Taylor like instability in the plasma fluid. As a result of this instability blobs and bubbles are formed in the ionospheric F-region. The varying densities in the boundaries of these bubbles and blobs result in anomalous scattering of the radio waves passing through the medium. So, a vertical incidence sounding of the ionosphere with ionosonde show spread in the frequency or in the virtual range. This phenomenon of the spreading of returned frequency or sounding range is called as equatorial spread-F (ESF). The ESF occurs generally after sunset but their day-to-day variability in occurrence is not yet fully understood [*Sekar and Chakrabarty*, 2008; *Kelley*, 2009]. Although it originates over the magnetic equatorial region, it can extend to several degrees in latitude. A spread-F pattern from the digisonde station in Ahmedabad is shown in Figure 1.18. This is a post-midnight (0222 hour local time) spread-F that is usually known to occur due to fossil-bubble (i.e., bubbles transported from other longitude sector) [*Sekar et al.*, 2007].

1.5.4 Latitudinal Coupling

The traveling ionospheric disturbances (TIDs) generated during geomagnetic storms can propagate towards low-latitudes, is an example of wave dynamical latitudinal coupling. There are many works in the literature showing the presence of medium-scale TIDs during geomagnetic storms [*Hocke and Schlegel*, 1996; *Shiokawa*, 2002, and references therein]. Moreover, during geomagnetic storms there occurs thermospheric meridional circulation from polar to equatorial direction, which transports lighter elements like atomic oxygen towards low-latitudes [*Mayer et al.*, 1978; *Prölss*, 1980; *Pallamraju et al.*, 2004]. There are numerous case studies of the effects of the composition transport during geomagnetic storm [e.g., *Zhang and Shepherd*, 2000; *Bagiya et al.*, 2014]. These latitudinal couplings affect even up to the low- and equatorial-latitudes. Further, there are reports of coupling of interplanetary magnetic and electric fields over the equatorial region, wherein the interplanetary electric field fluctuations have been shown to be reflected over equatorial ionosphere [e.g., *Reddy et al.*, 1979; *Sastri*, 1988, 2002; *Sastri et al.*, 1997; *Basu*, 2005; *Chakrabarty et al.*, 2008; *Bagiya et al.*, 2014]. In this thesis work a new kind of latitudinal coupling during SSW event has been demonstrated and will be discussed in Chapter 6.

1.6 Solar Influence on the Upper Atmosphere

The sun, which is the main energy source to Earth, has its own cyclic variations due changes in its magnetic activity and its internal dynamics. There are many indices of measurement of activity level of the sun. Since the upper atmosphere is affected mainly by the EUV radiation, so an EUV index is best suited for this purpose, but these radiations are absorbed by Earth's atmosphere, so ground-based measurements are not possible. It has been found that the solar 10.7 cm radio flux (F10.7 index) varies in similar fashion with that of EUV radiation [e.g., *Floyd et al.*, 2005] and thus F10.7 index is used as a proxy for solar EUV or solar activity. The F10.7 index is measured in solar flux unit (sfu, 1 sfu = 10^{-22} W m^{-2} Hz^{-1}).

Traditionally, the most commonly used index is the Wolf sunspot number [*Izenman*, 2009]. The Wolf sunspot (R) is calculated using the formula $R = k(10N_g + n)$, where, k is a factor (< 1) that varies with location and instrumentation (also known as the observatory factor), N_g is the number of sunspot groups in the solar disk, and n is the total number of individual spots in all the groups. All these indices are related to each other and their correlations are very good. Figure 1.19 shows the variation of the sunspot numbers for the last (23^{rd}) and the current (24^{th}) cycle of solar activity. The strongest cyclic variation that is observed in the activity level of the sun is of 11 years (year on Earth). The solar internal magnetic field flips its polarity in this 11-year cycle. The sun completes one rotation about its own axis in 27-days. Due to this an observer on the Earth observes a strong 27-day variations and various sub-harmonics of 11-year and-27 day variations [*Willson*, 1982]. The sub-harmonics are observed due to the distribution or scatter of the sunspots in the solar disk. One can clearly see the presence of the 11-year solar-cycle variations and other smaller scale variabilities in Figure 1.19. The average thermal behavior of the regions where the UV and EUV radiations from the sun are absorbed are mainly controlled by the sun. This is because of the fact that the variations of spectral irradiance in the UV and EUV spectra are highest in the solar electromagnetic spectrum with changes in solar activity (increase by a factor of two in the high solar activity compared to low solar activity level [*Lean*, 1997]).

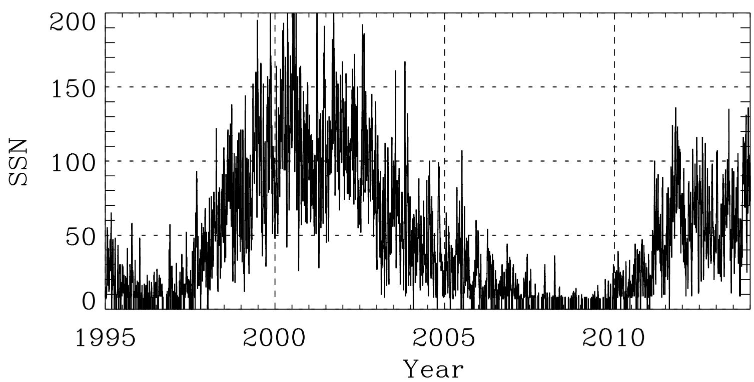

Figure 1.19: The sunspot numbers (SSN) values for the last and the current solar cycle are shown. One can clearly see the 11-year solar cycle variation and other smaller scale variations. (SSN data are obtained from NASA, OMNIWeb)

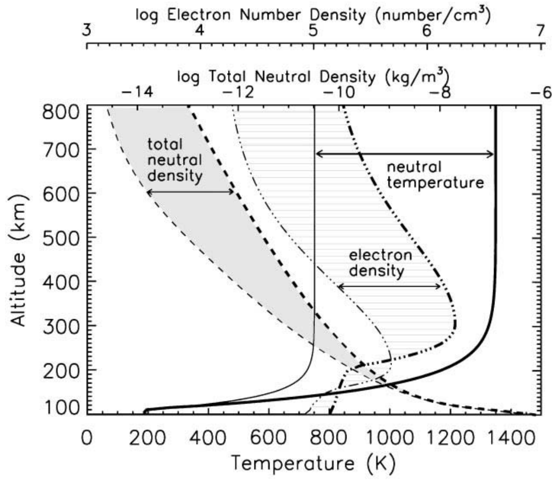

Figure 1.20: The increase in the ionospheric and thermospheric constituent and neutral temperature with solar activity is shown. In each case, the thick and thin curves represent the high and low solar activity, respectively. These profiles are obtained using the Mass Spectrometer and Incoherent Scatter (MSIS) and International Reference Ionosphere (IRI) models for solar activity levels of F10.7=70 (low) and F10.7=230 (high) activity. (After *Lean* [1997])

Figure 1.20 shows the modeled variations of the atmospheric total neutral density, temperature, and electron density for solar activity levels of F10.7=70 sfu and F10.7=230 sfu. One can note that all the three parameters increase with solar activity in the thermospheric altitudes.

1.7 Summary

In this chapter we discussed the various layers or spheres of the atmosphere of the Earth and the energetics and dynamics that persist within them. Different types of atmospheric waves, their generation and dissipation mechanism are introduced briefly. The global changes that occur due to changing wave dynamics are also introduced in the form of sudden stratospheric warming events. Various phenomena in the low-latitude atmosphere that arise due to different coupling and dynamical processes are also discussed. Results on these coupling processes will be discussed in the respective chapters. Due to changes in solar activity the atmospheric composition and thermal structure change. The influence of the solar activity on the thermospheric and ionospheric parameters is also discussed.

1.8 Aim of the Thesis

The upper atmosphere is affected by both solar and lower atmospheric processes. To understand the behavior of the upper atmosphere it is essential to know and quantify these two inputs and their influence on the upper atmosphere. In this thesis, efforts are made in this direction and the following three questions are addressed:

a) How do the lower atmospheric waves influence the upper atmosphere and does the solar influence affect this coupling?

b) How does the low-latitude ionosphere respond to the PW effects that exist during SSW events and does the solar forcing has any role to play in this regard?

c) Does SSW events influence the general circulation in the thermosphere?

1.9 Overview of the Thesis

The main datasets that are used in this thesis are explained in *Chapter 2* along with the instrumentation, installation, validation, and related theory.

The various methods of data analyses, such as, Fourier transform, wavelet transform, and periodograms that are used in this thesis work are explained in *Chapter 3*.

Chapter 4 provides detailed explanation of the vertical coupling of the atmospheres through both shorter and longer period waves at varying levels of solar activity.

Chapter 5 explains the vertical coupling of the atmospheres during SSW events and at varying levels of solar activity.

Chapter 6 presents the results on setting up of a new meridional circulation in the mesosphere-thermosphere winds that seems to get generated during SSW events.

The summary and future scope of the thesis are presented in *Chapter 7*.

Chapter 2

Experimental Techniques and Data

2.1 Introduction

There are many direct and indirect techniques to probe the upper atmosphere of the Earth. The direct probing methods are through sounding rockets and satellites, wherein, information on the parameter being measured can be obtained by in-situ means. Out of the direct methods, measurements on-board satellite provide a large spatial coverage. The indirect techniques involve remote sensing of different components of the atmosphere. Remote sensing can be both active and passive. In active techniques electromagnetic signals transmitted through the atmosphere are scattered and/or reflected by the atmospheric constituents under suitable conditions. The returned signals are then examined to retrieve and understand the atmospheric processes. Whereas, in passive remote sensing, the atmosphere is not perturbed by any radiation, but the naturally occurring radiations are measured [*Vladislav et al.*, 2008]. For the investigations carried out in this thesis work, mainly passive methods have been used.

Passive remote sensing involves detection of naturally occurring light photons. For example, the detection of photons emitted by atmospheric constituents that are excited by photochemical and chemical processes occurring in the atmosphere. In the current study, the main data set that has been used extensively is the oxygen dayglow emission intensities which are derived from the spectral images of the daytime sky. The spectral images are collected using a ground-based spectrograph, called, Multiwavelength Imaging Spectrograph using Echelle grating (MISE). While satellite-based remote sensing provides a broad spatial coverage, the ground-based observations provide high temporal information of the parameters being observed. But, due to the presence of direct solar scattered background during daytime, the dayglow emission measurements from ground-based observation is a very challenging task. In this chapter the details of dayglow emission intensity measurement techniques and the dayglow data extraction procedures are explained. Some other datasets that have been used in this study are also explained.

2.2 Brief Background on Dayglow Measurements

Conventionally, ground-based upper atmospheric airglow measurements are carried out mostly during nighttime and twilight-time using variety of instruments like photometers, spectrometers, interferometers, and imagers [*Hernandez*, 1971; *Hays and Sharp*, 1973; *Kulkarni*, 1976; *Shepherd*, 1979; *Mendillo and Baumgardner*, 1982; *Sivjee*, 1983; *Biondi and Sipler*, 1985; *Meriwether et al.*, 1986, 2013; *Sridharan et al.*, 1991; *Shiokawa et al.*, 1999; *Chakrabarti et al.*, 2001; *Meriwether*, 2006; *Makela and Otsuka*, 2011; *Makela et al.*, 2011, 2013]. The principal challenge to the measurement of dayglow emissions is the presence of the strong scattered solar background continuum during daytime. The first attempt to measure dayglow, although unsuccessful, was reported using a low-resolution photographic spectrograph on a balloon platform *Wallace* [1961]. Later using a higher resolution grating spectrograph at its second order of diffraction *Wallace* [1963] observed the OI 630.0 nm emission during daytime along with Fraunhofer absorption feature. *Wallace* [1963] estimated an emission intensity between 1.7 to 3.3 kR. But due to lower resolution of instrument their measurement was contaminated by Fraunhofer features. From sounding rocket platform *Wallace and McElroy* [1966] measured the OI 557.7 nm emission intensities. It is to be noted that the two cases stated above are from the balloon and rocket platforms.

However, the history of the ground-based measurements is very different. Considering the fact that the scattered light is polarized and dayglow emissions are unpolarized, *Noxon and Goody* [1962] and *Noxon* [1968] used scanning polarimetric techniques to measure oxygen dayglow emissions. Though their measurements were independent of background intensity, the cancellation procedure of the background is highly angle dependent with respect to the position of the sun. Due to this reason there have not been any reports in the literature of systematic measurements of dayglow using this technique.

The Fabry-Perot (FP) etalon has the property that by changing the gap and/or the refractive index of the medium between the two plates one can obtain very high spectral resolution and high-throughput fringe systems. *Jarrett and Hoey* [1963] claimed to have observed the OI 630.0 nm fringe system and from the line-width of the line they estimated the thermospheric temperature to be 800-1260 K. Similarly, using dual FP etalon *Bens et al.* [1965] reported to have measured the temperature to be of 1700±750 K. *Barmore* [1977] used a system with triple FP etalon to resolve the OI 630.0 nm emission and concluded that their temperature measurements are consistent with incoherent scatter radar measurements. *Cocks and Jacka* [1979] used dual FP etalon to measure the wind and temperature. In addition to solar background subtraction they had also applied correction for the Ring effect [*Grainger and Ring*, 1962]. They reported that temperature varied from 800 K in the morning to 1200 K in the noon for the low solar activity period of January-February 1976. But in all these techniques that used high resolution FP etalons there were problems with optical alignment and temperature stability of the components, and remains a challenging task today. There are, however, developmental activities that are still underway [e.g., *Gerrard and Meriwether*, 2011], even using electrically tunable liquid crystal and piezo-electric FP etalons.

Using a pressure-tuned low-resolution FP etalon along with temperature tuned narrow-band (0.3 nm) interference filter, radial chopper, and up/down counting system *Narayanan et al.* [1989] and *Sridharan et al.* [1992a] presented a technique that could retrieve dayglow emission intensities that are submerged in the solar scattered background continuum. In this technique, under tuned condition of the FP etalon, photons are collected from two well-separated spectral zones (using a mechanical chopper) representing two nearby wavelength intervals (separated by ∼0.05 nm) with one containing the information of the line emissions along with the background and the other that of background contribution alone. The difference in the number of photon counts from these two spectral zones was used to yield the information on the OI 630.0 nm emission. Their system was completely computer controlled and the optical alignment procedure was simple as it used a single etalon and pressure controlled chamber for housing the low resolution FP etalon. As a continuation of this effort, *Sridharan et al.* [1993] used spiral mask and, renovated that instrument for operation at multiple wavelengths and was called the multiwavelength daytime photometer (MWDPM) [*Sridharan et al.*, 1998]. This technique using optical mask produced several new results on the behavior of the daytime low- and equatorial-latitude electrodynamics [e.g., *Sridharan et al.*, 1992b, 1994; *Pallamraju*, 1996; *Pallam Raju et al.*, 1996; *Pallam Raju and Sridharan*, 1998; *Chakrabarty et al.*, 2005], and daytime aurora from high latitudes [*Pallam Raju et al.*, 1995; *Sridharan et al.*, 1995; *Pallamraju and Sridharan*, 1998] and virtually initiated the field of daytime optical aeronomy. All these FP-based techniques described above have a very narrow field-of-view (FOV) and need direct or mirror scanning methods to obtain multi-directional information.

Michelson interferometers were also used to make similar kind of instruments which were mainly used in nighttime and satellite-based platforms [*Shepherd*, 1979; *Shepherd et al.*, 1985, 1993]. The Visible Airglow Experiment (VAE) photometer was a part of all the three Atmospheric Explorer (AE) satellite missions [*Hays et al.*, 1973]. The High Resolution Doppler Imager (HRDI) [*Hays et al.*, 1993] and the WIND Imaging Interferometer (WINDII) [*Shepherd et al.*, 1993; *Shepherd*, 2002] were part of the Upper Atmosphere Research Satellite (UARS) mission. The VAE, HRDI, and WINDII were used to measure both aurora and airglow. There are many other satellite based measurements and the information presented here is non-exhaustive. To obtain high spatial and temporal information slit spectrographs emerged towards the end of the last century.

Echelle Grating Imaging Spectrographs:
With the advent of narrow band-width interference filters and array detectors, echelle grating spectrographs have been explored for potential daytime optical airglow measurements. It is known that echelle gratings yields high-spectral resolution spectra, however, the order overlap prevented their wide usage [*Shepherd*, 2002]. *Chakrabarti et al.* [2001] made use of Charge Coupled Device (CCD) detectors and echelle-grating to make a High Throughput Imaging Echelle Spectrograph (HiTIES), to obtain the spectral image of the night sky lights with a spectral resolution of 0.03 nm at 630.0 nm over a large FOV. HiTIES was followed up with a high spectral resolution variant called HIgh Resolution Imaging Spectrograph using Echelle grating (HIRISE) [*Pallamraju et al.*, 2002], which was capable of making daytime optical airglow emission intensity measurements. Innovatively augmenting it with multiwavelength capability, the HIRISE was modified to carry out investigations at 557.7, 630.0, and 777.4 nm wavelengths and the new instrument is known as the Multiwavelengh Imaging Spectrograph using Echelle grating (MISE) [*Pallamraju et al.*, 2013]. The principal dataset that have been used in this thesis work for the investigation of various atmospheric phenomena have been obtained using MISE. The detailed technical specifications of MISE are discussed later in this chapter. Below we describe the production mechanisms of the principal dayglow emissions that are used in this thesis.

2.3 Production Mechanisms of Dayglow

In this study OI 557.7 nm, OI 630.0 nm, and OI 777.4 nm emissions are used which results from the radiative de-excitation of the $O(^1S)$, $O(^1D)$, and $O(^5P)$ states, respectively [*Torr and Torr*, 1982]. Figure 2.1 shows the energy levels of these states along with their average life-times at the exited levels. One may note that the $O(^5P) \rightarrow O(^5S)$ is an allowed transition, while the other two cases involve meta-stable (or forbidden) states. The life-times of the three excited states are 0.74, 110, and 2.7 $\times$ 10^{-8} sec, respectively, for $O(^1S)$, $O(^1D)$, and $O(^5P)$. But at the upper atmospheric densities they can easily de-excite by emitting photons before their energy is quenched by collisions. The detailed discussions on each of the wavelengths are given below.

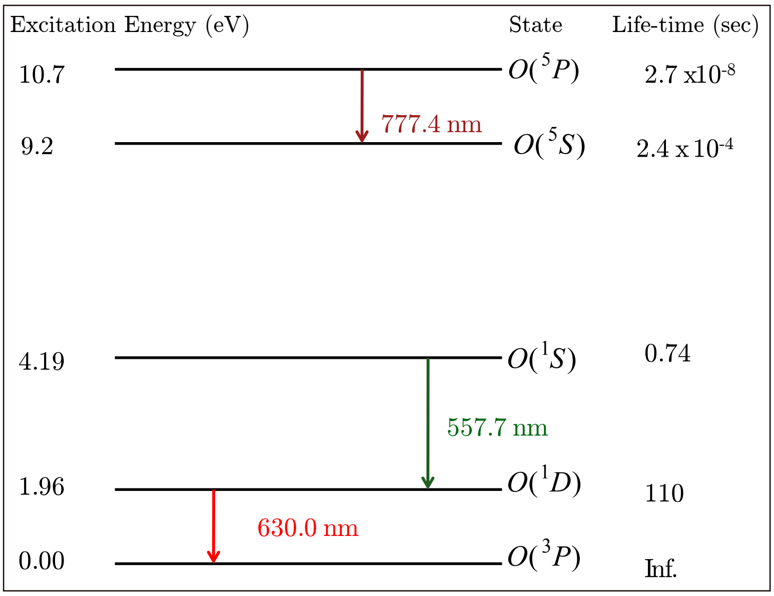

Figure 2.1: The energy levels of the oxygen atom along with other parameters which are responsible for the OI 557.7 nm, OI 630.0 nm, and OI 777.4 nm emissions.

2.3.1 OI 557.7 nm or Oxygen Green Line

This emission originates from the transition of the atomic oxygen from $O(^1S)$ to $O(^1D)$ state. The emission line arises from different sources, such as electron impact, dissociative recombination, photo-dissociation of O_2, and some chemical reactions. Detailed information of the production processes of green line can be found in several papers in the literature [e.g., *Frederick et al.*, 1976; *Rees*, 1989]. The production and loss processes are described below.

Production of $\boldsymbol{O(^1S)}$: The dominant production mechanisms for 557.7 nm are through:

i) Photoelectron impact excitation: Photoelectrons (e_{ph}) with sufficient energies can excite $O(^1S)$. The reaction is:

$$O + e_{ph} \rightarrow O(^1S) + e_{ph} \tag{2.1}$$

here, only photoelectrons are considered as thermal electrons (e_{th}) are not energetic enough to excite $O(^1S)$. The production rate of OI 557.7 nm emission corresponding to this reaction as a function of altitude (z) is given by:

$$P_1^{557.7}(z) = [O](z) \int \sigma_{^1S}(E)\phi(E, z, \alpha_s)dE \tag{2.2}$$

where $[O](z)$ is the atomic oxygen density, $\sigma_{^1S}(E)$ is the excitation cross section given by *Doering and Gulcicek* [1989], $\phi(E, z, \alpha_s)$ is the photoelectron flux at energy E, altitude z, and at solar zenith angle (SZA=α_s).

ii) Collisional deactivation of N_2: The photoelectron impact excitation of N_2 and then energy transfer through collision,

$$N_2 + e_{ph} \rightarrow N_2(A^3\Sigma_u^+), \tag{2.3}$$

$$N_2(A^3\Sigma_u^+) + O \rightarrow N_2 + O(^1S) \tag{2.4}$$

The production of $O(^1S)$ by the above reaction has double peaks, one above 130 km, and the other below 120 km [*Witasse et al.*, 1999; *Culot et al.*, 2004]. The production rate is given by (see. [*Witasse et al.*, 1999]):

$$P_2^{557.7}(z) = \beta_2 k_2 [N_2(A^3\Sigma_u^+)](z)[O](z) \tag{2.5}$$

where β_2 is the efficiency for the production of $O(^1S)$ and k_2 is the rate coefficient.

iii) Photodissociation by the solar photons in the wavelength range of (90 nm - 120 nm),

$$O_2 + h\nu \rightarrow O(^1S) + O \tag{2.6}$$

The production rate for this is:

$$P_3^{557.7}(z) = [O_2](z) \int\limits_{90-120\,nm} \sigma_{sr}(\lambda)I(\lambda, z)d\lambda \tag{2.7}$$

where $[O_2](z)$ is the molecular oxygen density and σ_{sr} is the photodissociation cross section taken from *Torr et al.* [1980]. The $I(\lambda, z)$ is the attenuated solar flux intensity [*Witasse et al.*, 1999].

iv) Dissociative recombination,

$$O_2^+ + e_{th} \rightarrow O(^1S) + O \tag{2.8}$$

whose reaction rate is given by:

$$P_4^{777.4}(z) = \beta_4 k_4 [O_2^+](z) N_e(z) \tag{2.9}$$

where β_5 is the efficiency for the production of $O[^1S]$, k_5 is the rate coefficient, and $O_2^+(z)$ is the molecular oxygen ion density [*Guberman*, 1988; *Witasse et al.*, 1999].

v) Three-body recombination: *Chapman* [1931] suggested that an oxygen atom is excited to the $O(^1S)$ state by the three body recombination with two other atoms.

$$O + O + O \rightarrow O_2 + O(^1S) \tag{2.10}$$

Later, from a laboratory experiment *Barth and Hildebrandt* [1961] found that the emission intensity derived from the above reaction is very small (as the reaction rate is small) compared to the experimentally observed emission intensity. So, they suggested the following three body reaction known as the Barth mechanism.

$$O + O + M \rightarrow O_2^* + M \tag{2.11}$$

$$O_2^* + O \rightarrow O(^1S) + O_2 \tag{2.12}$$

where, O_2^* is the excited state of O_2 and M stands for O_2 or N_2 molecules (the third body). The production rate of this reaction is given by *McDade et al.* [1986]. Among the above mentioned four processes, the Barth mechanism is very dominant at around 100 km altitude.

The loss of $O(^1S)$ occurs due to following two processes:

i) Radiative transition: De-excitation by emitting photon [*Baluja and Zeippen*, 1988; *Witasse et al.*, 1999].

$$O(^1S) \rightarrow O(^1D) + h\nu \text{ (557.7 nm, 297.2 nm)} \tag{2.13}$$

Or, **ii) Collisional deactivation**,

$$O(^1D) + X \rightarrow O + X \tag{2.14}$$

where X may be N_2, O_2, O, or e_{th} [*Witasse et al.*, 1999]. Due to the dominance of the Barth mechanism, the height of maximum emission occurs at about 100 km

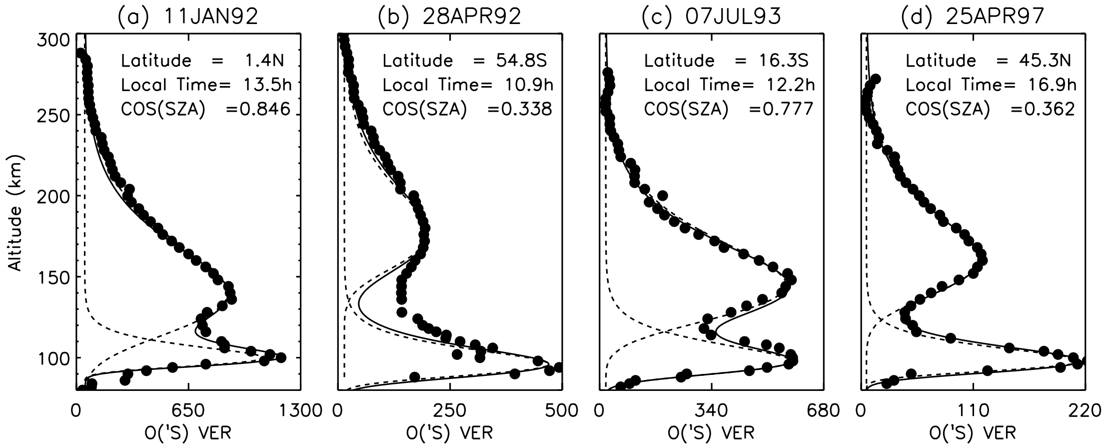

Figure 2.2: OI 557.7 nm volume emission rate observed by WINDII on UARS for different days (11 January 1992, 28 April 1992, 7 July 1993, and 25 April 1997) at different local times. One can note that there are two peaks in the emission rates. The dots are WINDII observed values. The dashed lines are the Chapman function fitted for the two layers at E- and F-region altitudes and the continuous line is the sum of the two fitted curves. (After *Zhang and Shepherd* [2005])

as measured by rocket [*Kulkarni*, 1976] and satellite-based payloads [*Zhang and Shepherd*, 2005]. Figure 2.2 shows vertical profiles of the OI 557.7 nm volume emission rates as observed by WINDII. One can see that there are two peaks in the volume emission rates, one at around 100 km altitude region and the other at the lower F-region. The height of the emission rate peak at F-layer varies with SZA with 180 km in the morning to about 140 km in the afternoon. The magnitude of the emission rate increases with increasing solar irradiance and cosine of SZA.

2.3.2 OI 630.0 nm or Oxygen Red Line

The OI 630.0 nm emission is a result of transition from $O(^1D)$ to $O(^3P)$ state as can be noted from Figure 2.1. Details of various production mechanisms and reaction rates can be found in literature [e.g., *Solomon et al.*, 1988; *Solomon and Abreu*, 1989; *Witasse et al.*, 1999]. In addition to the electron impact excitation, dissociative recombination, photodissociation (as in the case of $O(^1S)$, but with lower energy requirement) this state originate as a result of the cascading from the $O(^1S)$ as well. These reactions are explained below.

i) Photoelectron impact excitation: The ground state of oxygen can be excited by photo-electrons,

$$O + e_{ph} \rightarrow O(^1D) + e_{ph} \tag{2.15}$$

The production rate for the above is:

$$P_{1'}^{630.0}(z) = [O](z) \int \sigma_{^1D}(E)\phi(E, z, \alpha_s)dE \tag{2.16}$$

In addition to photoelectrons, the thermal electrons can also induce this process (for a brief review see [*Mantas and Carlson*, 1991]) as the energy required for this excitation is relatively less. Excitation by thermal electron is important mainly over high-latitudes [*Wickwar and Kofman*, 1984].

ii) Dissociative recombination: O_2^+ recombines with e_{th} to produce $O(^1D)$.

$$O_2^+ + e_{th} \rightarrow O(^1D) + O \tag{2.17}$$

A review on this reaction and reaction rate coefficients can be found in *Guberman* [1988]. The reaction rate coefficient for this reaction decreases with increasing vibrational level of the molecular ion.

iii) Photodissociation: The molecular oxygen (O_2) dissociates by solar photons in the Schumann-Runge continuum wavelength range (135-175 nm)

$$O_2 + h\nu \rightarrow O(^1D) + O \tag{2.18}$$

The associated production rate was given by:

$$P_{2'}^{630.0}(z) = [O_2](z) \int\limits_{135-175\,nm} \sigma_{sr}(\lambda)I(\lambda, z)d\lambda \tag{2.19}$$

iv) Cascading from $\boldsymbol{O(^1S)}$: Each 557.7 nm photon emitted from $O(^1S)$ gives rise to a $O(^1D)$ atom,

$$O(^1S) \rightarrow O(^1D) + h\nu \text{ (557.7 nm)} \tag{2.20}$$

The $O(^1D)$ state may also be produced in the following two chemical reactions:

$$N(^2D) + O_2 \rightarrow NO + O(^1D) \tag{2.21}$$

$$N^+ + O_2 \rightarrow NO^+ + O(^1D) \tag{2.22}$$

The loss process of $O(^1D)$ are:

i) Collisional quenching:

$$O(^1D) + X \rightarrow O + X \tag{2.23}$$

where X may be N_2, O_2, O, or e_{th}.

Or, **ii) Radiative transition** to red doublet:

$$O(^1D) \rightarrow O + h\nu \ (630.0 \text{ nm}, 636.4 \text{ nm}) \tag{2.24}$$

The intensity ratio of 630.0 nm to 630.4 nm is 3 : 1 [*Kvifte and Vegard*, 1947]. Out of all these processes the first three processes are dominant. Depending on all these production mechanisms the peak height of this emission lies at around 230 km altitude and have a layer-width of around 100 km. The detailed production or loss rates and the rate coefficients for the above reactions are given in [*Witasse et al.*, 1999, and references therein].

2.3.3 OI 777.4 nm Line

This emission comes from the transition of $O(^5P)$ to $O(^5S)$ state. Radiative recombination of O^+ with electron gives rise to its excited state $O(^5P)$ [*Tinsley et al.*, 1973].

$$O^+ + e \rightarrow O(^5P) \tag{2.25}$$

and the observed emission rate is proportional to $\int [O^+]^2 ds$, where s is the distance along the line of sight of the observation [*Christensen et al.*, 1978; *Tinsley et al.*, 1997].

The loss of $O(^5P)$ is through radiative transition:

$$O(^5P) \rightarrow O(^5S) + h\nu(777.4 \text{ nm}) \tag{2.26}$$

Unlike 557.7 nm and 630.0 nm, the 777.4 nm emission is from an allowed transition. This emission peaks at the peak of the F-region, where the densities of O^+ and electrons are expected to be the largest. Since at F-region peak heights, the electron number density equals O^+ density, the intensity of OI 777.4 nm emission is proportional to the square of the F-region peak electron density. Thus, this emission is used widely to study the F-region plasma behavior during nighttime [e.g., *Moore and Weber*, 1981; *Tinsley et al.*, 1997; *Lanchester et al.*, 2009].

2.4 Multiwavelengh Imaging Spectrograph using Echelle grating (MISE)

As stated above, MISE is designed innovatively such that it has both multiwavelength capability as in HiTIES and high-resolution feature of HIRISE. MISE is a slit spectrograph that uses echelle grating as the dispersing element, an all-sky lens as the objective, apochromatic lenses for collimating and reimaging multiple wavelengths onto the same image plane, and cooled CCD camera as the detector. Figure 2.3 shows the schematic of MISE with all the components and mechanical design. The details of these components are given below and specifications are listed in Table 2.1.

2.4.1 Components of MISE

(i) **Objective Lens:** The objective lens in the front-end of MISE is an all-sky lens also called fish-eye lens because of its property similar to a fish's eye under water which can see the whole sky (from one side of the horizon to the other) due to refraction of light. This type of lens allows the entry of light from a large FOV. The fish-eye lens used in MISE as its objective lens has a focal length of $\sim$12 mm.

(ii) **Slit Assembly and Field Lens:** The light from the objective passes through a narrow slit ($\sim$0.12 mm in width and $\sim$39 mm in length). As we will see later, if the light falling on the echelle grating of MISE is not fully normal i.e., the γ angle (or lateral angle) is non zero, then $\cos(\gamma)$ deformation introduces a curvature at the image plane. Therefore, to reduce the curvature in the image of this spectrograph, the input slit is curved in the opposite sense, which almost cancels out the curvature deformation introduced by the grating. The field lens behind the slit restricts the beam

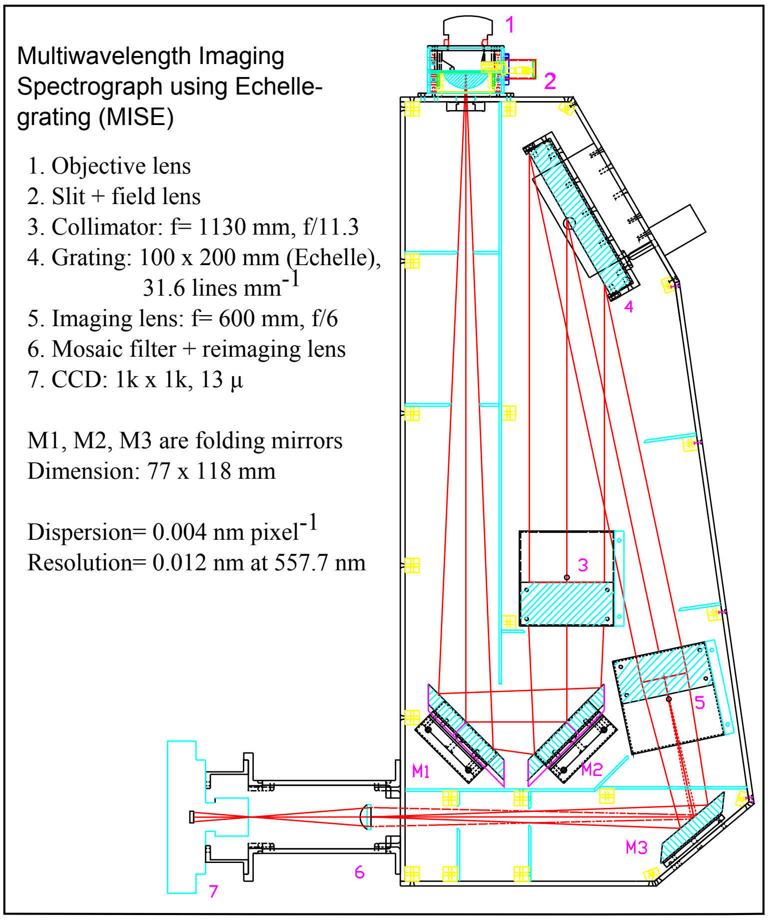

Figure 2.3: Schematic of MISE. MISE uses a 31.6 lines mm^{-1} echelle grating, an $f/11$ input optics and 13 micron 1k$\times$1k pixels detector to achieve a spectral resolution of 0.0120, 0.0147, and 0.0177 nm at 557.7 nm, 630.0 nm, and 777.4 nm, respectively. The red lines show the optical ray path.

divergence of the large FOV objective lens and thus allows the light to fall onto the $f/11$ apochromatic collimator lens.

(iii) **Collimating and Imaging Lenses:** The collimating and imaging lenses used here are of apochromatic type. These lenses have the property that they correct the chromatic aberration and thereby allow multiple wavelengths to be focused at the same image plane. Unlike achromatic lens, which corrects chromatic aberrations for two wavelengths (typically red and blue), apochromatic lenses are used to correct for three wavelengths as can be anticipated from Figure 2.4. Similarly, superachromat is used to focus four wavelengths. The function of the $f/11$ collimating lens is to collimate

Table 2.1: Characteristics of MISE.

Slit length	3.9 cm
Slit width	0.012 cm
Throughput (AΩ)	2.8785×10^{-4} cm^2 sr
Collimator	f=113 cm (f/11 Apochromat)
Grating	31.6 lines mm^{-1}, blaze angle 63.5^o
	(Size: 110×220×30 mm)
Camera lens	f=60 cm ($f/6$ Apochromat)
Total optical trans., τ	0.010197 (557.7 nm);
	0.030775 (630.0 nm); 0.066338 (777.4 nm)
CCD (e^- ph^{-1})	quantum eff., q(λ): q (557.7 nm)=0.95,
	q(630.0 nm)=0.93, q (777.4 nm)=0.8,
	Gain, g=1.5259 e^- DN^{-1}
Total efficiency, Q(λ)	Q (557.7 nm)=0.62259,
	Q (630.0 nm)=0.6095, Q(777.4 nm)=0.5243 DN ph^{-1},
	13μ, 1k×1k, E2V Chip
No. of rows (n_{rows})	110 for 8 pixel binning along the slit
Dispersion, d (nm $pixel^{-1}$)	d(557.7 nm)=0.004,
	d(630.0 nm)=0.0049, d(777.4 nm)=0.0059

the light falling on it from the field lens. The diffracted light from the grating is reimaged by the $f/6$ lens and thus the beam size is reduced by a factor of about two to fit the beam onto the mosaic filter assembly of about 24×24 mm size.

(iv) **Echelle Grating:** To obtain high spectral resolution spectra, an echelle grating is used in designing MISE. Unlike the usual gratings, the echelles have coarse groove spacing and work at very high incidence and diffraction angles. Normal gratings have a groove density of the order of thousand lines per mm and are used at first or second order of diffraction. Whereas, echelles have tens of lines per mm and work at very high diffraction orders

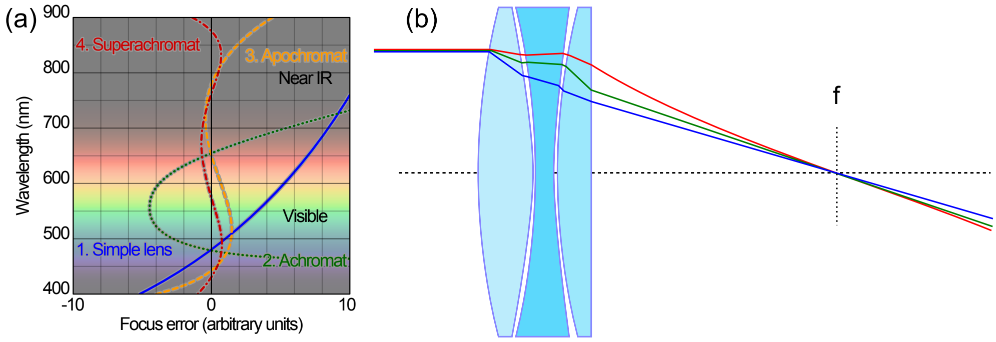

Figure 2.4: (a) Comparison of chromatic focus shift for visible and near infrared wavelengths of a typical simple lens (1 wavelength with no focus error), achromatic doublet (2 wavelengths), apochromatic lens (3 wavelengths) and superachromat lens (4 wavelengths). (b) Schematic of the lens arrangements to fabricate apochromat. (These two figures are obtained from the Wikipedia link *https://en.wikipedia.org/wiki/Apochromat* on the date 25 July 2014).

(>40). The grating equation is given by

$$n\lambda = d[\sin\alpha + \sin\beta]\cos\gamma \tag{2.27}$$

where, d is the groove spacing, α and β are incident and diffraction angles, γ is the lateral angle, λ is wavelength, and n is order of diffraction as depicted in Figure 2.5. Figure 2.5(b) shows the γ angle, which makes the diffracted lights from the off-axis to be shifted so that the diffraction pattern gets curved.

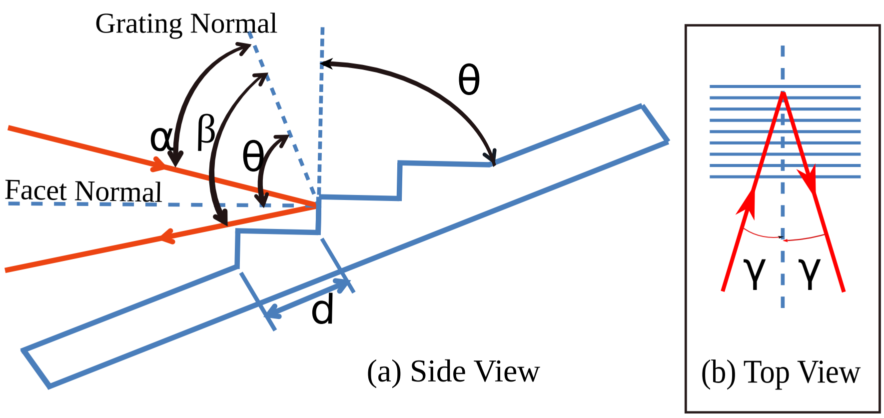

Figure 2.5: Echelle grating geometry and depiction of various parameters, such as d, the groove spacing; α, the incident angle; β, the diffraction angle; θ, the blaze angle; and γ, the lateral angle.

Considering $\gamma = 0$, i.e., normal incidence along the ruling direction, the angular dispersion can be obtained by differentiating Eq. (2.27) w.r.t. β,

$$\frac{\mathrm{d}\beta}{\mathrm{d}\lambda} = \frac{n}{d\cos\beta} \tag{2.28}$$

Substituting for n/d from Eq. (2.27) in Eq. (2.28):

$$\frac{\mathrm{d}\beta}{\mathrm{d}\lambda} = \frac{\sin\alpha + \sin\beta}{\lambda\cos\beta} \tag{2.29}$$

Therefore, it can be seen from Eq. (2.29) that for a given wavelength, the angular dispersion depends solely on α and β. The dispersion is high for high angles of incidence and diffraction. Gratings that are designed to operate at high incidence and diffraction angles are called echelle gratings. The efficiency (ratio of incident intensity to diffracted intensity) of such grating is high at their blaze angle, θ ($= (\alpha + \beta)/2$), and so α and β are chosen close to θ. For a greater efficiency of grating, the facet length ($d\cos\theta$) is required to be large, and at high blaze angles the facet length will be large for large values of d, and hence the groove density of echelle gratings are coarser than regular gratings. According to Eq. (2.27), it can be seen that for a given wavelength, greater values of angles α and β and larger groove spacing, d, can be supported at high values of n. Thus, echelles typically operate at high orders of diffraction (>40).

Although echelle gratings provide high-spectral resolution, at high diffraction orders there would be several wavelengths of different orders that would appear at the same location. Figure 2.6 shows an estimation of the wavelength range that falls on a given pre-defined diffraction angle range obtained using the condition $n_1\lambda_1 = n_2\lambda_2$. For example, at 90$^{\text{th}}$ order, the wavelength range is about 8 nm (625.0 - 633.0 nm). One can note that regions with wavelength gaps increase with increasing wavelength and decreasing diffraction order. The dashed vertical lines indicate the wavelength that are of relevance to the current thesis work. One may note that the 557.7, 630.0, and 777.4 nm wavelengths falls at diffraction orders 102, 90, and 73, respectively. Thus, there are many possibilities by which different wavelengths and orders satisfy the $n_1\lambda_1 = n_2\lambda_2$ condition and fall in the

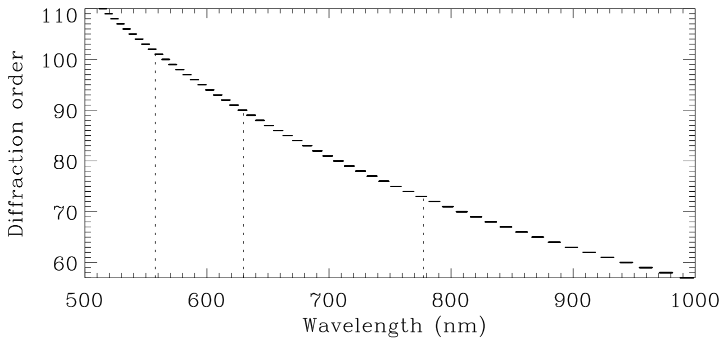

Figure 2.6: Estimation of the wavelength range (horizontal bars) at different diffraction orders for a predefined diffraction angle range. For example, for the 90$^{\text{th}}$ order the wavelength range is about 8 nm (625.0 - 633.0 nm). One can note that regions with wavelength gaps increase with increasing wavelength and decreasing diffraction order. The wavelength gaps can be seen from 700 nm onwards (adapted from *Chakrabarti et al.* [2001] but for technical specifications of MISE). The dashed lines indicate the positions of the three wavelengths of relevance to this thesis work.

same diffraction angle and overlap each other. This problem of order overlap mainly prevented the wide use of echelle gratings in the past. In recent times, as narrow-bandwidth interference filters which allow light from a narrow wavelength range have become available, the usage of echelle gratings have gained importance [e.g., *Pallamraju et al.*, 2000, 2001, 2002, 2004, 2010, 2013; *Pallamraju and Chakrabarti*, 2006; *Chakrabarti et al.*, 2001, 2012; *Galand et al.*, 2004; *Marshall et al.*, 2011].

(v) **Filter Assembly and Macro Lens:** The light from the reimaging lens is filtered by a mosaic of three interference filters having central wavelengths around of 557.7, 630.0, and 777.4 nm. The full-width at half maxima (FWHM) of these filters vary from 10-20 nm. Given the optical components and diffraction orders one can estimate the positions of the individual wavelengths on the filter plane by ray-trace simulation. Figure 2.7 shows the result of ray-trace simulation for MISE which indicate the location of the OI 557.7 nm, OI 630.0 nm, and OI 777.4 nm lines on the CCD chip. Based on this simulation, interference filters at these three wavelengths were cut and glued to one another on the sides to form a mosaic of filters that enable investigations at multiple wavelengths over a large FOV, simultaneously. A macro lens just behind the filter assembly refocuses the spectral image onto the CCD-chip.

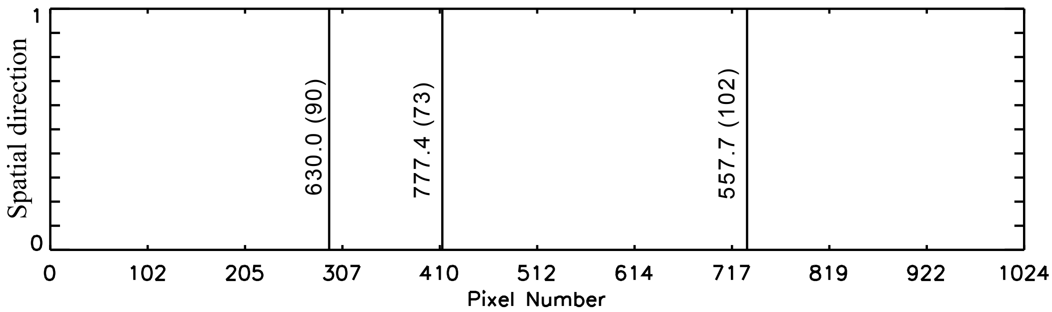

Figure 2.7: Ray-trace simulation result showing the relative positions of different wavelengths that would appear on a detector of 1k×1k pixels. This was carried out to determine the specifications of the grating that would be required (ruling density, blaze angle, etc.) to achieve the goal of making simultaneous measurements at OI 557.7 nm, OI 630.0 nm, and OI 777.4 nm emissions.

(vi) **CCD Detector:** In order to obtain both temporal and spatial information simultaneously, array detectors like, CCD, Intensified CCD (ICCD), and Electron Multiplied CCD (EMCCD) have come to use in the recent past. CCD detector works on the principle of photoelectric effect. Light photons falling on the semiconductor-chip generate free electrons in the conduction band. Charges accumulated in the conduction band are converted into counts with the help of electronic circuits. In order to reduce the thermal noise arising from the camera electronics, the CCD detectors are cooled. A 1k×1k, 13 μm pixel, and 13.3 mm chip back-illuminated CCD camera that is operated at -33 °C is used in MISE. In order to increase the signal to noise ratio (SNR) on-chip binning is used along the direction of the spectral lines that corresponds to spatial region in the sky. More technical details about CCD are given in Table 2.1.

(vii) **Data Acquisition System:** The data collection in MISE is fully programmable. Scripts written in Microsoft visual basic language enable operation of CCD that is interfaced with MaximDL software. The exposure times of CCD are adjusted according to the SZA to avoid saturation of the CCD chip and at the same time optimize to have a fill-in factor of ~70% of well-depth. The exposure times vary from 300 seconds during twilights to 2 seconds in the noon.

2.4.2 Commissioning of MISE at Field Station

MISE has been installed with a dome and hood arrangement atop a tall building in Jawaharal Nehru Technological University, Hyderabad (JNTUH; 17.5° N, 78.5° E; 8.5° N magnetic latitude), India under Physical Research Laboratory and JNTUH collaboration. Figure 2.8 shows the position of the instrument and the geomagnetic meridians in the continental map along with the stations of some other measurements, such as, EEJ strength and total electron content (TEC), that are used in this thesis work. The geophysical importance of this place is that it falls in low-latitudes and is in between the northern-crest and trough of the EIA. Figure 2.9 shows a photograph of the dome and hood arrangement. The opening of the dome and the hood is made in such a way that it is parallel and in line with the slit of the spectrograph so that a large FOV along north-south (latitudinal) direction can be viewed by this spectrograph.

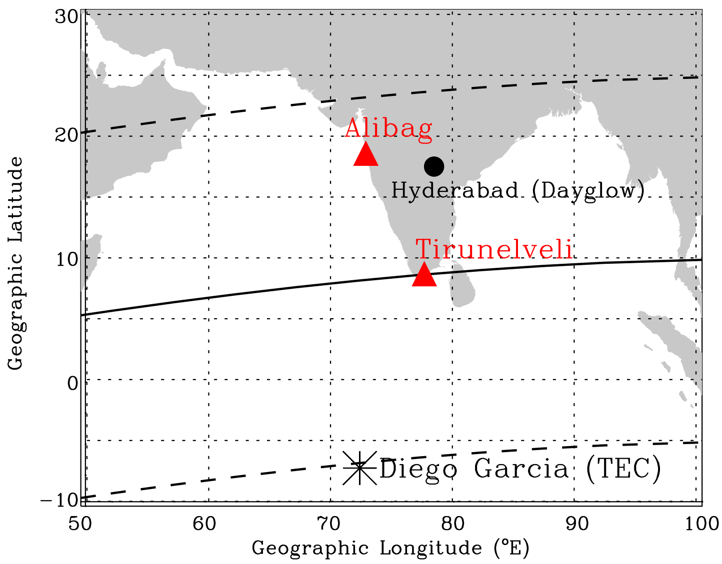

Figure 2.8: The location of MISE installation site along with the positions of the other measurement sites that are used in this thesis work are depicted. The continuous line is the geomagnetic equator and the dashed lines represent the ±15° latitudes i.e., the approximate positions of the crest regions of the EIA.

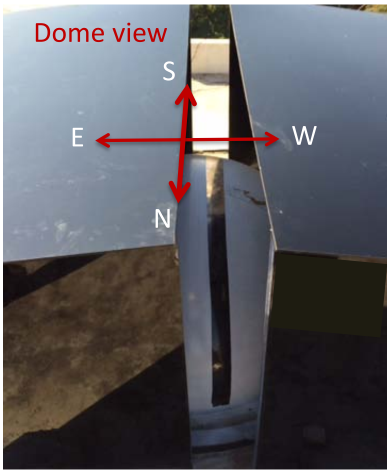

Figure 2.9: Dome and hood arrangement that are made for MISE that is installed at the field station in JNTUH. As the slit and hence the opening for light is along the north-south direction one can obtain information of the sky along the north-south meridian.

2.4.3 Calibration of MISE

MISE obtains spectral images of the sky light which contain information on the spatial and temporal variations in intensities. Wavelength calibration is made by comparing the sky spectrum with standard solar spectrum. A wavelength calibrated spectral image obtained with MISE is shown in Figure 2.10.

(i) **Flat-field and Van-Rhijn effect correction:** MISE, being an all-sky spectrograph, will need very broad uniform constant source for flat-field correction, which is not practical. So, constant-current incandescent source has been used. This source was placed at different view angles at the same radial distance from the center of the objective lens. Images at all these angles are combined to simulate a flat profile for the spectrograph for each of the three wavelengths as shown in Figure 2.11 for a region close to 630.0 nm. The thin lines show the plots of the counts obtained by averaging a few columns of the CCD counts near the 630.0 nm wavelength position for various view angles. The thick line shows the envelope joining the peak intensity values of all the individual profiles. A normalized version of this envelope is used for flat field correction. Airglow emissions can be assumed to be present in uniform-altitude layers. The Van-Rhijn effect is a manifes-

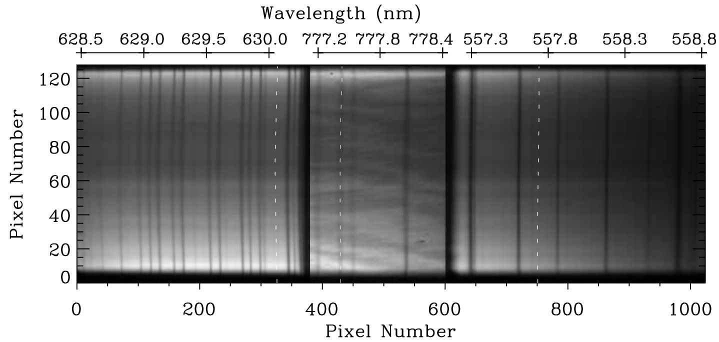

Figure 2.10: Sample of spectral image formed by MISE. The bottom axis shows the pixel numbers and the one on the top shows the wavelength corresponding to the different spectral regions. The y-axis shows the pixel numbers of rows that are binned in 8 pixels and essentially corresponds to different spatial locations in the sky along the slit orientation. The two broad vertical dark zones correspond to the regions where different filters have been glued together. The dashed white vertical line shows the location of the dayglow emission lines in each panel. One can note that the optical emission lines in the actual measurement as shown here appear at the same location as predicted (shown in Figure 2.7). The brightness scale for the 777.4 nm spectral panel had been enhanced by four times so that all the three spectral panels can be viewed at the same time. The intensity and view angle calibrations are explained below.

tation of the higher dayglow emission volume from observation away from zenith of the instrument. This can be corrected using the formula:

$$\frac{I_\theta}{I_0} = \frac{1}{\sqrt{1 - \left(\frac{R}{R+h}\right)^2 \sin^2\theta}} \tag{2.30}$$

where, θ is the zenith angle, R is radius of the earth and I_0 and I_θ are the airglow intensities at zenith angles 0 and θ, respectively. In other words, the slant columnar airglow intensity is more, in general, than the zenith intensity.

(ii) **View angle calibration:** For calibration of spatial location to which a pixel on the chip corresponds to, laboratory test has been carried out with a point light source. Keeping the point light source at different known angular positions with respect to the objective lens of MISE one can calibrate each pixel of the CCD. Figure 2.12 shows a plot of pixel vs. view angles obtained by identifying the positions of peak of the emissions at different angular

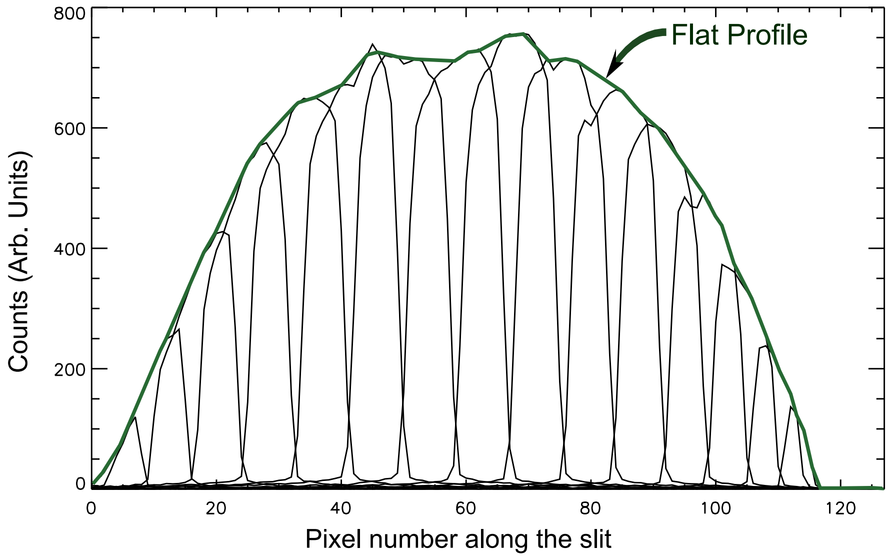

Figure 2.11: Estimation of the flat profile from images of a constant current source placed at different viewing directions. All the profiles are taken at same exposure times and same current was supplied to the tungsten filament incandescent standard source.

positions of the light source.

Considering average emission altitudes of 130, 230, and 300 km for the three oxygen emissions of OI 557.7 nm, OI 630.0 nm, and OI 777.4, respectively (as will be discussed in section 2.3), one can estimate the spatial coverage at different emission altitudes. Figure 2.13 represents a schematic of spatial coverage of MISE by considering the instrument to be placed at 8.5° N geomagnetic latitude (which corresponds to Hyderabad, India). One can see that the higher altitude emission covers more spatial region as compared to the lower ones. Also, it should be noted that lower elevation angles contains more spatial volume from where emissions emanate, so Van-Rhijn correction (as discussed above) needs to be applied for carrying out inter-region comparisons.

(iii) **Intensity calibration:** The intensity calibration can be done in two ways: (a) by using a broad curved standard source with uniform intensity at all the viewing angles and (b) by back calculation method. In the absence of such broad custom made source, the second method has been used as described below. Considering the specifications of all the components that have been

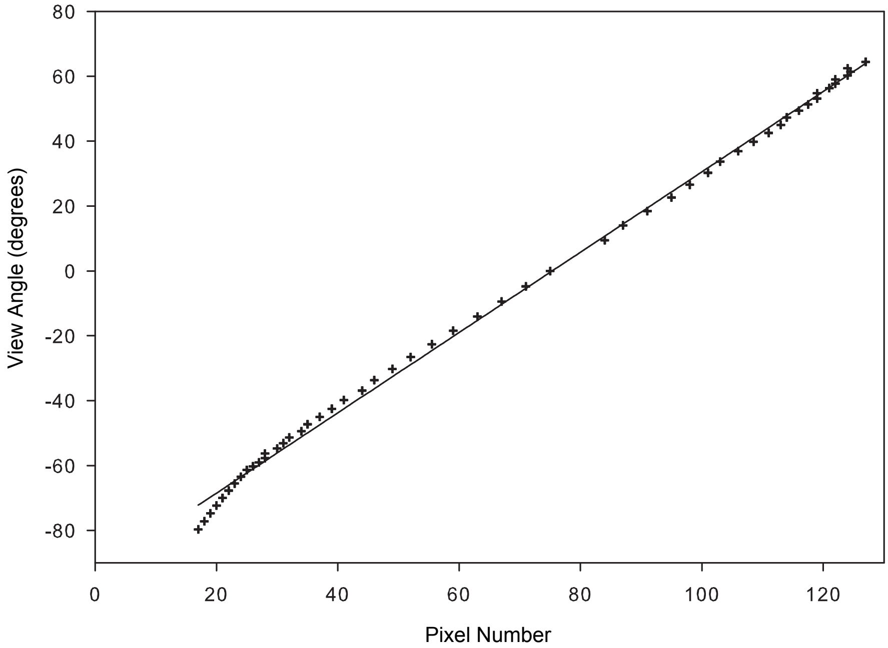

Figure 2.12: View angles measured from zenith in degrees with respect to pixel position. The plus signs represent the observations and the continuous line is the least square fitted line.

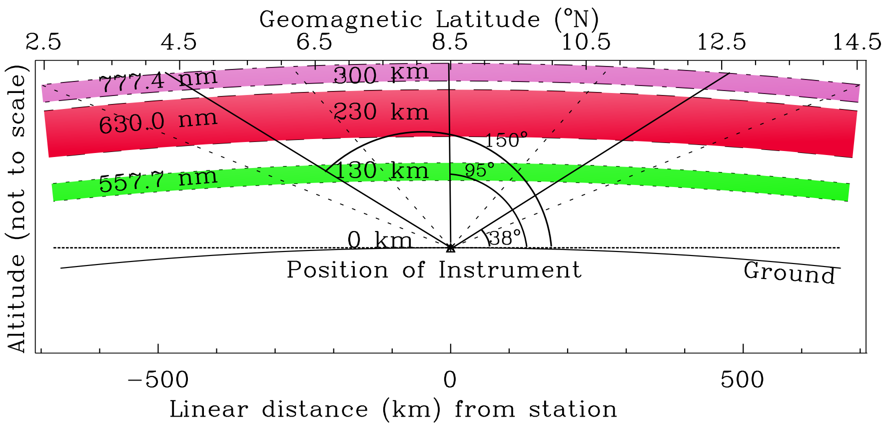

Figure 2.13: Schematic of the MISE's sky viewing geometry. Different dayglow layers and their average altitudes from which the OI 557.7, OI 630.0, and OI 777.4 nm emissions emanate are shown. The spatial average of the three viewing directions correspond to elevation angles of approximately 38°, 95°, and 150° with respect to the northern horizon. It can be seen that for the current FOV (~140°), the latitude extent covered for OI 557.7, OI 630.0, and OI 777.4 nm are about 5°, 9°, and 11°, respectively, at their respective heights. Note that the y-axis is not to scale and shows the approximate heights of the layers at 130, 230, and 300 km.

used in this instrument as given in Table 2.1, an estimate of the sensitivity of the spectrograph has been made to arrive at the emission intensity of airglow during daytime. If B is the airglow emission intensity (in Rayleighs (R), 1 R=10^{10} photons m^{-2} s^{-1} [*Chamberlain*, 1961; *Baker and Romick*, 1976]) before entering the instrument, then N counts that are registered on the CCD can be given as:

$$N(\lambda) = B(\lambda)S(\lambda)t \tag{2.31}$$

where, S is the sensitivity of the instrument, and t is the time of integration. N, B, and S vary with wavelength. S is the sensitivity of the instrument expressed as Data Numbers (DN) s^{-1} R^{-1}. As shown in *Pallamraju et al.* [2002] at any given pixel, the sensitivity per Angstrom can be written as:

$$S_{pix}(\lambda) = (10^6/4\pi) \times Q(\lambda) \times A \times \Omega\tau(\lambda) \times d(\lambda)/n_{rows} \tag{2.32}$$

where, $Q(\lambda)$ is the overall efficiency of the CCD (quantum efficiency $q(\lambda)$/gain, g); $\tau(\lambda)$ is the optical efficiency of the instrument, A is the area of the slit, Ω is the solid angle of the sky that the slit 'sees', d is the dispersion in nm pixel^{-1}, and n$_{rows}$ are the number of rows that have been obtained after on-chip binning in the spatial dimension. From the values given in Table 2.1, it can be seen that the sensitivity of MISE at the different wavelengths of interest is:

$$S_{pix}(\text{OI } 630.0\,\text{nm}) = 1.8837 \times 10^{-5}(\text{DN}\,\text{nm}\,\text{R}^{-1}\,\text{s}^{-1}) \tag{2.33}$$

$$S_{pix}(\text{OI } 557.7\,\text{nm}) = 0.5205 \times 10^{-5}(\text{DN}\,\text{nm}\,\text{R}^{-1}\,\text{s}^{-1}) \tag{2.34}$$

$$S_{pix}(\text{OI } 777.4\,\text{nm}) = 4.2057 \times 10^{-5}(\text{DN}\,\text{nm}\,\text{R}^{-1}\,\text{s}^{-1}) \tag{2.35}$$

Therefore, dividing the data numbers obtained by the CCD with the sensitivity values at that wavelength, one can estimate the absolute emission intensities.

2.4.4 Dayglow Emission Intensity Extraction

The dayglow emission intensity is extracted from MISE data by comparing the sky spectra with standard solar spectrum and removing atmospheric scattering contribution by applying a similar method as used by *Pallamraju et al.* [2000, 2002]. Figure 2.14 shows the spectra of daysky at different wavelength panels as shown in Figure 2.10. The panel (a) in Figure 2.14(i-iii) shows the scattered solar background continuum matched to the daysky spectra in wavelength and scaled to it at continuum regions at the OI 630.0 nm, OI 557.7 nm, and OI 777.4 nm spectral regions, respectively. The x- and y-axes show the wavelength and the sky brightness at that spectral region for a representative plot obtained at 15 hour local time (LT) (at SZA=46°) from Hyderabad on 20 March 2011. The airglow emission wavelength in each panel is shown as a vertical dashed line (in panels b and c).

To extract the daytime airglow emission signal embedded in the solar-scattered background, the daysky spectrum is compared with the solar spectrum. The ways in which the daysky spectra differ from the solar spectrum at any given wavelength are in terms of: (1) dayglow emissions, (2) telluric absorptions, and (3) atmospheric scattering. Scattering contribution of light, which is also called the Ring effect [*Grainger and Ring*, 1962], exists in all the Fraunhofer absorption regions and it is believed to be due to rotational Raman scattering [e.g., *Conde et al.*, 1992; *Pallamraju et al.*, 2000]. Incidentally, none of the emission wavelengths being discussed here suffer from any telluric absorptions and therefore, the contribution of Ring effect (due to scattering) alone is to be taken care of and it is done by the method described by *Pallamraju et al.* [2000]. It has been shown in that work that the Ring effect at two nearby or adjacent spectral regions of identical equivalent widths (normalized depth$\times$half width) is the same. Therefore, when the daysky spectrum is compared with the solar spectrum [*Delbouille et al.*, 1973] that is scaled at the continuum regions, the difference between them at the wavelength region of emission corresponds to the contribution of daytime optical emissions and of scattering. The best possible match in wavelength and intensity of the daysky spectrum with that of the solar spectrum is achieved by sequentially iterating the daysky spectra in sub-pixel domain and sum of squares of the differences are obtained at a nearby Fraunhofer region. The region where the sum of differences is the least indicates the location of best match.

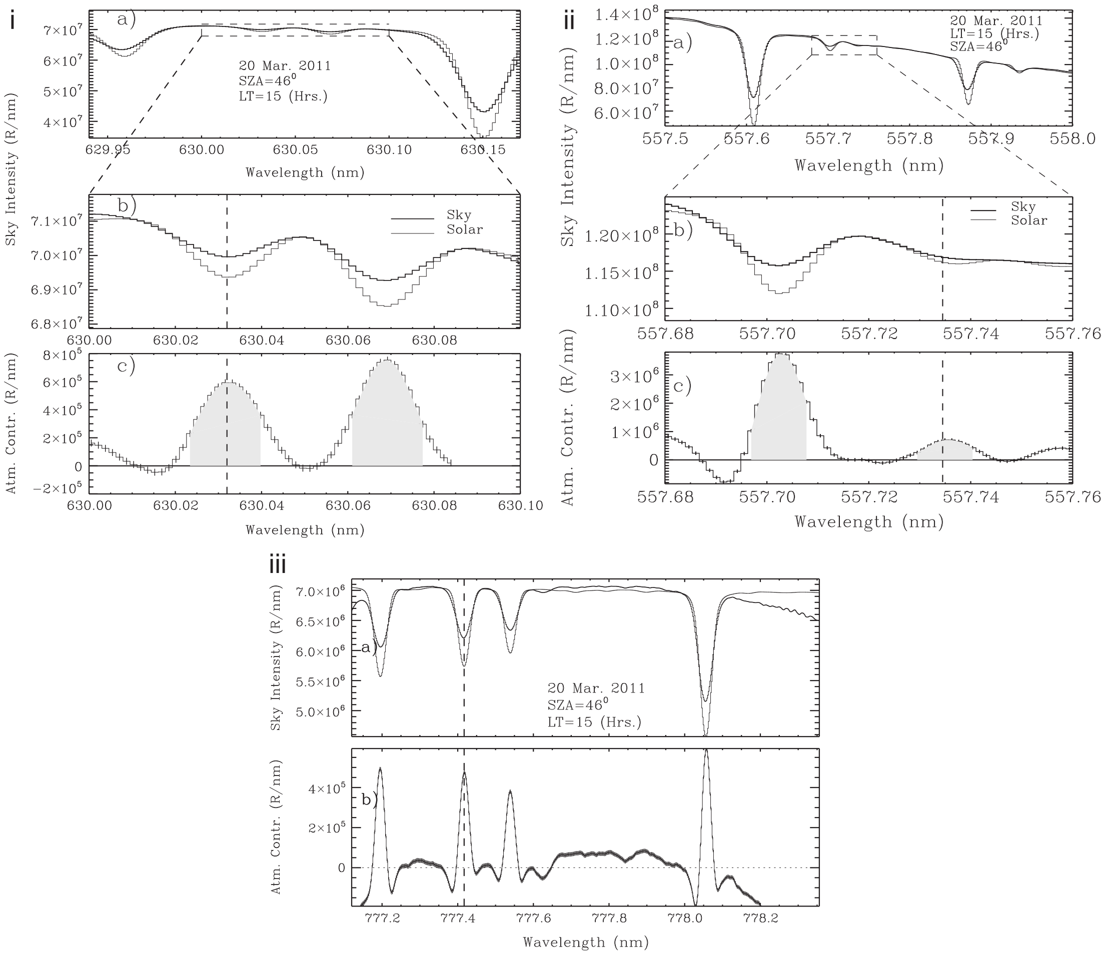

Figure 2.14: (i) Panel (a) shows the sky intensity as a function of wavelength as obtained on 20 March 2011 at 15 LT for OI 630.0 nm spectral panel. Solar spectrum is matched to the daysky spectrum at the continuum level. Panel (b) shows the emission line of interest (wavelength shown by dashed vertical line) and the ring effect region in close-up. It can be noted that the daysky spectrum (darker line) is shallower as compared to the solar spectrum (thinner line). Panel (c) shows the difference between the daysky and solar spectra which corresponds to the atmospheric contribution. The curve with the dashed vertical line (curve1) shows the spectral region of emission along with the scattering effect and the other (curve2) shows only the scattering effect. Differences in their areas obtained by considering proper weight of the equivalent width (normalized line depth$\times$half-value width) to the Fraunhofer region containing the scattering contribution corresponds to the contribution of the daytime airglow emission intensity at that wavelength for a given time. (ii) Same as in (i) but for OI 557.7 nm spectral panel. (iii) Same as in (i) but for OI 777.4 nm (no close-up).

If I_{c1} is the normalized intensity at the continuum level, I_{d1} is the intensity at the depth, and λw_1 is the half-width of that absorption region at the emission wavelength, and the corresponding values at the neighboring region (which does not have any emission or suffer from telluric absorption) are I_{c2}, I_{d2}, and λw_2, then, the contribution of the dayglow emission intensity at that wavelength can be given as: [Area under curve 1] - [Area under curve 2]$\times f$, where, the factor f is given by:

$$[(I_{c1} - I_{d1})\lambda w_1]/[(I_{c2} - I_{d2})\lambda w_2] \tag{2.36}$$

which scales the amount of scattering contribution from the region 2 to be taken into account in the region 1. The area under curve1 (the one with dashed vertical line in panels (c) of Figure 2.14(i-ii) and panel (b) of Figure 2.14(iii) will consists of contribution from both the dayglow and the scattering, while the area under curve2 (the second shadowed curve without vertical dashed line) will consist of only the contribution due to the scattering effect. The factor, f, as estimated using the solar spectrum as the reference is around 0.19, 0.80, and 0.70 for 557.7 nm, 630.0 nm, and 777.4 nm emission wavelengths, respectively. However, as mentioned above, this factor also depends on solar zenith angle.

(a) **OI 630.0 nm:** For the extraction of redline (OI 630.0304 nm) emission intensity, the equivalent widths of spectral regions 630.0214-630.0394 nm and 630.0594-630.0774 nm are considered. The difference between their areas is equal to the OI 630.0 nm dayglow as described in detail in *Pallamraju et al.* [2002].

(b) **OI 557.7 nm:** Similar procedure as that used for redline is applied for the green line (OI 557.7345 nm) emission as well, wherein contributions from 557.7285-557.7405 nm and 557.6964-557.7084 nm spectral regions are considered. However, unlike the redline, in this case, the nearest Fraunhofer absorption regions are quite deep compared to the one at the green emission line, and therefore the factor for scattering contribution is much smaller than compared with that of the redline. *Marshall et al.* [2011] also used such an approach as indicated in *Pallamraju et al.* [2000] for making the green line emission measurements.

(c) **OI 777.4 nm:** The spectral region from 777.4042-777.4298 nm and 778.0440-778.0696 nm consist of the regions of OI 777.4170 nm dayglow emission and that of the scattering contribution. To the best of our knowledge ground-based daytime emission intensities at this wavelength are reported first by this work.

Panels (b) of Figure 2.14(i-ii) show the comparison between the solar and daysky spectra at OI 630.0 nm and OI 557.7 nm spectral regions. Panels (c) of Figure 2.14(i-ii) and panel (b) of Figure 2.14(iii) shows the difference between the solar and daysky spectra (the atmospheric contribution) at all the three spectral regions of interest. In practice, at every given time, the daysky spectra are iteratively matched with the solar spectrum for matching in wavelength. At the best (spectral) match location the solar spectrum is scaled at the continuum regions of the daysky spectrum. This process is repeated for the next time interval to obtain the daytime optical emission intensities at that time. Thus, emissions for a complete day are obtained.

The y-axis of Figure 2.14(i-iii) shows the sky scattered background continuum in Rayleighs nm^{-1} as estimated using the sensitivity values of the instrument at that wavelength. Figure 2.15 shows the magnitude of scattered sky background at all the three wavelengths as a function of local time on 20 March 2011. It can be seen that the observed background continuum is a function of the solar black-body radiation convolved with the atmospheric scattering, and thus it is a function of wavelength and SZA. The scattered solar background continuum values vary from 10-90, 10-60, and 5-10 MR nm^{-1} in the 557.7 nm, 630.0 nm, and 777.4 nm spectral regions, respectively, for this day.

2.4.5 Error Estimation in Dayglow Signals

As explained above, the dayglow emission intensities measured in this work are derived from the spectral images recorded by CCD detector. There involves various types of uncertainties in signals obtained using CCD detectors. For example, dark noise, readout noise, quantization noise, statistical noise. The dark noise arises due to the thermal electrons produced in the electronic components which

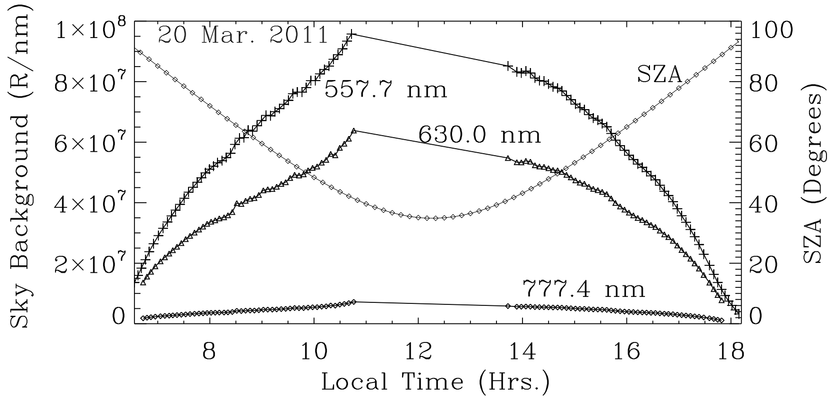

Figure 2.15: The scattered sky background at all the three wavelengths as a function of local time on 20 March 2011 is shown. It can be noted that the scattered sky background varies as a function of SZA from 10 to 90, 10 to 60, and 5 to 10 MR nm^{-1} for 557.7 nm, 630.0 nm, and 777.4 nm spectral regions, respectively. Solar zenith angle values as a function of time is also shown.

increases with temperature - for every 6 K decrease in temperature the noise decreases by a factor of 2. But for the case of cooled CCDs and for strong signal and background, such as in case of dayglow, it is not significant. Read noise depends on the CCD readout rates, which arises due to the inhomogeneity in the performance of the detector array and associated electronics and could be significant if the signal is weak or the exposure times are small, which is not applicable here. Quantization or digitization noise arise while converting analog-signal to digital signal by AD converter. In this process, an analog signal of specific amplitude is associated with a number and in this way the analog current is approximated to counts. This noise is also insignificant for high count observations. In the case of CCD, one may note that counts occur due to photon inducing electrons from the detector and the statistics of these airglow photons follow Poisson distribution. Thus, for CCD counts the standard deviation is given by, $\sigma = \sqrt{mean}$. The SNR is given by

$$SNR = \frac{S}{\sqrt{(S+B)+D+R}} \tag{2.37}$$

where, S, B, D, and R stands for signal, background, dark-noise, and readout-noise, respectively. The measurement uncertainty is equal to $1/SNR$. Since the dayglow observations have strong signal and strong background, the readout noise and the dark noises are negligible. And thus,

$$SNR = \frac{S}{\sqrt{(S+B)}} \tag{2.38}$$

The co-adding, binning, averaging have been taken into account based on the sampling statistics [*Bevington and Robinson*, 2003]. By considering all the parameters as described in the CEDAR (Coupling, Energetics and Dynamics of Atmospheric Regions, http://cedarweb.hao.ucar.edu) tutorial [*Pallamraju*, 2003], the SNR of the measurements at OI 557.7 nm, OI 630.0 nm, and OI 777.4 nm turn out to vary throughout the day in the range of 5-28, 2-18, and 3-8, respectively. The SNR is higher during low background level hours (twilight-hours) compared to noon.

2.4.6 Validation of Emission Intensities Obtained by MISE

The dayglow emission intensities extracted from the MISE data have been compared with empirical and physics-based models. A comparison is made for the OI 630.0 nm and OI 557.7 nm obtained by our technique (MISE) with that of the empirical model estimates as given by *Zhang and Shepherd* [2004, 2005] (Figure 2.16). The empirical model is based on the data obtained from WINDII measurements onboard UARS. The inputs to the empirical model are the SZA and solar F10.7 flux on that day. It may be noted that the empirical model is most applicable for SZA<80° [*Zhang and Shepherd*, 2005]. In Figure 2.16 the solid line represents the dayglow predicted for 12 January and the dashed line shows the empirical model values for 20 March of year 2011. It can be noted that the diurnal pattern of the emission intensities agrees reasonably well with our ground-based measurements. As it can be expected, the finer features due to the atmospheric dynamics that vary from day-to-day cannot be captured by the empirical model values. Given the uncertainties in estimating the emission magnitudes in our measurements and also due to those of WINDII, it can be seen that the agreement is quite good. OI 777.4 nm emissions were not measured onboard UARS, and hence its variability is compared with that obtained by the GLOW model [*Solomon*, 1992]. GLOW model uses MSIS-90 neutral atmosphere, IRI-90

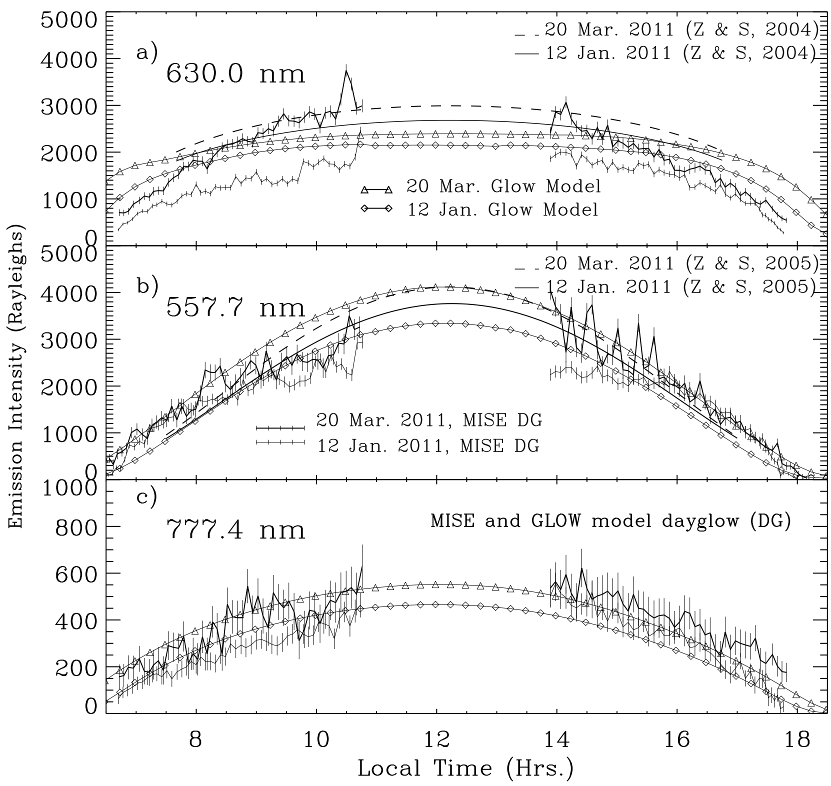

Figure 2.16: The column integrated dayglow emission intensities obtained for a couple of days (12 January and 20 March 2011) along with $\pm 1\sigma$ uncertainties are shown. Each datum point is obtained for an average of 5-min. integration. Panels (a), (b), and (c) show the emission intensities at OI 630.0 nm, OI 557.7 nm, OI 777.4 nm emission regions. These intensities have been compared with those obtained by empirical model given by *Zhang and Shepherd* [2004, 2005] and that of the GLOW model estimates. One can see a remarkable similarity in the overall diurnal behavior (shape of the emissions) between the measurements of MISE and the empirical and model output. The Ap, SSN, and F10.7 cm solar flux values for both the days are 6, 15, 77 (12 January) and 6, 21, 91 (20 March), respectively. Thus, the differences in intensities between the emissions on these two days at each wavelength are solely due to the differences brought in due to variations in solar zenith angles and the associated dynamics that exist at those altitudes.

predictions of electron densities, and solar EUV flux values to estimate volume emission rates for different wavelengths governed by the respective production mechanisms for these emissions [e.g., *Solomon et al.*, 1988; *Solomon and Abreu*, 1989]. The two days of emissions estimated by the GLOW model are represented by diamonds (12 January) and triangles (20 March) and are shown for all the wavelengths.

It can be noted that the shapes in the diurnal variation in intensities as measured by MISE are different for different emissions. OI 630.0 nm emission intensity shows a flat peak during 10-15 LT, while the OI 557.7 nm emission intensities show a steeper increase in emission from the morning hours to noon and a faster decrease thereafter when compared with the redline emission intensities. The OI 777.4 nm intensity also show flat variations from 9 to 16 LT. The GLOW and WINDII data based empirical models also show broadly a similar behavior as that observed in the case of MISE measurements. There are, however, significant differences in smaller time-scales, which are due to the dynamical features that exist in the upper atmosphere. One of the aims of the work carried out in this thesis using such optical investigations from the data obtained from MISE is to characterize the daytime wave dynamics in the upper atmosphere.

2.5 Other Datasets

Other than the main data sets (optical dayglow emissions) that were obtained from the ground-based instrument (MISE), additional ground- and satellite-based data sets have also been used for this thesis work. For example, ground magnetometer based EEJ strength, GPS ranging based TEC, and satellite remote sensing data of temperature and wind. These data sets are explained below.

2.5.1 Equatorial Electrojet (EEJ)

Above the geomagnetic equator of the Earth there is a strong jet of east-west current, called the EEJ, which induces north south magnetic field on the ground. This current arises due to the effect of polarization field being produced by separation of charged particles. Theoretical details of the generation of the EEJ have been given in section 1.5.2. The strength of the current depends on the east-west wind and the electron or ion number density. The ambient winds at the EEJ altitudes are perturbed by the waves propagating from lower atmosphere. Thus, the variations in the EEJ strengths provide indirect information of the wave dynamical activities at that altitude.

The strength of the EEJ can be derived from measurements of the magnetic field induced by the current. Over the Indian longitudes, the horizontal component of geomagnetic field (H) data at 1-minute resolution are collected with magnetometers located at the equatorial station, Tirunelveli (TIR) (Geog. 8.7° N, 77.7° E; 0.1° N magnetic latitude) and an off-equatorial station, Alibag (ABG) (Geog. 18.6° N, 72.9° E; 10.3° N magnetic latitude). To estimate the strength of the EEJ induced magnetic field on the ground in the Indian longitudes, variations of H relative to its nighttime values at Alibag (ΔH_{ABG}) for quiet day are subtracted from the corresponding values at Tirunelveli (ΔH_{TIR}), $\Delta H_{TIR} - \Delta H_{ABG}$ [*Chandra and Rastogi*, 1974; *Reddy*, 1989]. This type of EEJ retrieval using two or more stations data removes the contribution of other global effects like those associated with the ring current.

For the measurement of horizontal component mainly fluxgate magnetometers are used. Fluxgate magnetometers work on the principle of magnetic induction. When an external magnetic field passes through a known altering magnetic field region/gate it will perturb the known field pattern. From the deformation of the known field one can calculate the magnitude and direction of the induced external magnetic field. These measurements have an accuracy of 0.1 nT.

2.5.2 Total Electron Content (TEC)

The ionospheric TEC can be estimated by various radio probing techniques, such as, ionospheric radio occultation, radio sounding of the ionosphere using ionosonde (by simulation of topside profile), studying radio waves from carrier of navigation signals, etc. The carrier signals from the navigational satellites, such as, Global Positioning System (GPS, American), GLONASS (Russian), Galileo (European), etc., can be used for this purposes. The GPS is a constellation of satellites, which uses radio waves for positioning and navigation purposes. While passing through the ionosphere, these radio waves are modulated by the ionospheric electrons and their distributions. Below we describe the details of the TEC derivation from the GPS signals.

2.5.2.1 Theory of Ionospheric TEC Calculations

The ionosphere of the Earth contains ions and free electrons. The natural frequency of oscillation of the ionospheric plasma i.e., the plasma frequency lies in the radio frequency range. Thus, for radio waves, the ionosphere acts as a dispersive medium [*Rishbeth and Garriott*, 1969]. The dispersion relation (relation between wave frequency, ω and wave vector, $\boldsymbol{k}$) for radio waves propagating through an ionized medium is given by [*Chen*, 1984]:

$$\omega^2 = \omega_p^2 + c^2k^2 \tag{2.39}$$

where c is the speed of light in free space and ω_p ($=2\pi f_p$) is the plasma frequency. This relationship is also valid for the radio or electromagnetic waves propagating through a plasma under the action of magnetic field, but when $\boldsymbol{k}$ is perpendicular to magnetic field. The phase velocity (v_p) and group velocity (v_g) can be calculate from Eq. (2.39) as:

$$v_p = \frac{c}{\sqrt{1-\left(\frac{f_p}{f}\right)^2}} \tag{2.40}$$

and

$$v_g = c\sqrt{1-\left(\frac{f_p}{f}\right)^2} \tag{2.41}$$

thus, the phase and group refractive indices ($n_p = c/v_p$ and $n_g = c/v_g$) are given by

$$n_p = \left(1-\frac{f_p^2}{f^2}\right)^{\frac{1}{2}} \approx 1-\frac{40.3N_e}{f^2} \tag{2.42}$$

$$n_g = \left(1-\frac{f_p^2}{f^2}\right)^{-\frac{1}{2}} \approx 1+\frac{40.3N_e}{f^2} \tag{2.43}$$

where, the plasma frequency (f_p) is given by $\sqrt{\frac{N_e e^2}{4\pi^2\epsilon_0 m}}$ (in sec^{-1}), e is the electron charge, m is the electron mass, N_e is electron number density, ϵ_o is the permittivity of free space, and f is frequency of radio wave signal (in sec^{-1}). The approximations in Eqs. (2.42) and (2.43) are made using Binomial theorem.

The signal group delay introduced by the ionosphere is measured in distance (d_{ion}) and is given by distance covered by the signal minus the geometrical distance (distance that it would have covered if velocity of light equals free space velocity). i.e.,

$$d^g_{ion} = \int_r^s n_g dl - \int_r^s dl = \int_r^s (n_g - 1)dl = \int_r^s \left(\frac{40.3N_e(l)}{f^2}\right) dl = \frac{40.3}{f^2} \int_r^s N_e(l)dl \tag{2.44}$$

where, r and s are the positions of the receiver and the satellite, dl is a line element along the satellite to receiver signal path, and $N_e(l)$ is the electron density along the signal path.

The TEC is defined as the number of electrons present in a column of unit cross-sectional area from the satellite to the ground receiver, i.e.,

$$TEC^{slant} = \int_r^s N_e(l)dl \tag{2.45}$$

Combining Eq. (2.44) and Eq. (2.45), we get

$$d^g_{ion} \equiv \frac{40.3}{f^2} TEC^{slant} \tag{2.46}$$

This implies that the group delay introduced by ionosphere is inversely proportional to the square of the signal frequency and thus can be estimated using differential technique using two different frequencies. With the advent of dual frequency GPS receivers, the ionospheric delay and thus the TEC could be estimated. GPS transmits two L-band carrier frequencies at L1 (f1=1575.42 MHz) and L2 (f2=1227.60 MHz). Using expression (2.46) for the dual frequency receivers one can write the TEC^{slant} as:

$$TEC^{slant} \equiv \frac{f_1^2.f_2^2}{40.3(f_1^2 - f_2^2)}.(P_1 - P_2) + TEC_{bias} \tag{2.47}$$

where, $P1$, $P2$ are the pseudoranges of $L1$, $L2$, respectively, TEC_{bias} presents the instrumental (satellite + receiver) bias correction term.

In addition to group delay, another effect that radio signals experience while propagating through the ionosphere is the carrier phase advance. From Eq. (2.42) one can derive the expression for phase advance similar to group delay. The expression is found to be:

$$d^p_{ion} \equiv -\frac{40.3}{f^2} TEC^{slant} \tag{2.48}$$

The negative value of d_{ion}^p indicate that the phase gets advanced on passing through the ionosphere. The slant TEC can also be calculated using the carrier phases at two frequencies of $L1$ and $L2$ using the formula:

$$TEC^{slant} \equiv \frac{f_1^2 . f_2^2}{40.3(f_1^2 - f_2^2)}.(\hat{L_2} - \hat{L_1}) + TEC_{bias} + TEC_{pa} \tag{2.49}$$

where, $\hat{L_1}$ and $\hat{L_2}$ are the phase advances (in distance unit) at the two carrier frequencies. The term TEC_{pa} represents phase ambiguity. TEC estimated from pseudoranges is called code TEC, while that from phase is called carrier TEC. For absolute value, code TEC is better as it is not affected by phase ambiguity and for relative values carrier TEC is preferable (e.g., see *Rideout and Coster* [2006]; *Jakowski et al.* [2011]). While deriving TEC from carrier phase advances, the phase ambiguity and phase lock (cycle slip) should be taken into account [*Rideout and Coster*, 2006]. In practice, a combination of the above two is used to calculate the TEC. The TEC is measured in TEC unit (TECu), 1 TECu=10^{16} electrons m^{-2}.

To obtain the vertical TEC (VTEC) at sub-ionospheric or pierce-point a thin shell model is assumed at an ionospheric height of 350 km [*Klobuchar*, 1996; *Rama Rao et al.*, 2006; *Bagiya et al.*, 2009] and is given by:

$$VTEC = TEC^{slant}.\cos\left(\sin^{-1}\left(\frac{R_e \cos\theta}{R_e + h_{max}}\right)\right) \tag{2.50}$$

where, R_e is the radius of the Earth (6378 km), h_{max} is the height of ionospheric shell (350 km), θ is the elevation angle of the satellite at the ground station (in radians). In addition to the ionosphere, the plasmasphere and the troposphere also influence the propagation of radio signals from satellite to ground but the delay due to these regions are negligible in comparison to the ionospheric delay. A greater details about GPS system, applications, errors, etc., can be found in literature (e.g., [*Parkinson et al.*, 1996, p. 489] and [*Jin*, 2013, p. 21]).

2.5.2.2 Derivation of TEC

RINEX (Receiver INdependent Exchange Format) observation and navigation files [*Gurtner*, 1993] are provided by the international GNSS service through its worldwide network. There is no well-documented systematic software for the extraction of TEC from these data files. In the current work, an open-source software, called, GPS toolkit (GPSTk) has been used. GPSTk is a collection of various subroutines and is used by a very wide group of people, such as, geodesy, geomatics, etc. [*Tolman et al.*, 2004; *Harris and Mach*, 2007]. The 30 second time resolution RINEX data is archived at Scripps Orbit and Permanent Array Center (http://sopac.ucsd.edu/cgi-bin/dbDataBySite.cgi) of University of California, San Diego. The monthly satellite differential code bias is obtained from the University of Bern (ftp://ftp.unibe.-ch/aiub/CODE/). The receiver bias correction is done using the most direct method, the zero-TEC-method [*Rideout and Coster*, 2006]. Average of 15 days nighttime minimum TEC is up- or down-shifted to 5 TEC unit, as in low-latitudes nighttime ionosphere may not be expected to be close to zero-TEC level. This shift in nighttime minimum is taken as receiver bias. As suggested by *Rama Rao et al.* [2006], GPS satellites with elevation angles greater than 45° are considered in this thesis work, which removes dependence of the TEC on the ionospheric pierce-point height and latitude, in addition to multipath effects.

2.5.3 TIDI Wind and SABER Temperature

Thermosphere Ionosphere Mesosphere energetics and Dynamics (TIMED) satellite was launched in December 2001 to monitor the dynamics of the mesosphere and lower thermosphere regions of the Earth's atmosphere. It was launched in a low-Earth polar orbit with an inclination of 74.1° and at an altitude of 625 km. So, TIMED satellite can reach up to 74° in latitude in both the hemispheres. Among other instruments, TIMED carried TIMED Doppler Interferometer (TIDI) and Sounding of the Atmosphere using Broadband Emission Radiometry (SABER) scientific payloads. Details of these two instruments and data obtained from them are briefly explained below.

(a) **TIDI:** TIMED Doppler Interferometer (TIDI) is a Fabry-Perot interferometer designed to investigate vector wind from 70-120 km altitude region with a vertical resolution of ~2 km at 3 ms^{-1} accuracies. Orthogonal orientation of the four TIDI telescopes allows it to measure winds in both the directions of the satellite track. Two telescopes at the same side view the same spatial location after a 9-minute gap and considering that within this time the dynamics has not changed, both meridional and zonal components are derived. TIDI limb-viewed observations provide vector wind fields from the Doppler shift in the emissions of OI 557.7 nm and in O_2(0-0) atmospheric band at 762 nm [*Killeen et al.*, 1999, 2006]. Depending on the available emissions, it measures winds from 70-120 km during day and 80-103 km during night. TIMED has a yaw rotation period of 60 days which limits the TIDI latitudinal coverage for a particular side of the track. The combination of the coldside (anti-sunward) and warmside (sun-ward) provides ± 90° latitudinal coverage. TIMED satellite orbits the Earth in 98 minutes (15 orbits per day) and the local time of the orbit does not change much within a day [*Wu et al.*, 2006]. The zonally averaged winds have errors of 7 ms^{-1} and 15 ms^{-1} during day and night, respectively.

(b) **SABER:** The Sounding of the Atmosphere using Broadband Emission Radiometry (SABER) instrument is also in orbit on-board the TIMED satellite. Unlike TIDI measurements, the satellite yaw-maneuver after approximately 60 days restricts the latitude coverage of this instrument. Thus, this instrument provides atmospheric temperatures from 53° in one hemisphere to 82° in the other hemisphere. SABER is basically a broadband radiometer which scans the sky in limb-viewing mode to measure radiance emitted from the atmosphere at 10 selected spectral bands from 1.27 to 15 μm. More detailed description can be found in *Russell III et al.* [1999]. The kinetic temperature is retrieved from the atmospheric 15 μm CO_2 limb emissions. Below 74 km the error involved in temperature retrieval is ±0.5 K, while above 75 km it varies with season, latitude, and altitude due to systematic error that arises mainly because of determination of abundance uncertainty in CO_2 [*García-Comas et al.*, 2008]. In winter polar region it is ±1-2 K below 95 km and ±4-5 K at 100 km. Errors in lower thermospheric kinetic temperature are large for the polar summer season.

2.6 Summary

The instruments and the data sets that are used in this thesis work are presented in this chapter. A brief historical account is given on the daytime airglow emission measurement techniques. The main instrument, MISE, that is used for obtaining the dayglow emission intensities along with the various elements used in this technique are described. The dayglow data analysis and calibration procedures are also detailed. The ground-based measurement of EEJ and the GPS-based measurement of TEC are also explained. Other than the ground-based measurements, the satellite-based measurements of temperature and wind that are used in this thesis are also explained briefly.

Chapter 3

Time Series Analysis Methods

3.1 Introduction

A wave propagating through the atmosphere perturbs the ambient parameters, such as the density, temperature, and winds. So, a study of the variabilities in these physical parameters as a function of time enables information on the wave dynamics of the different altitude regions of the atmosphere to which these observed parameters correspond to. The measurements of the atmospheric parameters with time constitute the time series. There are several time series analysis methods such as Fourier transform, least-square fitting of sines and cosines, Lomb-Scargle method, empirical mode decomposition, maximum entropy method, multi-spectral analysis (e.g., bi-spectrum analysis), Wigner distribution function, and wavelet transform. All these methods have their individual advantages and shortcomings. The time series analysis methods which are used in this thesis work are introduced in this chapter with an intention to provide detailed information on analysis procedures used, and refrain from discussing these details while presenting the results in other chapters. The relevant sections of this chapter are referred to as and when required in other chapters. The most well-know used technique for the analysis of time series is the Fourier analysis which can provide the frequency information for datasets that are equally spaced in time. For many reasons, geophysical measurements are very often unequally spaced in time. Interpolation of unevenly spaced data into equally spaced is not an appropriate option as in most cases, it enhances the power at low frequency components. Thus, for unevenly spaced data the most appropriate method of spectral analysis is the Lomb-Scargle [*Lomb*, 1976; *Scargle*, 1982] periodogram. In order to obtain information on the temporal occurrence of a particular frequency, in addition to frequency information, wavelet analysis [*Torrence and Compo*, 1998] can be used for datasets that are continuous. All these methods are implemented in IDL (Interactive Data Language) routines.

3.2 Time Series Analysis

The time series analysis involves extraction of information on the frequency, time period, amplitude, and temporal occurrence of physically varying features that are present in the data. Below we describe some of the commonly used time series analysis methods that are used in this work.

3.2.1 Fourier Analysis

The Fourier transform $F(\omega)$ of a continuous time series $f(t)$ is given by

$$F(\omega) = \int_{-\infty}^{+\infty} f(t)e^{-j\omega t}\,dt \tag{3.1}$$

where, $j = \sqrt{-1}$. The inverse transform is given by

$$f(t) = \int_{-\infty}^{+\infty} F(\omega)e^{j\omega t}\,d\omega \tag{3.2}$$

In practice, data obtained in an experimental observation are discrete function of time, $f(t_i)$, $i = 1, ..., N$. The Fourier transform for such functions is given by

$$F(\omega_u) = \frac{1}{N}\sum_{i=1}^{N} f(t_i)e^{-j\omega_u t_i} \tag{3.3}$$

for $u = 1, 2......, N$. This is also called the Discrete Fourier Transform (DFT). Similarly, the inverse DFT is given by

$$f(t_i) = \sum_{u=1}^{N} F(\omega_u)e^{j\omega_u t_i} \tag{3.4}$$

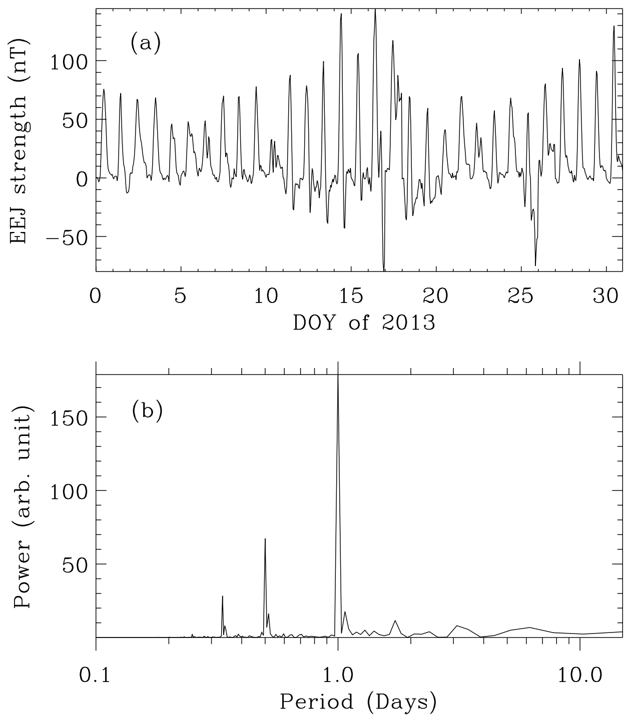

Figure 3.1: (a) Hourly values of the EEJ strength and (b) Fourier spectrum of EEJ. One can note the presence of the diurnal, semidiurnal, terdiurnal, and some planetary waves (though with comparatively low power).

The factor $1/N$ is the normalization factor which can be used in front of either forward or reverse transform. This factor can also be equal to $1/\sqrt{N}$ but have to be used for both forward and reverse transform cases, such that the multiplication of the two factors equal $1/N$.

It takes approximately N^2 multiplications and summations to calculate the DFT. In practice, for faster calculation, Fast Fourier Transform (FFT) is used which requires a maximum of $N \log N$ calculations. To demonstrate an example of Fourier analysis, Figure 3.1(a) shows hourly values of EEJ variations for the month of January 2013 and Figure 3.1(b) shows its Fourier spectrum. One can clearly see presence of tidal components of diurnal, semidiurnal, terdiurnal, and some planetary waves.

In many geophysical observations, the time-series obtained are not equally spaced in time due to various practical considerations. In such cases, least square fitting of sines and cosines, or an equivalent of that, called the Lomb-Scargle analysis method is used.

3.2.2 Lomb-Scargle Analysis

For an arbitrarily sampled data set, $h(t_i)$, $i = 1, 2, ..., N_o$, the classical periodogram (spectral power as a function of frequency) [*Scargle*, 1982] is defined as

$$\begin{aligned} P_h(\omega) &= \frac{1}{N_o}|DFT(\omega)|^2 \\ &= \frac{1}{N_o}\left|\sum_{i=1}^{N_o} h(t_i)e^{-j\omega t_i}\right|^2 \\ &= \frac{1}{N_o}\left[\left(\sum_i h_i \cos\omega t_i\right)^2 + \left(\sum_i h_i \sin\omega t_i\right)^2\right] \end{aligned} \tag{3.5}$$

This can be evaluated for any value of ω. If h contains a sinusoidal component of frequency ω_o, then at and near $\omega = \omega_o$ the factors h_i and $e^{-j\omega t_i}$ are in phase and makes a large contribution in the sums. At other values of ω the terms in the sum are randomly positive and negative and thus the sum is minimum. It can be shown that the statistical properties of Eq. (3.5) remain the same if it is modified as below:

$$P_h(\omega) \equiv \frac{1}{2}\left\{\frac{[\sum_i (h_i)\cos\omega(t_i-\tau)]^2}{\sum_i \cos^2\omega(t_i-\tau)} + \frac{[\sum_i (h_i)\sin\omega(t_i-\tau)]^2}{\sum_i \sin^2\omega(t_i-\tau)}\right\} \tag{3.6}$$

where, τ is a time offset parameter. This form of Eq. (3.6) makes $P_h(\omega)$ time-translation invariant and is equivalent to the least square fitting of sines and cosines to the data [*Scargle*, 1982]. *Horne and Baliunas* [1986] showed that for proper normalization of the periodogram, Eq. (3.6) has to be normalized with the total variance of the data. Also, for removing any contribution from the long-term trend the mean values can be subtracted. For a given set of data values, h_i, $i = 1, 2, ..., N_o$ with respective observation times t_i, the normalized Lomb-Scargle periodogram is defined by:

$$P_N(\omega) \equiv \frac{1}{2\sigma^2}\left\{\frac{[\sum_i (h_i-\bar{h})\cos\omega(t_i-\tau)]^2}{\sum_i \cos^2\omega(t_i-\tau)} + \frac{[\sum_i (h_i-\bar{h})\sin\omega(t_i-\tau)]^2}{\sum_i \sin^2\omega(t_i-\tau)}\right\} \tag{3.7}$$

where, $\omega = 2\pi f$ is the angular frequency corresponding to the normal frequency f, $\bar{h}$ and σ are the mean and standard deviation of h_i. The time-offset τ is given by

$$\tan(2\omega\tau) = \frac{\sum_i \sin 2\omega t_i}{\sum_i \cos 2\omega t_i} \tag{3.8}$$

The uncertainty in the frequency has been shown to be [*Horne and Baliunas*, 1986]

$$\delta\omega = \frac{3\pi\sigma_N}{2\sqrt{N_o}TA}, \tag{3.9}$$

where, A is the amplitude of the signal, σ_N is the standard deviation of the noise after the signal has been subtracted, and T is the total length of the data set.

The $P_N(\omega)$ in Eq. (3.7) thus calculated has several advantages over Fourier Transform [*Horne and Baliunas*, 1986]. They are:

(i) The constant τ makes $P_N(\omega)$ independent of shifting all the t_i's by any constant.

(ii) This form of $P_N(\omega)$ is exactly equivalent to extracting harmonic components using the least square fitting of sines and cosines to the time series.

(iii) If the signal h_i contains only noise, then $P_N(\omega)$ will follow an exponential probability distribution. This property thus provides a convenient way to estimate that whether a given peak is a true signal or it is the result of randomly distributed noise.

Some of the parameters related to Lomb-Scargle periodogram are discussed below.

3.2.2.1 The False Alarm Probability (FAP)

The FAP provides us information of significance level of the frequencies. As stated above, if a signal contains purely random Gaussian noise, then $P_N(\omega)$ follows exponential distribution (say, e^{-z}) [*Scargle*, 1982]. It means that for a particular frequency ω_o the probability that $P_N(\omega_o)$ is higher than or equal to z is $\Pr[P_N(\omega_o) > z]$=e^{-z}. Suppose that z is the highest peak in a periodogram that sampled N_i independent frequencies. Then, the probability that each independent frequency is smaller than z is $1 - e^{-z}$ and that every frequency is lower than z is $[1 - e^{-z}]^{N_i}$. Thus, the probability that some peak in the periodogram is higher than or equal to z is the FAP (F) and is given by

$$F = 1 - [1 - e^{-z}]^{N_i}. \tag{3.10}$$

Any power below F is regarded as statistically insignificant. So, the quantity 1-F is the probability that the given time-series contains the signature of a real signal.

But, in practice, many geophysical time-series spectra have the property that the spectral power increases with decreasing frequency (red-noise). So, to determine the proper significance level for a particular peak, one needs to choose appropriate background spectrum. For most of the geophysical time series the background spectrum is either white-noise (flat spectrum) or red-noise (the lower frequency or the slowly varying components have higher power due to their long span in the time series and reverse is the case for higher frequency components). There occur noises due to the interaction of the lower frequency components with the white noise, the presence of non-stationary behavior at higher frequency signals, and the finite length of the time series. The white-noise can be taken care of by transforming the time series to a normal distribution with zero mean and unit variance. For the estimation of red-noise, proper simulation has to be performed. A simple model for red-noise is the univariate lag-1 autoregressive AR(1) process [*Torrence and Compo*, 1998; *Ghil et al.*, 2002]:

$$h_i = \alpha_l h_{i-1} + r_i \tag{3.11}$$

where, α_l is the assumed lag-1 autocorrelation, $h_0 = 0$, and r_i is random noise taken from Gaussian white-noise. The DFT of Eq. (3.11), after normalization is [*Gilman et al.*, 1963; *Torrence and Compo*, 1998]

$$P_k = \frac{1-\alpha_l^2}{1+\alpha_l^2 - 2\alpha_l \cos(2\pi k/N_o)} \tag{3.12}$$

where $k = 0, ..., N_o/2$ is the frequency index. Choosing an appropriate α and using Eq. (3.12) one can simulate a red-noise spectrum for a given data set using Monte-Carlo method. Note, for $\alpha_l = 0$, Eq. (3.12) gives white-noise [*Torrence and Compo*, 1998]. Mean theoretical spectra from Monte Carlo simulation of such model for large number of iterations can be used as an approximation for red-noise spectra. When a particular feature of the data spectrum lies well above this theoretical noise spectrum, it is often considered to be statistically significant. A routine for such simulations can be found in *Schulz and Mudelsee* [2002].

3.2.2.2 The Number of Independent Frequencies

Frequencies ranging from $2\pi/T$ to Nyquist frequency can be obtained from a time series, where T is the total time interval. But many of the frequencies within this range will not be independent. The total number of independent frequencies is used as an input in calculating the FAP. To determine the correct number of independent frequencies, *Horne and Baliunas* [1986] carried out simulations using a large number of pseudo-Gaussian noise datasets with varying gaps in time coordinates. Based on the highest peaks in the periodograms of all these datasets they simulated the FAP function (Eq. (3.10)) with N_i as variable parameter. Based on that simulation they arrived at N_i value as a function of N_o value as

$$N_i = -6.362 + 1.193N_o + 0.00098N_o^2 \tag{3.13}$$

All the independent frequencies so obtained are not significant. By arbitrarily choosing some 615 random data points from the data set shown in Figure 3.1(a) a time-series with unequal spacing is made. The random numbers are generated using pseudo-random number generation technique. The Lomb-Scargle normalized periodogram of this unequally spaced data set is shown in Figure 3.2(b) for the EEJ of January 2013. Here the dashed line corresponds to the 95% false alarm level (FAL) and the periodicities beyond this threshold alone are considered significant in our analysis. One can see the presence of the same periods as seen from the Fourier spectral analysis in Figure 3.1 (with equally spaced data).

3.2.2.3 Amplitude and Phase Spectra

The Lomb-Scargle-normalized power (Eq. (3.7)) can be expressed as:

$$P_N(\omega) \equiv \frac{1}{2\sigma^2}\frac{N_o}{2}(a^2 + b^2) \tag{3.14}$$

where,

$$a = \frac{\sqrt{\frac{2}{N_o}}\sum_{i=1}^{N_o} h_i \cos\omega(t_i - \tau)}{\left(\sum_{i=1}^{N_o}\cos^2\omega(t_i - \tau)\right)^{1/2}}, \tag{3.15}$$

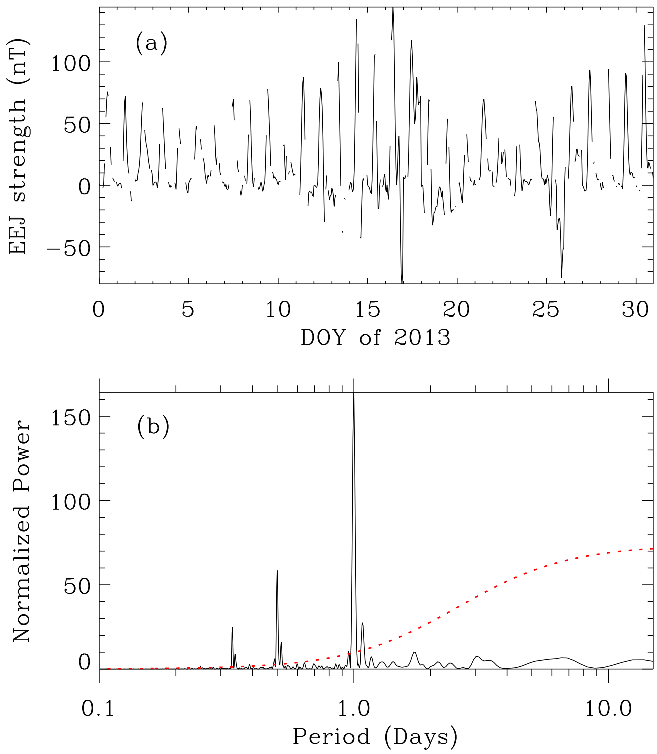

Figure 3.2: (a) Random data gaps have been introduced in the EEJ strength data as shown in Figure 3.1(a). (b) The Lomb-Scargle periodogram of unequally spaced data of (a) above are shown. The presence of the same periodicities as those observed from the Fourier transform are also observed here as can be seen in (b). The dashed line represent the 95% confidence limit derived based on Monte-Carlo simulation.

$$b = \frac{\sqrt{\frac{2}{N_o}} \sum_{i=1}^{N_o} h_i \sin\omega(t_i - \tau)}{\left(\sum_{i=1}^{N_o} \sin^2\omega(t_i - \tau)\right)^{1/2}}, \tag{3.16}$$

and the given time series (h_i) can be fitted to:

$$h_f(t_i) = a\cos\omega(t_i - \tau) + b\sin\omega(t_i - \tau) \tag{3.17}$$

Then the amplitude spectra is

$$\begin{aligned} A(\omega) &= \sqrt{a^2 + b^2} \\ &= \sqrt{\frac{2}{N_o} 2\sigma^2 P_N(\omega)} \end{aligned} \tag{3.18}$$

The Eq. (3.17) can also be expressed as:

$$h_f(t_i) = A(\omega)\cos[\omega(t_i - \tau) + \phi] \tag{3.19}$$

where, $\phi = -\tan^{-1}(b/a)$. The phase spectrum is defined by the cosine argument of $h_f(t_i)$ at the time $t_i = 0$, i.e.,

$$\varphi_i = -\omega\tau + \phi \tag{3.20}$$

Thus, using Eq. (3.18) and (3.20), the Lomb-Scarge amplitude and phase spectra can be calculated [*Hocke*, 1998].

3.2.3 Wavelet Analysis

Both the Fourier and the Lomb-Scargle analyses consider that the frequencies obtained are present for the whole interval of time, i.e., they consider the signals as stationary and therefore do not provide any temporal information. Thus there is an ambiguity in space time localization of a certain frequency. In order to obtain the power of a certain frequency at a given time and their temporal variation many multi-resolution analysis methods are commonly used, such as, Windowed or Short-Time Fourier Transform (WFT/STFT), Wavelet-transform, and Wigner distribution. Two of these, that are used in this thesis work are explained below with their respective merits and shortcomings.

3.2.3.1 Short Time Fourier Transform (STFT)

The STFT of a time series, $f(t)$, is given by

$$STFT(d,\omega) \equiv \int_{-\infty}^{+\infty} f(t)W(t-d)e^{-j\omega t}\,dt \tag{3.21}$$

or, for discrete case,

$$STFT(d,\omega) \equiv \sum_{-\infty}^{+\infty} f(t)W(t-d)e^{-j\omega t} \tag{3.22}$$

Here, the given signal $f(t)$ is split up into several time segments using the time translation window function $W(t-d)$ with d as the translation parameter. Then, each of the segments are Fourier analyzed to find the frequency information. At each time interval the frequencies are accumulated to get the time and frequency information simultaneously. Typical examples of window functions are

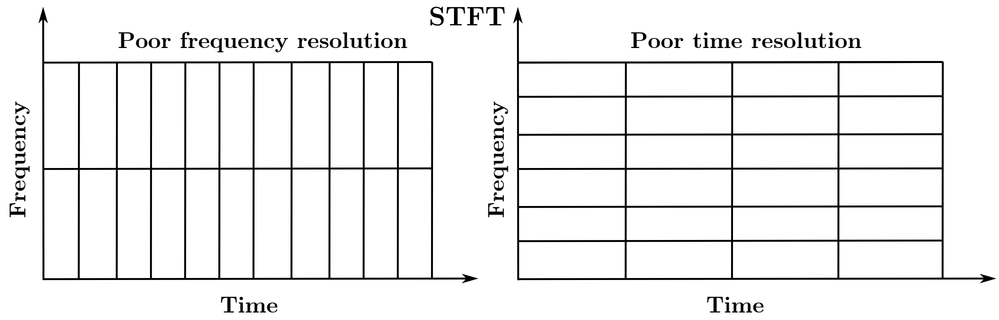

Figure 3.3: Box representation of the time and frequency resolution of STFT method.

rectangular, Gaussian, Hanning, and Hamming. Within each window the signal is considered as stationary, and the time corresponding to the center of the window is used to provide temporal location. The decision of window width is not well defined. Also signals for which the time period is larger than the window length (i.e., very low frequency signals) cannot be detected in the spectrum as they will appear as DC (flat) component within the window. Thus, the width of the window limits the time and frequency resolution. Figure 3.3 shows a pictorial representation of the time frequency space in box representation. The width and height of the boxes represent the time and the frequency resolutions, respectively. One can note that with increasing frequency, the time resolution remains same. Increasing the temporal resolution will make the time interval too short which results in a broader frequency resolution. Similarly, increasing frequency resolution will result in a poorer temporal resolution. This is like an uncertainty principle – both the parameters can not be measured with 100% accuracy! To overcome these difficulties the Wavelet analysis method has been developed.

3.2.3.2 Wavelet Transform

Wavelets were in use since 1909 [*Haar*, 1910] but the concept of wavelet transform originated in 1980s. It was the geophysicist Jean Morlet and others [*Morlet et al.*, 1982] invented the term wavelet and later formalized by *Grossmann and Morlet* [1984] and *Goupillaud et al.* [1984]. *Daubechies* [1988] proposed systematic method to construct orthogonal wavelets. *Mallat* [1989] introduced the fast method of calculation of wavelet transform.

For the analysis of non-stationary or rapidly varying time series or for the cases where, in addition to frequency information, the time of occurrence of the frequencies is needed, the wavelet transform is used. The wavelet transform has wide variety of applications in economy and medical fields in addition to the science and engineering. The continuous wavelet transform (CWT) of a square-integrable function $f(t)$ is the convolution of $f(t)$ with a translated and scaled version of the basic signal (called mother wavelet), $\psi(t)$, and is given by

$$W_{t,\psi}(s,d) = \frac{1}{\sqrt{|s|}} \int_{-\infty}^{+\infty} f(t)\psi^*\left(\frac{t-d}{s}\right) dt \tag{3.23}$$

where, $\psi\left(\frac{t-d}{s}\right)$ is called daughter wavelet as it is derived from mother wavelet by translation and scaling and the superscript $(^*)$ on it represents its complex conjugate; s and d are the scaling and shift (dilation) parameters. The factor $1/\sqrt{|s|}$ is used for normalization. The mother wavelet $\psi(t)$ should satisfy the admissibility condition, which is given below:

Admissibility condition: The admissibility factor (C_ψ) should be finite, i.e.,

$$C_\psi = \int_{-\infty}^{+\infty} \frac{|\Psi(\omega)|^2}{|\omega|} d\omega < \infty \tag{3.24}$$

where $\Psi(\omega)$ is the Fourier transform of $\psi(t)$. This condition is required to ensure that the inverse transform is possible. With this condition the wavelet function must have zero mean and localized in both time and frequency space. Thus, the Gaussian or rectangular windows do not satisfy this condition as they can be localized but are of non-zero mean [*Farge*, 1992].

Examples of wavelets: Depending on the type of signal to be analyzed, various types of mother wavelets are used, for example, Morlet, Haar, Mexican hat, derivative of Gaussian, etc. Here we discuss about Morlet wavelet as it is the most widely used mother wavelet in geophysical applications. The Morlet wavelet consists of a plane sinusoidal wave modulated by Gaussian as given below in Eq. (3.25) and is depicted schematically in Figure 3.4.

$$\psi_o(\eta) = \pi^{-1/4}\, e^{j\omega_o\eta}\, e^{-\eta^2/2} \tag{3.25}$$

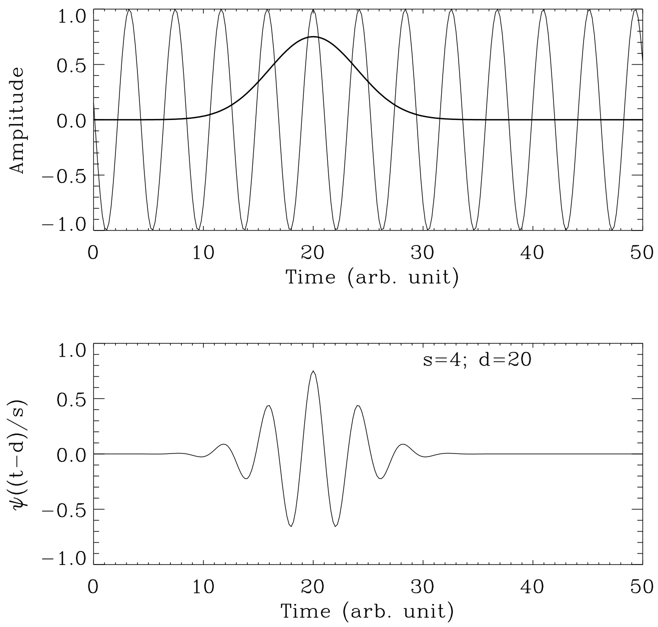

Figure 3.4: The Morlet wavelet (bottom) along with its composite functions $\Re(e^{j\omega_o t})$ and $e^{-t^2/2}$ (top) are shown ($\Re$ means real part).

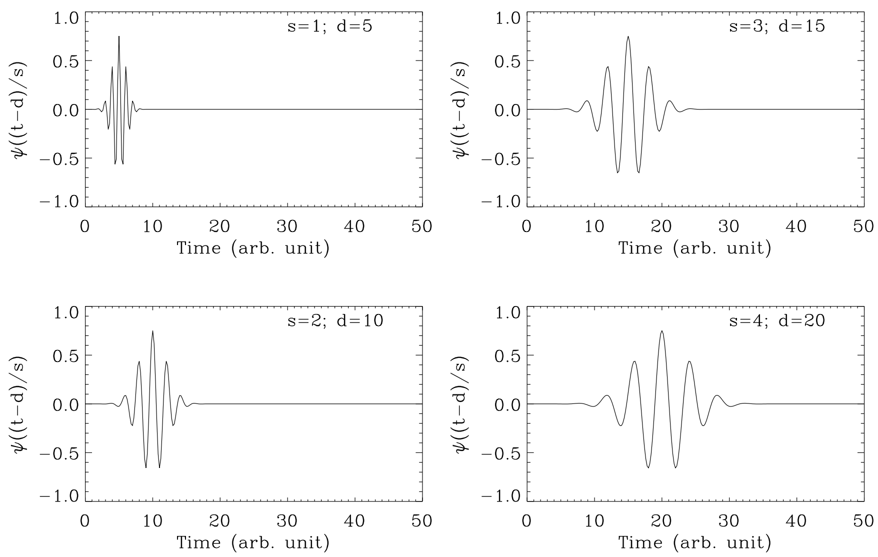

Figure 3.5: Morlet daughter wavelets with different scales and translations. The scaling parameter makes the wavelet function broader, while the translation parameter just translates the central position.

where, η is a non-dimensional time parameter and ω_o is the non-dimensional frequency which has been taken as 6 to satisfy the admissibility condition [*Farge*, 1992]. A few daughter wavelets obtained by translation and scaling of the Morlet function are shown in Figure 3.5. One can note that with increasing scale (s), the width of the scaling parameter increases. The scale is inversely proportional to frequency; larger scales correspond to smaller frequencies and expanded daughter wavelet.

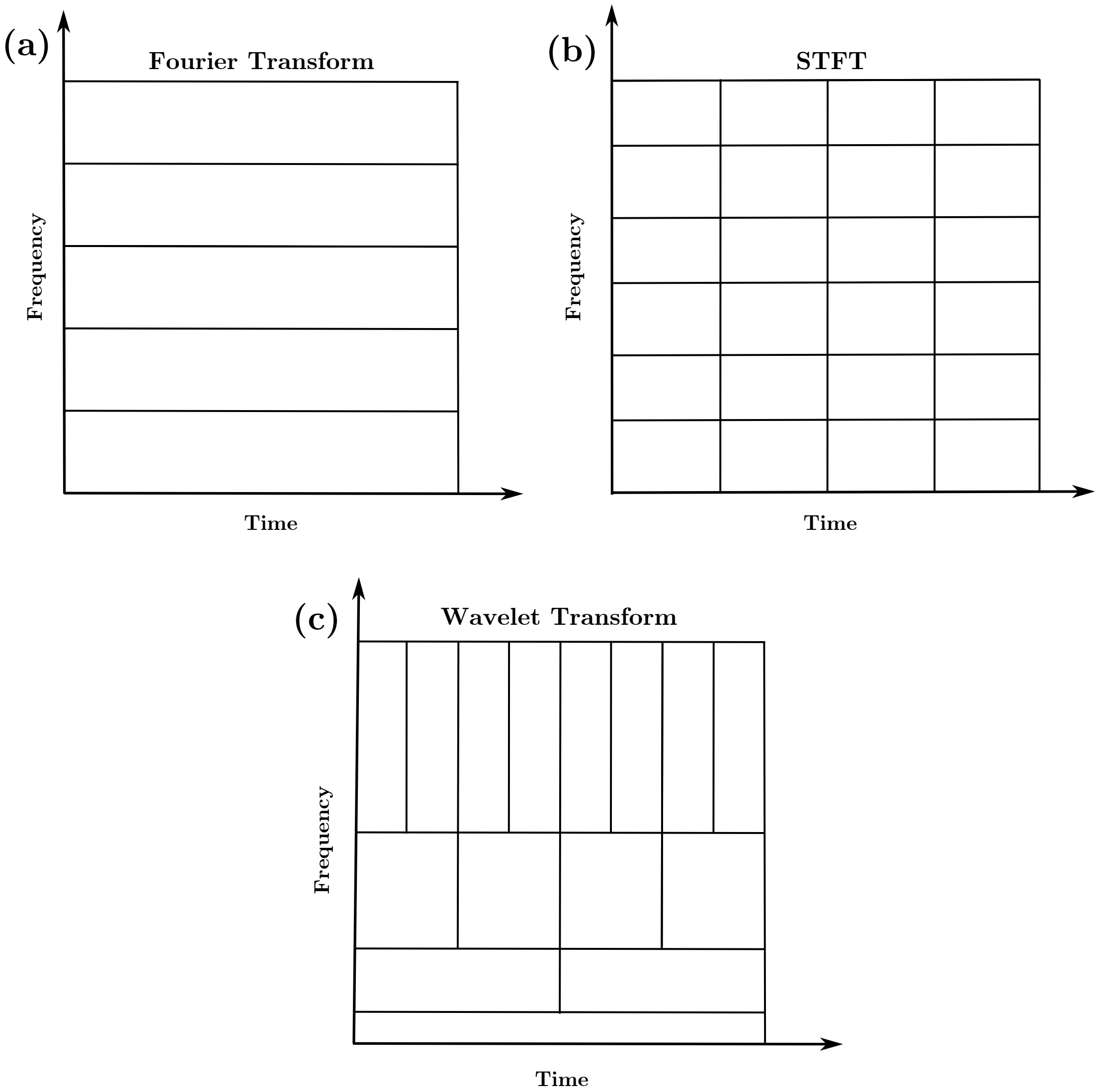

Figure 3.6: Box representation of the time and frequency resolutions for Fourier, STFT, and wavelet transforms. One can note that for wavelet transform, with increasing frequency the time resolution also increases.

Figure 3.6(c) shows the box representation of the frequency (1/scale) and time (translation) for the wavelet transform. For comparison, the box representations for Fourier and STFT are shown in Figure 3.6(a) and Figure 3.6(b). One can see that for wavelet transform, for the lower values of scales (i.e. higher frequencies) the time resolution is good and for the higher values of scales i.e., for lower frequencies the time resolution is low. Whereas, Fourier-transform does not provide time information and STFT has limitations as explained in previous section. Thus, the wavelet transform provides flexible time-frequency window which adjust automatically; shrinks down while observing higher frequency components and expands for low frequency components.

In choosing the wavelet function several factors should be considered [*Torrence and Compo*, 1998]. Some of them are given below:

(a) **Complex or real:** A complex wavelet function captures both amplitude and phase of the signal which are essential parameters for geophysical applications. Also, complex wavelets are better adapted for capturing oscillatory behavior. Whereas, real wavelets are used to isolate peaks or discontinuities.

(b) **Width:** The width is defined as the e-folding time of the wavelet amplitude. A narrow width (in time) function will provide better time resolution and poor frequency resolution, while a broad function will provide better frequency resolution and poor time resolution.

(c) **Shape:** Depending on the type of variations in the signal to be studied, the shapes of the wavelet functions are chosen. For example, for sinusoidal type variations Morlet, and for sharp jump in signal, Haar functions are used. If one is primarily interested in the wavelet power spectra only, then the choice of wavelet function is not critical, and any one of the functions will give the same qualitative results as the other.

3.2.3.3 CWT of Discrete data

In practice, the measurements carried out are discrete in time. Let, x_n, $n = 0, 1, ...N-1$, be the discrete time series, then the wavelet transform is given by [*Torrence and Compo*, 1998]

$$W_n(s) = \sum_{n'=0}^{N-1} x_{n'} \psi^* \left[\frac{(n' - n)\delta t}{s} \right] \tag{3.26}$$

where, δt is the spacing of the time series data points. By varying the time index, n, and translating it one can calculate the wavelet coefficients. A faster method to calculate the wavelet coefficients can be obtained by using convolution theorem. According to the theorem, the wavelet transform will be the inverse Fourier transform of the product of the Fourier transforms of the signal ($\hat{x}_k$), and the conjugate of the mother wavelet [*Daubechies*, 1988].

$$W_n(s) = \sum_{k=0}^{N-1} \hat{x}_k \hat{\psi}^*(s\omega_k) e^{i\omega_k n\delta t} \tag{3.27}$$

where $\hat{x}_k$ is the Fourier transform of x_n and is given by

$$\hat{x}_k = \frac{1}{N} \sum_{n=0}^{N-1} x_n e^{-j2\pi kn/N} \tag{3.28}$$

and the Fourier transform of the function $\psi(t/s)$ is given by $\psi^*(s\omega_k)$. The angular frequency ω_k, is defined by:

$$\omega_k = \begin{cases} \frac{2\pi k}{N\delta t} & \text{if } k \le N/2 \\ -\frac{2\pi k}{N\delta t} & \text{if } k > N/2 \end{cases} \tag{3.29}$$

The wavelet function is in general complex, so $W_n(s)$ is also complex. The power is given by $|W_n(s)|^2$. The amplitude of the signal is given by $|W_n(s)|$ and the phase is given by $\tan^{-1}[\Im\{W_n(s)\}/\Re\{W_n(s)\}]$, where, $\Im\{W_n(s)\}$ and $\Re\{W_n(s)\}$ are the imaginary and real parts of $W_n(s)$. Below we explain some features of the wavelet transform.

Choice of scales:

For convenience, wavelet scales are usually chosen at fractional powers of 2:

$$s_i = s_0 2^{i\delta i}, \quad i = 0, 1, ..., I \tag{3.30}$$

$$I = \delta i^{-1} \log_2(N\delta t/s_0) \tag{3.31}$$

where s_0 is the smallest resolvable scale and I determines the largest scale. The s_0 is chosen in such a way that the corresponding Fourier period is approximately $2\delta t$ (δt being the sampling interval for discrete data sets). For the Morlet wavelet, a δi of about 0.5 is the largest value that still gives adequate sampling in space. Smaller values of δi give finer resolution [*Torrence and Compo*, 1998].

Wavelet Scale and Fourier Frequency

Meyers et al. [1993] showed that the wavelet scales are not necessarily inversely proportional to the frequency. The relationship can be derived analytically for a particular wavelet function by substituting a cosine function in (3.27) and computing the scale s at which wavelet spectral power is maximum. For Morlet function, with ω_o=6, the relation is $\lambda = 1.03s$, where λ is the Fourier period. This indicates that for Morlet wavelet the wavelet scale is almost equal to the Fourier period.

Cone of Influence

In practice, the time series data are of finite-length and thus errors will occur at the extreme ends of the wavelet power spectrum as Fourier transform for the wavelet analysis assumes data to be cyclic. One solution is to pad the time series at both ends by zeros to bring the total length N up to the next higher power of two. This makes the transform faster and limits edge effect. The process of zero padding introduces discontinuities at the endpoints and for larger scale variations it reduces the amplitude near the edges. The cone of influence (COI) is the region of the wavelet spectrum in which edge effects become important. It is defined as the e-folding time for the autocorrelation of wavelet power at each scale. For Morlet wavelet the e-folding time (τ_s) is given by $\tau_s = \sqrt{2}s$.

Figure 3.7 shows the wavelet transform of the same EEJ data set that has been analyzed with other two methods. From the wavelet spectra one can see the presence of all the tidal and planetary wave components along with their temporal information. Notably, the same periodicities as seen in the cases of Fourier transform and Lomb-Scargle method are also clearly visible here along with their temporal occurrences. From this wavelet transform, one can find the amplitudes and phases of particular period with respect to time. For example, Figure 3.7(b) shows the amplitude spectra of semidiurnal tides (period=0.5 day). One can note that the amplitude is very high at around DOY 14-15 of 2013. Similarly, the diurnal period is maximum throughout the period of observation. The presence of quasi-2-day (between DOY 16-20) and 8-9 days can also be

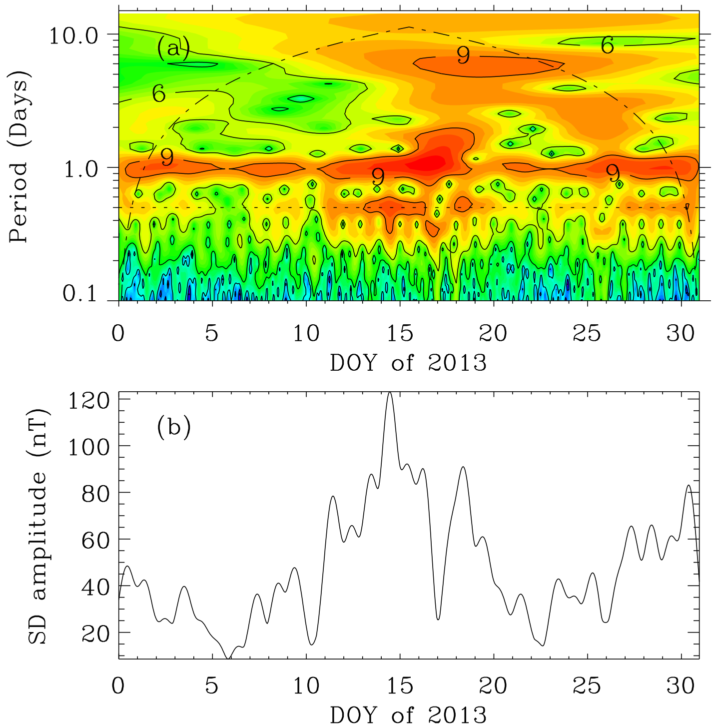

Figure 3.7: (a) The wavelet transform of the EEJ strength for the month of January 2013 as shown in Figure 3.1(a). The occurrence of the same periodicities as seen in the cases of Fourier transform and Lomb-Scargle method are clearly visible along with their temporal occurrences. (b) The amplitude spectra of the semidiurnal component is shown. The dashed horizontal line in (a) marks the place of the semidiurnal component and the dashed-dotted lines represent the cone of influence.

noted. The wavelet spectra of two independent data sets can be compared for the investigation of the simultaneous occurrences using the cross-wavelet (scalar multiplication of the wavelet spectra of the two individual data sets) spectra. The scope of wavelet analysis is very broad and we will see its application in the investigations of the coupling of the atmospheres in the next chapters.

3.3 General Discussion

The natural processes are continuous, but, the data that we obtain are sampled at discrete intervals due to various practical considerations. The maximum frequency that can be obtained from a given data sampling rate is equal to 1/(2 times of sampling interval), i.e., Nyquist frequency. While sampling the data sets, we must take into account that the signal that we are interested in should have frequency lower than the Nyquist frequency of the time series to be made. Also, there occurs aliasing of frequencies due to inappropriate sampling. Here is an example of frequency aliasing: Consider, we have a signal $y(t) = \cos(2\pi t * 9)$ as shown in Figure 3.8. Now we sample the same signal at equally spaced intervals as shown in figure by circled points. So, a spectral analysis will show a prominent peak at a frequency as if it is generated by the dashed line. This occurred due to under sampling of the data sets. This type of aliasing problem can be avoided by having enough samples and more appreciably by taking random sample. On the other hand, while studying a low frequency signal, a high frequency signal can also contribute to the power of it as observed in the case of Figure 3.8. In order to avoid any false contribution to the low-frequency components from high frequency ones a low-pass filter may be used. Also, still lower frequency components (like seasonal components) can also contribute to the power of moderate frequency components. These type of seasonal behavior can be removed by detrending the time series using least square fitting of the seasonal components. Wavelet transform needs equally spaced data as input and it is one of its limitations. But the property of the wavelet that it automatically filters out various frequency components makes it less vulnerable to frequency aliasing unless there is a situation as shown in Figure 3.8 that arises due to insufficient sampling. A comprehensive review of some of the spectral analysis methodology can be found in *Tary et al.* [2014].

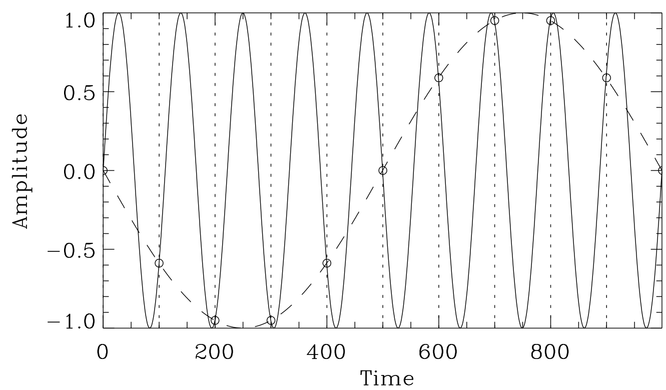

Figure 3.8: An example of frequency aliasing that arises due to inappropriate sampling.

3.4 Summary

In this chapter, the time series analysis methods that are used in this thesis work are presented briefly. The Fourier transform is best suited for finding frequency components in an equally spaced time series. Lomb-Scargle is an equivalent method for the period analysis of unequally spaced data and is also suitable for equally spaced data points. For understanding the cause and effects of certain phenomena/processes the time of occurrence is very often an important information. In such cases, the Wavelet transform is used for retrieving the time and frequency information simultaneously. The aliasing (leakage of spectral power to a lower-frequency component which actually is not present in the time series) occurs in the frequency spectrum due to sampling issues. The aliasing problem can be alleviated by choosing or testing random samples or unequally spaced time series.

Chapter 4

Dependence of Vertical Coupling on Solar Activity

4.1 Background

In this chapter, we present the wave dynamical vertical coupling of the atmospheres and its variation with solar activity. The wave dynamical characteristics of both shorter and longer period waves are discussed here. For the study of shorter period waves, high data cadence is required, which are available mainly through ground-based study. However, for studies of waves of longer periodicities, data sets from ground, satellite, and assimilative models can be used. As explained in Chapter 1, the propagation and dissipation of waves depends on the background condition, which varies with solar activity. Thus, the wave influence on the upper atmosphere shows solar activity dependence. In this chapter, results obtained on the vertical coupling of atmospheres and its solar activity dependence for long and short time-scale are presented. Long and short period waves are presented in sections 4.2 and 4.3. A summary is presented in section 4.4.

4.2 Longer Period Waves (Planetary-Scale)

In this section, we will examine influences of large-scale (planetary-scale) waves on the upper atmosphere in the context of wave dynamical vertical coupling of atmospheres.

4.2.1 Introduction

With the advent of various advanced ground- and satellite-based measurements, which provide information on the temporal variation and altitude structure of a given parameter for a given location, it is found that various layers are, to a significant extent, dynamically coupled [e.g., *Immel et al.*, 2006; *Pallamraju et al.*, 2012]. The dynamical coupling between lower and upper atmosphere can happen by the propagation of waves of various time-periods and scale-sizes. The wave influence is mainly through the dissipation of gravity waves [e.g., *Hines*, 1960; *Hocke and Schlegel*, 1996; *Fritts and Alexander*, 2003], tides [e.g., *Forbes*, 1982; *Pedatella and Forbes*, 2010] and planetary waves [e.g., *Salby*, 1984; *Forbes*, 1995; *Pancheva et al.*, 2008]. The wave dynamics in the upper atmosphere can be due to the superposition of waves due to all the sources mentioned above.

Planetary waves are global-scale oscillations in the neutral atmosphere with periods between 2-30 days [*Salby*, 1984] and wavelengths of the order of the radius of Earth. The most commonly observed planetary waves which, in general, are produced in the troposphere, are of periods that are around 2, 5, 10, 16, and 25 days. These planetary waves are identified as manifestations of the normal modes of the atmosphere [*Salby*, 1984]. From a numerical study, *Salby* [1981a] had shown that depending on the background atmospheric conditions such as non-isothermality, magnitude and direction of winds, these normal modes can undergo spectral broadening, dissipation, and Doppler shifts.

The 5-day wave is generally referred to as a westward propagating rotational Rossby mode wave of wavenumber one and having a period of 4 - 6.5 days [*Salby*, 1981b, 1984; *Meyer and Forbes*, 1997; *Niranjan Kumar et al.*, 2012; *Sassi et al.*, 2012]. The 10-day (theoretically, 8.3 - 10.6 days [*Salby*, 1984]) wave is also a westward propagating Rossby-normal-mode of wavenumber one. The 16-day wave is the second symmetric Rossby-normal-mode resonant oscillation of the atmosphere. Depending on the background atmospheric conditions, the 16-day wave can have periods between 11.2 - 20 days with 16-day as median value [*Salby*, 1984]. The 25-day wave is also a normal-mode and may be distorted by the background flow due to its slow movement. The behavior of these planetary waves, or Rossby-normal-modes, shows dramatic features, such as amplification, propagation to upper atmosphere, etc., during SSW events. Details of the ambient conditions of the atmospheres during SSW events have been presented in Chapter 1. Though the SSW is a polar latitude event, it is found that it influences the dynamics of the low-latitude atmosphere-ionosphere system significantly through atmospheric coupling [e.g., *Fejer*, 2011; *Chau et al.*, 2012; *Guharay and Sekar*, 2012], in particular, the 16-day mode planetary wave has been found to be highly associated with SSW activity [*Pancheva et al.*, 2008].

The dynamical coupling between the lower and upper atmosphere in terms of planetary waves has been a subject of intense research [e.g., *Fejer*, 2011]. From theoretical and modeling studies, it is demonstrated that the planetary waves do not propagate directly above about 100-110 km [*Pogoreltsev et al.*, 2007]. However, their influence is communicated through their interaction with other dynamical features and are reported in various parameters in the MLT and ionosphere (MLTI) regions, such as, mesospheric wind [e.g., *Gurubaran et al.*, 2001], mesospheric temperature [e.g., *Sassi et al.*, 2012], TEC [e.g., *Goncharenko et al.*, 2010; *Sripathi and Bhattacharyya*, 2012], mesospheric airglow [e.g., *Takahashi et al.*, 2002], EEJ [e.g., *Parish et al.*, 1994; *Abdu et al.*, 2006; *Vineeth et al.*, 2007] and F-region ionospheric parameters [e.g., *Fejer*, 2011; *Chau et al.*, 2012]. It is suggested that the planetary wave influence is transmitted to the MLT region by three possible mechanisms: i) through interaction with propagating gravity waves, ii) through interaction with tidal waves, and iii) the electrodynamical coupling in the E-region (80 - 120 km) at equatorial-latitudes. This third mechanism, in turn, contributes to the modification of several equatorial- and low-latitude phenomena such as the EIA and the ETWA.

While long-period tidal and planetary wave type variations of periods 2-30 days can be studied using satellite-based measurements of atmospheric parameters, simultaneous ground-based measurements of emissions originating at multiple altitudes have the advantage that they provide information at a high temporal cadence on the wave dynamics that are present at those altitudes at the same time. The importance of the ground-based investigations of the daytime upper atmospheric dynamics has, in the recent past, been gaining momentum, especially due to several results that showed an influence of daytime upper atmospheric phenomena on the nighttime plasma processes [e.g., *Raghavarao et al.*, 1988b; *Sridharan et al.*, 1994; *Pallam Raju et al.*, 1996; *Pallamraju et al.*, 2004; *Pallamraju and Chakrabarti*, 2006; *Pallamraju et al.*, 2010; *Valladares et al.*, 2001; *Prakash et al.*, 2009].

The objective of this section is to characterize the upper atmospheric response to various forcings from above (solar input) as well as below (waves in general). In this regard, an effort has been made to investigate the dynamical coupling between lower and upper atmospheres in terms of planetary wave signatures during different levels of solar activity. The wave dynamical behaviors of atmospheres at various altitudes are investigated for inter-relationships and compared with the influence of solar variability to assess the relative response of the upper atmospheric behavior to the solar versus the lower atmospheric influences.

4.2.2 Data Set

To study the vertical coupling of atmospheric regions, measurements representing different altitudes of the atmosphere are considered. As mentioned in section 2.3 the dayglow emission intensities at OI 557.7, OI 630.0, and OI 777.4 nm, represent altitude regions approximately at 130 km, 230 km, and peak height of the F-region, respectively [*Kulkarni*, 1976; *Witasse et al.*, 1999; *Pallamraju et al.*, 2013]. TEC is known to represent the variability the ionosphere. The variability of the EEJ strength (which originates at around 105 km altitude) represents the behavior of the lower thermosphere. The details of TEC and EEJ measurements can be found in section 2.5.

To investigate the behavior of lower atmosphere, stratospheric winds are used. The National Centers for Environmental Prediction (NCEP) and National Center for Atmospheric Research (NCAR) have cooperated in a project (denoted "reanalysis") which involves the recovery of land surface, ship, rawinsonde, pilot-balloon, aircraft, satellite, and other data [*Kalnay et al.*, 1996]. Daily-averaged and 4 times a day data at a 2.5°× 2.5° latitude-longitude grid for the whole globe and for 17 pressure levels from the Earth's surface up to 10 hPa for several atmospheric parameters (wind, temperature, pressure, etc.) are made available. For the current study, the zonal wind at 10 hPa (which approximately corresponds to an altitude of 30 km) is used to assess the characteristics of the planetary waves in the lower atmosphere.

The dayglow emission intensities for January to March of the years 2011 and 2012 are used here. As the investigations in this study pertain to the effect of large-scale (planetary) waves on the upper atmosphere, the results are expected to be independent of the view orientation of dayglow emission intensity chosen, so we used only the northernmost viewing direction (as shown in Figure 2.13) data in this study.

During our observational period, GPS-TEC data from stations within Indian longitudes and in the vicinity of northern hemisphere's crest-location of the EIA were either irregular or not available. So, as the winter anomaly subsided in this low solar epoch [*Nanan et al.*, 2012], TEC data from a magnetically conjugate location in the southern hemisphere, (Diego Garcia: Geog. Lat. 7.27° S, Long. 72.4° E; 15.3° S MLAT), has been used. Further, it is expected that the variations between these two conjugate locations are nearly identical. Moreover, comparisons of the standard score of the hourly averaged daily afternoon TEC from a GPS receiver near the northern hemispheric EIA crest region (for those days on which data were available) showed similar temporal variations with that of the Diego Garcia. In fact, for the year 2011 the standard score ($z = (x_i - \bar{x})/\sigma$; where x is daily daytime averaged TEC, σ is standard deviation, and $\bar{x}$ is the mean of all x's) of the common data from the two stations nearly overlay on each other as shown in Figure 4.1. For the year 2012 there were minor differences at smaller timescales (periods of 2-3 days).

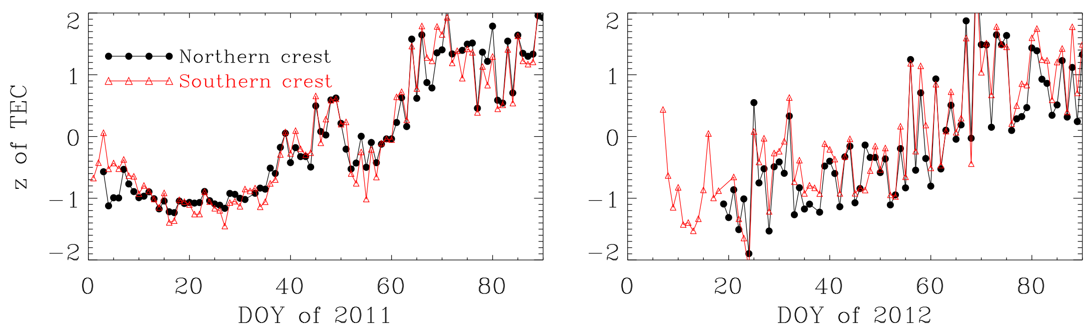

Figure 4.1: The standard score (z) of the TEC obtained from the northern and southern crest of EIA are shown. The northern crest TEC data corresponds to Ahmedabad and the southern crest corresponds to Diego Garcia Island. For this Figure the Ahmedabad data for 2011 has been obtained from GAGAN project and the 2012 data is from the receiver in Physical Research Laboratory. As there are less data sets available for northern crest in 2012, we used Southern crest data in this chapter.

4.2.3 Results and Discussion

Figure 4.2 shows all the clear sky days' dayglow data of January to March for the years of 2011 (left panel) and 2012 (right panel). The subplots (a) & (d), (b) & (e), and (c) & (f) show daily dayglow emission intensity variations in Rayleighs at OI 777.4, OI 630.0, and OI 557.7 nm, respectively. The data gap around noon-time arises due to strong solar glare which enters directly into the slit of the spectrograph and saturates the CCD, thereby preventing any useful measurements. For the dayglow emission intensities, the durations covered in this study are from DOY 7 to 90 for 2011 and from DOY 12 to 85 for 2012 comprising 52 and 35 days in those years.

The production mechanisms for the OI 630.0, OI 557.7, and OI 777.4 nm emissions are given in Chapter 2. As the production mechanisms are dependent on the solar ionizing radiation available at a given location, the SZA dependent variation is an inherent feature as can be seen in Figure 4.2. In addition to the SZA-dependent variation, the dayglow intensity variations are also expected to contain the neutral dynamical features of both shorter-scale (gravity wave) and

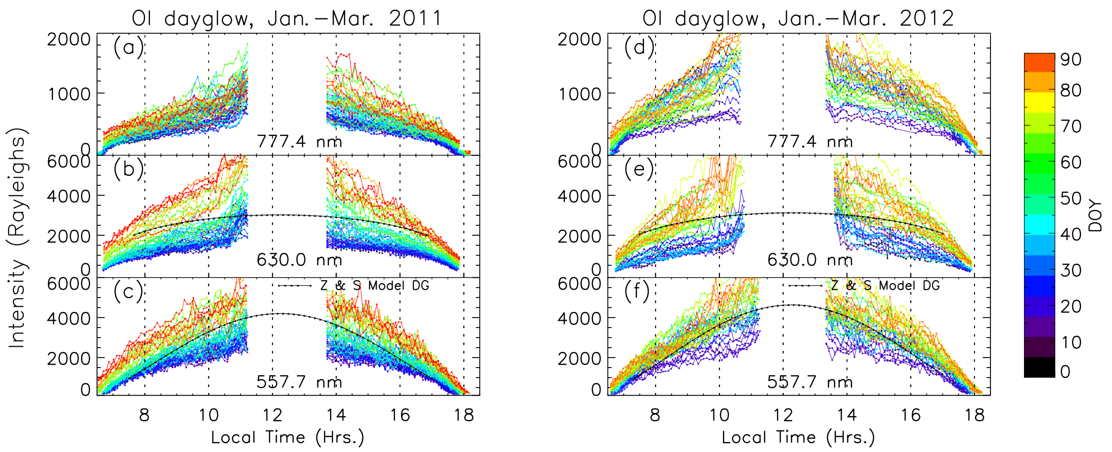

Figure 4.2: The daily dayglow emission intensities at the three wavelengths: OI 777.4 nm, OI 630.0 nm, and OI 557.7 nm for all the clear sky days during January to March of 2011 (left panel) and 2012 (right panel) for the 38° elevation angle with respect to North (as shown in Figure 2.13). Days covered in this study are from DOY 7 to 90 for 2011 and from 12 to 85 for 2012. The smooth curves in the two lower panels are the dayglow emissions as estimated using the Zhang and Shepherd empirical model [*Zhang and Shepherd*, 2004, 2005] for DOY=40. It can be noted that the dayglow emission intensities are higher in 2012 due to higher solar activity as compared to 2011.

longer-scale (planetary wave) periodicities. There are periodicities in the gravity wave regime (few minutes to few hours) in all these emissions, which will be discussed in section 4.3. The solid black lines in panels (b) & (e), and (c) & (f) of Figure 4.2 are the empirical model predictions for OI 630.0 nm and OI 557.7 nm as presented by *Zhang and Shepherd* [2004, 2005]. To repeat, these models are based on measurements made by WINDII and the inputs to them are the SZA and solar F10.7 cm flux on that day. It may be noted that these models are applicable for SZA $< 80°$.

Although the daily variation of dayglow intensities averaged during various local time hours reveal that the planetary wave type periods near to 5-day, 10-day, and 16-day are found to be present at all local times from morning to evening, only the averaged afternoon (1430 to 1730 local time, LT) dayglow intensity data are used here, as the data during this period has fewer gaps and is present for greater number of days. In Figure 4.3, panels (a) shows the dayglow emission intensities at the three wavelengths, (b) shows the daytime peak-EEJ strength

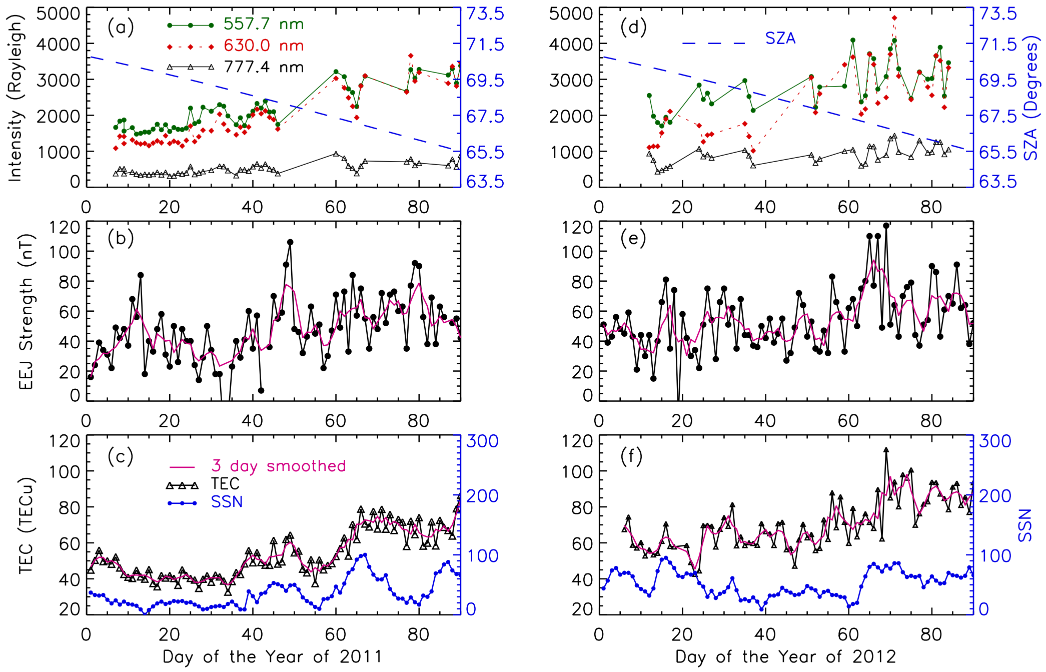

Figure 4.3: Daily variations of dayglow intensities averaged during 1430 to 1730 LT are shown in panels (a) and (d) for 2011 (left panel) and 2012 (right panel). The dashed lines in (a) and (d) are the solar zenith angles at 1600 LT. The daytime peak-EEJ variations are shown in middle panels (b) and (e). TEC values averaged during 1430-1730 LT and SSN are shown in the bottom panels (c) and (f). 3-day moving average curves are over-plotted in each of the EEJ strength and TEC data. While calculating this running mean of EEJ strength the DOY 33, 34 (SSW days) of 2011 and DOY 24 (magnetic storm of Disturbance-storm-time (Dst) index of -90 nT) of 2012 are excluded.

values, and (c) depicts the TEC and daily SSN values. The left panel is for the year 2011 and the right panel is for that of 2012. These two data durations in 2011 and 2012 have almost the same SZA variation but have different solar activity levels. SZA at 1600 LT (average of 1430 to 1730 LT) of each day is plotted in the top panel as the dashed curve. The gross increase in the magnitudes of dayglow emission intensities and the TEC values as seen in 2012 are mainly in response to the increased solar activity (as the period chosen has similar SZA variation). The TEC values show similar behavior with that of the SSN in 2011 to a larger extent as compared to 2012. Lesser similarity of TEC with SSN in 2012 may be due to the mixed influences of solar and lower atmospheric wave activity, which will be described in the next section.

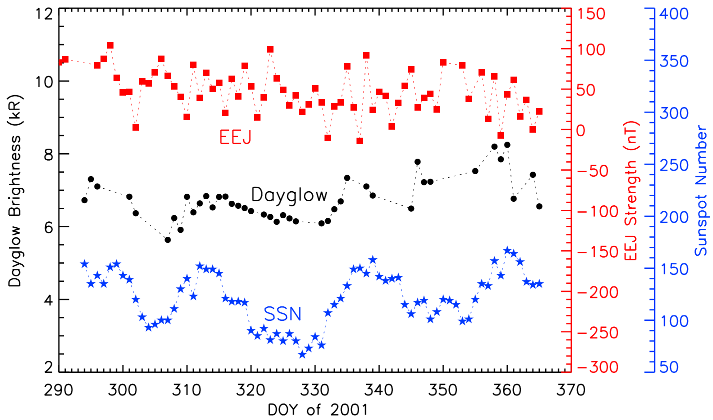

Figure 4.4: Variation of the daily-averaged intensity of the OI 630.0 nm dayglow emissions as obtained from Carmen Alto, Chile, which has similar magnetic latitude (10.5° S) as that of the Hyderabad (8.5° N). The daily sunspot numbers, and daily-averaged equatorial electrojet strengths obtained by ΔH_{Jic}-ΔH_{Piu} are also shown. The averaged dayglow emission brightness varies almost in phase with that of the daily sunspot number and not the EEJ indicating that the long-timescale variability in the emissions are controlled by the variation in the solar flux. (After *Pallamraju et al.* [2010]).

At a first look of Figure 4.3, the 2011 dayglow variations show relatively greater resemblance with that of the EEJ strengths as opposed to that in the SSN. This is in contrast to a previous study using OI 630.0 nm dayglow, EEJ, and SSN variations obtained during the high solar activity period of 2001 as shown by *Pallamraju et al.* [2010]. That result is reproduced here as Figure 4.4, wherein OI 630.0 nm dayglow intensities were obtained from Carmen Alto (23.1° S, 70.6° W; 10.6° S MLAT) in Chile. Carmen Alto is located in similar magnetic latitude as the present observing station, Hyderabad, but in the southern hemisphere. *Pallamraju et al.* [2010] found that the OI 630.0 nm dayglow emission intensity variations in 2001 followed very closely with that of the SSN and not the EEJ. EEJ in the American longitudes had been obtained by subtracting the H values obtained over a low-geomagnetic latitude station, Piura (Piu), from those of the equatorial station Jicamarca, (Jic), (ΔH_{Jic}-ΔH_{Piu}). The authors showed that the solar periodicities of 9-12, 12-15, and 24 days, were present in the OI 630.0 nm dayglow data, which were not seen in the EEJ strength. As the 630.0 nm dayglow production mechanisms depend on photoelectron and EUV fluxes, the co-variability in dayglow and SSN was found to be consistent. However, in the present analysis of the data of 2011 the situation seems different, most likely due to the lower solar activity during the year 2011 as compared to 2001. As the variations in the dayglow emissions show similarity with lower atmospheric and solar related variations to varying degrees, possible influences from the lower atmosphere and direct solar forcing have been investigated. More quantitative analysis are given below.

Lower Atmospheric and Solar forcings: It is known that the temporal variation of various solar parameters such as SSN, F10.7 cm flux, and EUV flux vary in similar fashion. However, in order to compare with the earlier published data we have used variations in SSN in this study. To quantify the variability seen in our data, Lomb-Scargle periodogram analysis has been carried out, as described in Chapter 3 [*Lomb*, 1976; *Scargle*, 1982; *Horne and Baliunas*, 1986; *Press and Rybicki*, 1989; *Torrence and Compo*, 1998]. Figure 4.5 shows the periodograms (solid lines) for all the data shown in Figure 4.3 along with their respective 90% false alarm level (FAL, dashed lines). Also, to investigate the possible wave activity in the lower atmosphere, the zonal winds at 10 hPa pressure level are also considered for analysis. Panels (a) to (g) show the periodograms of SSN, TEC, OI 777.4 nm (DG7), OI 630.0 nm (DG6), and OI 557.7 nm (DG5) dayglow intensities, EEJ strength, and zonal wind at 10 hPa level, respectively, for 2011. Similarly, the right side panels (h) to (n) show periodograms of these parameters for 2012. One can note that there are striking similarities in the periodicities nearly at 5-6, 8-11, and 15-17 days between EEJ, OI 557.7, OI 630.0 and OI 777.4 nm emission intensities (although the amplitude in some cases is just below the 90% FAL). These 5-6, 8-11, and 15-17 days periodicities are most likely due to 5-, 10-, and 16-days free normal modes, respectively.

The zonal wind around our observation location (averaged over 10°-20°N latitude, 75°-85°E longitude, and at 10 hPa pressure level which corresponds to about 30 km altitude, obtained from NCAR/NCEP reanalysis) is treated as an indicator of the presence of planetary wave activity [*Sassi et al.*, 2012]. The periodicities of 5-6, 8-11, and quasi-16-days (11.2 –20 days) that are seen in

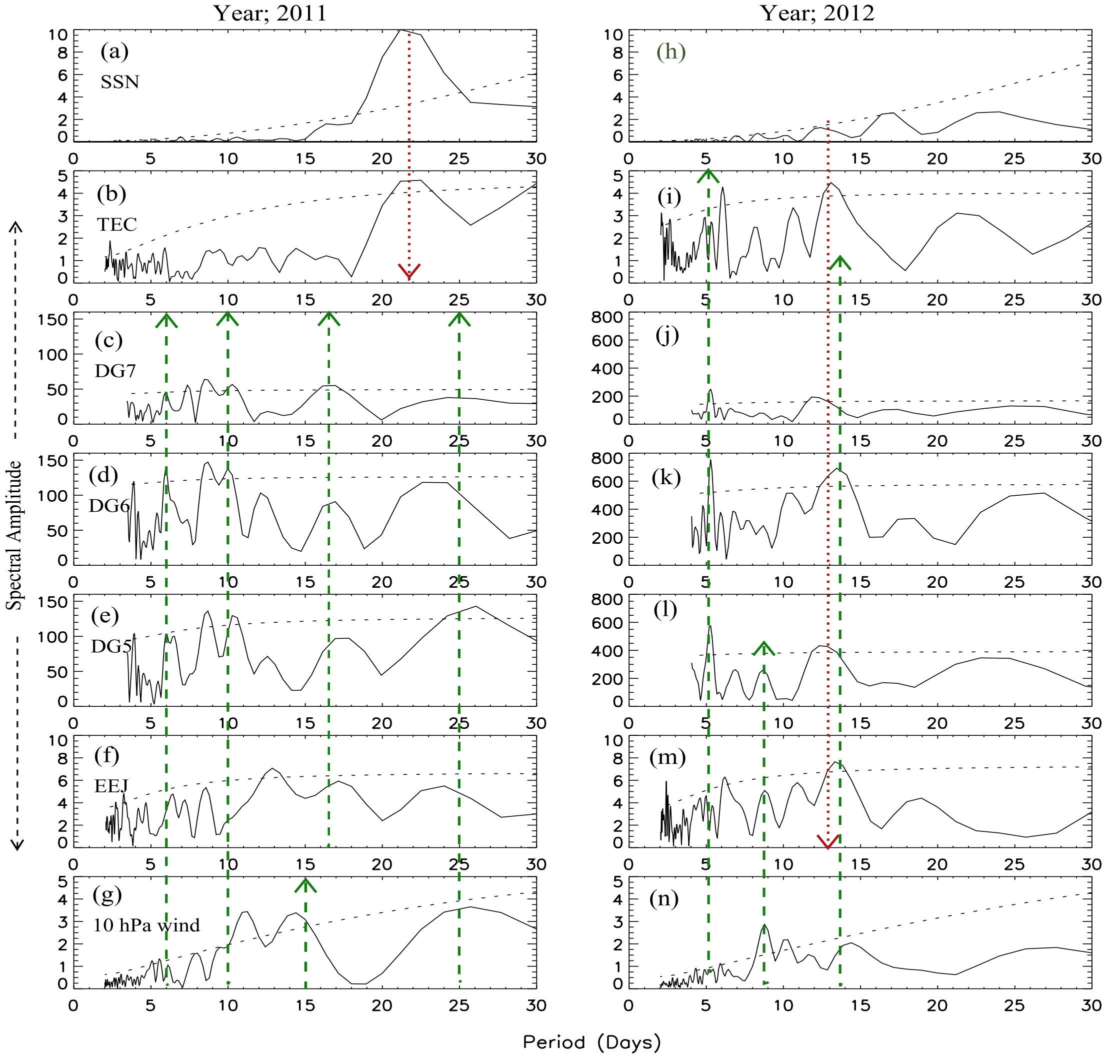

Figure 4.5: Normalized Lomb-Scargle periodograms are depicted for the parameters shown in Figure 4.3. Panels (a) – (g) represents periodograms of SSN, TEC, OI 777.4 nm, OI 630.0 nm, OI 557.7 nm dayglows, EEJ strength, and 10 hPa zonal wind, respectively. Left panel is for the year 2011 and the right one is that for 2012. The tags: DG5, DG6, and DG7 stand for the dayglow intensities of the OI 557.7 nm, OI 630.0 nm, and OI 777.4 nm emission lines, respectively. The dashed curves are the 90% FAL. Here the vertical arrows are traced to aid the eye and to show the direction of influence, upward arrow (dashed) indicate waves of lower atmospheric origin into the upper atmosphere and the downward arrows (dotted) for the solar forcing on the upper atmosphere. It can be noted that the 5-6, 8-11, quasi-16, and 25 days periods are present in all the atmospheric parameters and 22 day period is present in SSN and TEC in 2011. In the case of 2012, mixed responses are seen. Periodicities of 5-6 day and quasi-16-day are present in all the atmospheric parameters. However, the quasi-16-day period seen in the upper atmosphere could be an influence from lower atmospheric origin below or from above due to direct solar forcing.

dayglow emission intensities and in the EEJ strength, are also seen to be present in the low-latitude zonal wind at 10 hPa level for the year 2011 (upward dashed arrows are drawn to aid the eye to show the possible forcing from below). It is striking to note such a similarity, in spite of the fact that these are independent measurements and result from different processes. Although the power level of the 25-day period is slightly lower than the 90% FAL, it is notable that its presence is seen in all the lower and upper atmospheric datasets. It may seem that the 24-25 days periodicity in the all the atmospheric parameters (except the TEC, as it has different production and transport mechanism) is due to Doppler shifted period of solar 22-day period. However, it is believed that this is unlikely the case, as (a) the TEC which is an atmospheric parameter responds to the solar 22-day variation, while the other parameters do not, and (b) it is known that the 25-day is a normal mode oscillation of the lower atmosphere [*Sassi et al.*, 2012]. In 2011, when the solar activity level was relatively lower (average SSN=35) as compared with that of 2001 (average SSN=123), it seems that the forcings due to lower atmospheric components in the upper atmosphere are dominant (Figure 4.5). Further, as all the atmospheric parameters reported here are of different types with their own individual sources of production or variation, the commensurate amplification in amplitudes of the periods in these parameters are not expected as they can have different damping and dissipation rate at their respective altitudes.

To investigate the characteristics of this coupling during other solar activity levels, similar analysis was also carried out for the year 2012 (right panels). One can see a mixed situation in the data observed for this year wherein the periodicities that correspond to both solar and lower atmosphere are present in the upper atmosphere. The 5-6 day periodicity is present in all the atmospheric parameters including TEC. The 8-10 day period, which is dominant in the 10 hPa wind, seems also to be existing in other atmospheric parameters, such as EEJ and 557.7 nm dayglow (though below the 90% FAL). Detailed analysis in earlier works (*Willson* [1982]; *Pallamraju et al.* [2010]) of solar irradiance shows that there exist various short-term periodicities of 7, 9, 10, 15, 19, 21, 22, 23, 24, 25, and 26 days which may be due to the variation of the sunspot areas. One can see here that in 2012, the Lomb-Scargle periodogram of the sunspot number also has significant power (FAL > 90%) in the 8-9 and 12-13 day periodicities. Thus, the period of 13-15 day in the TEC and optical emissions could be due to the solar forcings (modified by Doppler shift) as well. Especially, in this period range, the periodicities seen in the upper atmosphere are also present in the datasets of the 10 hPa level zonal wind and the EEJ. This indicates possible influence from both solar forcing from above and lower atmospheric wave forcing from below on the upper atmosphere and therefore, the relative effects cannot be obtained unambiguously as these two are convolved effects.

Figure 4.5 shows that there are several wave periodicities that are common to both the lower atmospheric and the upper atmospheric parameters. The Lomb-Scargle periodograms provide information on the presence of a particular frequency in a given dataset, but not the time of occurrence of a particular frequency. To investigate whether the periodicities obtained in these independent measurements are, if at all, simultaneous in their duration of occurrence, wavelet analysis is performed on all the individual datasets. Here, for the estimation of the wavelet spectra, Morlet mother wavelet function is used [*Torrence and Compo*, 1998]. For optical data, the analysis is restricted to only that duration when almost continuous data is available (with at most two missing data points/days being interpolated). For 2011, DOY 7-46 and for 2012, DOY 51-85 are used for the wavelet analysis. Figure 4.6 shows the wavelet spectra of all the datasets shown in Figure 4.5. Panels (a) – (g) show the result of the wavelet analysis of SSN, TEC, OI 777.4, OI 630.0, OI 557.7 nm emissions, EEJ, and 10 hPa zonal wind, respectively, for 2011. Right side panels show the wavelet spectra of corresponding parameters for 2012. The x-axis shows the DOY and the y-axis represents periods in days. Normalized power values are plotted in each panel and the scale is given on the right. It is striking to note that several periodicities, 5-6, 8-11, and quasi-16-days are seen nearly simultaneously in all the atmospheric measurements in 2011 during DOY 20-45. The results arrived at from this analysis add credence to the suggestion that there seems to be a significant influence of lower atmospheric forcing on the upper atmospheric wave

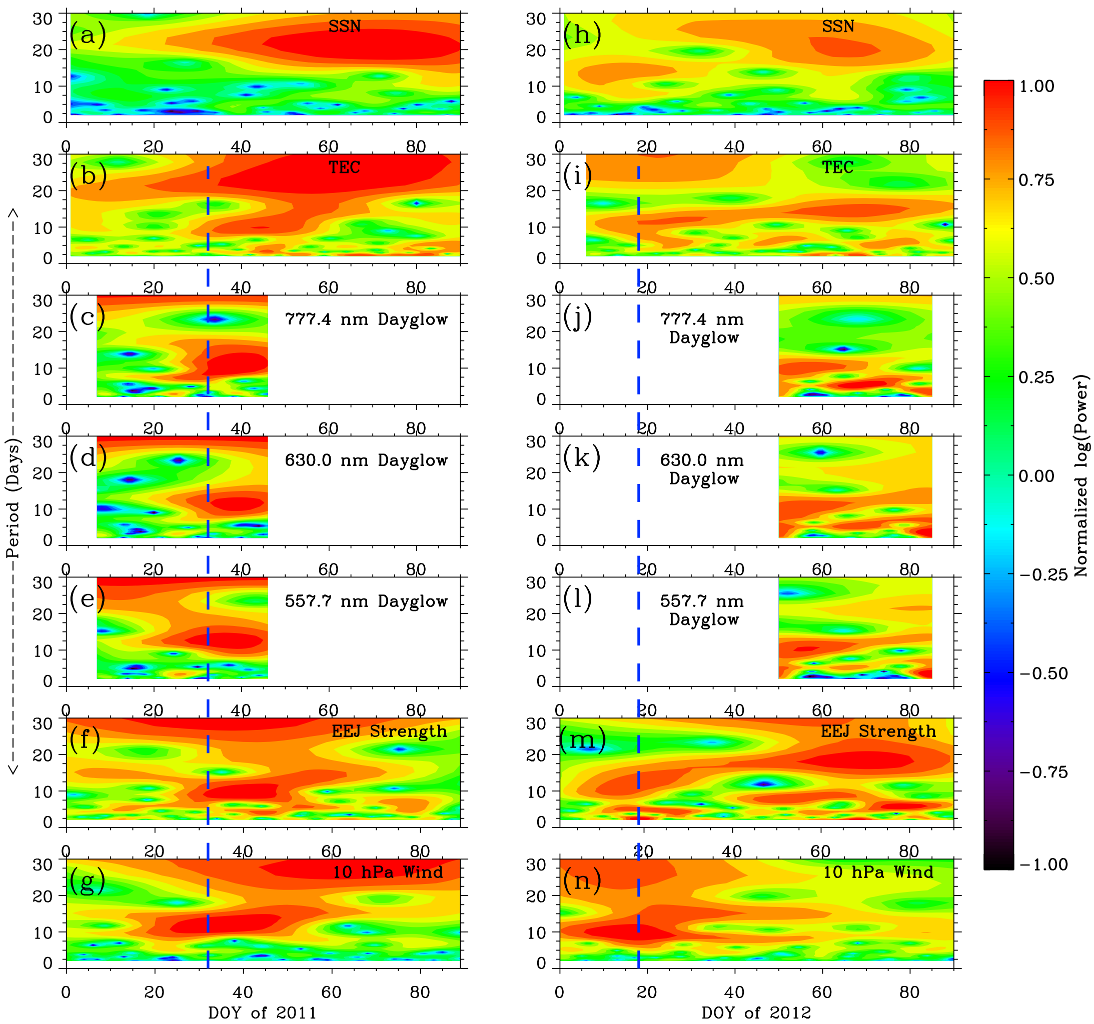

Figure 4.6: Normalized wavelet spectra showing the temporal occurrence of the periods seen in Figure 4.5. One can note that the 5-6, 8-11, and quasi-16-day periodicities occur in the same time duration in all the lower and upper atmospheric parameters, especially, in 2011 (left panels) indicating lower atmospheric influence on the upper atmosphere. In 2012 data shown in the right panels, 5-6 day and 8-10 day periodicities during DOYs 51-85 in all the atmospheric parameters and to some extent in SSN occur simultaneously. The concomitant occurrence of quasi-16-day period between DOY 5-35 in 10 hPa wind, EEJ, TEC, and SSN implies a possible mixed influence from both solar and lower atmosphere on the upper atmosphere in 2012. The two vertical dashed lines mark the onset of the minor SSW.

dynamics. As can be seen in Figures 4.5 and 4.6, the solar influence is significant only on the TEC variations in 2011.

For 2012, the occurrence of 5 and 10 days periodicities in similar duration (DOYs 50-85) in TEC, all the optical emissions, the EEJ strength, and in the 10 hPa zonal wind shows the influence of the lower-atmosphere related processes in the upper atmospheric regions. The quasi-16-day period is present simultaneously in between DOYs 5 to 30 in all the atmospheric parameters, namely, 10 hPa zonal wind, EEJ strength, and TEC. SSN also has a significant period of 10-15 days in the same duration. This simultaneous presence of quasi-16-day periodicity in atmospheric and solar parameters implies a possible influence both from lower atmosphere and solar activity. It may be noticed that there is a broad similarity in the overall wavelet contours of EEJ, TEC, and SSN. Therefore, the broad picture that seems to emerge is that, the influences of both solar and lower atmospheric regions are seen to exist in the upper atmosphere in 2012, as opposed to 2011, when the influence from the lower atmosphere is dominant.

There was a minor-SSW event starting from DOY 32 in 2011 (shown by vertical dashed lines in Figure 4.6), when the temperature at 60° N latitude and at 10 hPa pressure level increased by more than 35°C within a week but the zonal wind did not reverse, indicating that the event was a minor one. It is important to note that several of the wave dynamical features (such as waves of 8-11, and quasi-16-days) occurred simultaneously even before the arrival of the minor-SSW, which indicates that the vertical coupling of atmospheres in low solar activity exists, irrespective of the occurrence of the minor SSW event. Similar was the case for the minor-SSW event starting from DOY 18 in 2012.

The combined optical, radio, and magnetometer results presented here show that the vertical coupling of atmospheres is stronger during low solar activity epoch (2011) when the average SSN was 35. In 2012, when the average SSN during our observation was 52, the effects of both the planetary wave associated activity and that of the solar activity are seen in the upper atmosphere. *Pallamraju et al.* [2010] presented optical dayglow data from 2001 (when average SSN was 123) and showed that almost all of its variations were of solar origin and none from the lower (MLT) region dynamics as manifested in the EEJ. The upper atmospheric behavior has conventionally been considered to be varying solely under the influence of solar activity and to a much smaller degree on the lower atmospheric forcings. Our results reveal a broader picture wherein, there seems to be an interplay between the influences of lower atmospheric processes and solar activity on the upper atmosphere. From the present results it is proposed that, lower atmospheric behavior influences the upper atmosphere at least until the SSN value of 35, there exists a transition from the influences of lower atmospheric origin to a mixed behavior between average SSNs of 35 to 52 and another transition from mixed effect to that purely of solar origin occur in between SSN values of 52 to 123. Further studies with long-term data sets are required to ascertain these boundaries more quantitatively in terms of the number of sunspots.

It is known that the planetary waves modulate the gravity waves and tides, which then affect the upper atmosphere. Both, neutral and the plasma components are affected due to such secondary effects of planetary waves especially in the equatorial region. From modeling studies, *Liu et al.* [2010] have shown that the gravity waves are more favorable to propagate to altitudes up to 150 km during low solar activity period. The details of solar activity dependence of gravity waves in the thermosphere are given section 4.3. Using numerical simulations, *Wan et al.* [2012] have shown that the neutral coupling of the atmosphere via non-migrating diurnal eastward wavenumber-3 (DE3) tidal influence decreases with increasing solar activity, while the electrodynamical coupling remains unchanged. Those results suggest that during higher solar activity, the influence of planetary wave to the upper atmosphere would be smaller, which is similar to the result reported in this study. Further, our detailed investigations using measurements of multiple datasets not only provided empirical evidence to the conjectures and modeling studies reported earlier but also characterized the vertical coupling of atmospheres from lower to higher altitudes with solar activity.

Further, there are reports on the influence of the lower atmospheric forcing (via planetary waves) on the upper atmospheric dynamics even in the high solar activity epochs (wherein the SSN varied between 60 and 110) [e.g., *Liu and*

Roble, 2005; *Liu et al.*, 2010; *Pedatella and Forbes*, 2010]. On closer scrutiny, we found that even though the solar activity was high, the lower atmospheric forcings on the upper atmosphere occurred mainly during SSW events only, as most likely the warming events provided additional sources of energy. Based on our present results and simulation studies of [*Wan et al.*, 2012] it can be seen that the temperature and density gradients in the MLT height region play an important role in the lower atmospheric wave propagation to the upper atmosphere. In summary, our study indicates that the atmospheric conditions are favorable for waves to propagate vertically in the low solar activity epoch. If there are SSW events during such period, it would enhance the strength of the propagation of waves enabling a stronger vertical coupling of atmospheres. During high solar activity epochs the upper atmospheric dynamics are predominantly controlled by those of solar flux variability and not of those due to the planetary wave type effects from the lower altitudes. However, SSW events during high solar activity period can enable vertical couplings from below.

4.2.4 Conclusion: Longer Period Waves

Data observed from multiple instruments showed that the planetary wave type oscillations of periods 5-6, 8-11, quasi-16, and 25 days not only influence the upper atmosphere through the electrodynamic coupling but also through the neutral atmospheric coupling, as all the neutral and plasma parameters bear the signatures of these oscillations. The relative importance of the forcing from below and from above due to incidence of solar flux directly is found to be varying with the strength of solar activity. Lower atmospheric influences on the upper atmosphere are found to be stronger during the low solar activity period of 2011 compared to the moderate solar activity period of 2012. Dayglow data of the high solar activity period (2001; Figure 4.4) showed a clear correlation in the behavior of the upper atmosphere with that of the direct solar forcing but weaker to no influence from lower atmospheric (from EEJ) wave activity [*Pallamraju et al.*, 2010]. Based on the influence/presence of planetary waves on the atmospheric parameters and on the level of solar activity for the three different activity phases, it is proposed that: (i) the effect on upper atmospheric dynamics due to lower atmosphere exists at least until the period when the average SSN is $\leq$35, (ii) there is a transition from the lower atmospheric forcing to mixed behavior between average SSNs of 35 to 52, and (iii) another transition from mixed effects to those purely of solar origin occurs between SSN values of 52 to 123. SSW events enhance the vertical coupling and are proposed to be responsible for enabling this coupling even during high solar activity epoch.

4.3 Shorter Period Waves (Gravity Waves)

In the first part (section 4.2), wave-dynamical characteristics of planetary waves at varying levels of solar activity are presented. In this section, we will deal with the characteristics of shorter period waves (gravity waves) in the upper atmosphere in the context of wave dynamical vertical coupling of atmospheres.

4.3.1 Introduction

It is known that most of the waves and instabilities present in the atmosphere are generated in the troposphere. The troposphere is the region of the atmosphere where the temperature gradient is negative and thus it supports significant convective activity. Many of these waves can propagate upward and dominate the motions at upper atmospheric altitudes [e.g., *Hines*, 1960; *Laštovička*, 2009; *Vadas and Liu*, 2009]. The wave propagation into the upper atmosphere is affected by various types of dissipations such as eddy diffusion, radiative damping, wave-induced diffusion, non-linear wave-wave interaction, thermal diffusion, kinematic molecular viscosity, and ion-drag [*Hines*, 1960; *Pitteway and Hines*, 1963; *Lindzen*, 1981; *Fritts*, 1984; *Vadas and Fritts*, 2005]. Among them, the first three are dominant below the turbopause ($\sim$100 km altitude) and the last three are active above turbopause. At very high altitudes the last two are the only dissipative factors. The waves are stable and do not interact with each other or with themselves at lower amplitudes, but with decreasing atmospheric density, wave amplitude increases and at some height the waves become unstable due to non-linear effects and break down. From numerical simulations, it was shown that the non-linear wave-wave interaction is maximum at the MLT altitudes [*Yiğit et al.*, 2008]. Thus, many of these waves dissipate at mesospheric altitudes and accelerate the mean flow, which, in turn, excites secondary waves with much longer horizontal scale sizes [*Vadas and Liu*, 2009]. The dominant dissipation parameters in the lower thermosphere are molecular kinematic viscosity and thermal diffusivity [*Vadas and Fritts*, 2005]. The molecular kinematic viscosity (ν_{mol}) is given by

$$\nu_{mol} = 3.563 \times 10^{-7} T^{0.6}/\rho \quad [\mathrm{m^2s^{-1}}] \tag{4.1}$$

and the thermal diffusivity (α_{td}) is given by

$$\alpha_{td} = \kappa/\rho c_p \quad [\mathrm{m^2s^{-1}}] \tag{4.2}$$

where, κ is the thermal conductivity, ρ is the number density [kg.m^{-3}], T is the ambient neutral temperature, and c_p is the specific heat at constant pressure. Both the dissipation parameters are inversely proportional to density and weakly proportional to temperature [*Vadas and Fritts*, 2005; *Yiğit and Medvedev*, 2010] and are associated with transport processes.

Solar and lower atmospheric forcings at MLT heights has been studied widely by many researchers using radar winds [*Gurubaran et al.*, 2001; *Kovalam et al.*, 2006], Lidar [e.g., *Rauthe et al.*, 2008; *Hoffmann et al.*, 2011], sounding rocket [*Hirota*, 1984], VLF radio sounding [e.g., *Bošková and Laštovička*, 2001], and airglow measurements [*Takahashi et al.*, 1992; *Chakrabarty*, 2004; *Taylor et al.*, 2007]. Though, the effects of individual gravity wave forcing into the thermospheric regions have been studied to significant extent, the detailed dynamical influence are not well-understood, particularly during daytime, due to lack of continuous neutral atmospheric measurements spanning different levels of solar activity. Satellite-based continuous measurements of dayglow are available [*Shepherd et al.*, 1993], but the inherent constraints the satellite measurements have is their poor temporal resolution that prevents a detailed study of gravity waves. A few modeling works have so far been conducted to study the thermal and dynamical effects of the dissipation of gravity waves in the thermosphere during varying levels of solar activity [e.g., *Fritts and Vadas*, 2008; *Yiğit and Medvedev*, 2010]. The importance of gravity waves in the thermospheric dynamics has been studied for long time and is reported in the literature [*Hines*, 1960; *Hines*, 1973, 1991; *Lindzen*, 1981; *Hocke and Schlegel*, 1996; *Oliver et al.*, 1997; *Chakrabarty*, 2004].

For the study of gravity waves at different altitudes of the thermosphere multiwavelength airglow measurement offers an affordable means. Nighttime airglow measurements are widely used for the investigations of the thermosphere [*Taylor et al.*, 1997, 2007; *Smith et al.*, 2000; *Shiokawa et al.*, 2009; *Lakshmi Narayanan et al.*, 2010; *Sekar et al.*, 2012], but due to the presence of lunar background these measurements are not available during full-moon periods. Again, due to the technical difficulty of measuring the daytime airglow in the presence of the strong scattered sunlight, few daytime measurements have been reported in the literature. Further, in the recent past there has been an increase in the studies of daytime upper atmosphere by ground-based measurements as innovative techniques have become available [*Pallamraju et al.*, 2000, 2002, 2013, 2014; *Chakrabarti et al.*, 2012; *Marshall et al.*, 2011].

It is essential to understand the wave characteristics in the daytime as it has been found that the daytime upper atmosphere prepares the background and makes it conducive for the growth of seed perturbations that generate the post-sunset plasma irregularities [*Raghavarao et al.*, 1988b; *Sridharan et al.*, 1994; *Mendillo et al.*, 2001; *Pallamraju and Chakrabarti*, 2006]. Thus, in order to understand the seeding mechanism better it is required that the waves during the daytime are characterized.

With increasing level of solar activity, the incoming extreme ultraviolet and X-ray radiations increase which results in the change of background conditions, such as, density and temperature in the thermosphere. Due to this varying background condition, the dissipation characteristics of the waves change. In section 4.2 we showed that the vertical coupling of atmospheres via the planetary wave type variations is stronger during low solar activity and weaker during high solar activity. In this section, an attempt is made to understand the behavior of the thermospheric gravity waves by statistically characterizing their nature at different levels of solar activity using the variabilities in the thermospheric oxygen dayglow emission intensities that emanate from multiple altitudes and the EEJ.

4.3.2 Data Description

To investigate the behavior of the gravity waves in the thermosphere, the daytime oxygen airglow emission intensities at multiple wavelengths and the EEJ strength measurements have been used. Here also, the dayglow emission intensities at wavelengths 557.7, 630.0, and 777.4 nm obtained by MISE from Hyderabad, India are used. As explained in section 2.3, the altitudes at which the three oxygen emissions at wavelengths 557.7, 630.0, and 777.4 nm emanate are about 130 km (average of two peaks from 100 and $\sim$160 km), 230 km, and ionospheric F-peak, respectively. So, the behavior of these three emissions can provide information on the dynamical conditions prevalent at those altitudes. All the dayglow emission data that are obtained from this instrument during January to March for the years 2011 to 2013 are presented in Figure 4.7. The first two columns for years 2011 and 2012 have been shown in Figure 4.2. They are shown again along with that in the year 2013 for the sake of completeness. The additional axis on the top of Figure 4.7 represents the DOY and those DOYs on which the dayglow data are available (marked below this axis). One may note that in addition to the daily and seasonal solar zenith angle related variation, there are small-scale (temporal) variations of minutes to a few hours in these emissions. The typical uncertainties involved in the measurements are of the order of 100, 100, and 50 Rayleighs for the OI 557.7, OI 630.0, and OI 777.4 nm emissions, respectively. As also indicated earlier, the data gap during the noon in all the years arises due to the strong solar-glare saturating the CCD images. The variations present in these emissions in the gravity wave regime are of interest in this study.

The EEJ strength data during the same interval (January to March) of the three years are also used to obtain information on the waves at altitudes of around 105 km region. The details of EEJ data and measurements are given in section 2.5.1.

Background Conditions: Both the oxygen dayglow emission intensity and

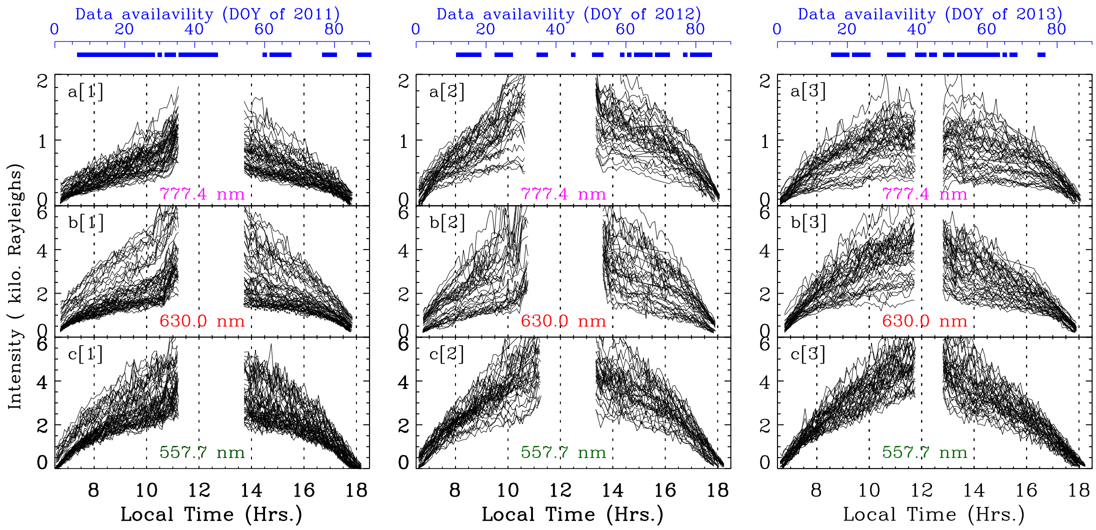

Figure 4.7: The daily values of the dayglow emission intensities for the three years (2011 to 2013, left to right) of data available and for the three wavelengths (top to bottom) are shown. The additional axes at the top represent the DOY. Those DOYs on which dayglow data are available are marked below this axis. One can note that in addition to daily broad solar zenith angle type variations, there are also small-scale variations of minutes to a few hours. The typical uncertainties involved in the measurements are of the order of 50, 100, and 100 Rayleighs for the 777.4, 630.0, and 557.7 nm emissions, respectively.

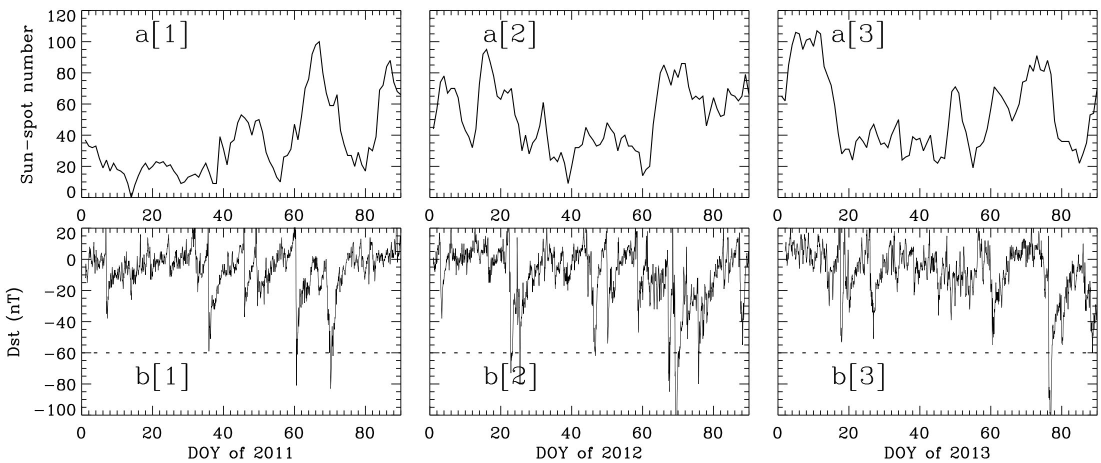

Figure 4.8: (a) Sun-spot numbers during the January to March of 2011-2013 (left to right). (b) Dst index values for the three months in these three years are shown. It is noticeable that the values of sun-spot numbers increase from 2011 to 2013. Also, the geomagnetic disturbances were more in number during 2012 compared to other two durations of 2011 and 2013.

the EEJ strength data are used in this study are collected during the January to March of the years 2011 to 2013, as the sky was mostly clear during this season and appreciable number of days of optical measurements were obtained. It may be noted that during these observational windows, the solar activity was at its rising phase of the 24th solar cycle as shown in Figure 4.8. The average SSN during these durations in the three years were 35, 52, and 53. The Dst index values are also shown in Figure 4.8(b), from which one can note that compared to 2011 and 2013, the year 2012 was a disturbed period with at least 6 geomagnetic storms having Dst index below -60 nT. The detailed results from the analysis of these data sets are presented below.

4.3.3 Results and Discussion

Figure 4.9(a) shows a sample daily variation of the OI 557.7 nm dayglow emission. The dominant variability in this data is the SZA related variation with an emission intensity maximum around noon and minima during twilights. In addition to this, there are smaller scale variations. To quantify the periodicities of these smaller scale variabilities, a 3-hour running mean is subtracted from the data to remove the dominant smoothly varying zenith angle type variations. While doing this, no interpolations are made for the noon-data gap. The dashed line in Figure 4.9(a) is the 3-hour moving average variation. The residuals are shown in the same plot having both positive and negative values around zero. Since the data are unequally spaced in time, the periodogram analysis is performed using the Lomb-Scargle [*Lomb*, 1976; *Scargle*, 1982; *Torrence and Compo*, 1998] technique. Details of these techniques are given in Chapter 3.

The periodogram of the residual is shown in Figure 4.9(b) along with the 95% significance level (or FAL). It can be noted that there are spectral peaks at frequencies (periods) 0.8 hr^{-1} (75 min), 3.2 hr^{-1} (19 min), 4.2 hr^{-1} (14 min) and 5.0 hr^{-1} (12 min). All such significant frequencies have been collated from such an analysis for all the dayglow data (as presented in Figure 4.7) and also for the EEJ strength data for the same duration. The frequencies beyond 95% significance level are binned at a frequency interval of 0.25 hr^{-1}. Then, a statistics

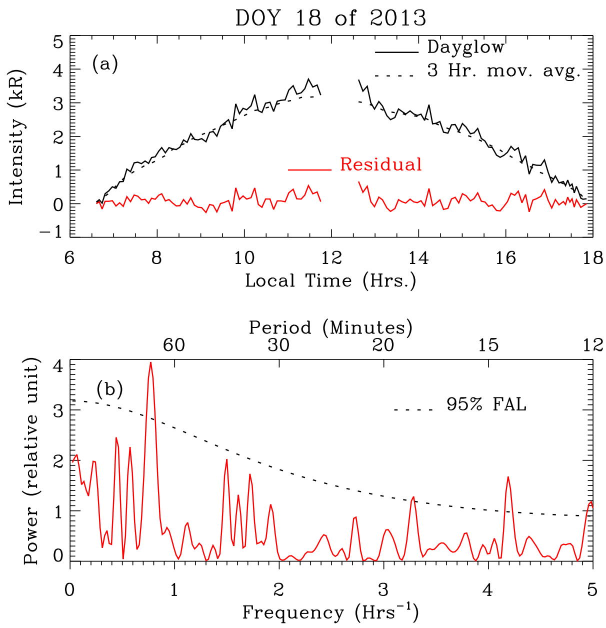

Figure 4.9: A sample day analysis of the OI 557.7 nm dayglow emission intensity for DOY 18 of 2013 is shown. (a) The daily variation of the dayglow emission intensity along with the 3-hour moving average and the residuals are shown. (b) Lomb-Scargle periodogram of the residuals obtained by subtracting the moving averaged signal from the original dayglow intensities are shown. The dashed line in (b) shows the 95% FAL. The frequencies with power >95% FAL are collated for each day and for each wavelength (more details are given in text).

of the percentage number of days in which waves of a particular frequency bin has occurred is made and is shown in Figure 4.10 for the dayglow emissions. In Figure 4.10, columns represent different years and rows represent different wavelengths. The x- and y-axes represent frequency bins (in hr^{-1}) or period corresponding to that frequency bin (in minutes) and % of days on which waves in a frequency bin have occurred. The numbers within the dashed rectangle, e.g., 176 for OI 777.4 nm in the year 2011, represent the total number of occurrences of gravity waves with frequencies (or periods) greater than 0.33 hr^{-1} (less than 3 hrs) and less than that of Brunt-Väisälä frequency at that altitude. It should be noted that the Brunt-Väisälä frequency varies with height [*Kelley*, 2009] and is 5 hr^{-1} (12 min), 4.5 hr^{-1} (13 min), and 4 hr^{-1} (12 min) for the OI 557.7, 630.0, and 777.4 nm peak emission altitudes, respectively. The average SSN during the January to March season of the years 2011, 2012, and 2013 are also shown in Figure 4.10.

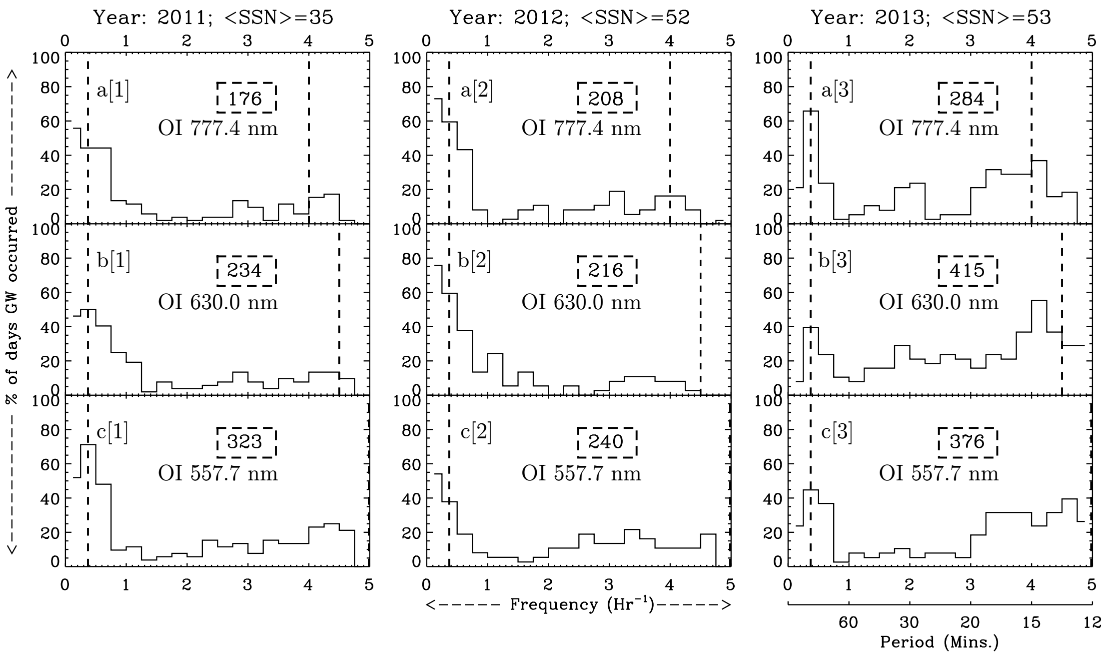

Figure 4.10: Statistics of various periodicities which occurred during January to March in the years 2011 to 2013 (left to right) and for different emissions (a to c) are presented. The dashed vertical lines mark the gravity wave frequency ranges (0.33 hr^{-1} to Brunt-Väisälä frequency) at their respective altitudes. The numbers within the dashed rectangle are the total number of percentage occurrences within the gravity wave frequency ranges. For example, the number 176 for the OI 777.4 nm emission in the year 2011 is sum of all the percentage occurrences within the two dashed lines at 0.33 and 4 hr^{-1}. One can note that for the highest altitude emission, OI 777.4 nm, the total percentage gravity wave occurrence days increase with year and for the other two lower altitude emissions, 630.0 and OI 557.7 nm, it is higher in 2013 compared to 2011. In the year 2012, there were 6 geomagnetic storms within January to March and some of them were recurrent and so the gravity wave behavior is not expected to represent purely that due to lower atmospheric forcings.

It can be noted from Figure 4.10 that the total percentage occurrences of gravity waves in all the three dayglow emissions are higher in 2013 as compared to that in 2011. Also, as shown in Figure 4.8 the solar activity in the year 2013 is higher ($\langle$SSN$\rangle$=53) compared to 2011 ($\langle$SSN$\rangle$=35). As mentioned above, in the year 2012, there were 6 geomagnetic storms with Dst indices less than -60 nT, so this year has been opted out of this discussion as it is known that storms influence both the neutral and electrodynamical conditions in the low-latitude upper atmosphere [e.g., *Mendillo*, 1971; *Prölss*, 1980; *Pallamraju et al.*, 2004]. Thus, the observations in the years 2011 and 2013 suggest that with an increase in the solar activity, the percentage occurrence days of gravity waves in the thermosphere increase.

From modeling studies *Yiğit and Medvedev* [2010] showed that the two most dominant dissipation parameters (molecular viscosity and thermal diffusivity) that are very active in the lower thermospheric altitudes have higher values (thereby implying greater dissipation of gravity waves) during low solar activity as compared to high solar activity. The dissipated gravity waves deposit their momentum in the form of air-drag at the altitudes of dissipation. Figure 4.11 shows a numerical simulation of the gravity wave drag estimated by *Yiğit and Medvedev* [2010] for both high and low solar activity background conditions. The gravity wave drag is a measure of the amount of waves dissipated in the medium. It can be noted from Figure 4.11 that the gravity wave dissipation at thermospheric

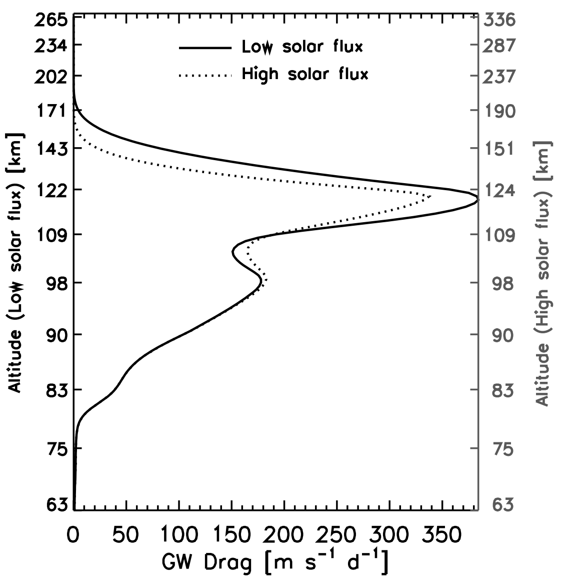

Figure 4.11: The gravity wave drag, a measure of momentum deposited due to its dissipation, as modeled by introducing the gravity wave parameterization into the global circulation model, is shown. It can be seen that the model results indicate that during high solar activity the gravity wave drag is less compared to low solar activity, implying that these waves are dissipated in smaller amount during high solar activity at lower thermospheric altitudes. (After [*Yiğit and Medvedev*, 2010]).

altitudes are lower in high solar activity compared to that of low solar activity. This happens, because of the fact that the two dominant dissipation parameters at lower thermospheric altitude, namely, the molecular kinematic viscosity and thermal diffusivity as given by Eqs. (4.1) and (4.2) are inversely proportional to density. With the increase of solar activity the thermospheric densities at higher altitudes increases (compared to lower solar activity) and thus there is a decrease in dissipation of gravity waves at lower altitudes, so they can reach relatively higher altitudes in the thermosphere during the high solar activity.

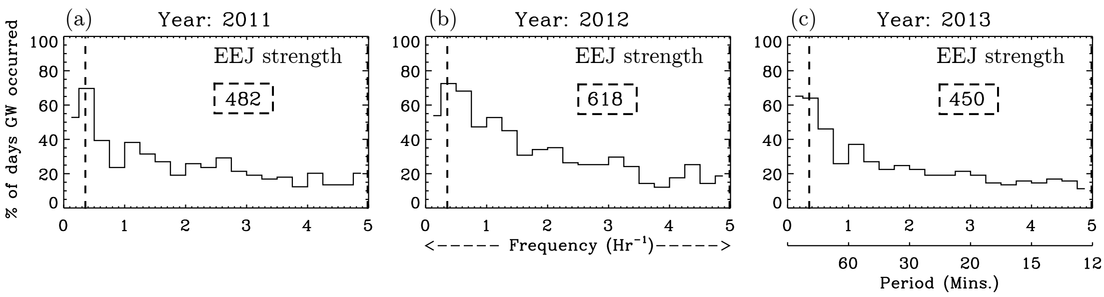

Figure 4.12: Similar to Figure 4 but for the EEJ data. Here one may note that the gravity wave occurrences in 2013 are little lower compared to that of 2011 and lower frequency components occur more in number compared to that of higher frequency.

Figure 4.12 shows similar statistics as that of Figure 4.10 but for the EEJ strength. The total percentage number of days of gravity wave occurrence values for the dayglow and EEJ strength are listed in Table 4.1, along with the altitudes of the parameters measured. One can note that unlike the dayglow emissions, where gravity waves are present in higher numbers during high solar activity year of 2013, the statistics in EEJ show lesser number of total percentage occurrences for the year 2013 as compared to that of 2011. In section 4.2 we showed that for planetary wave-dynamics the vertical coupling of the atmosphere is stronger during low solar activity compared to that of the high solar activity durations. Here, for the gravity waves (which are of much smaller time-period and scale sizes) we can see the same behavior in Figure 4.12. For simplicity, consider that the lower atmospheric gravity wave generation is of same amount for both 2011 and 2013 during the January to March season. Then the gravity wave percentage occurrences in the low solar activity year of 2011 are larger compared to 2013.

Parameter	Altitude	Year		
		2011	2012	2013
OI 777.4 (nm)	F-peak	176	208	284
OI 630.0 (nm)	~230 km	234	216	415
OI 557.7 (nm)	~130 km	323	240	376
EEJ str. (nT)	~105 km	482	618	450

Table 4.1: The total number of occurrences of gravity waves with frequencies (or periods) greater than 0.33 hr^{-1} (less than 3 hrs.) and less than that of Brunt-Väisälä frequency at that altitude.

The dayglow emission intensities do not show behavior similar to EEJ, which is due to the fact that they emanate from altitudes above the EEJ altitude and in between these two altitudes the dissipation parameters vary with solar activity.

In the case of the year 2012 one can see unusually high number of gravity wave occurrences in EEJ strength compared to other two years. This is opposite to the observations in the case of dayglow in which it is lower compared to other two years. This is most likely due to geomagnetic variations to which EEJ and dayglow have varied responses. The dayglow emission can be affected by both compositional and electrodynamical variations during geomagnetic storms [*Zhang and Shepherd*, 2000; *Culot et al.*, 2005; *Pallamraju and Chakrabarti*, 2005], whereas, the EEJ strength is affected by local winds and by local and global electrodynamic processes [*Reddy and Devasia*, 1978; *Fejer and Scherliess*, 1995]. During geomagnetic storms, the high-latitude heating events produce waves of periods in the higher gravity wave period range, called TIDs, which can propagate towards low-latitudes and thus can influence the low-latitude upper atmospheric dynamics and hence, the dayglow emission intensities. The EEJ is disturbed by magnetospheric influences, such as, prompt penetration electric field, disturbance dynamo electric field, etc. From Figure 4.12 one can see that in the year 2012 the occurrences of the lower frequency (1-2 hr^{-1}) waves are higher compared to the other two years, which is very likely due to occurrences of higher number of geomagnetic storms. The 2012 data are presented here so as to appreciate the

Frequency range (hr^{-1})	Year								
	2011			2012			2013		
	777.4	630.0	557.7	777.4	630.0	557.7	777.4	630.0	557.7
(2–BV)/n; (H)	6.49	8.65	13.94	9.46	5.68	13.06	18.42	27.37	21.49
(1–2)/n; (L)	5.77	8.17	7.21	5.41	12.16	4.73	11.18	17.11	7.89
H/L	1.12	1.06	1.93	1.75	0.47	2.76	1.65	1.60	2.72

Table 4.2: Percentage occurrences per bin in the given frequency ranges and the ratios of high (H) to low (L) frequency gravity wave occurrences. Where n represents the number of frequency bins.

consequences of multifarious processes taking place during geomagnetic storms, but are not included in the discussion on the comparison of wave activity between high and low solar epochs.

From Figure 4.10 one can note that there is a differential behavior in terms of the percentage occurrences of gravity waves in the high (2 to BV hr^{-1}; H) and the low frequency (1 to 2 hr^{-1}; L) regimes, which is, the higher frequency components occur in greater amount compared to lower frequencies. In order to study the behavior of the high- and low-frequency waves, the frequencies that are shown in Figure 4.10 are classified into two ranges of low-and-mid (1 to 2 hr^{-1}) and higher (2 to BV hr^{-1}). The percentage number of days of wave occurrences per bin (total percentage occurrences in all the bins divided by number of bins) in these two ranges and the ratio between high to low (H/L) frequency ranges are given in Table 4.2. One can note from the Table 4.2 that the number of occurrences of high frequency components are higher compared to that of the low-and-moderate frequencies for all the wavelengths, which can also be noted from Figure 4.10.

To quantify the differential characteristics of higher and low-frequency components, the ratio of percentage occurrences as given in Table 4.2 are used. From a comparison of the H/L ratio for the year 2011 with 2013 for all the wavelengths one can note that in addition to the greater percentage occurrence during high solar activity, the higher frequency components occurred in higher amount during high solar activity compared to that of lower frequency. For example, the H/L ratio of OI 777.4, 630.0, and 557.7 nm in 2013 are 1.65, 1.60, and 2.72, respectively and in 2011 are 1.12, 1.06, and 1.75. From these rations it is clear that 2013 H/L ratios are greater compared to that in 2011. Thus, to summarize, this analysis indicates that the waves of higher frequencies are more favored in the upper atmosphere compared to lower frequency and that they are far more in numbers during higher solar activity periods. From numerical modeling simulation studies, *Fritts and Vadas* [2008] showed that larger frequency components propagate in larger amount to the upper atmosphere compared to lower frequency ones (figures 2 to 4 of their paper). They also showed that with the increasing solar activity the larger frequency components propagate higher in altitudes. The ratios between high- to low-frequency occurrences as derived experimentally, in this study, provide experimental evidence to the *Fritts and Vadas* [2008] simulation results.

4.3.4 Conclusion: Shorter Period Waves

The conclusions that can be arrived at from the investigations of gravity wave variations are listed below:

1) In the upper atmosphere, the occurrences of periodicities in the gravity wave regime are greater for the higher solar activity period (of year 2013) compared to that of lower solar activity (of year 2011). The changes in the dissipation parameters with changing solar activity are responsible for this.

2) Gravity waves of higher frequencies have been found to be present in greater numbers at thermospheric altitudes compared to that of low-and-moderate frequencies, which is independent of solar activity and is in accordance with earlier simulation studies.

3) The ratios of high- to low-frequency gravity waves have been found to be greater for higher solar activity epoch compared to that of relatively low solar activity epoch, which provides an experimental confirmation for the earlier simulation studies.

4) Like planetary waves, gravity waves also propagate to the MLT region in higher numbers during low solar activity, but their dissipation at lower thermospheric

altitudes is stronger during low solar activity compared to that of high solar activity level.

4.4 Summary

In this chapter, we have discussed the wave dynamical vertical coupling of the atmospheres for both short- and long-period waves. In both the cases we have seen that wave influence from lower atmosphere to the upper atmosphere is more efficient during low solar activity compared to high solar activity. But, due to the changes in the background atmosphere the dissipation parameters are altered. Due to such alteration, the gravity waves are dissipated more during the low solar activity, especially in the lower thermosphere. Thus, the presence of gravity waves in the thermospheric altitudes is predominant during high solar activity periods, as their dissipation in the lower thermospheric altitudes is comparatively less.

Chapter 5

Dependence of Vertical Coupling on Strength of SSW

5.1 Background

In Chapter 4, we have shown that the wave dynamical vertical coupling of the atmospheres is solar activity dependent. Also, we have seen the signatures of various planetary waves in both lower and upper atmospheric parameters, even though their times of occurrences and magnitudes of spectral power are not the same. Further, we have seen that the quasi-16-day planetary waves have higher spectral powers around the occurrence of SSW. Since the emission intensity measurements during the time of analysis were available for only three years (2001, 2011, and 2012), a general characterization of the influence of the quasi-16-day waves related to SSW on the upper atmosphere and its solar activity dependence is not performed. In order to study these features more extensively we have used systematic data sets such as EEJ and TEC that span for several years and report the results so obtained in this Chapter.

The low-latitude upper atmosphere of the Earth is dynamically coupled to both lower atmosphere and high-latitudes. While the neutral motions are affected via waves from the lower atmosphere and by temperature gradients created due to incoming solar radiation, the plasma motions are driven by electrodynamical processes. Since both plasma and neutral species share the same volume in space their motions are coupled to each other in the upper atmosphere. Waves generated in the lower atmosphere propagate to the upper atmosphere under favorable background conditions and influence the upper atmospheric (or F-region) dynamics by altering the conductivities of the E-region. This is because of the fact that the F-region is electrodynamically coupled to the E-region, especially over the low- and equatorial-latitudes.

Even though the SSW is a northern hemispheric winter time polar latitude phenomenon, the whole atmosphere of the Earth responds to these large-scale meteorological events [*Fuller-Rowell et al.*, 2011]. During SSW events both meridional and zonal circulation change their direction drastically ([e.g., *Espy*, 2003; *Cho et al.*, 2011] and more recently by [*Laskar and Pallamraju*, 2014]). Due to this, there occurs significant variations in the dynamics from the troposphere to the thermosphere. The waves propagating from the lower atmosphere face these altered background conditions and hence get modulated. Also, during SSW events the planetary waves, that are mainly generated in the troposphere, get amplified and the stratospheric and mesospheric zonal winds are also altered drastically rendering the conditions conducive for the propagation of the small-scale waves which are already modulated by the planetary waves [*Liu et al.*, 2010; *Yiğit and Medvedev*, 2012]. The interaction between enhanced planetary waves and tides and the interaction between tides and modified middle atmosphere modulates the tidal components, which register their signature in the upper atmospheric parameters [*Jin et al.*, 2012; *Pedatella and Liu*, 2013; *Guharay et al.*, 2014]. Also, nonlinear interaction between planetary waves and tides produces additional waves at sum and difference frequencies of the two original waves [*Teitelbaum and Vial*, 1991] which fall mainly in the tidal domain.

The quasi-16-day waves are the strongest normal mode oscillation of the atmosphere [*Andrews et al.*, 1987]. These waves are found in the upper atmosphere throughout the years [e.g., *Forbes and Leveroni*, 1992; *Forbes*, 1995; *Espy and Witt*, 1996; *Luo et al.*, 2000], but their enhanced association with the SSW events has been reported by many researches in recent times [e.g., *Vineeth et al.*, 2007, 2011; *Pedatella and Forbes*, 2009; *Sripathi and Bhattacharyya*, 2012; *Laskar et al.*,

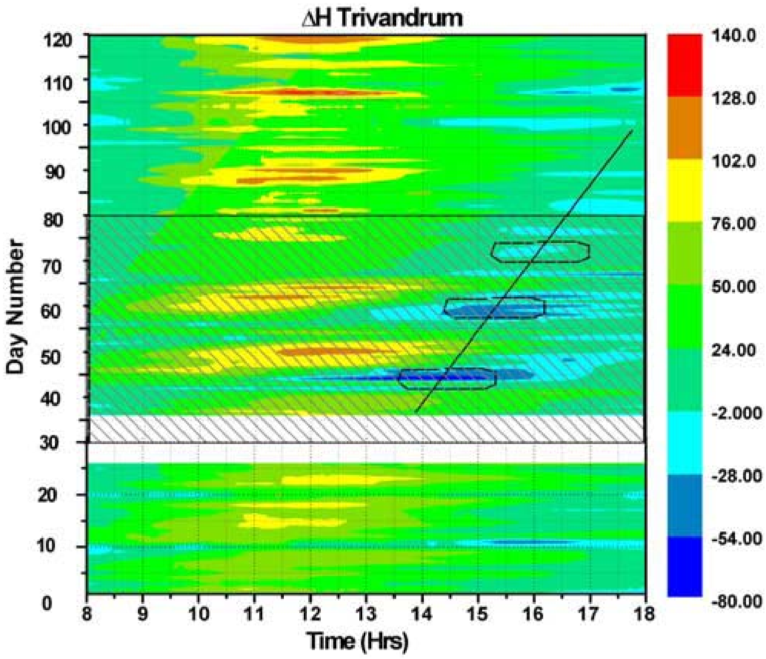

Figure 5.1: Horizontal component of magnetic field (ΔH) variations over Trivandrum (December 01, 2005 - March 31, 2006). Oval represents depletions in the EEJ (i.e. CEJ). The line connecting the ovals depicts the shift of CEJ maxima towards later local time with days (After [*Vineeth et al.*, 2007]).

2013]. Using anomalies in the horizontal component of magnetic field (ΔH) over Trivandrum, *Vineeth et al.* [2007] showed that there occurs enhancement and depletion in ΔH values with an approximate periodicity of 16 days (as shown in Figure 5.1). They also showed that the afternoon counter electrojet (CEJ) event minimum has a phase shift with respect to local time.

It is known that lunar gravitational pull on the Earth's atmosphere produces a strong semidiurnal (12 hours period) component. The EEJ daily variations show this semidiurnal behavior very dominantly. It has been shown that the lunar semidiurnal tidal effects on EEJ and TEC are enhanced [*Fejer et al.*, 2010; *Park et al.*, 2012] during SSW. Also, there occurs a morning enhancement and afternoon depletion in the equatorial ionospheric $\mathbf{E}\times\mathbf{B}$ (as can be seen in Figure 5.2) drifts and the maximum of perturbation shifts towards later local time with day of the year. This has been explained to be due to the enhancement of the semidiurnal tides due to effects that are present during SSW events, such as amplification of planetary waves and alteration in circulation in both zonal and

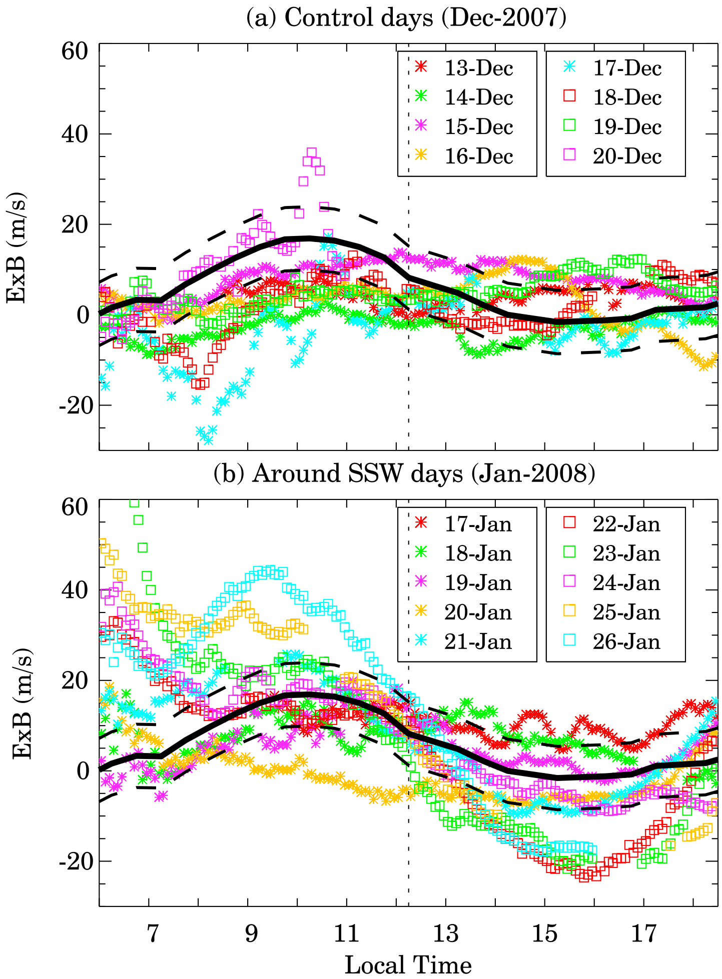

Figure 5.2: Daytime vertical E×B drifts measured over Jicamarca during (a) December 13 - 20, 2007 (control days) and (b) January 17 - 26, 2008 (around SSW days), as function of local time. Data for different days are indicated with different symbols and colors. The expected average and standard deviation of quiet-time values are indicated with black solid and dashed curves, respectively, obtained from the model of *Scherliess and Fejer* [1999] (After [*Chau et al.*, 2009]).

meridional directions. The shift of the maximum towards later local times had been explained to be due to the interaction of lunar-tide with solar semidiurnal tide during SSW [e.g., *Fejer*, 2011].

All these earlier results presented above suggest that there is a connection between SSW events, diurnal tides, and quasi-16-day waves, which may also vary with solar activity. Mostly there are individual reports or case studies of SSW events and general studies comprising many events are sparse. In this chapter we study the atmospheric behavior during several SSW events at varying levels of solar activity to understand the SSW-time vertical coupling of atmospheres.

By studying large-scale oscillation using data sets such as the stratospheric wind, EEJ strength, TEC, and multiwavelength dayglow intensities which originate from different altitudes of the upper atmosphere, it has been shown in Chapter 4 that the planetary wave influence on the upper atmosphere is solar activity dependent [*Laskar et al.*, 2013]. From an earlier study of the long term magnetometer data it was reported that the SSW related lunar tidal amplification do not show solar activity dependence [*Yamazaki et al.*, 2012]. But in a later work using 100 years of mid-latitude magnetometer data from eight stations, *Yamazaki and Kosch* [2014] reported that both lunar and solar semidiurnal tidal influence on the upper atmosphere show solar activity dependence. Moreover, using Jicamarca vertical drift velocity measurements *Fejer et al.* [2011] showed that the lunar tidal perturbations are of smaller amplitudes during high solar flux, compared to low solar flux condition. From numerical simulation [*Pedatella and Liu*, 2013] and empirical data [*Laskar et al.*, 2013], it has been shown that the upper atmosphere is influenced dominantly by the lower atmospheric forcing during low solar activity and the influences are weak during high solar activity. So, to summarize the current understanding, it can be said that, it is well established that during low solar activity epoch the upper atmosphere is influenced dominantly by the lower atmosphere. But for high solar activity conditions the agreement is not unanimous.

Here, in this chapter we report the results obtained from the investigations on the behavior of the magnetometer based measurement of EEJ and GPS-based measurement of TEC for low to high solar activity conditions to elucidate the behavior of the upper atmosphere during SSW and at different levels of solar activity. Clear signatures of the interaction between enhanced planetary waves and tides during SSW and the resulting influence on the upper atmospheric EEJ strength along with the TEC values are presented to demonstrate the vertical coupling of atmospheres and its dependence on the strength of SSW at different levels of solar activity.

5.2 Data Set

To obtain information on the low-latitude coupled ionosphere-thermosphere system during SSW and at different levels of solar activity, the EEJ strength and TEC data are used in this study. The details of these data sets can be found in section 2.5. Hourly averaged EEJ data are obtained from the geomagnetic observatories of the Indian Institute of Geomagnetism. The TEC data has been obtained from a southern hemispheric station, Diego Garcia (7.27° S, 72.4° E; 15.3° S MLAT), that is located approximately in the same longitude sector as that used for obtaining the EEJ strength. Moreover, this station falls right below the southern crest of the EIA. While calculating vertical TEC values in low-latitudes, satellites with elevation angles greater than 50° are considered which remove the dependence of TEC on ionospheric pierce-point height and latitude, in addition to multipath effects [*Rama Rao et al.*, 2006; *Bagiya et al.*, 2009]. To obtain the information on the lower atmospheric altitudes at high-latitudes, where the SSW occurs, the NCEP/NCAR reanalysis stratospheric temperature and wind data from those regions has been used as described below.

Parameter	Year							
	2005	2006	2007	2009	2010	2011	2012	2013
ΔT_{SSW}	40	60	40	60	40	35	30	45
T_{peak_SSW}	240	260	245	265	237	235	245	248
U_{east}	10	-25	-8	-35	-6	25	5	-12
SSW str.	minor	Major	Major	Major	Major	minor	minor	Major
<SSN>	30	10	14	1	16	24	46	51

Table 5.1: Some of the atmospheric and solar parameters during the years 2005 to 2013. Here, ΔT_{SSW} is stratospheric temperature anomaly at 90° N; T_{peak_SSW} is peak stratospheric temperature during SSW at 90° N; U_{east} is peak eastward zonal mean stratospheric wind at 60° N during SSW; SSW str. is SSW strength; <SSN> is average SSN. The year 2008 is not included here, reasons for this are explained in main text.

The NCEP/NCAR reanalysis data as explained in section 4.2.2 are used here to obtain the information on arctic latitude stratosphere. In this study, the stratospheric temperature at 10 hPa (∼30 km) from 90° N is used to obtain the temperature anomaly. From the NCEP/NCAR zonal mean zonal wind it can be seen that three minor and six major warming events occurred during the years 2005-2013 (excluding those in the year 2008, wherein both major and minor events occurred one following the other). The nature of SSW event and average SSN (<SSN>) during the observation period of January-February months in all the years are presented in Table 5.1. One can note that these events span solar activity levels with average SSN ranging from 1 to 51.

5.3 Analysis Methodology

The EEJ strength and TEC data during the January-February months of the years 2005 to 2013 are used in this study. In order to investigate the interaction between local time dependent waves and large-scale planetary wave type oscillations during SSW events the following approach has been adopted. For each day, data are binned in hourly intervals and then the data from a particular hourly bin are arranged as a function of DOY to make a time series of 60 data points (for the 60 days) as shown in the left side panel (a) in Figure 5.3 for the EEJ strength data of the year 2006. Lomb-Scargle periodograms [*Lomb*, 1976; *Scargle*, 1982; *Torrence and Compo*, 1998] of each of the time series in the left panels are shown in the right panels (b) in Figure 5.3. The details of the periodogram techniques are given in section 3.2.2. The plots are placed one below the other according to bins that are arranged by local time. Such analysis has the advantage that it reveals the local time dependence, if any, of waves (such as, solar tides of different periodicities and planetary-scale waves). One can note the presence of periods 12-16 days in these periodograms. Also, there is a systematic pattern in the planetary wave type periodicities of 12-16 days in the EEJ, which is seen to be prominent throughout the daytime hours. Such method of determination of the dominant periods at different hours in the time series as shown in Figure 5.3(b)

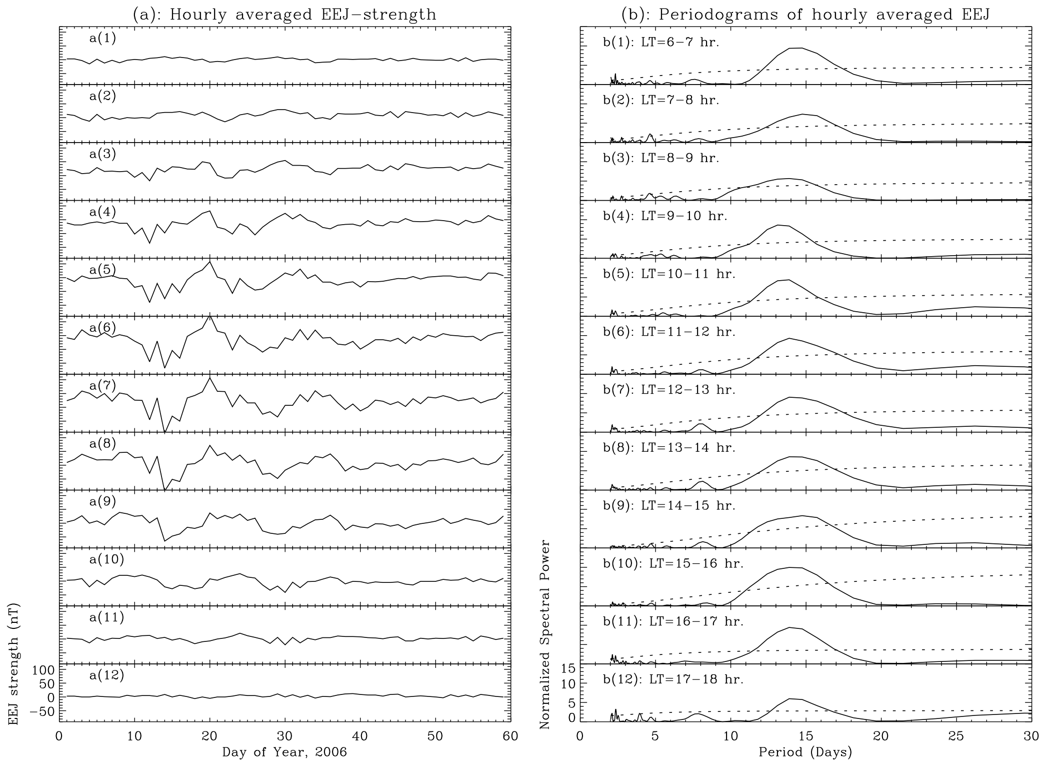

Figure 5.3: (a) Hourly-binned daily values of EEJ strength and (b) their corresponding normalized Lomb-Scargle periodograms for the year 2006 are presented. This type of binned daily values average out the gravity wave type periods of less than one hour. Moreover, they show periods that are dependent on local time (like solar tides). Also, as the larger-scale planetary waves modulate these local time dependent tidal waves, the periodogram spectral power is a direct measure of the interaction strength between tidal and planetary waves. Dashed lines in the right panel represent the 90% significance levels. Here one can note a systematic variation of statistically significant periodicities with respect to local time for the wave periods between 11-20 days (i.e., the quasi-16-day periods are present here at all the local times).

for 2006 has been carried out for all the years (2005-2013) in both the observed parameters, namely, the EEJ and the TEC. The details of these periods and their dependence on SSW strength and solar activity level are described in the next section. As both major and minor events occurred in the year 2008 one after the other in quick succession, the events in this year have not been considered in the current analysis. Moreover, the TEC data also do not exist in this year for this station.

5.4 Results and Discussion

The periodograms in Figure 5.3 show the presence of waves in the planetary wave regime (2-30 days). However, the most dominant waves that have been observed are of quasi-16-day type. For bravity, all the periodograms (similar to that shown in Figure 5.3(b)) at different local times in all the years have been converted into contour plots as shown in Figure 5.4. These contour plots are made after normalizing the periodograms with their respective 90% significance level values. The left (a) and right (b) panels show the periodogram contours for the EEJ strength and the TEC from Diego Garcia. Each column represents data for 8 years from 2005-2013, wherein the x-axis represents the periods in days and the y-axis is the local time. The color bar represents the relative spectral powers compared to the strongest power of the year 2009 - the year of strongest SSW event of the past decade. This is done in order to compare the inter-year variation in powers for a given periodicity. Here, all the periods greater than the relative power of ∼0.6 (dark green) are above 90% significance level.

In Figure 5.4, one can see the presence of waves of 2, 5-6, 9-10, and 27-days periods, in addition to the dominant quasi-16-day wave. The quasi-16-day waves originate mainly in the lower-atmosphere and are very sensitive to the stratospheric and mesospheric mean zonal winds [*Luo et al.*, 2000]. Also, they do not propagate directly to the upper atmosphere but their influence is transmitted via interaction with gravity waves and tides. So, the large-scale waves and periodicities that appear in Figures 5.3 and 5.4 are believed to be associated with both variabilities of tides and planetary waves from the lower atmosphere.

From Figure 5.4, one can note that the relative powers of the periods in the quasi-16-day range are very prominent and are present in almost all the years presented here. The maxima of power at quasi-16-day period range do not vary greatly with respect to local time in the years 2006, 2007, and 2009, while for 2005, 2012, and 2013 one can note that the periods with maxima in power shift from shorter to longer periods from morning to evening. Qualitatively, it is notable that the periodicities in the EEJ and the TEC are similar. This happens due

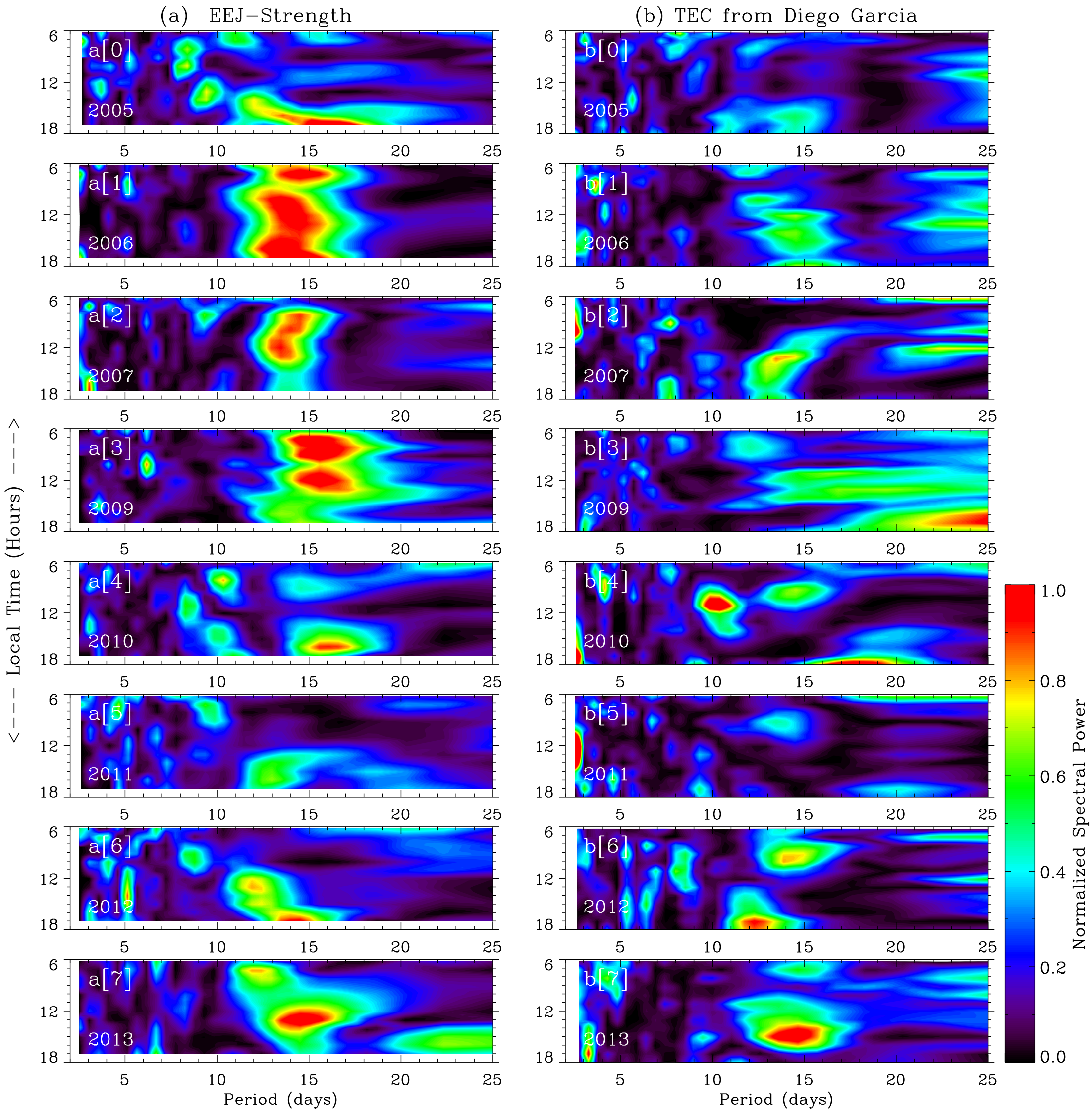

Figure 5.4: Contour plot of the Lomb-Scargle periodograms corresponding to all the local times as shown in Figure 5.3(b) are presented here in the subplot a[1]. Similarly, periodograms of EEJ in left panel (a) and TEC in right panel (b) for the observation durations in the years 2005-2013 are shown. The spectral powers are normalized with respect to their respective 90% significance level values. The color bar represents the strength/relative power of the significant periods and all the periods with relative power greater than ∼0.6 (dark green) are above 90% significance level. It should be noted that during the major warming cases of 2006, 2009, and 2013 both the EEJ and the EIA crest region station, Diego Garcia, show strong quasi-16-day periodicities.

to the fact that the low-latitude E-region electric field acts as a dominant driver for the redistribution of F-region plasma processes. Other than the quasi-16-day periods one can note the presence of periodicities at 2.5, 5-6, 8-10, and 25 days in most of the years in Figure 5.4. The 2- and 5-day waves are the normal-mode oscillation of the lower atmosphere [*Salby*, 1984]. In addition to the Doppler-shifted 10-day normal-mode oscillation origin, the 8-10 day waves have also been reported to be related with the quasi-periodic variations of solar wind high-speed streams and recurrent geomagnetic activity [*Thayer et al.*, 2008]. Thus, some of the wave activities seen in these upper atmospheric parameters are due to both solar and lower atmospheric origin. It should also be mentioned that during our observational windows, the geomagnetic storm occurrences (as characterized by Kp>5) do not show such quasi-16-day type variations. So, the quasi-16-day periods reported here have not originated from geomagnetic disturbances but are of lower atmospheric origin.

The average spectral power in periodicities in the quasi-16-day range (11.5 to 20 days) during 6 to 18 hours local time in the contour plots shown in Figure 5.4 are plotted in Figure 5.5 for both the EEJ strength and the TEC as a function of year. The letters 'm' and 'M' above the x-axis stand for 'minor' and 'Major' SSW events, respectively, that occurred during those observational windows. The dashed line (with '+' symbol) in Figure 5.5 shows the northern polar latitude (90° N) stratospheric temperature anomalies (ΔT) that occurred during the SSW events. The ΔT values are calculated by averaging the stratospheric temperature in an interval with nearly constant variation prior to its enhancement due to SSW.

In the absence of any index or parameter which represents the true strength of SSW the (ΔT) values are used as an indicator of the strength. It is expected that the ΔT values represent the stratospheric behavior in response to the SSW events. Strikingly, there are three maxima in both temperature anomaly and spectral powers of EEJ and TEC which occurred during the three strong major SSW years of 2006, 2009, and 2013. Also, during the three minor warmings in the years 2005, 2011, and 2012, the spectral powers are minimum. These observations suggest that the strength of the SSW decides the spectral power of quasi-16-day

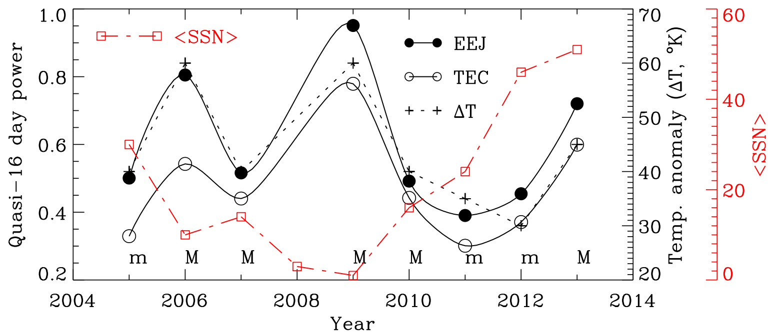

Figure 5.5: The mean normalized power of the quasi-16-day periodicities (the power spectra as shown in Figure 5.4 are averaged between 11.5 to 20 day periods and for the whole day) in EEJ strength and TEC are shown. The letters 'm' and 'M' represent 'minor' and 'Major' SSW events that occurred in the given year. The dashed curve shows the high latitude stratospheric temperature anomaly (ΔT) on the peak of the SSW related warming that represents the lower atmospheric behavior. One can note that the amplitudes have three peaks during the three strong major SSW events in the years, 2006, 2009, and 2013 and three minima during the minor events of 2005, 2011, and 2012. It can be noted that there is a clear and systematic correspondence between the quasi-16-day amplitudes and the polar stratospheric temperature anomaly. The average SSN values are also shown with its axis at the right. It may also be noted that the relatively higher solar activity year of 2013 showed a strong coupling due to increased lower atmospheric activity during strong SSW event.

waves in the upper atmospheric parameters. The quasi-16-day type variations in the EEJ and ionospheric parameters are widely shown to be enhanced during SSW events [*Pancheva et al.*, 2009]. Notably, the three major events of 2006, 2009, and 2013 were the top three major events (in terms of strength) in the last two decades. Thus, the higher spectral power in these three major events implies that the stronger the SSW event, the stronger will be its effect on the low-latitude upper atmosphere. This happens because during major warmings the semidiurnal tidal (both solar and lunar) and planetary wave amplitudes are amplified and their combined action registers a greater influence on the ionosphere [*Stening et al.*, 1997; *Pedatella and Liu*, 2013].

It can be noticed from Figure 5.5 that there are statistically significant (normalized values greater than 0.6, the 90% significance limit) quasi-16-day periods in all the years in addition to those in the three strong major warming years mentioned above. In spite of the fact that the SSWs in 2005, 2011, and 2012 were minor in nature, they showed appreciable amplitudes in the quasi-16-day power. Notably, these three minor events occurred during low solar activity epoch. As discussed in Chapter 4, *Laskar et al.* [2013] used empirical data to show that the vertical coupling of lower to the upper atmosphere is higher/lower during low/high solar activity. Using numerical simulations *Pedatella and Liu* [2013] showed that for same level of SSW activity the lower atmospheric influence on the upper atmosphere is greater during low solar activity period in comparison to that at high solar activity, wherein, solar influences dominate. In the present case, one can note that the major SSW event of 2013, which occurred in relatively higher solar activity (average SSN of 51), shows strong spectral power in the quasi-16-day periods. In our earlier study [*Laskar et al.*, 2013], it was conjectured that even during high solar activity if there occurs a major SSW event then it would provide additional energy which will significantly influence the upper atmosphere. In this work, the observation of the SSW event of 2013 is an experimental evidence to that conjecture. Support for this conjecture is also obtained from the published literature wherein the existence of perturbations in the ionosphere due to lower atmospheric forcings were reported during high solar activity epochs of 2001-2003 and 2013 [e.g., *Liu and Roble*, 2005; *Fejer et al.*, 2010; *Pedatella and Liu*, 2013; *Goncharenko et al.*, 2013a], −which actually occurred in simultaneity with major SSW events. These earlier reports have to be viewed in light of our conjecture that if the lower atmospheric forcing is stronger, as it happens during strong SSW events, then they can affect the upper atmosphere appreciably even during high solar activity periods. The current study thus demonstrates these features and places things in perspective with larger and independent data sets during low, moderate, and higher solar activity epochs. The present study also reveals the plausible conditions in which an SSW event show greater effect on the upper atmosphere based on various waves and background dynamics as discussed below.

As mentioned above, the enhanced planetary waves and middle atmospheric dynamics during SSW events modulate the tidal waves (mainly semidiurnal)

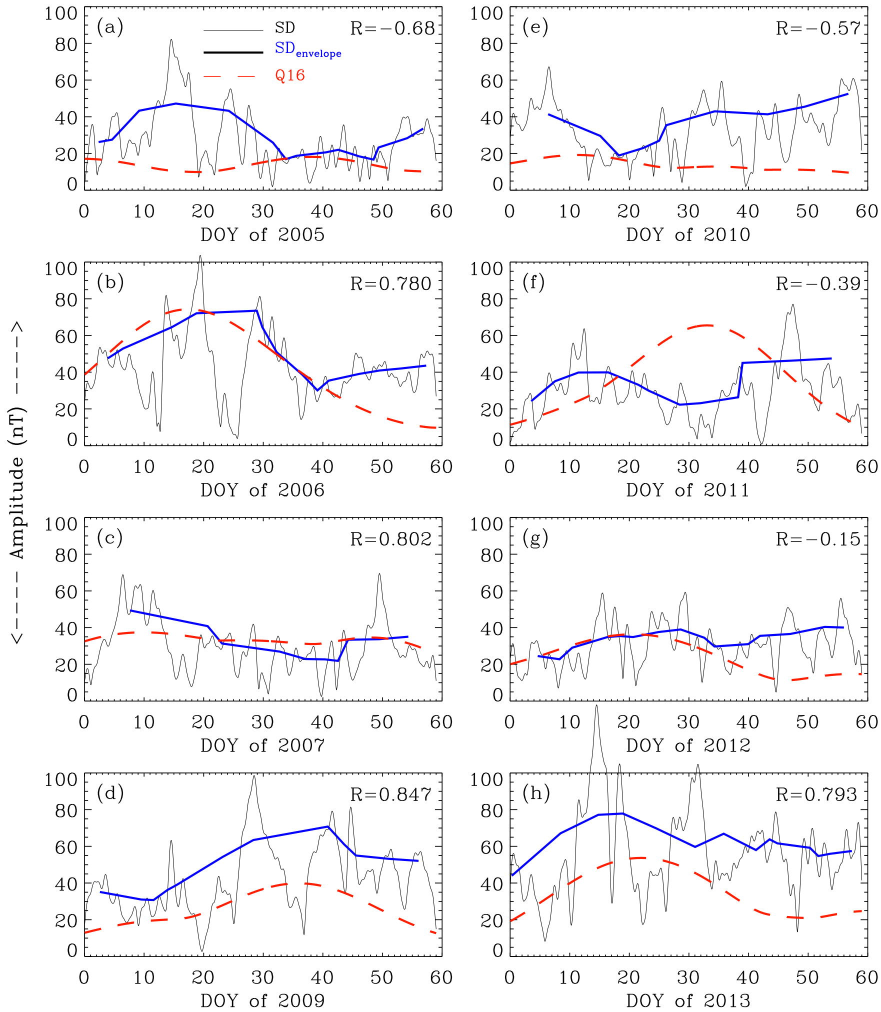

Figure 5.6: The amplitudes of the semidiurnal (SD; thin continuous lines), semidiurnal envelope (SD$_{envelope}$; thick continuous lines), and quasi-16-day (Q16; dashed) periods in the EEJ strengths are shown along with the correlation coefficient (R) between SD$_{envelope}$ and quasi-16-day wave amplitudes. One can note that there is a good correlation between these two parameters for the three strong major warming years of 2006, 2009, and 2013 (R values are 0.78, 0.85, and 0.79, respectively). This signifies that during the strong SSW events the interaction between semidiurnal and quasi-16-day waves is stronger.

which further influence the ionosphere through the electrodynamical processes. To study the behavior of these waves, the relative variation in amplitudes of quasi-16-day and semidiurnal waves had been looked into. Figure 5.6 shows the amplitudes of the semidiurnal (SD; thin continuous lines), an estimate of the SD envelope (SD$_{envelope}$; thick continuous lines), and quasi-16-day (dashed) periodic variations in the hourly values of EEJ strength during the years of the current study. These amplitudes are obtained using the wavelet-based spectral analysis technique [*Torrence and Compo*, 1998] which is discussed in Chapter 3. The $SD_{envelope}$ values are obtained by a 2-point smoothing of the curve joining the maxima of the 3-day (72 hours) smoothed semidiurnal amplitudes. Interestingly, one may note from Figure 5.6 that the amplitudes of both SD tidal and quasi-16-day amplitudes are high and broadly vary in similar fashion (as if semidiurnal tides are modulated by the quasi-16-day waves) around the peak of SSW event, especially for the three strong major SSW events of 2006, 2009, and 2013. The cross-correlation coefficients (R) between $SD_{envelope}$ and quasi-16-day amplitudes are also shown within the plots. One can note that for the three strong major SSW years 2006, 2009, and 2013 the correlation coefficient values are 0.78, 0.85, and 0.79, respectively. For the less major and the minor events the correlation coefficients are negative (except 2007, which was a late winter SSW event), which may possibly be due to interaction of tides with some other planetary wave or with middle atmospheric dynamics [*Jin et al.*, 2012].

From the results presented above one may conclude that during the three strong major SSW events of 2006, 2009, and 2013 there were strong interactions between semidiurnal tides and quasi-16-day waves. Further, recent modeling studies suggest that the middle atmospheric dynamics play a dominant role in coupling the lower atmosphere and upper atmosphere during SSW events [*Jin et al.*, 2012; *Pedatella and Liu*, 2013]. This study thus provides experimental evidence to our conjecture proposed earlier which revealed new aspects of interactions on vertical coupling of atmospheres. These new findings call for a detailed modeling and simulation studies, which are beyond the scope of the present work, and are a topic of research that will be carried out in the future.

5.5 Summary

Using two independently measured upper atmospheric parameters, namely the EEJ and the TEC, the vertical coupling of atmospheres during SSW events at varying levels of solar activity has been investigated. Individual SSW events during the years 2005-2013 have been considered. There were three very strong SSW events during 2006, 2009, and 2013 of which the first two occurred during the low solar activity epoch and the 2013 event occurred during the so-called maximum of the 24th solar cycle. The main findings of this work are summarized below:

1. The spectral powers of the quasi-16-day wave oscillations in the EEJ and the TEC (over the crest of the EIA) are found to vary in similar fashion with the arctic-latitude stratospheric temperature anomaly. The quasi-16-day spectral powers were found to be strong during the three strong major warming cases in 2006, 2009, and 2013, and weaker during the minor warming events in 2005, 2011, and 2012, implying that the intenseness of the SSW event decides the strength of vertical coupling.

2. It is observed that for those major events for which the quasi-16-day amplitudes are high, the broad variations in the amplitudes of semidiurnal tide and the quasi-16-day amplitudes are quite similar. This suggests that there occurs strong interaction between semidiurnal tides and quasi-16-day planetary waves during the strong major SSW events. This interaction has been found to be weaker for less-major and minor SSW events.

3. Even though the 2013 event occurred during relatively high solar activity epoch, the powers in the quasi-16-day period in both the EEJ and the TEC were significantly strong. This observation supports the *Laskar et al.* [2013] proposition that even during high solar activity if an SSW event occurs, then the upper atmosphere is influenced significantly by lower atmospheric forcings due to additional energy that becomes available for enabling the vertical coupling of atmosphere through the planetary waves and middle atmospheric dynamics.

To conclude, the vertical coupling of the atmospheres in terms of the magnitude of spectral amplitude is found to be dependent on the strength of SSW, solar activity, and interaction between tides and planetary waves.

Chapter 6

Mesosphere-Thermosphere Circulation During SSW

6.1 Background

A brief account on SSW events, their cause, and a few of their effects have been mentioned in Chapter 1. In Chapter 4 we have seen that during SSW events the quasi-16-day waves are amplified. In Chapter 5 the spectral characteristics of quasi-16-day wave during the eight recent SSW events from 2005 to 2013 are presented. It has been found that the spectral powers of quasi-16-day waves and semidiurnal tides depend on the strength of the SSW events. The spectral powers are stronger for the strong major SSW events and comparatively low for the less-major and the minor events. In the current chapter we report the effect of these high-latitude lower-atmospheric events (i.e., SSW) on the low-latitude oxygen dayglow emission intensities and present evidences of setting up of a mesosphere-thermosphere meridional circulation cell due to these events.

As explained in Chapter 1 the SSW event is an arctic-latitude phenomenon in which the stratosphere warms up by tens of Kelvins within a few days. Even though the SSW is mainly a northern hemispheric winter-time stratospheric phenomenon, numerous observational and modeling studies have demonstrated its influence on the global atmospheric and ionospheric parameters, such as MLT temperature, wind, and general circulation [e.g., *Liu and Roble*, 2002; *Guharay* *and Sekar*, 2012; *Chandran et al.*, 2013], TEC [e.g., *Pedatella and Forbes*, 2010; *Yue et al.*, 2010; *Pancheva and Mukhtarov*, 2011; *Goncharenko et al.*, 2013b], EEJ strength [e.g., *Parish et al.*, 1994; *Vineeth et al.*, 2009], and F-region vertical drifts [e.g., *Chau et al.*, 2009; *Fejer et al.*, 2011]. The responses in the lower atmospheric parameters were mainly in terms of horizontal mass transport, generation of secondary planetary waves, enhanced semidiurnal tides and planetary waves, and perturbation in general circulation. Whereas, in the ionospheric parameters the responses were mainly reported to be in the form of enhanced semidiurnal tidal amplitudes during SSW events which were supported by several modeling studies [e.g., *Fuller-Rowell et al.*, 2011; *Pedatella and Liu*, 2013]. Due to the enhanced semidiurnal tides various electrodynamic parameters, such as the EEJ, TEC, and $\mathbf{E}\times\mathbf{B}$ drift show an enhancement/depletion in the morning/afternoon hours. A brief introduction of these effects are given in section 5.1.

Most of the works reported so far on the influence of SSW on the low-latitude upper atmosphere were concentrated mainly on the electrodynamic components, most likely due to the fact that the semidiurnal tidal amplitudes alter the equatorial dynamo mechanism due to which modifications are brought out in plasma parameters [*Chau et al.*, 2009; *Sridharan et al.*, 2009]. But, the experimental results on the low-latitude thermospheric neutral constituents during SSW events are sparse due to a lack of data sets that represent the neutral behavior directly. *Liu et al.* [2011] made use of the neutral thermospheric density measurement by CHAMP and GRACE satellites and showed about 30 to 45% decrease in thermospheric density at sub-solar latitudes during the 2009 SSW event. However, *Fuller-Rowell et al.* [2011] revisited the same (CHAMP) data and questioned the inference on the compression of the thermosphere which they attributed to the local time sampling of CHAMP data. Instead, *Fuller-Rowell et al.* [2011] showed that there was a global thermospheric density increase by about 5% when lower atmospheric wave forcing was incorporated into the whole atmosphere model. From these results and other of this kind [e.g., *Liu and Roble*, 2002; *Pedatella and Liu*, 2013], it can be seen that there is a lack of comprehensive understanding of the upper atmospheric neutral behavior during SSW. In order to gain a greater understanding of the influence of high-latitude phenomena (such as SSW) on the neutral component of low-latitude upper atmosphere, systematic daytime optical investigations have been carried out from a low-latitude location, Hyderabad (17.5° N, 78.5° E), in India. Measurements during four recent SSW warmings of the years 2010, 2011, 2012, and 2013 are used to investigate the characteristic behavior of the low-latitude thermosphere in response to the SSW events.

6.2 SSW Events in 2010, 2011, 2012, and 2013

Figure 6.1 summarizes some of the geophysical conditions that were existing during the first 50 days of the years 2010 to 2013. The occurrence time of the SSW event has been defined by different researchers/communities based on some measurable quantity of interest that is affected by dynamical changes during that time. For example, WMO used temperature and wind at 10 hPa pressure level and at 60° N latitudes [*Andrews et al.*, 1987]. As mentioned in Chapter 1, according to WMO, if the stratospheric temperature at 10 hPa pressure level and poleward of 60° N increases by more than 25 K within a week then it is termed

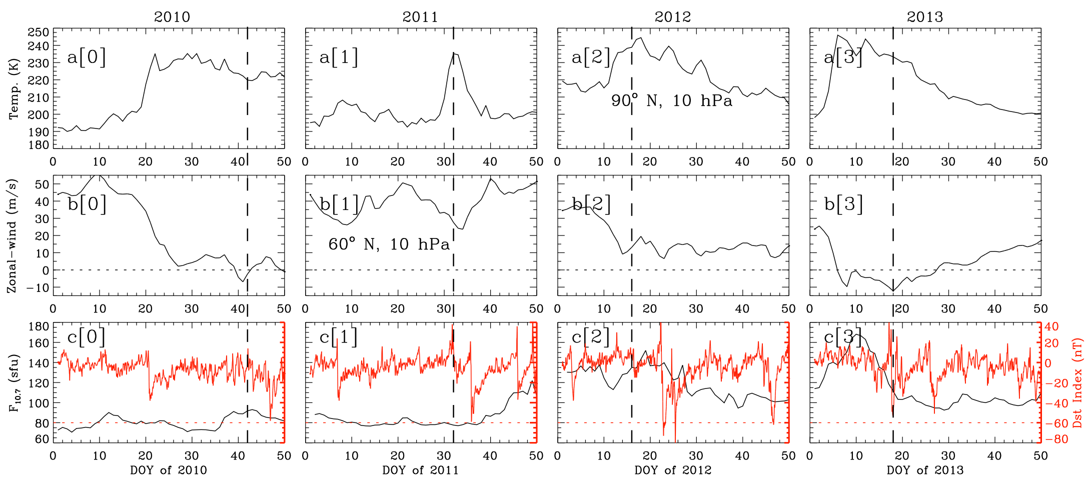

Figure 6.1: Day-to-day variations of relevant geophysical parameters are shown for the years 2010 to 2013 (columns). (a) Temperature at 90° N and at 10 hPa pressure level, (b) mean zonal wind magnitudes at 60° N and at 10 hPa level, and (c) the F10.7 cm flux and Dst index. Vertical dashed lines show the days on which the arctic-latitude lower thermospheric temperature shows an enhancement in response to SSW.

as SSW. Based on this definition (and temperature at 90° N and at 10 hPa), one can note from Figure 6.1 (panel a) that there were four SSW events, one each in the past four years, and the effects persisted approximately during DOYs 20 to 50, 30 to 38, 12 to 34, and 5 to 30 in the years 2010, 2011, 2012, and 2013, respectively. For 2011 and 2012 SSW events, the magnitudes of the zonal eastward winds at 60° N and at 10 hPa altitudes were weakened in consonance with increasing stratospheric temperature but did not reverse their direction and thus, they are minor in nature. Whereas, during 2010 and 2013, the usual winter time eastward zonal winds reversed to westward indicating that the events were major. The solar activity during SSW events in 2010 and 2011 events was relatively weaker compared to the other two events (in 2012 and 2013) as can be seen from the daily averaged F10.7 index. Figure 6.1(c) also shows the hourly averaged values of Dst index whose axes are shown on the right side of the plots. Unlike the years 2010, 2011, and 2013, in which the magnitudes of peak Dst index were greater than -60 nT, in the year 2012 a magnetic disturbance of -73 nT occurred in near-simultaneity with the SSW event.

6.3 Measurements and Observations

Measurements of the daytime atomic oxygen airglow emission intensities at multiple wavelengths are made from Hyderabad, India, using MISE instrument. The details of MISE and the data extraction procedures from it have been given in Chapter 2 and in *Pallamraju et al.* [2013]. The column integrated dayglow emission intensities obtained at OI 557.7, OI 630.0, and OI 777.4 nm represent the behavior of the atmosphere at altitudes from where they emanate, which are dependent on their production mechanisms, and are approximately 130 km (average of the two peaks at 100 km and 160 km), 230 km, and peak height of the ionospheric F-region, respectively.

The daily variations in dayglow emission intensities in Rayleighs for a few days in-and-around the SSW events during the past four events (year 2010, leftmost; 2013 rightmost columns) and at the three wavelengths (OI 777.4 nm (panel a),

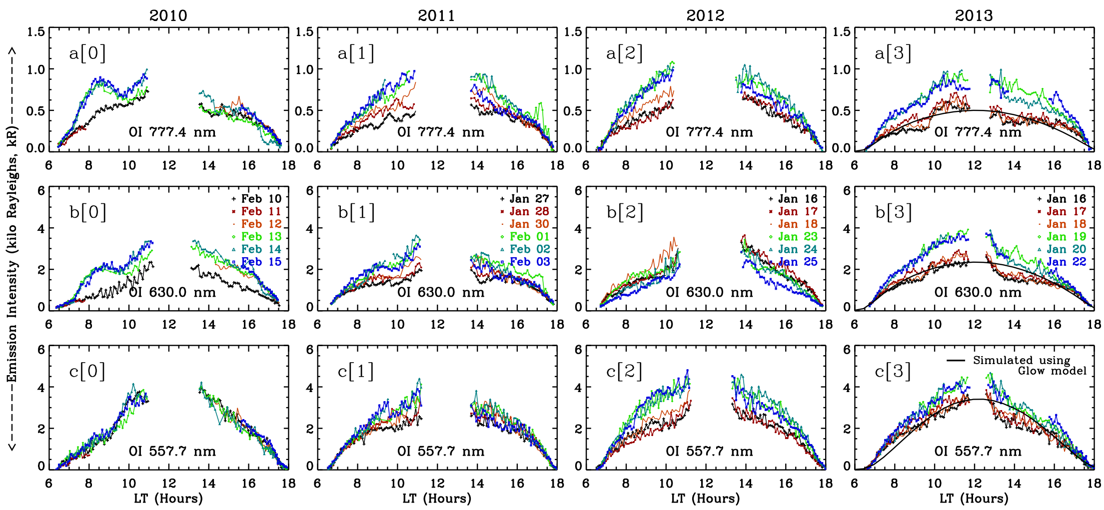

Figure 6.2: Daily variations of the oxygen dayglow emission intensities for a few days in-and-around the SSW events during 2010 to 2013 are shown. Days in each year are represented by colors as depicted by legends in the middle row. It can be seen that the dayglow intensities throughout the day are enhanced systematically on some days during SSW events. The smoothly varying daily behavior in the year 2013 are the emission intensities estimated using the GLOW model and are used to remove the dominant diurnal solar zenith angle contribution from the observed dayglow emission intensities. Only a few days are included here for brevity. More days are considered in this work as shown in Figure 6.4.

630.0 nm (panel b), and OI 557.7 nm (panel c)) are shown in Figure 6.2. Data for different days are represented by different colors. Cloudy sky conditions prevented observations during 11, 12, and 15 February in 2010 and during 19 to 22 January in 2012. It can be seen that there are two groups of temporal variations (one is the normal diurnal behavior in intensities and the other enhanced in intensities in comparison with those of 'normal' group) at all the wavelengths (except the OI 557.7 nm in 2010). It may be noted that the enhancements in dayglow emission intensities are throughout the day (for the enhanced group) with relatively higher amount of enhancement in the morning hours. There have been reports of the morning enhancement and afternoon depletion in the ionospheric parameters, such as, **E**×**B** drift, TEC, which were explained to be due to enhanced quasi-semidiurnal tides during SSW which are modulated by enhanced PWs and middle atmospheric dynamics [e.g., *Chau et al.*, 2009; *Jin et al.*, 2012]. However, in the present case of dayglow measurements, in addition to the usual enhance-

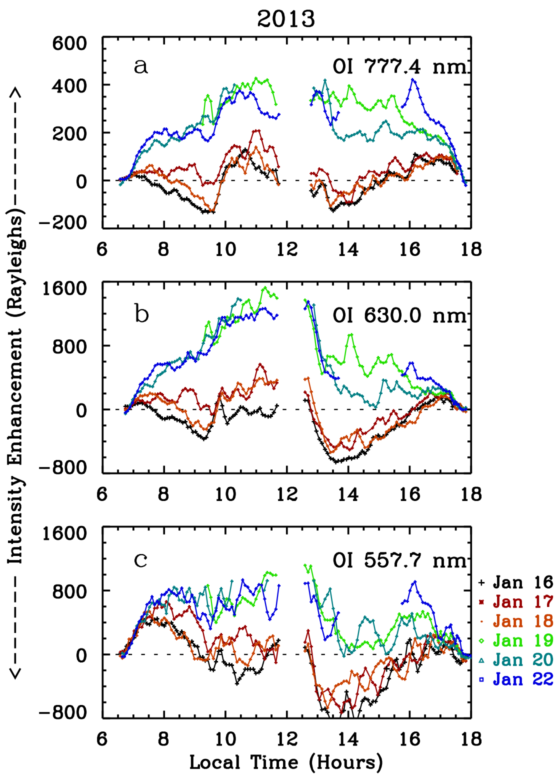

Figure 6.3: Enhancements in observed OI dayglow intensities as obtained by subtracting the GLOW model estimates from the measured intensities. Panels a, b, and c corresponds to OI 777.4 nm, OI 630.0 nm, and OI 557.7 nm, respectively for the year 2013.

ment in the morning hours, the afternoon sector also shows enhanced emissions. This suggests that, in addition to the semidiurnal tidal contribution some other mechanism is also contributing to these dayglow intensity enhancements.

In order to quantify the amount of enhancement in intensities that are other than the normal intensity due to daily solar zenith angle variation, a physics-based photochemical model, called GLOW model [*Solomon and Abreu*, 1989], derived emissions have been used. The MISE measured emissions compare well with the GLOW model predictions [*Pallamraju et al.*, 2013]. Simulated profiles using GLOW model dayglow emission intensity are over-plotted in Figure 6.2 for DOY 18 in the year 2013. Similar profiles are also estimated for the first day listed in Figure 6.2 to approximate the contribution of dayglow intensity under normal (non-SSW) conditions and remove the dominant daily solar zenith angle related variations for each year.

Figure 6.3 shows plot of the differences between the measured dayglow and the modeled GLOW emissions for all the three wavelengths under study. As it can be seen, the enhancements in intensities are present for almost the whole day. Such plots have been obtained for all the years at the three wavelengths. The emission enhancements from such curves are integrated to obtain one data point per day per wavelength as shown in Figure 6.4(a). This type of averaging is expected to average out, to a great extent, the contributions of quasi-semidiurnal tidal components that are known to be enhanced during morning hours and depleted in the afternoon hours during SSW events [*Chau et al.*, 2009]. Thus, the remaining contribution in enhancement is mainly due to effects other than semidiurnal tidal contribution. The diurnal and other tides are not of appreciable amplitudes to bring such variations. It is clear from Figure 6.4(a) that the systematic enhancements in daytime intensities at all the emission wavelengths are seen to occur within the SSW duration as mentioned above. This observation suggests a strong possibility of an effect initiated by the SSW at high-latitudes. Arguments are presented in the discussion section with supporting evidences to show that these enhancements in oxygen emission intensities over low-latitudes in all these years are caused by the effects associated with SSW-time dynamical conditions in the MLT altitudes of northern hemisphere.

It may be noted from Figure 6.4(a) that the daily averaged intensity enhancements increase around the duration of SSW occurrence and return to normal levels after the end of SSW events as can be seen clearly, especially, for the year 2011 for which longest span of optical data set are available with fewest data-gaps. It is also striking to note from Figure 6.4(a) that enhancement in intensities at all the wavelengths for the case of 2013 are higher compared to that of 2011 which is believed to be due to the fact that the 2013 SSW event was stronger compared to 2011 event. Further, the low-latitude upper thermospheric behavior is shown to be more sensitive to lower atmospheric forcing or high-latitude disturbances during low solar activity epoch [*Fuller-Rowell et al.*, 2011; *Laskar et al.*, 2013] and so even though 2011 was a minor event it produced an appreciable response (in terms of emission intensity enhancement) in comparison to that of major event

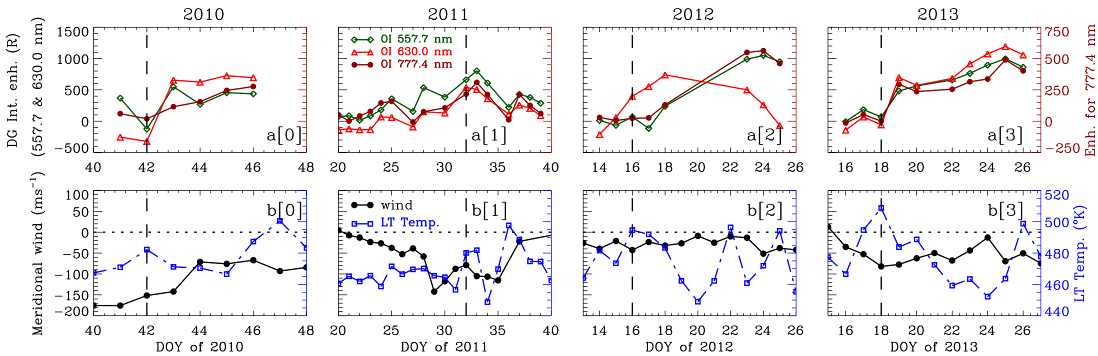

Figure 6.4: (a) The daily averaged dayglow emission intensity enhancements (observed-simulated) at low-latitudes for OI 557.7 (green), 630.0 (red), and for 777.4 nm (brown) as obtained from plots as shown in Figure 6.3 are shown. Dashed vertical line depicts the day on which peak in lower-thermospheric temperature was observed during a given SSW event. (b) TIDI measured representative MLT daily averaged zonal-mean wind (at 95 km altitude) 60° to 80° N latitudes (filled circles, left axis) along with the SABER measured lower thermospheric (LT; 119 km) kinetic temperature (squares, right axis) over arctic latitudes are shown. One can see a clear enhancement in dayglow intensities during SSW events. Notably, in all the years the MLT winds are equatorward (negative) in simultaneity with the observed dayglow emission intensity enhancements at all the three wavelengths as shown in panel (a).

in 2010 as can be seen in Figure 6.4(a). The relative variations in intensity enhancements in different emissions are most likely due to the differences in their production mechanisms as discussed in Chapter 2 and also due to the altitudes at which these emissions originate.

6.4 Results and Discussion

From the production mechanisms of the dayglow emissions, as mentioned in Chapter 2, it can be seen that the variations in intensities of the atmospheric dayglow emissions are brought about mainly due to (i) variations in the sources of energy (solar flux, [e.g., *Zhang and Shepherd*, 2004, 2005; *Pallamraju et al.*, 2010], (ii) variations in the densities of the constituents due to wave induced perturbations/modifications [*Chakrabarty*, 2004; *Pallamraju et al.*, 2010], and (iii) compositional changes (such as, those brought about by geo-magnetic disturbances)

[*Pallamraju et al.*, 2002; *Culot et al.*, 2005; *Shepherd and Shepherd*, 2011]. As discussed in section 6.3, except for the 2012 event the other three SSW events were magnetically quiet. Thus, emission enhancements other than those in the year 2012 are not expected to be due to geomagnetic storm effects. Also, the daily averaged F10.7 solar flux in the observation window in all these years were either decreasing (for 2013) or are very low and fairly stable (for 2010 and 2011), and therefore, the enhancements in the dayglow emission intensities reported here are clearly not due to an increase in the solar flux. Further, as mentioned above, the enhanced tidal (mainly semidiurnal) influences are expected to produce enhancement of the emission intensities only in the morning hours and decrease in the afternoon hours but not an enhancement for the whole day as seen in the present case. Therefore, the plausible cause for the enhancements in dayglow intensities is considered to be due to compositional changes brought about directly or indirectly due to the SSW event during which the dynamical conditions in the mesosphere thermosphere region are altered drastically.

During SSW events the usual winter-time stratospheric eastward zonal wind at high-latitudes becomes westwards which allows eastward gravity waves to propagate to the MLT region. Because of this eastward gravity wave forcing, there occurs an upward and equatorward circulation in the MLT region [*Liu and Roble*, 2002]. This circulation induces adiabatic cooling in the mesosphere and warming in the lower thermosphere over high-latitudes as reported by both observational and modeling studies [*Walterscheid et al.*, 2000; *Liu and Roble*, 2002; *Funke et al.*, 2010].

In order to assess the high-latitude background conditions in terms of temperature and wind during the events in our observational windows during the SSW events of the past four years, thermospheric kinetic temperature data from SABER instrument on-board TIMED satellite and meridional wind from TIDI have been retrieved and are shown in Figure 6.4(b). The details of SABER temperature and TIDI wind are given in section 2.5.3. The kinetic temperature (data version: V1.07) is retrieved from the atmospheric 15 μm CO_2 limb emission. From 75 to 95 km altitudes in the winter polar region the error in kinetic temperature is ±1-2 K at altitudes of 100 km and above the error is ±4-5 K [*Russell III et al.*, 1999; *García-Comas et al.*, 2008]. Temperatures at the highest altitudes provided by SABER at around 120 km (average of 118 to 120 km) in the 60° to 85° N latitude & 20° to 140° E longitude bin are considered here. It can be seen that there is a signature of increase in lower thermospheric (120 km altitude) temperature during the SSW events of the years 2010 (DOY 42), 2011 (DOY 32), 2012 (DOY 16), and 2013 (DOY 18) by about 15, 15, 20, and 25 K, respectively, with respect to their pre-enhancement mean values of 465, 465, 475, and 485 K. The day of occurrence of these enhancements are indicated by vertical dashed lines in Figures 6.1, 6.4, and 6.5. The enhancements other than those marked by dashed vertical lines are due to geomagnetic storms as can be verified from the Dst index in Figure 6.1(c). One can note from the 2012 data that the magnitude of the lower thermospheric temperature enhancement due to SSW is comparable with that due to moderate geomagnetic storm on DOY 22 but the former is for longer duration. This suggests that the effect on upper atmosphere due to such dynamical changes in the MLT region during SSW duration can be higher or comparable in magnitude to that of moderate geomagnetic storms as the former lasts for longer duration.

Panel (b) of Figure 6.4 also show zonal mean (averaged over 0° to 360° longitudes) meridional winds (data level: 3, version: 10) in the MLT altitude (a representative height of 95 km is shown here) in the 60° to 80° N latitude region obtained by TIDI. The zonally averaged winds have errors of ±7 ms^{-1} and ±15 ms^{-1} during day and night, respectively. The details of the TIDI instrument and method of derivation of winds can be obtained from *Killeen et al.* [2006]. One may note that the meridional winds in Figure 6.4(b) are equatorward during the SSW events. This behavior of the wind has been observed in the whole MLT region (85-115 km), however, only a representative behavior at 95 km is shown here, as data availability is greater around this altitude level. One can note that the meridional wind in Figure 6.4(b[1]) starts becoming equatorward from DOY 21 while the stratospheric temperature shown in Figure 6.1(a[1]) started to rise from DOY 28. This seems to be consistent with previous studies [e.g., *Liu and Roble*, 2002;

Funke et al., 2010], which showed signature of the SSW much earlier in the mesospheric parameters than in those of stratosphere. It has been noted that during SSW events while the high-latitude MLT wind is equatorward for several days the lower-thermospheric temperature enhancement, on the other hand, persists only for a few days. The reason for this is not known, however, one of the possibilities may be that the lower thermospheric temperature enhancement occurs above the current highest altitude (of 120 km) that is obtainable by SABER.

To ascertain the existence of such equatorward wind in the whole northern hemisphere MLT region during SSW events, TIMED zonal mean zonal wind and temperature have been organized in 20° latitude bins for the four years of interest and are presented in Figure 6.5 at different latitude bins (0° - 20°, 20° - 40°, 40° - 60°, and 60° - 80° N). As that of Figure 6.4, here also, the temperature corresponds to about 119 km and meridional wind to 95 km altitude. It can be noted that the lower thermospheric temperatures are higher over high-latitudes as compared to those at low-latitudes with a clear latitudinal gradient in all the years indicating that the conditions are favorable for an equatorward wind circulation. Correspondingly, it may be noted that the meridional wind is equatorward from high-to-low latitudes. Further, it is seen that the equatorward wind in the MLT region becomes weaker from high- to low-latitudes. This could be due to the fact that the source of disturbance is in high-latitudes and also the Coriolis acceleration may enhance the zonal component of the equatorward wind at the cost of the meridional component as it approaches towards low-latitudes. The exact explanation for this is still open and will need precise measurements of mesosphere-thermosphere temperature and wind during SSW events for this. Nevertheless, due to the presence of such high-to-low latitude winds in the MLT region the dominant species in the lower thermosphere (oxygen) is transported towards low-latitudes due to wind-induced diffusion and advection [*Mayer et al.*, 1978]. At latitudes below 40° the winds are very low, so advective transport may play an important role there. The latitudinal characteristics and strength of such circulation depends on the magnitude of the SSW-time equatorward meridional wind, season, and Coriolis acceleration in the MLT region.

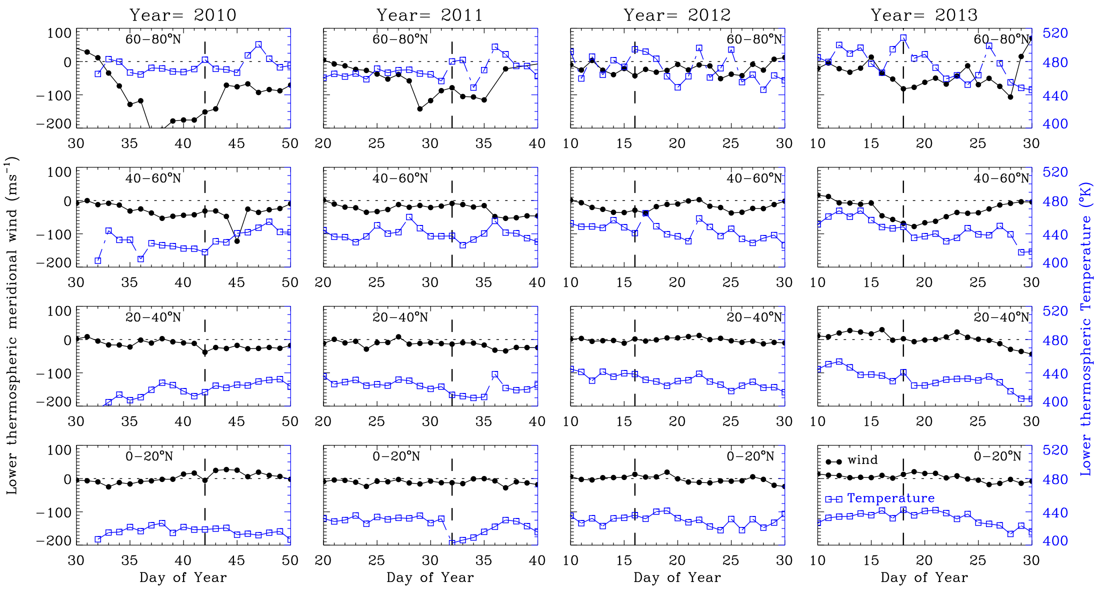

Figure 6.5: Longitudinally averaged TIMED Doppler interferometer (TIDI) measured meridional winds (positive for poleward) at 95 km and SABER measured temperatures at lower thermospheric heights (118-120 km), and at 20° latitude bins (0° to 20°, 20° to 40°, 40° to 60°, and 60° to 80° N) are shown. One can note that the winds are equatorward (negative) during the SSW events in all the years. One can also note that the temperatures are higher over high-latitudes compared to the low-latitudes with a clear latitudinal gradient in all the years, with commensurate equatorward meridional winds.

Due to the meridional wind-circulation as described above, the oxygen rich air through the lower thermosphere reaches the low-latitudes where it is superposed with SSW-time enhanced tides, daytime lower-thermospheric upward winds [*Roble*, 1977], thereby giving rise to enhancements in emissions at all the three wavelengths that emanate from varying heights. At higher altitudes these winds merge with the seasonal (hotter to cooler or south to north) trans-equatorial wind [*Mayer et al.*, 1978]. Photochemical modeling studies of airglow show that an increase in oxygen density contributes positively to an enhancement in the oxygen dayglow emission intensities [*Melndez-Alvira et al.*, 1995; *Pallamraju et al.*, 2004]. Thus, this transport of oxygen rich air from high-latitudes does seem plausible to explain the enhancement in the observed daytime oxygen airglow intensities obtained over low-latitudes during SSW periods.

Liu and Roble [2002] used Thermosphere, Ionosphere, Mesosphere, and Electrodynamics General Circulation Model/Climate Community Model version 3 (TIME-GCM/CCM3) and demonstrated a depletion of atomic oxygen number density at around 100 km altitude over high-and-mid latitudes and enhancement over low-latitudes for a self-consistently simulated SSW event. Figures 14b and 14c of their work are reproduced here as Figure 6.6. In their simulation the stratospheric warming started on day 13 and peaked on day 25. They showed that the latitudinal distribution of the relative changes of atomic oxygen column density and height integrated green line emission rate at local midnight averaged between day 10 and day 25 show a decrease at arctic-latitudes and an increase around 20° N latitude (as can be seen in Figure 6.6(b)). It is notable that our dayglow observations are also obtained over a region at around 20° N latitudes. Thus, the modeling study, in a way, provides credence to our inference on the presence of oxygen emission intensities over low-latitudes. However, our results show enhancement in oxygen dayglow emission intensities, not only at OI 557.7 nm, as predicted by TIME-GCM/CCM3 model simulation results by *Liu and Roble* [2002], but also at the emissions (OI 630.0 and OI 777.4, which were not modelled earlier) that emanate at higher altitudes. Thus, the modeling result of *Liu and Roble* [2002] supports our proposition of the mesosphere-thermosphere meridional circulation during SSW events.

Further, the argument of depletion of oxygen in the lower thermosphere over high-latitudes is also supported by the observation of oxygen dayglow emissions over high-latitudes from WINDII [*Shepherd and Shepherd*, 2011]. In that study, the OI 557.7 nm dayglow volume emission rate above 140 km over 50° to 70° N latitudes were found to be depleted during the SSW event of February 1993. Moreover, by using whole atmosphere general circulation model *Fuller-Rowell et al.* [2011] showed a possible global upper thermospheric warming and density increase by 5% during SSW event of January 2009. Thus, the current study provides experimental evidence to the numerical studies that alluded to thermospheric circulation during SSW events.

Considering the results in the present work over low-latitudes using dayglow and wind-and-temperature, in conjunction with those obtained for arctic high-

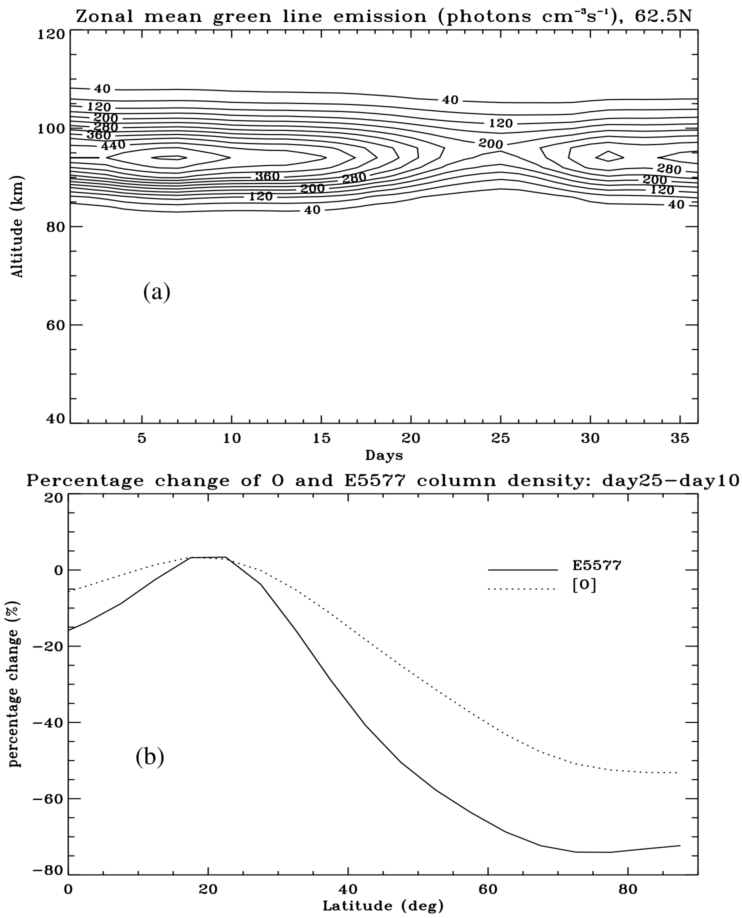

Figure 6.6: (a) Green line (557.7 nm) emission rate (photons cm^{-3}s^{-1}) at 62.5° N between day 1 and 36. (b) Latitudinal distribution of the relative changes of atomic oxygen column density (dotted line) and height integrated green line emission rate (solid line) at local midnight between day 10 and day 25. In this simulation the stratospheric warming started on day 13 and peaked on day 25. (After *Liu and Roble* [2002])

and-mid latitudes in both observational and modeling studies reported earlier, it is conjectured that a new meridional circulation in neutrals is set-up during SSW events which is responsible for the transport of oxygen to low-latitudes. This is similar (but opposite in direction) to the circulation that gets set up during SSW events in the stratosphere and lower-mesosphere that extend from pole to equator [*Andrews et al.*, 1987, p.276]. Moreover, pole to pole (winter to summer) residual circulation in the mesosphere has also been reported by *Espy* [2003] and *Cho et al.* [2011]. A simplistic schematic of the additional meridional circulation cell produced during SSW in the mesosphere-thermosphere is represented in Figure

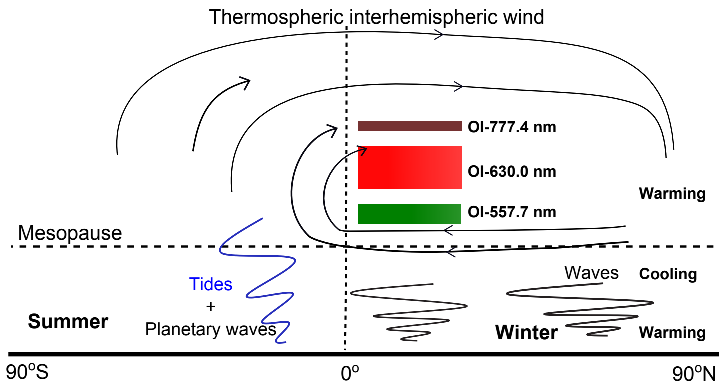

Figure 6.7: A simplistic schematic (not to scale) of the SSW-time additional meridional circulation cell that is proposed in the mesosphere-thermosphere is depicted. The lines with arrow-heads represent the direction and path of the winds. The dominant species in the lower thermosphere are transported with the wind through wind-induced diffusion. Due to this oxygen-rich air from high-to-low latitudes the low-latitude thermospheric oxygen emission intensities show enhancement for that duration. The horizontal color bars show the representative altitudes from where the oxygen emissions originate.

6.7, wherein, lines with arrow heads represent the direction and path of meridional wind. Due to such an MLT region circulation, the oxygen-rich air from high-latitudes reaches low-latitudes through the lower thermosphere where it is superposed with daytime upward winds in the lower thermosphere at low-latitudes that are also enhanced due to tidal activity during SSW, and then merges with the seasonal south-to-north trans-equatorial wind in the thermosphere. Because of such combined activity an increase in the oxygen number density over northern hemispheric low-latitudes is believed to occur which is attributed to be the cause of enhancement in the daytime optical emission intensities as reported in this study.

To the best of our knowledge, the observational evidence of setting up of the mesosphere-thermosphere meridional circulation during SSW events, as demonstrated here, has not been shown earlier. The results presented in this chapter, thus, bring to light the effect of the high-latitude stratospheric processes on the behavior of neutrals in the low-latitude thermosphere and the global-scale mesosphere-thermosphere circulation that seems to be existing during SSW events. What is reported here are the experimental observations and possible scenario of wind circulation. These results do call for more experimental observations of winds and temperatures in the mesosphere-thermosphere region and theoretical investigations to ascertain the intricacies of such feature. Detailed time-dependent physics-based modeling studies are also required to bring out all the effects that are associated with the SSW events globally.

6.5 Summary

The SSW events during the relatively low-and-moderate solar activity period of 2010 to 2013 are studied wherein, systematic investigation of their effect on low-latitude upper atmosphere is carried out using oxygen dayglow emission intensities at 557.7, 630.0, and 777.4 nm wavelengths. All these emissions are found to be enhanced within the SSW event durations in all these years. The enhancement in dayglow emission intensities in the case of the major warming in 2013 is found to be higher compared to the minor warming in 2011, suggesting that the optical emission enhancements over low-latitudes are influenced by SSW strength. SABER-measured lower thermospheric temperatures over high-latitudes were found to be enhanced during all the SSW events. These temperatures also show higher magnitudes over high-latitudes in comparison with those at low-latitudes, suggesting the existence of favorable condition to drive the winds towards low-latitudes. Independently measured meridional winds at MLT altitudes over arctic-latitudes by TIDI do confirm the existence of equatorward winds. Therefore, it is proposed that a meridional circulation in lower thermospheric winds is set up over arctic-latitudes which transports atomic oxygen towards low-latitudes during the SSW events. This redistribution of oxygen brought in due to this circulation is believed to be the cause of systematic enhancement in the dayglow emission intensities observed over low-latitudes. The current study is an experimental evidence to such circulation alluded to by numerical simulation studies carried out earlier for SSW events. This study also reveals the significance of the influence of the high-latitude stratospheric phenomena on the low latitude thermospheric behavior.

Chapter 7

Summary and Future Scope

7.1 Summary

The upper atmosphere of the Earth is influenced by incoming solar radiation and by waves from the lower atmosphere. In this thesis, coupling of the atmospheres has been studied wherein these two forcings have been considered. The main data set that has been used in this work has been obtained using Multiwavelength Imaging Spectrograph using Echelle-grating (MISE) [*Pallamraju et al.*, 2013]. MISE is a unique instrument capable of obtaining daytime sky spectra at high spectral resolutions which can be used to derive oxygen dayglow emission intensities at 557.7 nm, 630.0 nm, and 777.4 nm wavelengths. The details of MISE and the oxygen dayglow emission extraction procedures are explained in Chapter 2. In addition to dayglow emission intensity data, the equatorial electrojet (EEJ), the total electron content (TEC), the zonal mean wind and temperature data from stratosphere to lower thermosphere have been used in this study.

In this thesis work, it has been shown that the lower atmospheric influence on the upper atmosphere through waves is affected by the incident solar fluxes as the latter alters the atmospheric background condition, on which wave propagation and dissipation depend. In this regard, from investigations of oscillations of planetary wave regime at three different levels of solar activity, it has been shown that the vertical coupling of atmospheres through these large-scale waves is solar activity dependent. The oscillations in the gravity wave regime are also found to be present in higher numbers in the thermosphere during high solar activity, which is attributed to be due to reduction in dissipation during higher solar activity epoch. Further, the vertical coupling during Sudden Stratospheric Warming (SSW) events has been found to be dependent on the strength of SSW. Results reported earlier had shown that dynamical (vertical) coupling of the atmospheres during high-level of solar activity is weak. In this investigation we proposed and showed evidences that if an SSW event occurs during high solar activity epoch then the additional energy from the SSW event enhances the vertical coupling. In an another result using both ground- and satellite-based remote sensing measurements obtained during SSW events, the formation of a new circulation cell in the mesosphere-thermosphere system has been proposed based on our optical data set and with supporting satellite-based datasets on winds and temperatures in lower thermospheric altitudes.

Here, we briefly summarize the results obtained on the questions that we set out to answer in this thesis work (as given in section 1.8).

a) *How do the lower atmospheric waves influence the upper atmosphere and does the solar influence affect this coupling?*

   Answers to this question are detailed in *Chapter 4* wherein, we showed that the lower atmospheric influences on the upper atmosphere is stronger during the low solar activity period of 2011 compared to that of the high solar activity period of 2001. Based on the presence of PWs on the atmospheric parameters (dayglow, EEJ, TEC, and lower atmospheric zonal wind) and on the level of solar activity during three different phases, it has been proposed that: (i) the effect on upper atmospheric dynamics due to lower atmosphere exists during low solar activity period until the period when the average sunspot number (SSN) is ≤ 35, (ii) there is a transition from the lower atmospheric forcing to mixed behavior between average SSNs of 35 to 52, and (iii) another transition from mixed effect to those purely of solar origin occurs between SSN values of 52 to 123 [*Laskar et al.*, 2013]. Also, the gravity waves have been found to be present in higher numbers in the thermosphere during high solar activity compared to that at low solar activity level, which is due to the decrease in the wave dissipation during high solar activity epochs [*Laskar et al.*, 2015].

b) *How does the low-latitude ionosphere respond to the PW effects that exist during SSW events and does solar forcing has any role to play in this regard?*

The results discussed in *Chapter 5* provide answer to this question. Using the EEJ strength and the TEC data sets collected over a period of nearly a decade (2005 to 2013) we found that the most dominant planetary wave during SSW event is the quasi-16-day (Q16D) wave. The spectral characteristics of this Q16D wave and semi-diurnal tides have been investigated in the EEJ and TEC data sets. It has been observed that the spectral powers of Q16D waves are very high during the three very strong SSW events in the years 2006, 2009, and 2013 in comparison with those in other years. Also, the spectral powers of Q16D waves have been found to vary in similar fashion as that of the arctic-latitude stratospheric temperature enhancement. For these three major events, the amplitudes of the semi-diurnal tides and Q16D waves were found to be highly correlated and were maximum around the peak of SSW suggesting a strong interaction between the two waves. For the case of the minor events, however, this correlation was found to be poor and the Q16D spectral power was low. In spite of higher solar activity level, a strong coupling of atmospheres was noted during the 2013 SSW event, which was, however, explained to be due to the influence of the strong SSW event. These results suggest that the vertical coupling of atmospheres is stronger during strong major SSW events and they play an important role in enabling this coupling even during high solar activity epochs[*Laskar et al.*, 2014].

c) *Does SSW events influence the general circulation in the thermosphere?*

We have addressed this issue in *Chapter 6*. In that chapter we have considered four sudden stratospheric warming (SSW) events that occurred in the years 2010 to 2013. The multiwavelength thermospheric oxygen dayglow emissions over a low-latitude location showed systematic enhancement in intensities throughout the daytime hours during these SSW events. The northern hemispheric high-latitude temperatures obtained by SABER at 120 km altitude show a latitudinal gradient with a decrease in lower thermospheric temperature towards low-latitudes. Simultaneously, the TIDI winds showed equatorward motion in the mesosphere-lower-thermosphere (MLT) altitudes during these events. Both, the high-latitude lower thermospheric temperature enhancements, and the MLT region equatorward winds, occur simultaneously with the observed enhancements in the oxygen dayglow emission intensities at all the three wavelengths. Based on these measurements and other supporting information it is proposed that a new cell of meridional circulation in the MLT winds is set up during SSW events, which enables transport of atomic oxygen from high-to-low latitudes. Such an additional contribution of oxygen number density over low-latitudes interacts with lower thermospheric daytime dynamics in that region and is attributed to be the cause of the observed enhancement in the oxygen daytime optical emission intensities over low-latitudes. The results presented in this chapter provide experimental evidence to such a circulation alluded to by earlier simulation studies [*Laskar and Pallamraju*, 2014].

7.2 Future Scope

The results presented in this thesis are an effort to investigate the coupling of different altitude and latitude regions of the Earth's atmosphere at varying levels of solar activity. Through this work a significant understanding has been gained in terms of vertical coupling of the atmospheres during epochs of different levels of solar activity. Moreover, these results show a great potential in quantifying the couplings.

In terms of experiments, systematic measurement of the three oxygen emissions presented in this work along with other lower atmospheric, mesospheric, ionospheric, and thermospheric parameters over long durations will add to our current understanding and enable more accurate quantification of the upper atmospheric behavior with solar activity. In terms of modeling, it is possible to incorporate the present results in the dynamical atmospheric models to both reproduce the observations and also enabling prediction/estimation of such a behavior in different scenarios.

The zonal and meridional wind measurements in the mesosphere (through high-frequency or partial reflection radars) and thermospheric wind (through Fabry-Perot interferometers and in situ probes on-board satellites) are required to quantify the effect of the lower atmospheric waves on the mean flow. Again, long-term data sets over varying levels of solar activity would enable one to quantify the relative importance of the solar and lower atmospheric forcing.

In the present work, we showed the interaction between the two most dominant waves in the tidal (semidiurnal) and planetary wave (quasi-16-day) domains. In addition to these two, there are other waves that do have non-negligible impact on the upper atmosphere through their interaction with waves and with the mean flow. A detailed investigation on all such waves would significantly augment our understanding of the coupling processes with greater accuracies. Particularly, the interaction of the waves with mean flow can enhance and or dissipate waves and thus, a study on the characterization of waves along with measurement of the mean flow would yield new results.

Here, in this study we presented the frequency response of the gravity waves and their variation with solar activity and with altitudes. Similar study can be carried out for the scale-size distribution with multiwavelength airglow measurements at large view angles or from multiple stations. Also, the dominant scale or horizontal and vertical wavelength modes that are present at various altitudes can be explored.

In the current thesis work based on our optical observations and complementary data on MLT temperature and winds we have proposed the setting up of mesospheric and thermospheric meridional circulation cell during SSW events. Introduction of proper parameters that considers this circulation cell in the upper atmospheric global circulation models will be useful in order to represent the upper atmospheric dynamics more accurately.

"Now this is not the end

It is not even the beginning of the end

But it is, perhaps, the end of the beginning."

–Sir Winston Churchill (1942).

Bibliography

Abdu, M. A., T. K. Ramkumar, I. S. Batista, C. G. M. Brum, H. Takahashi, B. Reinisch, and J. Sobral (2006), Planetary wave signatures in the equatorial atmosphere-ionosphere system, and mesosphere- E- and F-region coupling, *J. Atmos. Sol. Terr. Phys.*, *68*(3-5), 509 – 522, doi:10.1016/j.jastp.2005.03.019.

Anandarao, B. G., and R. Raghavarao (1987), Structural changes in the currents and fields of the equatorial electrojet due to zonal and meridional winds, *J. Geophys. Res.*, *92*(A3), 2514, doi:10.1029/ja092ia03p02514.

Anderson, D. N. (1973), A theoretical study of the ionospheric F region equatorial anomaly —I. Theory, *Planetary and Space Science*, *21*(3), 409–419, doi:10.1016/0032-0633(73)90040-8.

Andrews, D. G. (2010), *An Introduction to Atmospheric Physics*, Cambridge University Press.

Andrews, D. G., J. R. Holton, and C. B. Leovy (1987), *Middle Atmosphere Dynamics*, 489 pp., Academic Press.

Appleton, E. V. (1946), Two Anomalies in the Ionosphere, *Nature*, *157*(3995), 691–691, doi:10.1038/157691a0.

Bagiya, M. S., H. P. Joshi, K. N. Iyer, M. Aggarwal, S. Ravindran, and B. M. Pathan (2009), TEC variations during low solar activity period (2005-2007) near the Equatorial Ionospheric Anomaly Crest region in India, *Ann. Geophys.*, *27*(3), 1047–1057, doi:10.5194/angeo-27-1047-2009.

Bagiya, M. S., et al. (2014), Effects of prolonged southward interplanetary magnetic field on low-latitude ionospheric electron density, *J. Geophys. Res. Space Physics*, *119*(7), 5764–5776, doi:10.1002/2014JA020156.

Baker, D. J., and G. J. Romick (1976), The rayleigh: interpretation of the unit in terms of column emission rate or apparent radiance expressed in SI units., *Appl. Opt.*, *15*(8), 1966–8, doi:10.1364/AO.15.001966.

Baluja, K. L., and C. J. Zeippen (1988), M1 and E2 transition probabilities for states within the $2p^4$ configuration of the O I isoelectronic sequence, *J. Phys. B At. Mol. Opt. Phys.*, *21*(9), 1455–1471, doi:10.1088/0953-4075/21/9/007.

Barmore, F. E. (1977), High resolution observations of the 6300 $\AA$ oxygen line in the day airglow, *Planet. Space Sci.*, *25*(2), 185–191, doi:10.1016/0032-0633(77)90023-X.

Barth, C. A., and A. F. Hildebrandt (1961), The 5577 $\AA$ airglow emission mechanism, *J. Geophys. Res.*, *66*(3), 985–986, doi:10.1029/JZ066i003p00985.

Basu, S. (2005), Two components of ionospheric plasma structuring at midlatitudes observed during the large magnetic storm of October 30, 2003, *Geophys. Res. Lett.*, *32*(12), doi: 10.1029/2004gl021669.

Beer, T. (1974), *Atmospheric Waves*, Wiley.

Bens, A. R., L. L. Cogger, and G. G. Shepherd (1965), Upper atmospheric temperatures from Doppler line widths-III: Observation of the OI dayglow emission at 6300 $\AA$, *Planet. Space Sci.*, *13*(6), 551–563, doi:10.1016/0032-0633(65)90168-6.

Bevington, P. R., and D. K. Robinson (2003), *Data reduction and error analysis for the physical sciences*, 320 pp., McGraw-Hill.

Biondi, M. A., and D. P. Sipler (1985), Horizontal and vertical winds and temperatures in the equatorial thermosphere: Measurements from Natal, Brazil during AugustSeptember 1982, *Planet. Space Sci.*, *33*(7), 817–823, doi:10.1016/0032-0633(85)90035-2.

Bošková, J., and J. Laštovička (2001), Seasonal Variation of Gravity Wave Activity in the Lower Ionosphere in Central Europe, *Stud. Geophys. Geod.*, *45*(1), 85–92, doi:10.1023/A: 1021706615038.

Bretherton, F. P. (1969), Momentum transport by gravity waves, *Q.J Royal Met. Soc.*, *95*(404), 213–243, doi:10.1002/qj.49709540402.

Chakrabarti, S., D. Pallamraju, and J. Baumgardner (2001), HiTIES: A High Throughput Imaging Echelle Spectrogragh for ground-based visible airglow and auroral studies, *J. Geophys. Res.*, *106*(A12), 30,337–30,348.

Chakrabarti, S., O.-P. Jokiaho, J. Baumgardner, T. Cook, J. Martel, and M. Galand (2012), High-throughput and multislit imaging spectrograph for extended sources, *Optical Engineering*, *51*(1), 013,003–1–013,003–6, doi:10.1117/1.OE.51.1.013003.

Chakrabarty, D. (2004), Thermospheric gravity wave modes over low and equatorial latitudes during daytime, *J. Geophys. Res.*, *109*(A12), A12,309, doi:10.1029/2003JA010169.

Chakrabarty, D., R. Sekar, R. Narayanan, C. V. Devasia, and B. M. Pathan (2005), Evidence for the interplanetary electric field effect on the OI 630.0 nm airglow over low latitude, *J. Geophys. Res.*, *110*(A11), doi:10.1029/2005JA011221.

Chakrabarty, D., R. Sekar, J. H. Sastri, and S. Ravindran (2008), Distinctive effects of interplanetary electric field and substorm on nighttime equatorial F layer: A case study, *Geophys. Res. Lett.*, *35*(19), doi:10.1029/2008gl035415.

Chamberlain, J. W. (1961), *Physics of the Aurora and Airglow*, 704 pp., Academic Press.

Chandra, H., and R. G. Rastogi (1974), Geomagnetic storm effects on ionospheric drifts and the equatorial Es over the magnetic equator, *Indian J. Radio Sp. Phys.*, *3*, 332–336.

Chandran, A., R. R. Garcia, R. L. Collins, and L. C. Chang (2013), Secondary planetary waves in the middle and upper atmosphere following the stratospheric sudden warming event of January 2012, *Geophys. Res. Lett.*, *40*(9), 1861–1867, doi:10.1002/grl.50373.

Chapman, S. (1931), Bakerian Lecture. Some Phenomena of the Upper Atmosphere, *Proc. R. Soc. London. Ser. A*, *132*(820), 353–374, doi:10.1098/rspa.1931.0105.

Charlton, A. J., and L. M. Polvani (2007), A new look at stratospheric sudden warmings. Part I: Climatology and modeling benchmarks, *Journal of Climate*, *20*(3), 449–469.

Charney, J. G., and P. G. Drazin (1961), Propagation of planetary-scale disturbances from the lower into the upper atmosphere, *J. Geophys. Res.*, *66*(1), 83–109, doi:10.1029/JZ066i001p00083.

Chau, J. L., B. G. Fejer, and L. P. Goncharenko (2009), Quiet variability of equatorial E×B drifts during a sudden stratospheric warming event, *Geophys. Res. Lett.*, *36*(5), doi:10.1029/2008GL036785.

Chau, J. L., L. P. Goncharenko, B. G. Fejer, and H.-L. Liu (2012), Equatorial and low latitude ionospheric effects during sudden stratospheric warming events, *Space Sci. Rev.*, *168*, 385–417, doi:10.1007/s11214-011-9797-5.

Chen, F. F. (1984), *Introduction to Plasma Physics and controlled fusion, 2nd edition*, 421 pp., Springer.

Cho, Y.-M., G. G. Shepherd, M. G. Shepherd, W. K. Hocking, N. J. Mitchell, and Y.-I. Won (2011), A study of temperature and meridional wind relationships at high northern latitudes, *J. Atmos. Sol. Terr. Phys.*, *73*(9), 936 – 943, doi:10.1016/j.jastp.2010.08.011.

Christensen, A. B., M. H. Rees, G. J. Romick, and G. G. Sivjee (1978), Oi (7774 å) and oi (8446 å) emissions in aurora, *Journal of Geophysical Research: Space Physics*, *83*(A4), 1421–1425, doi:10.1029/JA083iA04p01421.

Cocks, T. D., and F. Jacka (1979), Daytime thermospheric temperatures, wind velocities and emission intensities derived from ground based observations of the OIλ630 nm airglow line profile, *J. Atmos. Terr. Phys.*, *41*(4), 409–415.

Conde, M., P. Greet, and F. Jacka (1992), The ring effect in the sodium D2 Fraunhofer line of day skylight over Mawson, Antarctica, *J. Geophys. Res.*, *97*(D11), 11,561, doi:10.1029/92JD00768.

Culot, F., C. Lathuillere, J. Lilensten, and O. Witasse (2004), The OI 630 . 0 and 557 . 7 nm dayglow measured by WINDII and modeled by TRANSCAR, *Ann. Geophys.*, *22*, 1947–1960.

Culot, F., C. Lathuillre, and J. Lilensten (2005), Influence of geomagnetic activity on the OI 630.0 and 557.7 nm dayglow, *J. Geophys. Res.*, *110*(A1), doi:10.1029/2004JA010667.

Daubechies, I. (1988), Orthonormal bases of compactly supported wavelets, *Commun. Pure Appl. Math.*, *41*(7), 909–996, doi:10.1002/cpa.3160410705.

Delbouille, L., L. Neven, and G. Roland (1973), *Photometric Atlas of the Solar Spectrum from Lambda 3000 to Lambda 10000: 2994-6455*, v. 1, Inst. d'Astrophysique de L'Univ.

Doering, J. P., and E. E. Gulcicek (1989), Absolute differential and integral electron excitation cross sections for atomic oxygen 7. The $^3P \rightarrow {}^1D$ and $^3P \rightarrow {}^1S$ transitions from 4.0 to 30 eV, *Journal of Geophysical Research: Space Physics*, *94*(A2), 1541–1546, doi:10.1029/JA094iA02p01541.

Espy, P. J. (2003), Rapid, large-scale temperature changes in the polar mesosphere and their relationship to meridional flows, *Geophys. Res. Lett.*, *30*(5), 1240, doi:10.1029/2002GL016452.

Espy, P. J., and G. Witt (1996), Observation of a quasi 16-day oscillation in the polar summer mesospheric temperature, *Geophys. Res. Lett.*, *23*(10), 1071–1074, doi:10.1029/96GL01068.

Farge, M. (1992), Wavelet transforms and their applications to turbulence, *Annu. Rev. Fluid Mech.*, *24*(1), 395–458.

Farley, D. T. (1960), A theory of electrostatic fields in the ionosphere at nonpolar geomagnetic latitudes, *J. Geophys. Res.*, *65*(3), 869–877, doi:10.1029/JZ065i003p00869.

Fejer, B. G. (2011), Low latitude ionospheric electrodynamics, *Space Sci. Rev.*, *158*, 145–166, doi:10.1007/s11214-010-9690-7.

Fejer, B. G., and L. Scherliess (1995), Time dependent response of equatorial ionospheric electric fields to magnetospheric disturbances, *Geophys. Res. Lett.*, *22*(7), 851–854, doi:10.1029/95GL00390.

Fejer, B. G., M. E. Olson, J. L. Chau, C. Stolle, H. Lühr, L. P. Goncharenko, K. Yumoto, and T. Nagatsuma (2010), Lunar-dependent equatorial ionospheric electrodynamic effects during sudden stratospheric warmings, *J. Geophys. Res.*, *115*(A00G03), doi:10.1029/2010JA015273.

Fejer, B. G., B. D. Tracy, M. E. Olson, and J. L. Chau (2011), Enhanced lunar semidiurnal equatorial vertical plasma drifts during sudden stratospheric warmings, *Geophys. Res. Lett.*, *38*(21), doi:10.1029/2011GL049788.

Floyd, L., J. Newmark, J. Cook, L. Herring, and D. McMullin (2005), Solar EUV and UV spectral irradiances and solar indices, *J. Atmos. Sol. Terr. Phys.*, *67*(1-2), 3–15, doi:10.1016/j.jastp.2004.07.013.

Forbes, J. M. (1982), Atmospheric tides: 1. Model description and results for the solar diurnal component, *J. Geophys. Res.*, *87*(A7), 5222–5240.

Forbes, J. M. (1995), Tidal and planetary waves, *The Upper Mesosphere and Lower Thermosphere: A Review of Experiment and Theory, Geophys. Monogr. Ser*, *87*, 67–87.

Forbes, J. M., and H. B. Garrett (1979), Theoretical studies of atmospheric tides, *Rev. Geophys.*, *17*(8), 1951, doi:10.1029/rg017i008p01951.

Forbes, J. M., and S. Leveroni (1992), Quasi 16-day oscillation in the ionosphere, *Geophys. Res. Lett.*, *19*(10), 981–984.

Frederick, J. E., D. W. Rusch, G. A. Victor, W. E. Sharp, P. B. Hays, and H. C. Brinton (1976), The O I (λ5577 Å) airglow: Observations and excitation mechanisms, *J. Geophys. Res.*, *81*(22), 3923–3930, doi:10.1029/JA081i022p03923.

Fritts, D. C. (1984), Gravity wave saturation in the middle atmosphere: A review of theory and observations, *Rev. Geophys.*, *22*(3), 275–308.

Fritts, D. C., and M. J. Alexander (2003), Gravity wave dynamics and effects in the middle atmosphere, *Rev. Geophys.*, *41*(1), 1003, doi:10.1029/2001RG000106.

Fritts, D. C., and S. L. Vadas (2008), Gravity wave penetration into the thermosphere: sensitivity to solar cycle variations and mean winds, *Ann. Geophys.*, *26*(12), 3841–3861, doi:10.5194/angeo-26-3841-2008.

Fuller-Rowell, T., R. Akmaev, F. Wu, M. Fedrizzi, R. A. Viereck, and H. Wang (2011), Did the January 2009 sudden stratospheric warming cool or warm the thermosphere?, *Geophys. Res. Lett.*, *38*(18), doi:10.1029/2011GL048985.

Funke, B., M. Lpez-Puertas, D. Bermejo-Pantalen, M. Garca-Comas, G. P. Stiller, T. von Clarmann, M. Kiefer, and A. Linden (2010), Evidence for dynamical coupling from the lower atmosphere to the thermosphere during a major stratospheric warming, *Geophys. Res. Lett.*, *37*(13), doi:10.1029/2010GL043619.

Galand, M., J. Baumgardner, D. Pallamraju, S. Chakrabarti, U. P. Lvhaug, D. Lummerzheim, B. S. Lanchester, and M. H. Rees (2004), Spectral imaging of proton aurora and twilight at Tromso, Norway, *J. Geophys. Res.*, *109*(A7), doi:10.1029/2003JA010033.

García-Comas, M., et al. (2008), Errors in Sounding of the Atmosphere using Broadband Emission Radiometry (SABER) kinetic temperature caused by non-local-thermodynamic-equilibrium model parameters, *J. Geophys. Res.*, *113*(D24), D24,106, doi:10.1029/2008JD010105.

Gerrard, A. J., and J. W. Meriwether (2011), Initial daytime and nighttime SOFDI observations of thermospheric winds from Fabry-Perot doppler shift measurements of the 630-nm OI line-shape profile, *Ann. Geophys.*, *29*(9), 1529–1536, doi:10.5194/angeo-29-1529-2011.

Ghil, M., et al. (2002), Advanced spectral methods for climatic time series, *Rev. Geophys.*, *40*(1), 1003.

Gilman, D. L., F. J. Fuglister, and J. M. Mitchell (1963), On the power spectrum of "red noise", *J. Atmos. Sci.*, *20*(2), 182–184, doi:10.1175/1520-0469(1963)020⟨0182:OTPSON⟩2.0.CO;2.

Goncharenko, L., J. L. Chau, P. Condor, A. Coster, and L. Benkevitch (2013a), Ionospheric effects of sudden stratospheric warming during moderate-to-high solar activity: Case study of January 2013, *Geophys. Res. Lett.*, *40*(19), 4982–4986, doi:10.1002/grl.50980.

Goncharenko, L. P., A. J. Coster, J. L. Chau, and C. E. Valladares (2010), Impact of sudden stratospheric warmings on equatorial ionization anomaly, *J. Geophys. Res.*, *115*(A10), A00G07, doi:10.1029/2010JA015400.

Goncharenko, L. P., V. W. Hsu, C. G. M. Brum, S.-R. Zhang, and J. T. Fentzke (2013b), Wave signatures in the midlatitude ionosphere during a sudden stratospheric warming of January 2010, *J. Geophys. Res. Space Physics*, *118*(1), 472–487, doi:10.1029/2012JA018251.

Goupillaud, P., A. Grossmann, and J. Morlet (1984), Cycle-octave and related transforms in seismic signal analysis, *Geoexploration*, *23*(1), 85–102, doi:10.1016/0016-7142(84)90025-5.

Grainger, J. F., and J. Ring (1962), Anomalous fraunhofer line profiles, *Nature*, *193*, 762, doi:10.1038/193762a0.

Grossmann, A., and J. Morlet (1984), Decomposition of hardy functions into square integrable wavelets of constant shape, *SIAM J. Math. Anal.*, *15*(4), 723–736, doi:10.1137/0515056.

Guberman, S. L. (1988), The production of $O(^1D)$ from dissociative recombination of O_2^+, *Planet. Space Sci.*, *36*(1), 47–53, doi:10.1016/0032-0633(88)90145-6.

Guharay, A., and R. Sekar (2012), Signature of latitudinal coupling during a major sudden stratospheric warming in the tropics, *J. Atmos. Sol. Terr. Phys.*, *75*, 122–126.

Guharay, A., P. Batista, and B. Clemesha (2014), On the variability of the seasonal scale oscillations over Cachoeira Paulista (22.7S, 45W), Brazil, *Earth Planets Space*, *66*(1), 45, doi:10.1186/1880-5981-66-45.

Gurtner, W. (1993), The receiver independent exchange format version, http://igscb.jpl.nasa.gov:80/igscb/data/format/rinex2.txt.

Gurubaran, S., S. Sridharan, T. Ramkumar, and R. Rajaram (2001), The mesospheric quasi-2-day wave over Tirunelveli (8.7°N), *J. Atmos. Sol. Terr. Phys.*, *63*(10), 975–985, doi:10.1016/S1364-6826(01)00016-5.

Haar, A. (1910), Zur Theorie der orthogonalen Funktionensysteme, *Math. Ann.*, *69*(3), 331–371, doi:10.1007/BF01456326.

Hagan, M. E., R. G. Roble, and J. Hackney (2001), Migrating thermospheric tides, *J. Geophys. Res.*, *106*(A7), 12,739, doi:10.1029/2000ja000344.

Hargreaves, J. K. (1992), *The Solar-Terrestrial Environment*, Cambridge University Press.

Harris, R., and R. G. Mach (2007), The GPSTk: an open source GPS toolkit, *GPS Solutions*, *11*, 145–150, doi:10.1007/s10291-006-0043-7.

Hays, P. B., and W. E. Sharp (1973), Twilight airglow: 1. Photoelectrons and [O I] 5577-Angstrom radiation, *J. Geophys. Res.*, *78*(7), 1153–1166, doi:10.1029/JA078i007p01153.

Hays, P. B., G. Carignan, B. C. Kennedy, G. G. Shepherd, and J. C. G. Walker (1973), The visible-airglow experiment on atmosphere explorer, *Radio Science*, *8*(4), 369–377, doi:10.1029/RS008i004p00369.

Hays, P. B., V. J. Abreu, M. E. Dobbs, D. A. Gell, H. J. Grassl, and W. R. Skinner (1993), The high-resolution doppler imager on the upper atmosphere research satellite, *J. Geophys. Res.*, *98*(D6), 10,713–10,723, doi:10.1029/93JD00409.

Heelis, R. A., P. C. Kendall, R. J. Moffett, D. W. Windle, and H. Rishbeth (1974), Electrical coupling of the E- and F-regions and its effect on F-region drifts and winds, *Planet. Space Sci.*, *22*(5), 743–756, doi:10.1016/0032-0633(74)90144-5.

Heelis, R. A., G. Crowley, F. Rodrigues, A. Reynolds, R. Wilder, I. Azeem, and A. Maute (2012), The role of zonal winds in the production of a pre-reversal enhancement in the vertical ion drift in the low latitude ionosphere, *J. Geophys. Res.*, *117*(A8), A08,308, doi:10.1029/2012JA017547.

Hernandez, G. (1971), The signature profiles of $O(^1S)$ in the airglow, *Planet. Space Sci.*, *19*(5), 467–476, doi:10.1016/0032-0633(71)90162-0.

Hines, C. O. (1960), Internal atmospheric gravity waves at ionospheric heights, *Can. J. Phys.*, *38*, 1441.

Hines, C. O. (1973), A critique of multilayer analyses in application to the propagation of acoustic-gravity waves, *J. Geophys. Res.*, *78*(1), 265–273, doi:10.1029/JA078i001p00265.

Hines, C. O. (1991), The Saturation of Gravity Waves in the Middle Atmosphere. Part I: Critique of Linear-Instability Theory, *J. Atmos. Sci.*, *48*(11), 1348–1360, doi:10.1175/1520-0469(1991)048⟨1348:TSOGWI⟩2.0.CO;2.

Hirota, I. (1984), Climatology of gravity waves in the middle atmosphere, *J. Atmos. Terr. Phys.*, *46*(9), 767–773, doi:10.1016/0021-9169(84)90057-6.

Hocke, K. (1998), Phase estimation with the Lomb-Scargle periodogram method, *Ann. Geophys.*, *16*(3), 356–358.

Hocke, K., and K. Schlegel (1996), A review of atmospheric gravity waves and travelling ionospheric disturbances: 1982-1995, *Ann. Geophys.*, *14*, 917–940, doi:10.1007/s00585-996-0917-6.

Hoffmann, P., M. Rapp, W. Singer, and D. Keuer (2011), Trends of mesospheric gravity waves at northern middle latitudes during summer, *J. Geophys. Res.*, *116*, D00P08, doi:10.1029/2011JD015717.

Holton, J. R. (1980), The Dynamics of Sudden Stratospheric Warmings, *Annu. Rev. Earth Planet. Sci.*, *8*(1), 169–190, doi:10.1146/annurev.ea.08.050180.001125.

Holton, J. R. (2004), *An Introduction to Dynamic Meteorology*, Academic press.

Horne, J. H., and S. L. Baliunas (1986), A prescription for period analysis of unevenly sampled time series, *Astrophys. J.*, *302*, 757–763, doi:10.1086/164037.

Immel, T. J., E. Sagawa, S. L. England, S. B. Henderson, M. E. Hagan, S. B. Mende, H. U. Frey, C. M. Swenson, and L. J. Paxton (2006), Control of equatorial ionospheric morphology by atmospheric tides, *Geophys. Res. Lett.*, *33*(15), L15,108, doi:10.1029/2006GL026161.

Izenman, A. J. (2009), J. R. Wolf and the zürich sunspot relative numbers, *Math. Intell.*, *7*(1), 27–33, doi:10.1007/BF03023002.

Jakowski, N., C. Mayer, M. M. Hoque, and V. Wilken (2011), Total electron content models and their use in ionosphere monitoring, *Radio Science*, *46*(6), doi:10.1029/2010RS004620.

Jarrett, A. H., and M. J. Hoey (1963), A ground-level photographic observation of the day airglow emission of atomic oxygen at 6300 Å, *Planet. Space Sci.*, *11*(10), 1251–1252, doi:10.1016/0032-0633(63)90256-3.

Jin, H., Y. Miyoshi, D. Pancheva, P. Mukhtarov, H. Fujiwara, and H. Shinagawa (2012), Response of migrating tides to the stratospheric sudden warming in 2009 and their effects on the ionosphere studied by a whole atmosphere-ionosphere model GAIA with COSMIC and TIMED/SABER observations, *J. Geophys. Res.*, *117*(A10), A10,323, doi: 10.1029/2012JA017650.

Jin, S. (2013), *GNSS remote sensing : theory, methods and applications*, Springer, Dordrecht.

Kalnay, E., et al. (1996), The NCEP/NCAR 40-year reanalysis project, *Bull. Amer. Meteorol. Soc.*, *77*(3), 437–471, doi:10.1175/1520-0477(1996)077⟨0437:TNYRP⟩2.0.CO;2.

Kelley, M. C. (2009), *The Earth's Ionosphere: Plasma Physics & Electrodynamics*, vol. 96, Academic press.

Killeen, T. L., et al. (1999), TIMED Doppler interferometer (TIDI), in *SPIE's Int. Symp. Opt. Sci. Eng. Instrum.*, edited by A. M. Larar, pp. 289–301, International Society for Optics and Photonics, doi:10.1117/12.366383.

Killeen, T. L., Q. Wu, S. C. Solomon, D. A. Ortland, W. R. Skinner, R. J. Niciejewski, and D. A. Gell (2006), TIMED Doppler Interferometer: Overview and recent results, *J. Geophys. Res.*, *111*(A10), doi:10.1029/2005JA011484.

Klobuchar, J. (1996), Ionospheric effects on GPS, *Global Positioning System: Theory and applications.*, *1*, 485–515.

Kovalam, S., R. Vincent, and P. Love (2006), Gravity waves in the equatorial MLT region, *J. Atmos. Sol. Terr. Phys.*, *68*(3-5), 266–282, doi:10.1016/j.jastp.2005.05.009.

Kulkarni, P. V. (1976), Rocket study of 5577 $\AA$ OI emission at night over the magnetic equator, *J. Geophys. Res.*, *81*(22), 3740–3744, doi:10.1029/JA081i022p03740.

Kuttippurath, J., and G. Nikulin (2012), A comparative study of the major sudden stratospheric warmings in the arctic winters 2003/2004 – 2009/2010, *Atmospheric Chemistry and Physics*, *12*(17), 8115–8129, doi:10.5194/acp-12-8115-2012.

Kvifte, G., and L. Vegard (1947), On the emission of the forbidden lines from the metastable ground states ^1S_o and $^1D_2$ of the neutral oxygen atom, *Geofys, Publ*, *17*, 1.

Labitzke, K. (1977), Interannual variability of the winter stratosphere in the northern hemisphere, *Mon. Wea. Rev.*, *105*(6), 762–770, doi:10.1175/1520-0493(1977)105⟨0762:IVOTWS⟩2.0.CO;2.

Lakshmi Narayanan, V., S. Gurubaran, and K. Emperumal (2010), Airglow imaging observations of small-scale structures driven by convective instability in the upper mesosphere over Tirunelveli (8.7°N), *J. Geophys. Res.*, *115*(D19), D19,119, doi:10.1029/2009JD012937.

Lanchester, B. S., M. Ashrafi, and N. Ivchenko (2009), Simultaneous imaging of aurora on small scale in OI (777.4 nm) and $N_2$1P to estimate energy and flux of precipitation, *Ann. Geophys.*, *27*(7), 2881–2891, doi:10.5194/angeo-27-2881-2009.

Laskar, F. I., and D. Pallamraju (2014), Does sudden stratospheric warming induce meridional circulation in the mesosphere thermosphere system?, *J. Geophys. Res. Space Physics*, *119*(12), 10,133–10,143, doi:10.1002/2014JA020086.

Laskar, F. I., D. Pallamraju, T. V. Lakshmi, M. A. Reddy, B. M. Pathan, and S. Chakrabarti (2013), Investigations on vertical coupling of atmospheric regions using combined multiwavelength optical dayglow, magnetic, and radio measurements, *J. Geophys. Res. Space Physics*, *118*(7), 4618–4627, doi:10.1002/jgra.50426.

Laskar, F. I., D. Pallamraju, and B. Veenadhari (2014), Vertical coupling of atmospheres: dependence on strength of sudden stratospheric warming and solar activity, *Earth, Planets and Space*, *66*(1), 94, doi:10.1186/1880-5981-66-94.

Laskar, F. I., D. Pallamraju, B. Veenadhari, T. V. Lakshmi, M. A. Reddy, and S. Chakrabarti (2015), Gravity waves in the thermosphere: Solar activity dependence, *Advances in Space Research*, *55*(6), 1651–1659, doi:10.1016/j.asr.2014.12.040.

Laštovička, J. (2009), Lower ionosphere response to external forcing: A brief review, *Adv. Sp. Res.*, *43*, 1–14, doi:10.1016/j.asr.2008.10.001.

Lean, J. (1997), The Sun's variable radiation and its relevance for Earth, *Annu. Rev. Astron. Astrophys.*, *35*(1), 33–67, doi:10.1146/annurev.astro.35.1.33.

Lindzen, R. S. (1981), Turbulence and stress owing to gravity wave and tidal breakdown, *J. Geophys. Res. Ocean.*, *86*(C10), 9707–9714.

Liu, H., E. Doornbos, M. Yamamoto, and S. Tulasi Ram (2011), Strong thermospheric cooling during the 2009 major stratosphere warming, *Geophys. Res. Lett.*, *38*(12), doi:10.1029/2011GL047898.

Liu, H.-L., and R. G. Roble (2002), A study of a self-generated stratospheric sudden warming and its mesosphericlower thermospheric impacts using the coupled TIME-GCM/CCM3, *J. Geophys. Res.*, *107*(D23), ACL 15–1–ACL 15–18, doi:10.1029/2001JD001533.

Liu, H. L., and R. G. Roble (2005), Dynamical coupling of the stratosphere and mesosphere in the 2002 southern hemisphere major stratospheric sudden warming, *Geophys. Res. Lett.*, *32*(13), L13,804, doi:10.1029/2005GL022939.

Liu, H.-L., W. Wang, A. D. Richmond, and R. G. Roble (2010), Ionospheric variability due to planetary waves and tides for solar minimum conditions, *J. Geophys. Res.*, *115*(A6), A00G01, doi:10.1029/2009JA015188.

Lomb, N. R. (1976), Least-squares frequency analysis of unequally spaced data, *Astrophys. Space Sci.*, *39*, 447–462, doi:10.1007/BF00648343.

Longuet-Higgins, M. S. (1968), The eigenfunctions of laplace's tidal equations over a sphere, *Philosophical Transactions of the Royal Society A: Mathematical, Physical and Engineering Sciences*, *262*(1132), 511–607, doi:10.1098/rsta.1968.0003.

Lorenz, E. N. (1963), Deterministic nonperiodic flow, *J. Atmos. Sci.*, *20*(2), 130–141, doi:10.1175/1520-0469(1963)020⟨0130:DNF⟩2.0.CO;2.

Luo, Y., A. H. Manson, C. E. Meek, C. K. Meyer, and J. M. Forbes (2000), The quasi 16-day oscillations in the mesosphere and lower thermosphere at Saskatoon (52 °N, 107 °W), 1980-1996, *J. Geophys. Res.*, *105*(D2), 2125, doi:10.1029/1999JD900979.

Makela, J. J., and Y. Otsuka (2011), Overview of nighttime ionospheric instabilities at low- and mid-latitudes: Coupling aspects resulting in structuring at the mesoscale, *Space. Sci. Rev.*, *168*(1-4), 419–440, doi:10.1007/s11214-011-9816-6.

Makela, J. J., J. W. Meriwether, Y. Huang, and P. J. Sherwood (2011), Simulation and analysis of a multi-order imaging Fabry–Perot interferometer for the study of thermospheric winds and temperatures, *Appl. Opt.*, *50*(22), 4403–4416, doi:10.1364/ao.50.004403.

Makela, J. J., D. J. Fisher, J. W. Meriwether, R. A. Buriti, and A. F. Medeiros (2013), Near-continual ground-based nighttime observations of thermospheric neutral winds and temperatures over equatorial Brazil from 2009 to 2012, *J. Atmos. Sol. Terr. Phys.*, *103*, 94–102, doi:10.1016/j.jastp.2012.11.019.

Mallat, S. G. (1989), A theory for multiresolution signal decomposition: the wavelet representation, *IEEE Trans. Pattern Anal. Mach. Intell.*, *11*(7), 674–693, doi:10.1109/34.192463.

Mantas, G. P., and H. C. Carlson (1991), Reexamination of the O($^3P \rightarrow {}^1D$) excitation rate by thermal electron impact, *Geophys. Res. Lett.*, *18*(2), 159–162, doi:10.1029/91GL00019.

Marshall, R. A., S. Smith, J. Baumgardner, and S. Chakrabarti (2011), Continuous ground-based multiwavelength airglow measurements, *J. Geophys. Res.*, *116*(A11), A11,304, doi:10.1029/2011JA016901.

Matsuno, T. (1971), A dynamical model of the stratospheric sudden warming, *J. Atmos. Sci.*, *28*(8), 1479–1494, doi:10.1175/1520-0469(1971)028⟨1479:ADMOTS⟩2.0.CO;2.

Mayer, H. G., I. Harris, and N. W. Spencer (1978), Some properties of upper atmosphere dynamics, *Rev. Geophys.*, *16*(4), 539–565, doi:10.1029/RG016i004p00539.

McDade, I., D. Murtagh, R. Greer, P. Dickinson, G. Witt, J. Stegman, E. Llewellyn, L. Thomas, and D. Jenkins (1986), ETON 2: Quenching parameters for the proposed precursors of $O_2(b^1\Sigma_g^+)$ and $O(^1S)$ in the terrestrial nightglow, *Planetary and Space Science*, *34*(9), 789–800, doi:10.1016/0032-0633(86)90075-9.

Melndez-Alvira, D. J., D. G. Torr, P. G. Richards, W. R. Swift, M. R. Torr, T. Baldridge, and H. Rassoul (1995), Sensitivity of the 6300 $\AA$ twilight airglow to neutral composition, *J. Geophys. Res.*, *100*(A5), 7839–7853, doi:10.1029/94JA02487.

Mendillo, M. (1971), Ionospheric total electron content behaviour during geomagnetic storms, *Nature*, *234*(45), 23–24, doi:10.1038/10.1038/physci234023a0.

Mendillo, M., and J. Baumgardner (1982), Airglow characteristics of equatorial plasma depletions, *J. Geophys. Res.*, *87*(A9), 7641, doi:10.1029/JA087iA09p07641.

Mendillo, M., J. Meriwether, and M. Biondi (2001), Testing the thermospheric neutral wind suppression mechanism for day-to-day variability of equatorial spread F, *J. Geophys. Res.*, *106*(A3), 3655–3663, doi:10.1029/2000JA000148.

Meriwether, J. (2006), Studies of thermospheric dynamics with a Fabry–Perot interferometer network: A review, *J. Atmos. Sol. Terr. Phys.*, *68*(13), 1576–1589, doi:10.1016/j.jastp.2005.11.014.

Meriwether, J. W., J. W. Moody, M. A. Biondi, and R. G. Roble (1986), Optical interferometric measurements of nighttime equatorial thermospheric winds at Arequipa, Peru, *J. Geophys. Res.*, *91*(A5), 5557, doi:10.1029/JA091iA05p05557.

Meriwether, J. W., J. J. Makela, D. J. Fisher, R. A. Buriti, A. F. Medeiros, R. A. Akmaev, T. J. Fuller-Rowell, and F. Wu (2013), Comparisons of thermospheric wind and temperature measurements in equatorial Brazil to Whole Atmosphere Model Predictions, *J. Atmos. Sol. Terr. Phys.*, *103*, 103–112, doi:10.1016/j.jastp.2013.04.002.

Meyer, C. K., and J. M. Forbes (1997), A 6.5-day westward propagating planetary wave: Origin and characteristics, *J. Geophys. Res.*, *102*(D22), 26,173–26.

Meyers, S. D., B. G. Kelly, and J. J. O'Brien (1993), An introduction to wavelet analysis in oceanography and meteorology: With application to the dispersion of yanai waves, *Mon. Wea. Rev.*, *121*(10), 2858–2866, doi:10.1175/1520-0493(1993)121⟨2858:AITWAI⟩2.0.CO;2.

Moffett, R. J. (1979), The Equatorial Anomaly in the Electron Distribution of the Terrestrial F-Region, *Fundam. Cosm. Phys.*, *4*, 313–391.

Moore, J. G., and E. J. Weber (1981), OI 6300 and 7774 $\mathring{A}$ airglow measurements of equatorial plasma depletions, *J. Atmos. Terr. Phys.*, *43*(8), 851–858, doi:10.1016/0021-9169(81)90063-5.

Morlet, J., G. Arens, E. Fourgeau, and D. Glard (1982), Wave propagation and sampling theory — Part I: Complex signal and scattering in multilayered media, *Geophysics*, *47*(2), 203–221, doi:10.1190/1.1441328.

Nanan, B., C. Y. Chen, P. K. Rajesh, J. Y. Liu, and G. J. Bailey (2012), Modeling and observations of the low latitude ionosphere-plasmasphere system at long deep solar minimum, *J. Geophys. Res.*, *117*(A8), A08,316, doi:10.1029/2012JA017846.

Narayanan, R., J. N. Desai, N. K. Modi, R. Raghavarao, and R. Sridharan (1989), Dayglow photometry: a new approach, *Appl. Opt.*, *28*, 2138–2142, doi:10.1364/AO.28.002138.

Niranjan Kumar, K., A. Taori, S. Sathishkumar, V. Kamalakar, R. Ghodpage, S. Gurubaran, P. T. Patil, S. V. B. Rao, and A. K. Patra (2012), On the linkage of mesospheric planetary waves with those of the lower atmosphere and ionosphere: A case study from Indian low latitudes, *J. Geophys. Res.*, *117*(A11), doi:10.1029/2012JA018139.

Noxon, J. F. (1968), Day airglow, *Sp. Sci. Rev.*, *8*(1), 92–134, doi:10.1007/BF00362572.

Noxon, J. F., and R. M. Goody (1962), Observation of day airglow emission, *J. Atmos. Sci.*, *19*(4), 342–343, doi:10.1175/1520-0469(1962)019⟨0342:OODAE⟩2.0.CO;2.

Oliver, W. L., Y. Otsuka, M. Sato, T. Takami, and S. Fukao (1997), A climatology of F region gravity wave propagation over the middle and upper atmosphere radar, *J. Geophys. Res.*, *102*(A7), 14,499, doi:10.1029/97JA00491.

Pallam Raju, D., and R. Sridharan (1998), High resolution 2-D maps of OI 630.0 nm thermospheric dayglow from equatorial latitudes, *Ann. Geophys.*, *16*(8), 997–1006, doi:10.1007/s00585-998-0997-6.

Pallam Raju, D., R. Sridharan, R. Narayanan, N. K. Modi, R. Raghavarao, and B. H. Subbaraya (1995), Ground-based optical observations of daytime auroral emissions from Antarctica, *J. Atmos. Terr. Phys.*, *57*(13), 1591–1597, doi:10.1016/0021-9169(95)00089-K.

Pallam Raju, D., R. Sridharan, S. Gurubaran, and R. Raghavarao (1996), First results from ground-based daytime optical investigation of the development of the equatorial ionization anomaly, *Ann. Geophys.*, *14*(2), 238–245, doi:10.1007/s00585-996-0238-9.

Pallamraju, D. (1996), Studies of daytime upper atmospheric phenomena using ground-based optical techniques, Ph.D. thesis, Devi Ahilya Vishwa Vidyalaya of Indore.

Pallamraju, D. (2003), Errors in airglow and auroral emission measurements, in *CEDAR 2003*, http://cedarweb.hao.ucar.edu/workshop/videolist.html.

Pallamraju, D., and S. Chakrabarti (2005), First ground-based measurements of OI 6300 $\AA$ daytime aurora over boston in response to the 30 October 2003 geomagnetic storm, *Geophys. Res. Lett.*, *32*(3), L03S10, doi:10.1029/2004GL021417.

Pallamraju, D., and S. Chakrabarti (2006), Contributions of imaging echelle spectrographs to daytime optical aeronomy, *J. Atmos. Sol. Terr. Phys.*, *68*(13), 1459 – 1471, doi:10.1016/j.jastp.2005.05.013, passive Optics Aeronomy Passive Optics Workshop.

Pallamraju, D., and R. Sridharan (1998), Ground-based optical measurements of daytime auroral emissions: A new means of investigating space-weather related processes, *Proceedings of the Indian Academy of Sciences - Earth and Planetary Sciences*, *107*(3), 203–211, doi:10.1007/BF02840480.

Pallamraju, D., J. Baumgardner, and S. Chakrabarti (2000), A multiwavelength investigation of the ring effect in the day sky spectrum, *Geophys. Res. Lett.*, *27*(13), 1875–1878, doi:10.1029/1999gl010961.

Pallamraju, D., J. Baumgardner, S. Chakrabarti, and T. R. Pedersen (2001), Simultaneous ground based observations of an auroral arc in daytime/twilighttime OI 630.0 nm emission and by incoherent scatter radar, *J. Geophys. Res.*, *106*(A4), 5543–5549, doi:10.1029/2000JA000244.

Pallamraju, D., J. Baumgardner, and S. Chakrabarti (2002), HIRISE: A ground-based high-resolution imaging spectrograph using echelle grating for measuring daytime airglow/auroral emissions, *J. Atmos. Sol. Terr. Phys.*, *64*(12-14), 1581–1587, doi:10.1016/S1364-6826(02)00095-0.

Pallamraju, D., S. Chakrabarti, and C. E. Valladares (2004), Magnetic storm-induced enhancement in neutral composition at low latitudes as inferred by $O(^1D)$ dayglow measurements from Chile, *Ann. Geophys.*, *22*(9), 3241–3250, doi:10.5194/angeo-22-3241-2004.

Pallamraju, D., U. Das, and S. Chakrabarti (2010), Short- and long-timescale thermospheric variability as observed from OI 630.0 nm dayglow emissions from low latitudes, *J. Geophys. Res.*, *115*(A6), A06,312, doi:10.1029/2009JA015042.

Pallamraju, D., G. Lu, and C. Lin (2012), Overview of the special issue on the atmospheric coupling processes in the sunearth system, *J. Atmos. Sol. Terr. Phys.*, *7576*(0), 1 – 4, doi:10.1016/j.jastp.2012.01.002.

Pallamraju, D., F. I. Laskar, R. P. Singh, J. Baumgardner, and S. Chakrabarti (2013), MISE: A multiwavelength imaging spectrograph using echelle grating for daytime optical aeronomy investigations , *J. Atmos. Sol. Terr. Phys.*, *103*(0), 176 – 183, doi:10.1016/j.jastp.2012.12.003.

Pallamraju, D., et al. (2014), Daytime wave characteristics in the mesosphere lower thermosphere region: Results from the Balloon-borne Investigations of Regional-atmospheric Dynamics experiment, *J. Geophys. Res.*, *119*(3), 2229–2242, doi:10.1002/2013JA019368.

Pancheva, D., and P. Mukhtarov (2011), Stratospheric warmings: The atmosphere-ionosphere coupling paradigm, *J. Atmos. Sol. Terr. Phys.*, *73*(13), 1697–1702, doi:10.1016/j.jastp.2011.03.006.

Pancheva, D., et al. (2008), Planetary waves in coupling the stratosphere and mesosphere during the major stratospheric warming in 2003/2004, *J. Geophys. Res.*, *113*(D12), D12,105.

Pancheva, D., P. Mukhtarov, B. Andonov, N. J. Mitchell, and J. M. Forbes (2009), Planetary waves observed by TIMED/SABER in coupling the stratosphere–mesosphere–lower thermosphere during the winter of 2003/2004: Part 2 - Altitude and latitude planetary wave structure, *J. Atmos. Sol. Terr. Phys.*, *71*(1), 75–87.

Parish, H. F., J. M. Forbes, and F. Kamalabadi (1994), Planetary wave and solar emission signatures in the equatorial electrojet, *J. Geophys. Res.*, *99*(A1), 355–368, doi:10.1029/93JA02096.

Park, J., H. Lühr, M. Kunze, B. G. Fejer, and K. W. Min (2012), Effect of sudden stratospheric warming on lunar tidal modulation of the equatorial electrojet, *J. Geophys. Res.*, *117*(A3), A03,306, doi:10.1029/2011JA017351.

Parkinson, B. W., P. Enge, P. Axelrad, and J. J. S. Jr. (1996), *Global Positioning System: Theory and Applications, Volume II*, American Institute of Aeronautics and Astronautics, doi:10.2514/4.866395.

Paulikas, G. A. (1975), Precipitation of particles at low and middle latitudes, *Rev. Geophys.*, *13*(5), 709, doi:10.1029/rg013i005p00709.

Pedatella, N. M., and J. M. Forbes (2009), Modulation of the equatorial F-region by the quasi-16-day planetary wave, *Geophys. Res. Lett.*, *36*(9), L09,105, doi:10.1029/2009GL037809.

Pedatella, N. M., and J. M. Forbes (2010), Evidence for stratosphere sudden warming-ionosphere coupling due to vertically propagating tides, *Geophys. Res. Lett.*, *37*(11), L11,104, doi:10.1029/2010GL043560.

Pedatella, N. M., and H. Liu (2013), The influence of atmospheric tide and planetary wave variability during sudden stratosphere warmings on the low latitude ionosphere, *J. Geophys. Res. Space Physics*, *118*(8), 5333–5347, doi:10.1002/jgra.50492.

Pitteway, M. L. V., and C. O. Hines (1963), The viscous damping of atmospheric gravity waves, *Can. J. Phys.*, *41*(12), 1935–1948, doi:10.1139/p63-194.

Pogoreltsev, A. I., A. A. Vlasov, K. Frhlich, and C. Jacobi (2007), Planetary waves in coupling the lower and upper atmosphere, *J. Atmos. Sol. Terr. Phys.*, *69*(1718), 2083 – 2101, doi: 10.1016/j.jastp.2007.05.014.

Prakash, S., D. Pallamraju, and H. S. S. Sinha (2009), Role of the equatorial ionization anomaly in the development of the evening prereversal enhancement of the equatorial zonal electric field, *J. Geophys. Res.*, *114*(A2), A02,301, doi:10.1029/2007JA012808.

Press, W. H., and G. B. Rybicki (1989), Fast algorithm for spectral analysis of unevenly sampled data, *Astrophys. J.*, *338*, 277–280, doi:10.1086/167197.

Prölss, G. W. (1980), Magnetic storm associated perturbations of the upper atmosphere: Recent results obtained by satellite-borne gas analyzers, *Rev. Geophys.*, *18*(1), 183, doi:10.1029/RG018i001p00183.

Raghavarao, R., R. Sridharan, J. H. Sastri, V. V. Agashe, B. C. N. Rao, P. B. Rao, and V. V. Somayajulu (1988a), *The equatorial ionosphere; WITS handbook. World Ionosphere/Thermosphere Study, vol 1.*, 48–93 pp., SCOSTEP Secretariat, University of Illinois, Urbana.

Raghavarao, R., M. Nageswararao, J. H. Sastri, G. D. Vyas, and M. Sriramarao (1988b), Role of equatorial ionization anomaly in the initiation of equatorial spread F, *J. Geophys. Res.*, *93*(A6), 5959–5964, doi:10.1029/JA093iA06p05959.

Raghavarao, R., L. E. Wharton, N. W. Spencer, H. G. Mayr, and L. H. Brace (1991), An equatorial temperature and wind anomaly (ETWA), *Geophys. Res. Lett.*, *18*, 1193–1196, doi:10.1029/91GL01561.

Raghavarao, R., W. R. Hoegy, N. W. Spencer, and L. E. Wharton (1993), Neutral temperature anomaly in the equatorial thermosphere-a source of vertical winds, *Geophys. Res. Lett.*, *20*(11), 1023–1026, doi:10.1029/93GL01253.

Rama Rao, P. V. S., K. Niranjan, D. S. V. V. D. Prasad, S. Gopi Krishna, and G. Uma (2006), On the validity of the ionospheric pierce point (IPP) altitude of 350 km in the Indian equatorial and low-latitude sector, *Ann. Geophys.*, *24*(8), 2159–2168, doi:10.5194/angeo-24-2159-2006.

Rao, C. S. R., and P. L. Malhotra (1964), A study of geomagnetic anomaly during I.G.Y., *J. Atmos. Terr. Phys.*, *26*(11), 1075–1085, doi:10.1016/0021-9169(64)90093-5.

Rastogi, R. G., and J. A. Klobuchar (1990), Ionospheric electron content within the equatorial F2 layer anomaly belt, *J. Geophys. Res.*, *95*(A11), 19,045, doi:10.1029/JA095iA11p19045.

Rauthe, M., M. Gerding, and F.-J. Lübken (2008), Seasonal changes in gravity wave activity measured by lidars at mid-latitudes, *Atmos. Chem. Phys.*, *8*(22), 6775–6787, doi:10.5194/acp-8-6775-2008.

Reddy, C. A. (1989), The equatorial electrojet, *pure Appl. Geophys.*, *131*(3), 485–508, doi:10.1007/BF00876841.

Reddy, C. A., and C. V. Devasia (1978), Equivalent circuit analysis of neutral wind effects on equatorial electrojet, *Nature*, *273*(5659), 195–199, doi:10.1038/273195a0.

Reddy, C. A., V. V. Somayajulu, and C. V. Devasia (1979), Global scale electrodynamic coupling of the auroral and equatorial dynamo regions, *J. Atmos. Terr. Phys.*, *41*(2), 189–201, doi:10.1016/0021-9169(79)90012-6.

Rees, M. H. (1989), *Physics and Chemistry of the Upper Atmosphere*, 289 pp., Cambridge University Press.

Rideout, W., and A. Coster (2006), Automated GPS processing for global total electron content data, *GPS Solutions*, *10*, 219–228, doi:10.1007/s10291-006-0029-5.

Rishbeth, H. (1979), Ion-drag effects in the thermosphere, *J. Atmos. Terr. Phys.*, *41*(7-8), 885–894, doi:10.1016/0021-9169(79)90130-2.

Rishbeth, H. (1997), The ionospheric E-layer and F-layer dynamos — a tutorial review, *J. Atmos. Sol. Terr. Phys.*, *59*(15), 1873–1880, doi:10.1016/s1364-6826(97)00005-9.

Rishbeth, H., and O. K. Garriott (1969), *Introduction to Ionospheric Physics*, 331 pp., Academic Press.

Roble, R. (1977), *The Upper Atmosphere and Magnetosphere*, National Academy of Science, Washington, DC.

Russell III, J. M., M. G. Mlynczak, L. L. Gordley, J. J. Tansock, Jr., and R. W. Esplin (1999), Overview of the SABER experiment and preliminary calibration results, in *An Overv. SABER Exp. Prelim. calibration results*, edited by A. M. Larar, pp. 277–288, International Society for Optics and Photonics, doi:10.1117/12.366382.

Salby, M. L. (1981a), Rossby normal modes in nonuniform background configurations. Part II. equinox and solstice conditions, *J. Atmos. Sci.*, *38*(9), 1827–1840.

Salby, M. L. (1981b), Rossby normal modes in nonuniform background configurations. Part I: Simple fields, *J. Atmos. Sci.*, *38*(9), 1803–1826, doi:10.1175/1520-0469(1981)038⟨1803:RNMINB⟩2.0.CO;2.

Salby, M. L. (1984), Survey of planetary-scale traveling waves: The state of theory and observations, *Rev. Geophys.*, *22*(2), 209–236, doi:10.1029/RG022i002p00209.

Salby, M. L. (1996), *Fundamentals of Atmospheric Physics*, vol. 61, Academic press.

Sassi, F., R. Garcia, and K. Hoppel (2012), Large-scale rossby normal modes during some recent northern hemisphere winters, *J. Atmos. Sci.*, *69*(3), 820–839.

Sastri, J. H. (1988), Equatorial electric-fields of ionospheric disturbance dynamo orgin, *6*(6), 635–642.

Sastri, J. H. (2002), Equatorial geomagnetic and ionospheric effects of substorms, *Ind. J. Radio Space Physics*, *31*(6), 309–319.

Sastri, J. H., M. A. Abdu, and J. H. A. Sobral (1997), Response of equatorial ionosphere to episodes of asymmetric ring current activity, *Ann. Geophys.*, *15*(10), 1316–1323, doi:10.1007/s00585-997-1316-3.

Scargle, J. D. (1982), Studies in astronomical time series analysis. II - Statistical aspects of spectral analysis of unevenly spaced data, *Astrophys. J.*, *263*, 835–853, doi:10.1086/160554.

Scherliess, L., and B. G. Fejer (1999), Radar and satellite global equatorial F region vertical drift model, *J. Geophys. Res.*, *104*(A4), 6829–6842, doi:10.1029/1999JA900025.

Schulz, M., and M. Mudelsee (2002), REDFIT: estimating red-noise spectra directly from unevenly spaced paleoclimatic time series, *Computers & Geosciences*, *28*(3), 421–426.

Sekar, R., and D. Chakrabarty (2008), Equatorial spread-F research in India: a brief review, *Ind. J. Radio Space Physics*, *37*(1), 7.

Sekar, R., D. Chakrabarty, S. Sarkhel, A. K. Patra, C. V. Devasia, and M. C. Kelley (2007), Identification of active fossil bubbles based on coordinated VHF radar and airglow measurements, *Ann. Geophys.*, *25*(10), 2099–2102, doi:10.5194/angeo-25-2099-2007.

Sekar, R., D. Chakrabarty, and D. Pallamraju (2012), Optical signature of shear in the zonal plasma flow along with a tilted structure associated with equatorial spread F during a space weather event, *J. Atmos. Sol. Terr. Phys.*, *7576*(0), 57 – 63, doi:10.1016/j.jastp.2011.05.009.

Shepherd, G. G. (1979), Dayside cleft aurora and its ionospheric effects, *Rev. Geophys.*, *17*(8), 2017, doi:10.1029/RG017i008p02017.

Shepherd, G. G. (2002), *Spectral Imaging of the Atmosphere*, vol. 82, Academic press.

Shepherd, G. G., W. A. Gault, D. W. Miller, Z. Pasturczyk, S. F. Johnston, P. R. Kosteniuk, J. W. Haslett, D. J. W. Kendall, and J. R. Wimperis (1985), WAMDII: wide-angle Michelson Doppler imaging interferometer for Spacelab, *Appl. Opt.*, *24*(11), 1571, doi:10.1364/AO.24.001571.

Shepherd, G. G., et al. (1993), WINDII, the Wind Imaging Interferometer on the Upper Atmosphere Research Satellite, *J. Geophys. Res.*, *98*(D6), 10,725–10,750, doi:10.1029/93JD00227.

Shepherd, M. G., and G. G. Shepherd (2011), Stratospheric warming effects on thermospheric $O(^1S)$ dayglow dynamics, *J. Geophys. Res.*, *116*(A11), A11,327, doi:10.1029/2011JA016762.

Shiokawa, K. (2002), A large-scale traveling ionospheric disturbance during the magnetic storm of 15 September 1999, *J. Geophys. Res.*, *107*(A6), 1088, doi:10.1029/2001JA000245.

Shiokawa, K., Y. Katoh, M. Satoh, M. K. Ejiri, T. Ogawa, T. Nakamura, T. Tsuda, and R. H. Wiens (1999), Development of Optical Mesosphere Thermosphere Imagers (OMTI), *Earth Planets Space*, *51*(7-8), 887–896, doi:10.5636/eps.51.887.

Shiokawa, K., Y. Otsuka, and T. Ogawa (2009), Propagation characteristics of nighttime mesospheric and thermospheric waves observed by optical mesosphere thermosphere imagers at middle and low latitudes, *Earth Planets Space*, *61*(4), 479–491, doi:10.1186/BF03353165.

Sivaraman, M. R., R. Suhasini, and R. Raghavarao (1976), Role of ambipolar diffusion in the development of equatorial anomaly in solar maximum and minimum periods, *Ind. J. Radio Space Physics*, *5*, 136–140.

Sivjee, G. G. (1983), Differences in near UV ($\sim 3400 - 4300\,\AA$) optical emissions from midday cusp and nighttime auroras, *J. Geophys. Res.*, *88*(A1), 435, doi:10.1029/JA088iA01p00435.

Smith, S. M., M. Mendillo, J. Baumgardner, and R. R. Clark (2000), Mesospheric gravity wave imaging at a subauroral site: First results from Millstone Hill, *J. Geophys. Res.*, *105*(A12), 27,119, doi:10.1029/1999JA000343.

Solomon, S. (1992), Glow model version 0.95, *Tech. rep.*, Lab. for Atmos. and Space Phys., Univ. of Colo., Boulder.

Solomon, S. C., and V. J. Abreu (1989), The 630 nm dayglow, *J. Geophys. Res.*, *94*(A6), 6817–6824, doi:10.1029/JA094iA06p06817.

Solomon, S. C., P. B. Hays, and V. J. Abreu (1988), The auroral 6300 $\mathring{A}$ emission: Observations and modeling, *J. Geophys. Res.*, *93*(A9), 9867–9882, doi:10.1029/JA093iA09p09867.

Sridharan, R., S. Gurubaran, R. Raghavarao, and R. Suhasini (1991), Co-ordinated thermospheric and F-region measurements from low latitudes, *J. Atmos. Terr. Phys.*, *53*(6-7), 515–519, doi:10.1016/0021-9169(91)90078-L.

Sridharan, R., R. Narayanan, and N. K. Modi (1992a), Improved chopper mask for the dayglow photometer., *Appl. Opt.*, *31*(4), 425–6, doi:10.1364/AO.31.000425.

Sridharan, R., S. A. Haider, S. Gurubaran, R. Sekar, and R. Narayanan (1992b), OI 630.0-nm dayglow in the region of equatorial ionization anomaly: Temporal variability and its causative mechanism, *J. Geophys. Res.*, *97*(A9), 13,715–13,721, doi:10.1029/92JA00674.

Sridharan, R., R. Narayanan, N. K. Modi, and D. P. Raju (1993), Novel mask design for multiwavelength dayglow photometry., *Appl. Opt.*, *32*(22), 4178–80, doi:10.1364/AO.32.004178.

Sridharan, R., D. P. Raju, R. Raghavarao, and P. V. S. Ramarao (1994), Precursor to equatorial spread-F in OI 630.0 nm dayglow, *Geophys. Res. Lett.*, *21*(25), 2797–2800, doi:10.1029/94GL02732.

Sridharan, R., D. Pallam Raju, R. Narayanan, N. K. Modi, B. H. Subbaraya, and R. Raghavarao (1995), Daytime measurements of optical auroral emissions from Antarctica, *Current science*, *68*(8), 830–834.

Sridharan, R., N. K. Modi, D. P. Raju, R. Narayanan, T. K. Pant, A. Taori, and D. Chakrabarty (1998), A multiwavelength daytime photometer - a new tool for the investigation of atmospheric processes, *Meas. Sci. Technol.*, *9*(4), 585.

Sridharan, S., S. Sathishkumar, and S. Gurubaran (2009), Variabilities of mesospheric tides and equatorial electrojet strength during major stratospheric warming events, *Ann. Geophys.*, *27*(11), 4125–4130, doi:10.5194/angeo-27-4125-2009.

Sripathi, S., and A. Bhattacharyya (2012), Quiet time variability of the GPS TEC and EEJ strength over indian region associated with major sudden stratospheric warming events during 2005/2006, *J. Geophys. Res.*, *117*(A5), A05,305, doi:10.1029/2011JA017103.

Stening, R. J., J. M. Forbes, M. E. Hagan, and A. D. Richmond (1997), Experiments with a lunar atmospheric tidal model, *J. Geophys. Res.*, *102*(D12), 13,465–13,471, doi:10.1029/97JD00778.

Takahashi, H., Y. Sahai, P. P. Batista, and B. R. Clemesha (1992), Atmospheric gravity wave effect on the airglow O (0,1) and OH (9,4) band intensity and temperature variations observed from a low latitude station, *Adv. Sp. Res.*, *12*(10), 131–134, doi: 10.1016/0273-1177(92)90454-6.

Takahashi, H., R. Buriti, D. Gobbi, and P. Batista (2002), Equatorial planetary wave signatures observed in mesospheric airglow emissions, *J. Atmos. Sol. Terr. Phys.*, *64*(811), 1263–1272, doi:10.1016/S1364-6826(02)00040-8.

Tary, J. B., R. H. Herrera, J. Han, and M. van der Baan (2014), Spectral estimation – What is new? What is next?, *Reviews of Geophysics*, *52*(4), 723–749, doi:10.1002/2014RG000461.

Taylor, M. J., W. R. Pendleton, S. Clark, H. Takahashi, D. Gobbi, and R. A. Goldberg (1997), Image measurements of short-period gravity waves at equatorial latitudes, *J. Geophys. Res.*, *102*(D22), 26,283, doi:10.1029/96JD03515.

Taylor, M. J., W. R. Pendleton Jr, P.-D. Pautet, Y. Zhao, C. Olsen, H. K. S. Babu, A. F. Medeiros, and H. Takahashi (2007), Recent progress in mesospheric gravity wave studies using nigthglow imaging system, *Rev. Bras. Geofísica*, *25*, 49–58, doi:10.1590/S0102-261X2007000600007.

Teitelbaum, H., and F. Vial (1991), On tidal variability induced by nonlinear interaction with planetary waves, *J. Geophys. Res.*, *96*(A8), 14,169–14,178, doi:10.1029/91JA01019.

Thayer, J. P., J. Lei, J. M. Forbes, E. K. Sutton, and R. S. Nerem (2008), Thermospheric density oscillations due to periodic solar wind high-speed streams, *J. Geophys. Res.*, *113*(A6), A06,307, doi:10.1029/2008JA013190.

Tinsley, B. A., A. B. Christensen, J. Bittencourt, H. Gouveia, P. D. Angreji, and H. Takahashi (1973), Excitation of oxygen permitted line emissions in the tropical nightglow, *J. Geophys. Res.*, *78*(7), 1174–1186, doi:10.1029/JA078i007p01174.

Tinsley, B. A., R. P. Rohrbaugh, W. B. Hanson, and A. L. Broadfoot (1997), Images of transequatorial F region bubbles in 630- and 777-nm emissions compared with satellite measurements, *J. Geophys. Res.*, *102*(A2), 2057, doi:10.1029/95JA01398.

Tolman, B., R. B. Harris, T. Gaussiran, D. Munton, J. Little, R. Mach, S. Nelsen, B. Renfro, and D. Schlossberg (2004), The GPS toolkit: Open source GPS software, in *Proceedings 17th International Technical Meeting of the Satellite Division of the ION (ION GNSS 2004). Long Beach, California.*

Torr, M. R., and D. G. Torr (1982), The role of metastable species in the thermosphere, *Rev. Geophys. Sp. Phys.*, *20*(1), 91–144.

Torr, M. R., D. G. Torr, and H. E. Hinteregger (1980), Solar flux variability in the schumann-runge continuum as a function of solar cycle 21, *Journal of Geophysical Research: Space Physics*, *85*(A11), 6063–6068, doi:10.1029/JA085iA11p06063.

Torrence, C., and G. P. Compo (1998), A practical guide to wavelet analysis, *Bull. Amer. Meteor. Soc.*, *79*(1), 61–78, doi:10.1175/1520-0477(1998)079⟨0061:APGTWA⟩2.0.CO;2.

Vadas, S. L., and D. C. Fritts (2005), Thermospheric responses to gravity waves: Influences of increasing viscosity and thermal diffusivity, *J. Geophys. Res.*, *110*(D15), D15,103, doi:10.1029/2004JD005574.

Vadas, S. L., and H.-l. Liu (2009), Generation of large-scale gravity waves and neutral winds in the thermosphere from the dissipation of convectively generated gravity waves, *J. Geophys. Res.*, *114*(A10), A10,310, doi:10.1029/2009JA014108.

Valladares, C. E., S. Basu, K. Groves, M. P. Hagan, D. Hysell, A. J. Mazzella, and R. E. Sheehan (2001), Measurement of the latitudinal distributions of total electron content during equatorial spread F events, *J. Geophys. Res.*, *106*(A12), 29,133–29,152, doi:10.1029/2000JA000426.

Vineeth, C., T. K. Pant, C. V. Devasia, and R. Sridharan (2007), Atmosphere-ionosphere coupling observed over the dip equatorial MLTI region through the quasi 16-day wave, *Geophys. Res. Lett.*, *34*(12), L12,102, doi:10.1029/2007GL030010.

Vineeth, C., T. Kumar Pant, and R. Sridharan (2009), Equatorial counter electrojets and polar stratospheric sudden warmings – a classical example of high latitude-low latitude coupling?, *Ann. Geophys.*, *27*(8), 3147–3153, doi:10.5194/angeo-27-3147-2009.

Vineeth, C., T. K. Pant, S. G. Sumod, K. K. Kumar, S. Gurubaran, and R. Sridharan (2011), Planetary wave-tidal interactions over the equatorial mesosphere-lower thermosphere region and their possible implications for the equatorial electrojet, *J. Geophys. Res.*, *116*(A1), doi:10.1029/2010JA015895.

Vladislav, Y. K., I. S. Anatoly, and N. S. Nicolay (2008), *Airglow as an Indicator of Upper Atmospheric Structure and Dynamics*, Springer.

Walker, G. O., J. H. K. Ma, and E. Golton (1994), The equatorial ionospheric anomaly in electron content from solar minimum to solar maximum for South East Asia, *Ann. Geophys.*, *12*(2/3), 195–209, doi:10.1007/s00585-994-0195-0.

Wallace, L. (1961), An attempt to observe the day airglow, *J. Geophys. Res.*, *66*(5), 1585–1586, doi:10.1029/JZ066i005p01585.

Wallace, L. (1963), Observation of the day airglow, *J. Geophys. Res.*, *68*(5), 1559–1560, doi:10.1029/JZ068i005p01559.

Wallace, L., and M. B. McElroy (1966), The visual dayglow, *Planet. Space Sci.*, *14*(8), 677–708, doi:10.1016/0032-0633(66)90100-0.

Walterscheid, R. L., G. G. Sivjee, and R. G. Roble (2000), Mesospheric and lower thermospheric manifestations of a stratospheric warming event over Eureka, Canada (80°N), *Geophys. Res. Lett.*, *27*(18), 2897–2900, doi:10.1029/2000GL003768.

Wan, W., Z. Ren, F. Ding, J. Xiong, L. Liu, B. Ning, B. Zhao, G. Li, and M.-L. Zhang (2012), A simulation study for the couplings between DE3 tide and longitudinal WN4 structure in the thermosphere and ionosphere, *J. Atmos. Sol. Terr. Phys.*, *90-91*(0), 52 – 60, doi:10.1016/j.jastp.2012.04.011.

Wickwar, V. B., and W. Kofman (1984), Dayside red auroras at very high latitudes: The importance of thermal excitation, *Geophys. Res. Lett.*, *11*(9), 923–926, doi:10.1029/GL011i009p00923.

Willson, R. C. (1982), Solar irradiance variations and solar activity, *J. Geophys. Res.*, *87*(A6), 4319–4326, doi:10.1029/JA087iA06p04319.

Witasse, O., J. Lilensten, and C. Lathuillare (1999), Modeling the OI 630.0 and 557.7 nm thermospheric dayglow during EISCAT-WINDII coordinated measurements, *J. Geophys. Res.*, *104*(A11), 24,639–24,655.

Wu, Q., T. L. Killeen, D. A. Ortland, S. C. Solomon, R. D. Gablehouse, R. M. Johnson, W. R. Skinner, R. J. Niciejewski, and S. J. Franke (2006), TIMED Doppler interferometer (TIDI) observations of migrating diurnal and semidiurnal tides, *J. Atmos. Sol. Terr. Phys.*, *68*(3-5), 408–417, doi:10.1016/j.jastp.2005.02.031.

Yamazaki, Y., and M. J. Kosch (2014), Geomagnetic lunar and solar daily variations during the last 100 years, *J. Geophys. Res. Space Physics*, doi:10.1002/2014JA020203.

Yamazaki, Y., A. D. Richmond, and K. Yumoto (2012), Stratospheric warmings and the geomagnetic lunar tide: 1958-2007, *J. Geophys. Res.*, *117*(A4), doi:10.1029/2012JA017514.

Yiğit, E., and A. S. Medvedev (2010), Internal gravity waves in the thermosphere during low and high solar activity: Simulation study, *J. Geophys. Res.*, *115*(A8), doi:10.1029/2009JA015106.

Yiğit, E., and A. S. Medvedev (2012), Gravity waves in the thermosphere during a sudden stratospheric warming, *Geophys. Res. Lett.*, *39*(21), doi:10.1029/2012GL053812.

Yiğit, E., A. D. Aylward, and A. S. Medvedev (2008), Parameterization of the effects of vertically propagating gravity waves for thermosphere general circulation models: Sensitivity study, *J. Geophys. Res.*, *113*(D19), D19,106, doi:10.1029/2008JD010135.

Yue, X., W. S. Schreiner, J. Lei, C. Rocken, D. C. Hunt, Y.-H. Kuo, and W. Wan (2010), Global ionospheric response observed by COSMIC satellites during the January 2009 stratospheric sudden warming event, *J. Geophys. Res.*, *115*(A11), doi:10.1029/2010JA015466.

Zhang, S. P., and G. G. Shepherd (2000), Neutral winds in the lower thermosphere observed by WINDII during the April 4–5th, 1993 storm, *Geophys. Res. Lett.*, *27*(13), 1855–1858, doi:10.1029/2000GL000034.

Zhang, S. P., and G. G. Shepherd (2004), Solar influence on the $O(^1D)$ dayglow emission rate: Global-scale measurements by WINDII on UARS, *Geophys. Res. Lett.*, *31*(7), L07,804, doi: 10.1029/2004GL019447.

Zhang, S. P., and G. G. Shepherd (2005), On the response of the $O(^1S)$ dayglow emission rate to the sun's energy input: An empirical model deduced from WINDII/UARS global measurements, *J. Geophys. Res.*, *110*(A3), A03,304, doi:10.1029/2004JA010887.

List of Publications

Publications in Journals

1. **Laskar, F. I.**, D. Pallamraju, B. Veenadhari, T. Vijaya Lakshmi, M. Anji Reddy, and S. Chakrabarti "Gravity waves in the thermosphere: Solar activity dependence", *Advances in Space Research, 2015*, doi:10.1016/j.asr.2014.12.040

2. **Laskar, F. I.** and D. Pallamraju, "Does sudden stratospheric warming induce meridional circulation in the mesosphere thermosphere system?", *JGR Space Physics, 2014*, doi:10.1002/2014JA020086 (attached with this thesis).

3. **Laskar, F. I.**, D. Pallamraju, and B. Veenadhari, "Vertical coupling of atmospheres: Dependence on strength of sudden stratospheric warming and solar activity", *Earth, Planets and Space, 2014*, doi:10.1186/1880-5981-66-94 (attached with this thesis).

4. Bagiya, M. S., R Hazarika, **Fazlul I. Laskar**, et. al., "Effects of prolonged southward interplanetary magnetic field on low-latitude ionospheric electron density", *JGR Space Physics, 2014*, doi:10.1002/2014JA020156.

5. Pallamraju, D., J. Baumgardner, R.P. Singh, **Fazlul I. Laskar**, et. al., "Daytime wave characteristics in the mesosphere lower thermosphere region: Results from the balloon-borne investigations of regional-atmospheric dynamics experiment", *JGR. Space Physics, 2014*, doi:10.1002/2013JA019368.

6. **Laskar, F. I.**, D. Pallamraju, T.V. Lakshmi, M. Anji Reddy, B.M. Pathan, S. Chakrabarti, "Investigations on vertical coupling of atmospheric regions

using combined multiwavelength optical dayglow, magnetic, and radio measurements", *JGR Space Physics, 2013*, doi:10.1002/jgra.50426.

7. Pallamraju, D., **Fazlul I. Laskar**, R.P. Singh, J. Baumgardner, and S. Chakrabarti, "MISE: A Multiwavelength Imaging Spectrograph using Echelle grating for daytime optical aeronomy investigations", *Journal of Atm.-Sol. Terr. Phys, 2013*, doi:10.1016/j.jastp.2012.12.003.

Conference Papers

1. **Laskar, F. I.** and Duggirala Pallamraju, "Thermospheric meridional circulation during sudden stratospheric warming events", presented in *AGU Fall Meeting, San Francisco, USA, 2014.* [Poster by FIL]

2. Pallamraju, D., **Fazlul I. Laskar**, B. Veenadhari, T. V. Lakshmi, M. A. Reddy, and S. Chakrabarti, "The solar activity dependence of wave dynamical vertical coupling of atmospheres", presented in *AGU Fall Meeting, San Francisco, USA, 2014.* [Poster by FIL]

3. Pallamraju, D., Deepak Karan, **Fazlul I. Laskar**, Kedar Phadke, T. Vijaya Lakshmi, and M. Anji Reddy, "Wave dynamical coupling in the daytime as obtained from optical oxygen airglow emission intensities over low latitudes", presented in the *COSPAR Assembly, Moscow, Russia, 2014.* [Oral by DP]

4. Pallamraju, D., Jeffrey Baumgardner, Ravindra P. Singh, **Fazlul I. Laskar**, Timothy Cook, Tarun Pant, Supriya Chakrabarti, "Characteristics of neutral waves in the daytime MLT region", presented in the *COSPAR Assembly, Moscow, Russia, 2014.* [Oral by DP]

5. **Laskar, F. I.**, Duggirala Pallamraju, T. Vijaya Lakshmi, M. Anji Reddy, and B. Veenadhari, "Shorter period waves in the upper atmosphere: Solar activity dependence", presented in the *National Space Science Symposium 2014* held at Dibrugarh University, Assam, India during 29 Jan.-1 Feb. 2014. [Oral by FIL]

6. **Laskar, F. I.**, Duggirala Pallamraju, T. Vijaya Lakshmi, M. Anji Reddy, and BM. Pathan, "Vertical coupling of whole atmosphere: An investigation using multiwavelength optical dayglow, magnetic, and radio measurements", presented in the *National Space Science Symposium 2014* held at Dibrugarh University, Assam, India during 29 Jan.-1 Feb. 2014. [Oral by FIL]

7. **Laskar, F. I.**, Duggirala Pallamraju, and B. Veenadhari, "Neutral (direct) and electrodynamical (indirect) coupling of atmospheres: Solar activity and stratospheric sudden warming event dependence", presented in the *National Space Science Symposium 2014* held at Dibrugarh University, Assam, India during 29 Jan.-1 Feb. 2014. [**2nd Prize in student poster competition**; presented by FIL]

8. **Laskar, F. I.**, Duggirala Pallamraju, and B. Veenadhari, "Evidence of Neutral (Direct) and Electrodynamical (Indirect) Vertical Coupling of Atmospheres During Stratospheric Sudden Warming Events Using Multi-technique Observations", presented in the *International CAWSES II Symposium* held at Nagoya University, Japan during 18-22 November 2013. [Poster by FIL]

9. **Laskar, F. I.**, Duggirala Pallamraju, T. Vijaya Lakshmi, and S. Chakrabarti, "On dependence of solar activity on the strength of vertical coupling of atmospheres", presented in the *WATM24 workshop 2013* held at National Central University, Taiwan during 14-17 July 2013. [Oral by FIL]

10. Pallamraju, D., **Fazlul I. Laskar**, T. Vijaya Lakshmi, and S. Chakrabarti, "Optical investigations on the wave dynamics of the low- and equatorial latitude MLT region", presented in the *10^{th} AOGS meeting 2013* held at Brisbane, Australia during 24-28 June 2013. [Oral by DP]

11. **Laskar, F. I.**, Duggirala Pallamraju, T. Vijaya Lakshmi, S. Chakrabarti M. Anji Reddy, R. Raghavarao and B. M. Pathan, "Characterization of vertical and horizontal wave features in dayglow emissions as observed from a low-latitude station, Hyderabad, INDIA", presented in the *COSPAR Assembly, Mysore, India, 2012*. [Oral by DP].

12. Pallamraju, D., **Fazlul I. Laskar**, P A V S Ganesh, and Supriya Chakrabarti "Effect of compositional variations on the seasonal variability in the oxygen daytime optical emissions over mid-latitudes" presented in the *International Symposium on Equatorial Aeronomy* held at Paracas, Peru, during 12-16 March 2012. [Oral by DP]

13. Pallamraju, D., **Fazlul I. Laskar**, Thatiparthi Vijaya Lakshmi, and S. Chakrabarti, "Investigations on vertical coupling using multiwavelength daytime optical emissions from low-latitudes", presented in the *International Symposium on Equatorial Aeronomy* held at Paracas, Peru, during 12-16 March 2012. [Poster by DP]

14. **Laskar, F. I.**, Duggirala Pallamraju, Ravindra P. Singh, R. Narayanan, and S. Chakrabarti, "Multi-wavelength High-resolution Optical Technique for the Investigations of Daytime Upper Atmospheric Processes", presented in the *National Space Science Symposium 2012* held at Sri Venkateshwara University, Tirupati, India during 14-17 February 2012. [Oral by FIL].

15. **Laskar, F. I.**, Duggirala Pallamraju, Thatiparthi Vijaya Lakshmi, M. Anji Reddy, R Raghavarao, "First results on the characteristics of waves in the daytime upper atmosphere at multiple altitudes obtained from Hyderabad, a low latitude station", presented in the *National Space Science Symposium 2012* held at Sri Venkateshwara University, Tirupati, India, during 14-17 February 2012. [Poster by FIL]

Publications attached with thesis

1. **Laskar, Fazlul I.** and D. Pallamraju, *Does sudden stratospheric warming induce meridional circulation in the mesosphere thermosphere system?*, Journal of Geophysical Research, Space Physics **119**, 12, 10,133–10,143 (2014), doi: 10.1002/2014JA020086.

2. **Laskar, Fazlul I.**, D. Pallamraju, and B. Veenadhari, *Vertical coupling of atmospheres: dependence on strength of sudden stratospheric warming and solar activity*, Earth, Planets and Space **66**, 1, (2014), doi: 10.1186/1880-5981-66-94.

AGU PUBLICATIONS

JGR

Journal of Geophysical Research: Space Physics

BRIEF REPORT
10.1002/2014JA020086

Key Points:
- Enhancement in low-latitude oxygen dayglow intensity during SSW
- Mesosphere-thermospheric meridional circulation during SSW is proposed
- Meridional transport of oxygen due to circulation explains dayglow enhancement

Correspondence to:
D. Pallamraju,
raju@prl.res.in

Citation:
Laskar, F. I., and D. Pallamraju (2014), Does sudden stratospheric warming induce meridional circulation in the mesosphere thermosphere system?, *J. Geophys. Res. Space Physics*, *119*, 10,133–10,143, doi:10.1002/2014JA020086.

Received 15 APR 2014
Accepted 22 NOV 2014
Accepted article online 26 NOV 2014
Published online 17 DEC 2014

Does sudden stratospheric warming induce meridional circulation in the mesosphere thermosphere system?

Fazlul I. Laskar[1,2] and Duggirala Pallamraju[1]

[1]Space and Atmospheric Sciences Division, Physical Research Laboratory, Ahmedabad, India, [2]Indian Institute of Technology, Gandhinagar, India

Abstract Oxygen dayglow emissions at multiple wavelengths that emanate from different heights (from around 130 km to peak altitude of the ionospheric *F* region) over a low-latitude location showed systematic enhancements in intensities throughout the daytime hours during four sudden stratospheric warming (SSW) events that occurred in the years 2010–2013. The lower thermospheric temperatures at 120 km obtained from the Sounding of the Atmosphere using Broadband Emission Radiometry instrument are found to be enhanced during SSW events at arctic latitudes and show a gradient with a decrease toward low-latitudes. During these events, the Thermosphere-Ionosphere-Mesosphere Energetics and Dynamics Doppler Interferometer measurements showed equatorward winds in the mesosphere lower thermosphere (MLT) altitudes over high-latitudes. Both the high-latitude lower thermospheric temperature enhancements and the MLT region equatorward winds occur nearly simultaneously with the observed enhancements in the atomic oxygen dayglow emission intensities at all the wavelengths over low-latitudes. Based on these measurements and other supporting information, it is proposed that a new cell of meridional circulation in the MLT winds is set up during SSW events, which enables transport of atomic oxygen from high-to-low latitudes. Such an additional contribution of oxygen density over low-latitudes interacts with lower thermospheric daytime dynamics in that region and is attributed to be the cause for the observed enhancement in the oxygen daytime optical emission intensities over low-latitudes. The results presented here provide experimental evidence to such circulation alluded to by earlier simulation studies.

1. Introduction

Sudden stratospheric warming (SSW) event is an arctic latitude phenomenon in which the stratosphere warms up by tens of kelvins within a very few days. It is believed that the nonlinear interaction between wintertime-enhanced planetary waves (PW) and the zonal wind results in dramatic changes in zonal mean flow and the consequent momentum deposition warms up the polar stratosphere [e.g., *Matsuno*, 1971; *Labitzke*, 1972; *Andrews et al.*, 1987]. Even though the SSW is mainly a northern hemispheric wintertime phenomenon, numerous observational and modeling studies have demonstrated its influence on the global atmospheric and ionospheric parameters, such as mesosphere lower thermosphere (MLT) temperature, wind and general circulation [e.g., *Liu and Roble*, 2002; *Guharay and Sekar*, 2012; *Chandran et al.*, 2013], total electron content (TEC) [e.g., *Pedatella and Forbes*, 2010; *Yue et al.*, 2010; *Pancheva and Mukhtarov*, 2011; *Goncharenko et al.*, 2013], equatorial electrojet (EEJ) strength [e.g., *Vineeth et al.*, 2009; *Laskar et al.*, 2014], and *F* region vertical drifts [e.g., *Chau et al.*, 2009; *Fejer et al.*, 2011]. The responses in the lower atmospheric parameters were mainly in terms of horizontal mass transport, generation of secondary planetary waves, enhanced semidiurnal tides, and perturbation in general circulation. Whereas, in the ionospheric parameters, the responses that have been reported were mainly in terms of enhanced semidiurnal tidal amplitudes during SSW events which were supported by several modeling studies [e.g., *Fuller-Rowell et al.*, 2011; *Pedatella and Liu*, 2013; *Yamazaki and Richmond*, 2013]. Due to the enhanced semidiurnal tides, various electrodynamical parameters, such as the EEJ, TEC, and $E \times B$ drift, show an enhancement/decrement in the morning/afternoon hours. Further, the quasi 16 day planetary waves are found to be enhanced in proportion to the strength of SSW [*Laskar et al.*, 2014].

Most of the works reported so far on the influence of SSW on the low-latitude upper atmosphere were concentrated mainly on the electrodynamical components, most likely due to the fact that the semidiurnal tidal amplitudes alter the equatorial dynamo mechanism due to which modifications are brought out in

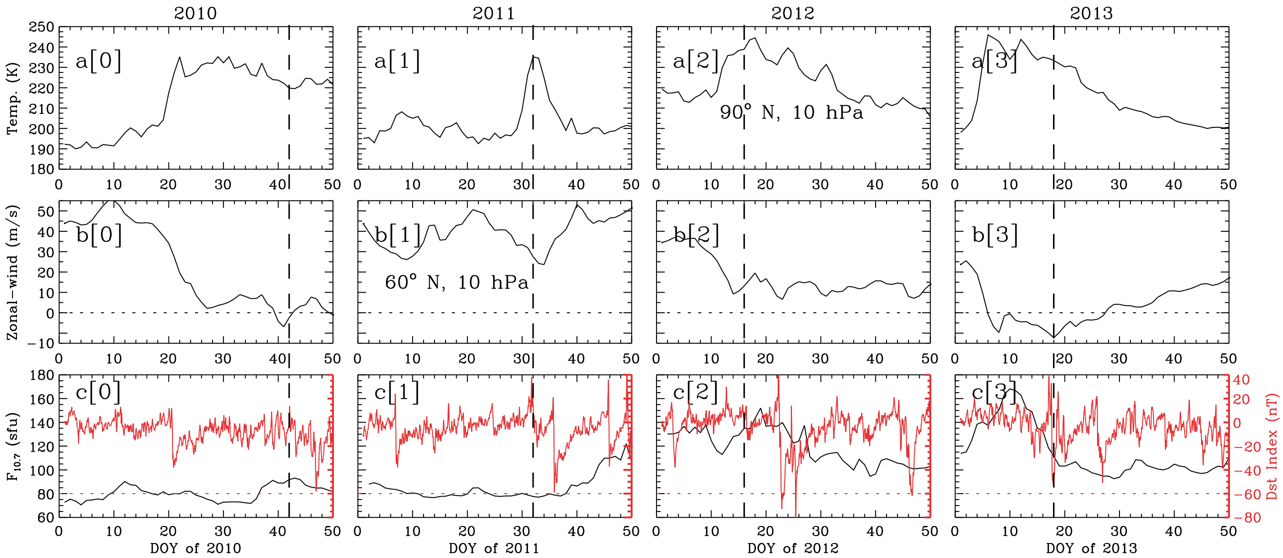

Figure 1. Day-to-day variations of relevant geophysical parameters are shown for the years 2010–2013 (columns). (a) Temperature at 90°N and at 10 hPa pressure level, (b) mean zonal wind magnitudes at 60°N and at 10 hPa level, and (c) the $F_{10.7}$ cm flux and *Dst* index. The vertical dashed line shows the day of enhancements in lower thermospheric temperature over arctic latitudes.

plasma parameters [e.g., *Chau et al.*, 2009; *Sridharan et al.*, 2009]. However, experimental results on the low-latitude thermospheric neutral constituents during SSW events are sparse due to lack of data sets that represent the neutral behavior directly. *Liu et al.* [2011] made use of Challenging Minisatellite Payload (CHAMP) and Gravity Recovery and Climate Experiment satellite data sets and showed a decrease of about 30–45% in thermospheric density at subsolar latitudes during the 2009 SSW event. However, *Fuller-Rowell et al.* [2011] revisited the same observations and interpreted that the compression of the thermosphere was due to the local time sampling of CHAMP data. Instead, they showed that there was a global thermospheric density increase by about 5% when lower atmospheric wave forcing was incorporated into the whole atmosphere model. From these results and others of this kind [e.g., *Liu and Roble*, 2002; *Pedatella and Liu*, 2013], it can be seen that there is a lack of comprehensive understanding of the upper atmospheric neutral behavior during SSW. In order to gain a greater understanding of the influence of this high-latitude phenomenon on the behavior of neutrals in the low-latitude upper atmosphere, systematic daytime optical investigations have been carried out from a low-latitude location, Hyderabad (17.5°N, 78.5°E), in India. Measurements during four recent SSW events in the years 2010, 2011, 2012, and 2013 are used to investigate the characteristic behavior of the low-latitude thermospheric response to the processes at high-latitudes during SSW events.

2. SSW Events of 2010, 2011, 2012, and 2013

Figure 1 summarizes some of the geophysical conditions that were existing during the first 50 days of the years 2010–2013. The occurrence time of the SSW event has been defined by different researchers/communities based on some measurable quantity of interest that is affected by dynamical changes during that time. For example, World Meteorological Organization (WMO) used temperature and wind at 10 hPa pressure level at 60°N latitude [*Andrews et al.*, 1987]. According to WMO, if the stratospheric temperature at 10 hPa pressure level poleward of 60°N increases by more than 25°K within a week, then it is termed as an SSW event. Based on this definition (and temperature at 90°N at 10 hPa level), one can note from Figure 1a that there were four SSW events, one each in the past 4 years, and the effects persisted approximately during day of the year (DOY) 20–50, 30–38, 12–34, and 5–30 in the years 2010, 2011, 2012, and 2013, respectively. Due to the interaction of the PWs with the mean flow and consequent heat deposition, the usual wintertime stratospheric eastward wind becomes weak or reverses its direction. If the zonal mean zonal wind at 10 hPa pressure level at 60°N becomes westward, then the SSW event is characterized as a major event, and if with the increase in temperature the zonal mean wind becomes weak but does not reverse its direction, then it is called a minor SSW event [e.g., *Charlton and Polvani*, 2007; *Chau et al.*, 2012]. Based on this definition, the

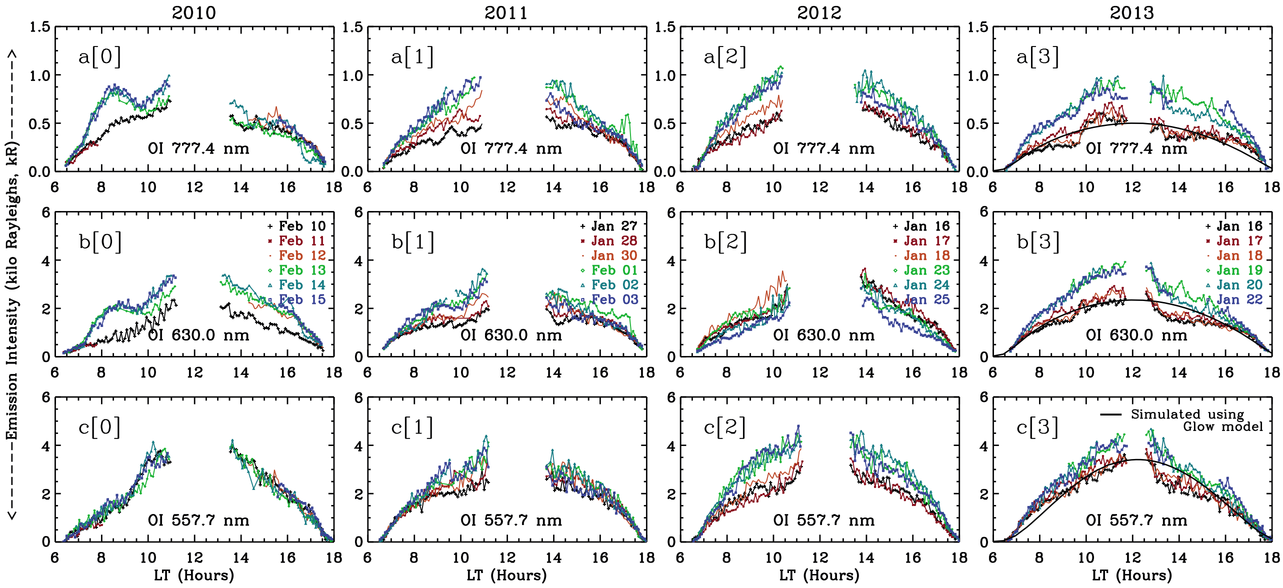

Figure 2. (a–c) Daily variations of the oxygen dayglow emission intensities in and around the SSW events during 2010–2013 are shown. The days in each year are represented by colors as depicted by legends in the middle row. It can be seen that the dayglow intensities throughout the day are enhanced systematically on days during SSW events. The smoothly varying daily behavior in the year 2013 are the emission intensities estimated using the glow model and are used to remove the dominant diurnal solar zenith angle contribution from the observed dayglow emission intensities. Only a few days are included here for brevity. More days are considered in this work as shown in Figure 4.

SSW events in years 2011 and 2012 were minor in nature, whereas, the ones during 2010 and 2013 were major (see Figure 1). The solar activity during SSW events in 2010 and 2011 was relatively weaker compared to the other two events (in 2012 and 2013) as can be seen from the daily averaged 10.7 cm solar radio flux ($F_{10.7}$) in solar flux unit (sfu; 1 sfu = 10^{-22} Wm^{-2} Hz^{-1}) in Figure 1c. Figure 1c also shows the hourly averaged values of *Dst* index whose axes are shown on the rightside of the plots. Unlike the years 2010, 2011, and 2013, in which the values of lowest *Dst* index were greater than −60 nT, in the year 2012, a magnetic disturbance of −73 nT occurred in near simultaneity with the SSW event. The vertical dashed line shows the day on which the lower thermospheric (below 120 km) temperature over arctic latitude has maximized. This has relevance to this study, and this reference has been followed through in Figures 4 and 5.

3. Observations and Results

Measurements of the daytime atomic oxygen (OI) airglow emission intensities at multiple wavelengths are being made from Hyderabad (17.5°N, 78.5°E), India, using a multiwavelength imaging echelle spectrograph (MISE). The details of this and similar kinds of spectrographs have been reported earlier [*Pallamraju et al.*, 2002, 2013]. The column-integrated dayglow emission intensities obtained at OI-557.7, OI-630.0, and OI-777.4 nm represent the behavior of the atmosphere at altitudes from where they emanate, which are dependent on their production mechanisms, and are approximately 130 km (average of the two peaks at 100 km and 160 km), 230 km, and peak height of the ionospheric *F* region, respectively. The three dayglow emissions are produced due to the radiative deexcitation of $O(^1S)$, $O(^1D)$, and $O(^5P)$ states, respectively. These atomic oxygen states are excited mainly due to ambient chemical and photochemical processes. The dominant production mechanisms of $O(^1S)$ state are (1) photoelectron impact on O, (2) photodissociation of O_2, (3) dissociative recombination of O_2^+, and (4) three-body recombination, $O + O + M \rightarrow O(^1S) + O + M$, where M stands for a third body which can be an atom or a molecule [*Solomon and Abreu*, 1989; *Witasse et al.*, 1999]. The $O(^1D)$ state is produced dominantly by the first three production mechanisms of $O(^1S)$ as stated above, albeit with relatively smaller excitation energy requirement as compared to the $O(^1S)$ state [*Witasse et al.*, 1999]. The $O(^5P)$ is mainly produced by radiative recombination ($O^+ + e \rightarrow O(^5P) + e$). Other than the deexcitation via emissions, the excited states are also lost due to collisional quenching with molecular nitrogen and oxygen.

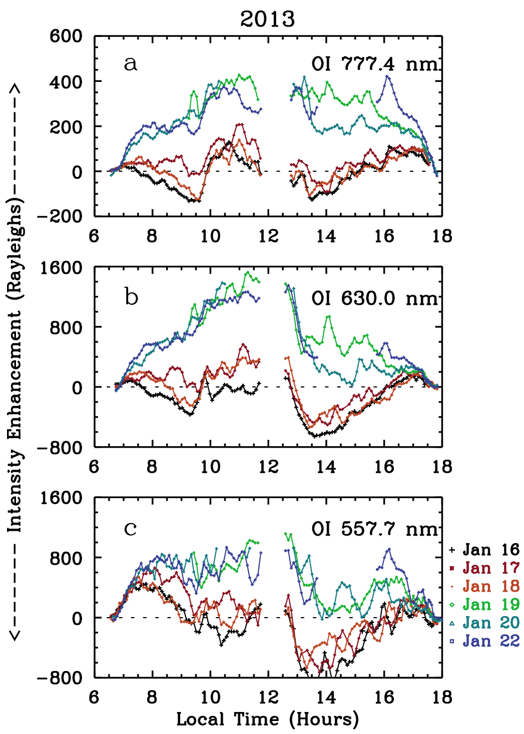

Figure 3. Enhancements in observed OI dayglow intensities as obtained by subtracting the glow model estimates from the measured intensities. The (a) OI-777.4 nm, (b) OI-630.0 nm, and (c) OI-557.7 nm, respectively, for the year 2013 are shown.

Figure 2 shows the daily variations in dayglow emission intensities in rayleighs (R, 1 R = 10^6 photons s^{-1} cm^{-2}) in and around the SSW events in the 4 years under consideration (year 2010, leftmost; 2013, rightmost columns) and at the three wavelengths (OI-777.4 nm: Figure 2a, 630.0 nm: Figure 2b, and OI-557.7 nm: Figure 2c). Data for different days are represented by different colors. The data gap for 1–2.5 h around local noon is due to the saturation of spectral images by incidence of solar glare directly into the slit of the MISE's foreoptics. Cloudy sky conditions prevented observations during 11, 12, and 15 February in 2010 and during 19–22 January in 2012. It can be seen that there are two groups of temporal variations in the dayglow emission intensities, one enhanced and other lower, at all the wavelengths (except the OI-557.7 nm in 2010). It may be noted that the enhancements in dayglow emission intensities are present throughout the day (for the enhanced group), with relatively higher amount of enhancement in the morning hours. Morning enhancement and afternoon depletion have been observed in the ionospheric parameters, such as the $E \times B$ drift and the TEC are explained to be due to enhanced quasi-semidiurnal tides during SSW, which are modulated by enhanced PWs and middle atmospheric dynamics [e.g., *Chau et al.*, 2009; *Jin et al.*, 2012]. However, in the present case of dayglow measurements, in addition to the usual enhancement in the morning hours, the afternoon sector also shows enhanced emissions. The small-scale waves (like gravity waves) are omnipresent and are not expected to occur preferentially and systematically during afternoon hours on all the days in all the years of our observations. Further, the changes in diurnal tide are brought about by in situ solar forcing and not by lower atmospheric waves. So it is very unlikely that the diurnal tides are responsible for the enhancements in the low-latitude dayglow emissions. Thus, it can be argued that in addition to the semidiurnal tidal contribution, some other mechanism must be contributing to the enhancements in the observed dayglow emission intensities.

In order to quantify the amount of enhancement that is other than that due to daily solar zenith angle variation, a physics-based photochemical model, called glow model [*Solomon and Abreu*, 1989], derived emissions have been used. The glow model uses Mass Spectrometer Incoherent Scatter model for neutral atmosphere, International Reference Ionosphere model output for the ionosphere, and solar flux models to predict the dayglow emissions at different wavelengths for a given day. The MISE-measured emissions compare well with the glow model predictions under quiet geomagnetic conditions [*Pallamraju et al.*, 2013]. Simulated profiles using glow model dayglow emission intensity are overplotted in Figure 2 for DOY 18 in the year 2013. Similar profiles are also estimated for the first day listed in Figure 2 in order to remove the dominant daily solar zenith angle-related variations for all the years. Figure 3 shows the differences between the measured dayglow and the glow-modeled emissions for all the three wavelengths under study for the year 2013. Such plots have been obtained for all the years at all the three wavelengths, and the emission enhancements from such curves are integrated to obtain one data point per day per wavelength as shown in Figure 4a. This type of averaging is expected to smooth out, to a great extent, the contributions of the smaller-scale waves and quasi-semi diurnal tidal components, and the resultant is mainly due to the effects that are other than tides and gravity waves. It is clear from Figure 4a that systematic enhancements in daytime intensities at all the emission wavelengths are seen to occur in and around the SSW duration as

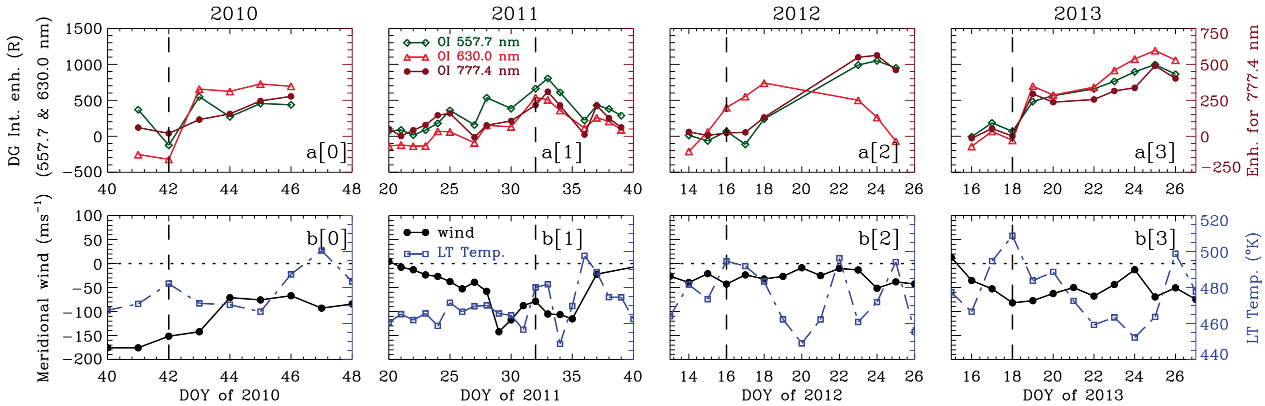

Figure 4. (a) The daily averaged dayglow emission intensity enhancements (observed-simulated) at low-latitudes for OI 557.7 (green), 630.0 (red), and for 777.4 nm (brown) as obtained from plots as shown in Figure 3. The dashed vertical line depicts the day on which peak of the lower thermospheric temperature was observed during a given SSW event. (b) TIDI-measured representative MLT daily averaged zonal mean wind (at 95 km altitude) 60°–80°N latitudes (filled circles, left axis) along with the SABER-measured lower thermospheric (local time; 119 km) kinetic temperature (squares, right axis) over arctic latitudes. A clear enhancement in dayglow intensities during SSW events can be seen. Notably, in all the years, the MLT winds are equatorward (negative) in simultaneity with the observed dayglow emission intensity enhancements at all the three wavelengths as shown in Figure 4a.

mentioned above, especially a maximum enhancement can be seen after the day (shown as a dashed vertical line) with increase in lower thermospheric temperature over high-latitudes. Arguments are presented in the Discussion section with supporting evidences to show that these enhancements in oxygen emission intensities over low-latitudes in all these years are caused due to the effects associated with SSW event at arctic latitudes.

It may be noted from Figure 4a that the daily averaged intensity enhancements are seen around the duration of SSW occurrence and return to normal levels after the cessation of SSW as can be seen clearly, especially, for the year 2011 for which longest span of optical data is available. From Figure 4a, it is notable that enhancements in intensities at all the wavelengths for the case of 2013 are higher compared to that of 2011, which is believed to be due to the fact that the 2013 SSW event was stronger and prolonged. The low-latitude upper thermospheric behavior is shown to be more sensitive to lower atmospheric forcing and high-latitude disturbances during low solar activity epoch [*Fuller-Rowell et al.*, 2011; *Laskar et al.*, 2013, 2014], and so even though 2011 was a minor event, it produced an appreciable response (in terms of emission intensity enhancement) in comparison to that of 2010 as can be seen in Figures 2 or 4a. Moreover, the 2010 SSW event was major and occurred during low solar activity period and thus showed a greater response/enhancement in intensities as can be seen in Figures 2a and 2b. Although 2013 event occurred during relatively higher solar activity level, it was much stronger in strength and longer in duration compared to 2010, and so the response in dayglow emissions was greater in 2013 as compared to 2010. The relative variation in intensity enhancements in these emissions is most likely due to the differences in their production mechanisms and the different altitudes at which these emissions originate.

4. Discussions

From the production mechanisms of the dayglow emissions mentioned above, it can be seen that the variations in intensities of the atmospheric dayglow emissions are brought about mainly due to (i) variations in the sources of energy (solar flux [e.g., *Zhang and Shepherd*, 2004, 2005; *Pallamraju et al.*, 2010]), (ii) variations in the densities of the constituents due to wave-induced perturbations/modifications [*Chakrabarty et al.*, 2004; *Pallamraju et al.*, 2010], and (iii) compositional changes (such as those brought about by geomagnetic disturbances) [*Pallamraju et al.*, 2002; *Culot et al.*, 2005; *Shepherd and Shepherd*, 2011]. As discussed in section 2, except for the 2012 event, the other three SSW events were relatively magnetically quiet, and so the emission enhancements other than those in the year 2012 are not expected to be due to geomagnetic storm effects. Also, the daily averaged $F_{10.7}$ solar flux in the observation windows in all these years were either decreasing (for 2013) or are very low and fairly stable (for 2010 and 2011), and therefore, the enhancements in the dayglow emission intensities reported here are clearly not due to an increase in the solar flux. Using numerical model simulations, earlier works [*Akmaev and Shved*, 1980; *Forbes et al.*, 1993] showed that tidal influence induces heating and O_2 and N_2 density enhancement in the thermosphere above 100 km, resulting in the depletion of atomic oxygen due to enhanced recombination rate. Also, the mixing effect due to dissipating tides in the thermosphere reduces the mass mixing ratio of atomic oxygen [*Yamazaki and Richmond*, 2013]. But in our observation, we see enhancement in atomic oxygen dayglow emissions throughout the day, which, to the first order, is unlikely to be due to tidal dissipations (however, these effects need to be quantified with greater experimental and simulation studies). Also, the gravity waves are not expected to produce an enhancement of the emission intensities in such systematic manner at all the local times as seen in the dayglow intensities consistently for the four SSW events that are presented here. Therefore, the plausible cause for the enhancements in dayglow intensities is considered to be due to compositional changes brought about directly or indirectly due to the large-scale processes that get formed during SSW events.

During SSW events, the usual wintertime stratospheric eastward zonal wind at high-latitudes becomes westward, which allows eastward gravity waves to propagate to the MLT region. Because of this eastward gravity wave forcing, there occurs an upward and equatorward circulation in the MLT region as seen in simulation studies [*Liu and Roble*, 2002]. This circulation induces adiabatic cooling in the mesosphere and warming in the lower thermosphere over high-latitudes as reported by both observational and modeling studies [*Walterscheid et al.*, 2000; *Liu and Roble*, 2002; *Funke et al.*, 2010]. In order to assess the high-latitude dynamical conditions, the temperature and wind during the events of our observations in the past 4 years are investigated. The thermospheric kinetic temperature data from Sounding of the Atmosphere using Broadband Emission Radiometry (SABER) instrument onboard Thermosphere-Ionosphere-Mesosphere Energetics and Dynamics (TIMED) satellite and meridional wind from TIMED Doppler Interferometer (TIDI) have been retrieved and are shown in Figure 4b. The kinetic temperature (data version: v1.07) is retrieved from the atmospheric 15 μm CO_2 limb emission. In the winter polar region, the error in kinetic temperature at around 75 to 95 km altitudes is ±1–2 K and increases to about ±4–5 K at altitudes of 100 km and above [*Russell et al.*, 1999; *García-Comas et al.*, 2008]. Temperatures at the highest altitudes possible by SABER at around 120 km (average of 118–120 km) in the 60°N–80°N latitude and 20°E–140°E longitude bin are considered here. It can be seen that there is a signature of increase in lower thermospheric (120 km altitude) temperature during the SSW events of the years 2010 (DOY 42), 2011 (DOY 32), 2012 (DOY 16), and 2013 (DOY 18) by about 15 (~465 to ~480), 15 (~465 to ~480), 20 (~475 to ~495), and 25 (~485 to ~510)°K, respectively. These enhancements are marked by dashed vertical lines, and the other enhancements are due to geomagnetic activity as can be verified from the reduced *Dst* index in Figure 1c. One can note from the 2012 data that the magnitude of the lower thermospheric temperature enhancement due to SSW is comparable with that due to moderate storm on DOY 22, but the former is for longer duration. This suggests that the effect on upper atmosphere due to dynamical changes during SSW can be greater or comparable to that of geomagnetic storms as the former lasts for longer duration.

Figure 4b also shows zonal mean (averaged over 0°–360° longitudes) meridional wind (data level 3, version 10) in the MLT altitude (a representative height of 95 km is shown here) in the 60°N–80°N latitude region obtained by TIDI. (As TIDI has fewer data points in a particular time-space bin and higher percentage error compared to SABER, an average of the whole longitude sector has been considered, as compared to SABER, to reduce statistical fluctuations.) The zonally averaged winds have errors of ±7 ms^{-1} and ±15 ms^{-1} during day and night, respectively. The details of the TIDI instrument and method of derivation of winds are described by *Killeen et al.* [2006]. One may note that the meridional winds in Figure 4b are equatorward in and around the SSW events. This behavior of winds has been observed in the whole MLT region (85–115 km); however, only a representative behavior at 95 km is shown here, as data availability around this altitude level is higher. One can note that the meridional wind for the year 2011 in Figure 4b starts becoming equatorward from DOY 21, while the stratospheric temperature for the same year as shown in Figure 1a started to rise from DOY 28. This seems to be consistent with some of the earlier studies [e.g., *Liu and Roble*, 2002; *Funke et al.*, 2010], which reported signatures of the SSW much earlier in the mesospheric parameters than in those of stratosphere.

It has been noted that during SSW events, while the high-latitude MLT wind is equatorward for several days, the lower thermospheric temperature enhancement, on the other hand, persists only for a few days. The exact reason for this is not known; however, one of the possibilities may be that the lower thermospheric temperature enhancement occurs at an altitude higher than the highest altitude (of 120 km) that is currently

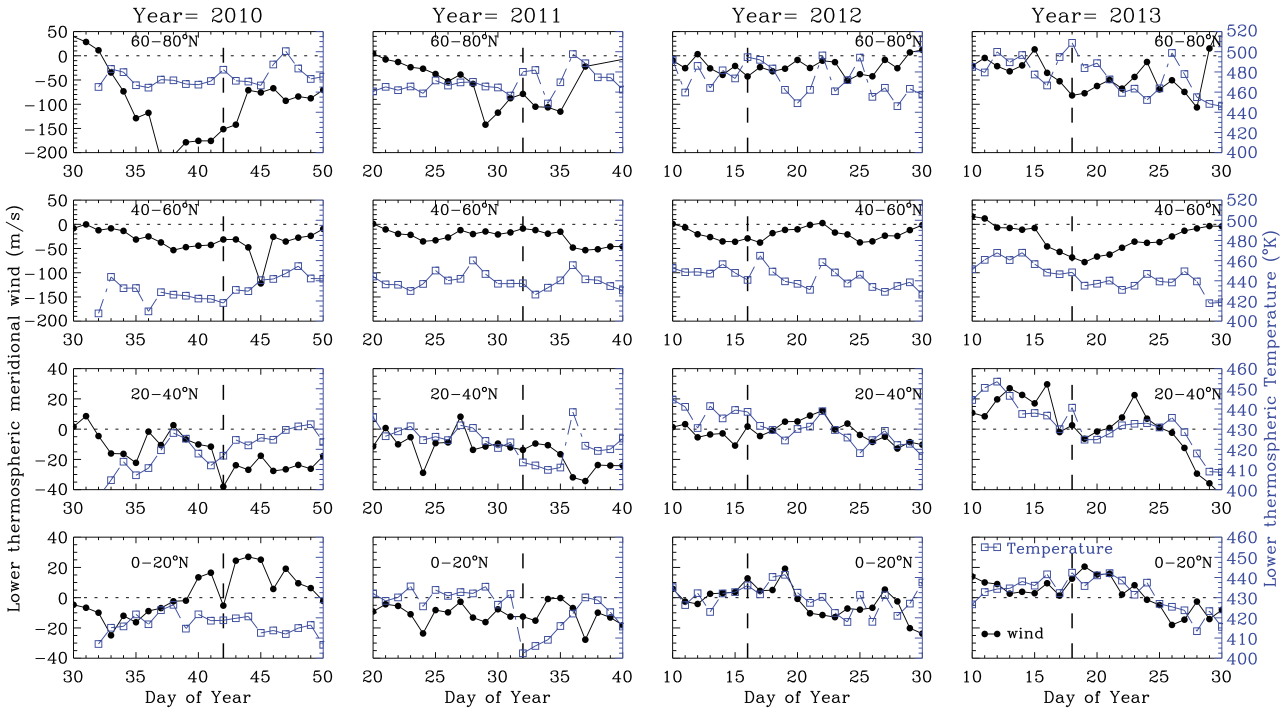

Figure 5. Longitudinally averaged TIMED Doppler interferometer (TIDI)-measured meridional winds (positive for poleward) at 95 km and SABER-measured temperatures at lower thermospheric heights (118–120 km) and at 20° latitude bins (0°N–20°N, 20°N–40°N, 40°N–60°N, and 60°N–80°N) are shown. One can note that the winds are equatorward (negative) during the SSW events in all the years. One can also note that the temperatures are higher over high-latitudes compared to the low-latitudes with a clear latitudinal gradient in all the years, with simultaneous equatorward meridional winds.

obtainable by SABER. Thus, assuming that the lower thermospheric temperature enhancement has occurred at altitudes greater than 120 km along with the equatorward turning of MLT winds, the peak warming at altitudes below 120 km has been seen with some delay. This is analogous to that in the stratospheric level, where the SSW-related warming first occur at upper stratosphere and then reaches 10 hPa pressure level with a delay of a few days. Interestingly, the low-latitude dayglow enhancements are found to be highest just after these arctic latitude temperature enhancements (below 120 km). The plausible reason for this will be explained in the following paragraphs.

Figure 5 shows the MLT region temperature and winds organized in 20° latitude bins (at 0°N–20°N, 20°N–40°N, 40°N–60°N, and 60°N–80°N) for the 4 years of interest. As in Figure 4, in Figure 5 as well, the temperatures and meridional winds correspond to about 119 km and 95 km altitudes. It can be noted that the lower thermospheric temperatures are higher over high-latitudes as compared to those at low-latitudes with a clear latitudinal gradient in all the years. Especially, in the year 2011, it can be noted that there exists a sudden cooling over lower thermosphere at low-latitudes (in the latitude range of 0°N–20°N). In other years, however, it is possible that the cooling might have occurred above 120 km (which is beyond the altitude of available information from SABER). This equatorward gradient in temperatures indicates that the conditions are favorable for an equatorward wind. It may be noted that the TIDI-measured meridional wind is equatorward from high-to-low latitudes. Further, it is seen that the equatorward wind in the MLT region becomes weaker from high-to-low latitudes. This is understandable; as one moves away from the source of activity, which is in high-latitudes, the strength of the winds is expected to decrease. It should also be appreciated that the Coriolis acceleration enhances the zonal component of the equatorward wind at the cost of the meridional one as it approaches toward low-latitudes. Nevertheless, due to the presence of such high-to-low-latitude winds in the MLT region, the dominant species in the lower thermosphere (oxygen) is transported toward low-latitudes due to wind-induced diffusion and advection [*Mayer et al.*, 1978]. At latitudes below 40°N, the wind strengths are smaller, and so diffusive transport may play an important role. The latitudinal characteristics and strength of such circulation depends on magnitude of the SSW-time equatorward meridional wind, season, and Coriolis acceleration in the MLT region.

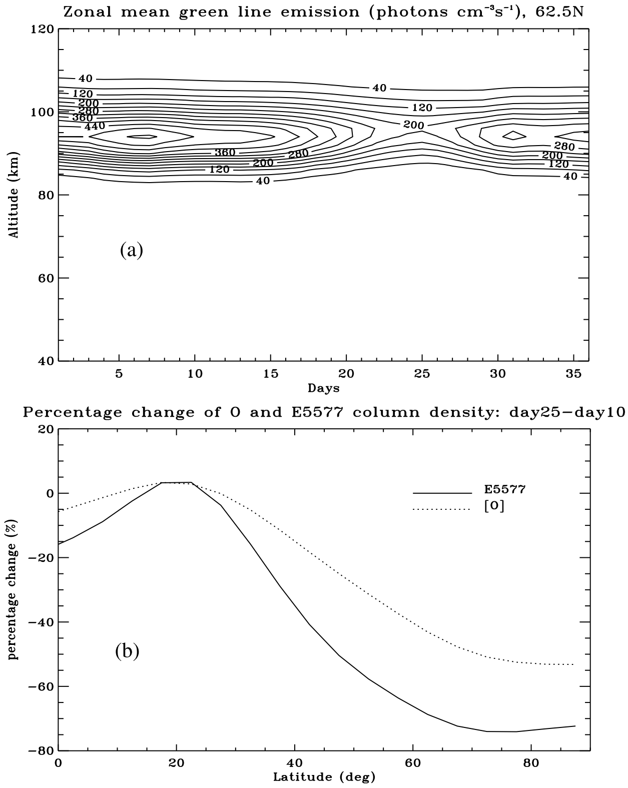

Figure 6. TIME-GCM/CCM3 simulation results on the dynamics during SSW events. (a) Green line (557.7 nm) emission rate (in photons cm^{-3} s^{-1}) at 62.5°N between day 1 and 36 showing a decrement with increase in SSW temperatures. (b) Latitudinal distribution of the relative changes of atomic oxygen column density (dotted line) and height-integrated green line emission rate (solid line) at local midnight between day 10 and day 25, indicating an increase in OI 557.7 nm airglow intensity owing to increase in oxygen density. In this simulation, the stratospheric warming started on day 13 and peaked on day 25 (from *Liu and Roble* [2002], reproduced with permission from Wiley publications).

Due to the presence of meridional wind in the equatorward direction as described above, the oxygen-rich air through the lower thermosphere reaches the low-latitudes, where it is superposed with SSW-time-enhanced tides and daytime lower thermospheric upward winds [*Roble*, 1977; *Akmaev and Shved*, 1980], thereby giving rise to a resultant enhancement in emissions at all the three wavelengths that emanate from varying heights. At higher altitudes, these winds merge with the seasonal (hotter to cooler thermospheric south to north) transequatorial wind [*Mayer et al.*, 1978]. Photochemical modeling studies of airglow show that an increase in oxygen densities contributes positively to an enhancement in the oxygen dayglow emission intensities [e.g., *Melendez-Alvira et al.*, 1995; *Pallamraju et al.*, 2004]. Thus, this transport of oxygen-rich air from high-latitudes does seem plausible to explain the enhancement in the observed daytime oxygen airglow intensities obtained over low-latitudes during SSW periods.

Figure 6 reproduced here from the work of *Liu and Roble* [2002] (Figures 14b and 14c of that study) supports the proposition being made in our work. *Liu and Roble* [2002] used thermosphere-ionosphere-mesosphere electrodynamics–general circulation model/Community Climate Model Version 3 (TIME-GCM/CCM3) and demonstrated a depletion of atomic oxygen number density at around 100 km altitude over high and middle latitudes and enhancement over low-latitudes for a self-consistently simulated SSW event. In their simulation, the stratospheric warming started on day 13 and peaked on day 25. The latitudinal distribution of the relative changes of atomic oxygen column density and height integrated green line emission rate at local midnight between day 10 and day 25 show a decrease at arctic latitudes and an increase around 20°N latitude (Figure 6b). It is notable that the dayglow observations reported in this paper are also obtained over a region at around 20°N latitudes. Thus, the modeling study, in a way, provides credence to our proposition of transport of oxygen densities from high-to-low latitudes during SSW. This transport is attributed to be the cause for the rise in the empirically measured daytime oxygen emission intensities over low-latitudes. Further, our results show enhancement in oxygen dayglow emission intensities, not only at OI-557.7 nm, as predicted by TIME-GCM/CCM3 model simulation results by *Liu and Roble* [2002], but also at the emission wavelengths of OI-630.0 and OI-777.4 nm that emanate from higher altitudes. Thus, both modeling and observational results support the proposition of the mesosphere-thermosphere meridional circulation during SSW events.

Further, the argument of depletion of oxygen in the lower thermosphere over high-latitudes is also supported by the observation of oxygen dayglow emissions over high-latitudes from Wind Imaging Interferometer onboard Upper Atmosphere Research Satellite [*Shepherd and Shepherd*, 2011]. In that study, the OI-557.7 nm dayglow volume emission rate above 140 km over 50°N–70°N latitudes was found to be depleted during the

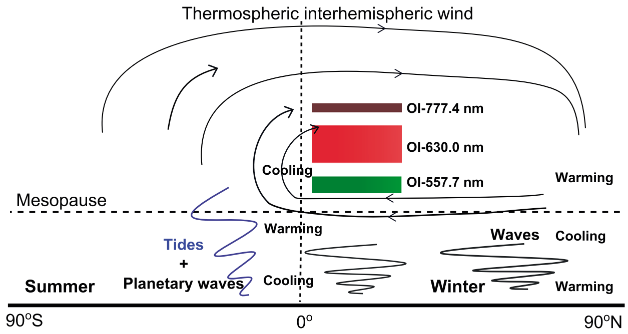

Figure 7. A simplistic schematic (not to scale) depicting the SSW-time additional meridional circulation cell that is proposed in the mesosphere-thermosphere system. The lines with arrowheads represent the direction and path of the winds. The dominant species in the lower thermosphere are transported with the wind through wind-induced diffusion. Due to this oxygen-rich air from high-to-low-latitude thermosphere, all the low-latitude thermospheric oxygen emission intensities show simultaneous enhancement. The horizontal color bars show the representative altitudes from where the oxygen emissions originate.

SSW event of February 1993. Moreover, by using whole atmosphere general circulation model, *Fuller-Rowell et al.* [2011] showed a possible global upper thermospheric warming and density increase by 5% during SSW event of January 2009. Thus, the current study provides a comprehensive experimental evidence to the numerical studies that alluded to thermospheric circulation during SSW events using several case studies.

Considering the results in the present paper for low-latitude dayglow and wind and temperature from northern hemisphere, in conjunction with those obtained for high and middle latitudes in both observational and modeling studies reported earlier, it is conjectured that a new meridional circulation in neutrals is set up during SSW events, which is responsible for the transport of oxygen to low-latitudes. This is similar (but opposite in direction) to the circulation that gets set up during SSW events in the stratosphere and lower mesosphere that extend from pole to equator [*Andrews et al.*, 1987, p. 276]. Moreover, it seems that our proposition is a part of the pole-to-pole (winter-to-summer) circulation in the mesosphere as indicated by *Espy et al.* [2003] and *Cho et al.* [2011]. Based on the arguments put forth and supporting evidences reported in literature, a simplistic schematic of the additional meridional circulation cell, produced during SSW in the mesosphere-thermosphere, is presented in Figure 7, wherein the lines with arrow heads represent the direction and path of meridional wind. Due to such an MLT region circulation, the oxygen-rich air from high-latitudes reaches low-latitudes through the lower thermosphere where it is superposed with daytime upward winds in the lower thermosphere, enhanced tidal activity during SSW, and then merges with the seasonal south-to-north transequatorial wind in the thermosphere. Because of such combined activity, an increase in the oxygen number density over northern hemispheric low-latitudes is believed to occur, which is attributed to be the cause of enhancement in the daytime optical emission intensities as reported in this study.

To the best of our knowledge, the observational evidence of setting up of the mesosphere-thermosphere meridional circulation during SSW events, as demonstrated here, has not been shown earlier. The results presented in this study, thus, bring to light the effect of the high-latitude stratospheric processes on the behavior of neutrals in the low-latitude thermosphere and the global scale mesosphere-thermosphere circulation that seems to be existing during SSW events. The results reported here describe the experimental observations and present a possible scenario of wind circulation. These results do call for more experimental observations of winds and temperatures (both in situ and remote) in the mesosphere-thermosphere region and detailed time-dependent physics-based modeling (that includes time-varying effects of tides and gravity waves) studies to bring to light all the consequences that are associated with the SSW events globally.

5. Summary

The SSW events during the relatively low and moderate solar activity period of 2010–2013 are studied, wherein systematic investigation of their effect on low-latitude upper atmosphere is carried out using oxygen dayglow emission intensities at 557.7, 630.0, and 777.4 nm. All these emissions are found to be enhanced within the SSW event durations in all these years. The enhancement in dayglow emission intensities in the case of the major warming in 2013 is found to be higher compared to the minor warming in 2011, suggesting that the optical emission enhancements depend on SSW strength. SABER-measured lower thermospheric temperatures over high-latitudes were found to be enhanced during all the SSW events. Independently measured TIDI meridional winds at MLT altitudes over arctic latitudes show the existence of equatorward winds during SSW events. The lower thermospheric heating over high-latitudes is produced by the downwelling/adiabatic compression. Therefore, it is proposed that an additional meridional circulation in lower thermospheric winds is set up, which transport atomic oxygen from high-to-low latitudes during the SSW events. This redistribution of oxygen brought in due to the circulation is believed to be the cause of systematic enhancement in the dayglow emission intensities observed over low-latitudes for all the SSW events that occurred in the past 4 years. The current study is an experimental evidence to such circulation alluded to by numerical simulation studies carried out earlier for SSW events. This study also reveals the significance of the influence of the high-latitude stratospheric phenomena on the low-latitude thermospheric behavior.

Acknowledgments
We are grateful to the SABER team for access to the data on http://saber.gats-inc.com and NOAA/OAR/ESRL PSD, Boulder, Colorado, USA, for the NCEP/NCAR Reanalysis data on the website at http://www.esrl.noaa.gov/psd/. We are thankful to the members of the TIMED/TIDI satellite team for providing access to the online data at ftp://tidi.engin.umich.edu/tidi/vector/. The $F_{10.7}$ solar flux and *Dst* index data are obtained from NASA OMNIWeb. We thank Stan Solomon for the GLOW model. We thank R. Sekar for going through a draft of this manuscript and suggesting improvements. This work is supported by Department of Space, Government of India.

Michael Liemohn thanks the reviewers for their assistance in evaluating this paper.

References

Akmaev, R. . A., and G. . M. Shved (1980), Modeling of the composition of the lower thermosphere taking into account of the dynamics with applications to tidal variations of the [OI] 5577 Å airglow, *J. Atmos. Terr. Phys.*, *42*, 705–716.

Andrews, D. G., J. R. Holton, and C. B. Leovy (1987), *Middle Atmosphere Dynamics*, 489 pp., Academic, San Diego, Calif.

Chakrabarty, D., R. Sekar, R. Narayanan, T. K. Pant, and K. Niranjan (2004), Thermospheric gravity wave modes over low and equatorial latitudes during daytime, *J. Geophys. Res.*, *109*, A12309, doi:10.1029/2003JA010169.

Chandran, A., R. R. Garcia, R. L. Collins, and L. C. Chang (2013), Secondary planetary waves in the middle and upper atmosphere following the stratospheric sudden warming event of January 2012, *Geophys. Res. Lett.*, *40*, 1861–1867, doi:10.1002/grl.50373.

Charlton, A. J., and L. M. Polvani (2007), A new look at stratospheric sudden warmings: Part I. Climatology and modeling benchmarks, *J. Clim.*, *20*, 449–469.

Chau, J. L., B. G. Fejer, and L. P. Goncharenko (2009), Quiet variability of equatorial E × B drifts during a sudden stratospheric warming event, *Geophys. Res. Lett.*, *36*, L05101, doi:10.1029/2008GL036785.

Chau, J. L., L. Goncharenko, B. Fejer, and H.-L. Liu (2012), Equatorial and low latitude ionospheric effects during sudden stratospheric warming events, *Space Sci. Rev.*, *168*, 385–417, doi:10.1007/s11214-011-9797-5.

Cho, Y.-M., G. G. Shepherd, M. G. Shepherd, W. K. Hocking, N. J. Mitchell, and Y.-I. Won (2011), A study of temperature and meridional wind relationships at high northern latitudes, *J. Atmos. Sol. Terr. Phys.*, *73*(9), 936–943, doi:10.1016/j.jastp.2010.08.011.

Culot, F., C. Lathuillère, and J. Lilensten (2005), Influence of geomagnetic activity on the O I 630.0 and 557.7 nm dayglow, *J. Geophys. Res.*, *110*, A01304, doi:10.1029/2004JA010667.

Espy, P. J., R. E. Hibbins, G. O. L. Jones, D. M. Riggin, and D. C. Fritts (2003), Rapid, large-scale temperature changes in the polar mesosphere and their relationship to meridional flows, *Geophys. Res. Lett.*, *30*(5), 1240, doi:10.1029/2002GL016452.

Fejer, B. G., B. D. Tracy, M. E. Olson, and J. L. Chau (2011), Enhanced lunar semidiurnal equatorial vertical plasma drifts during sudden stratospheric warmings, *Geophys. Res. Lett.*, *38*, L21104, doi:10.1029/2011GL049788.

Forbes, J. M., R. G. Roble, and C. G. Fesen (1993), Acceleration, heating, and compositional mixing of the thermosphere due to upward propagating tides, *J. Geophys. Res.*, *98*, 311–321, doi:10.1029/92JA00442.

Fuller-Rowell, T., R. Akmaev, F. Wu, M. Fedrizzi, R. A. Viereck, and H. Wang (2011), Did the January 2009 sudden stratospheric warming cool or warm the thermosphere?, *Geophys. Res. Lett.*, *38*, L18104, doi:10.1029/2011GL048985.

Funke, B., M. Lpez-Puertas, D. Bermejo-Pantalen, M. Garca-Comas, G. P. Stiller, T. von Clarmann, M. Kiefer, and A. Linden (2010), Evidence for dynamical coupling from the lower atmosphere to the thermosphere during a major stratospheric warming, *Geophys. Res. Lett.*, *37*, L13803, doi:10.1029/2010GL043619.

García-Comas, M., et al. (2008), Errors in Sounding of the Atmosphere using Broadband Emission Radiometry (SABER) kinetic temperature caused by non local thermodynamic-equilibrium model parameters, *J. Geophys. Res.*, *113*, D24106, doi:10.1029/2008JD010105.

Goncharenko, L., J. L. Chau, P. Condor, A. Coster, and L. Benkevitch (2013), Ionospheric effects of sudden stratospheric warming during moderate-to-high solar activity: Case study of January 2013, *Geophys. Res. Lett.*, *40*, 4982–4986, doi:10.1002/grl.50980.

Guharay, A., and R. Sekar (2012), Signature of latitudinal coupling during a major sudden stratospheric warming in the tropics, *J. Atmos. Sol. Terr. Phys.*, *75*, 122–126.

Jin, H., Y. Miyoshi, D. Pancheva, P. Mukhtarov, H. Fujiwara, and H. Shinagawa (2012), Response of migrating tides to the stratospheric sudden warming in 2009 and their effects on the ionosphere studied by a whole atmosphere-ionosphere model GAIA with COSMIC and TIMED/SABER observations, *J. Geophys. Res.*, *117*, A10323, doi:10.1029/2012JA017650.

Killeen, T. L., Q. Wu, S. C. Solomon, D. A. Ortland, W. R. Skinner, R. J. Niciejewski, and D. A. Gell (2006), TIMED Doppler interferometer: Overview and recent results, *J. Geophys. Res.*, *111*, A10S01, doi:10.1029/2005JA011484.

Labitzke, K. (1972), Temperature changes in the mesosphere and stratosphere connected with circulation changes in winter, *J. Atmos. Sci.*, *29*, 756–766, doi:10.1175/1520-0469(1972)029<0756:TCITMA>2.0.CO;2.

Laskar, F. I., D. Pallamraju, T. V. Lakshmi, M. A. Reddy, B. M. Pathan, and S. Chakrabarti (2013), Investigations on vertical coupling of atmospheric regions using combined multiwavelength optical dayglow, magnetic, and radio measurements, *J. Geophys. Res. Space Physics*, *118*, 4618–4627, doi:10.1002/jgra.50426.

Laskar, F. I., D. Pallamraju, and B. Veenadhari (2014), Vertical coupling of atmospheres: Dependence on strength of sudden stratospheric warming and solar activity, *Earth Planets Space*, *66*(1), 94, doi:10.1186/1880-5981-66-94.

Liu, H., E. Doornbos, M. Yamamoto, and S. T. Ram (2011), Strong thermospheric cooling during the 2009 major stratosphere warming, *Geophys. Res. Lett.*, *38*, L12102, doi:10.1029/2011GL047898.

Liu, H.-L., and R. G. Roble (2002), A study of a self-generated stratospheric sudden warming and its mesospheric–lower thermospheric impacts using the coupled TIME-GCM/CCM3, *J. Geophys. Res.*, *107*(D23), 4695, doi:10.1029/2001JD001533.

Matsuno, T. (1971), A dynamical model of the stratospheric sudden warming, *J. Atmos. Sci.*, *28*(8), 1479–1494, doi:10.1175/1520-0469(1971)028<1479:ADMOTS>2.0.CO;2.

Mayer, H. G., I. Harris, and N. W. Spencer (1978), Some properties of upper atmosphere dynamics, *Rev. Geophys.*, *16*, 539–565, doi:10.1029/RG016i004p00539.

Melendez-Alvira, D. J., D. G. Torr, P. G. Richards, W. R. Swift, M. R. Torr, T. Baldridge, and H. Rassoul (1995), Sensitivity of the 6300 Å twilight airglow to neutral composition, *J. Geophys. Res.*, *100*, 7839–7853, doi:10.1029/94JA02487.

Pallamraju, D., J. Baumgardner, and S. Chakrabarti (2002), HIRISE: A ground-based high-resolution imaging spectrograph using echelle grating for measuring daytime airglow/auroral emissions, *J. Atmos. Sol. Terr. Phys.*, *64*, 1581–1587, doi:10.1016/S1364-6826(02)00095-0.

Pallamraju, D., S. Chakrabarti, and C. E. Valladares (2004), Magnetic storm-induced enhancement in neutral composition at low latitudes as inferred by O(^{1}D) dayglow measurements from Chile, *Ann. Geophys.*, *22*(9), 3241–3250, doi:10.5194/angeo-22-3241-2004.

Pallamraju, D., U. Das, and S. Chakrabarti (2010), Short- and long-timescale thermospheric variability as observed from OI 630.0 nm dayglow emissions from low latitudes, *J. Geophys. Res.*, *115*, A06312, doi:10.1029/2009JA015042.

Pallamraju, D., F. I. Laskar, R. P. Singh, J. Baumgardner, and S. Chakrabarti (2013), MISE: A multiwavelength imaging spectrograph using echelle grating for daytime optical aeronomy investigations, *J. Atmos. Sol. Terr. Phys.*, *103*, 176–183, doi:10.1016/j.jastp.2012.12.003.

Pancheva, D., and P. Mukhtarov (2011), Stratospheric warmings: The atmosphere-ionosphere coupling paradigm, *J. Atmos. Sol. Terr. Phys.*, *73*, 1697–1702, doi:10.1016/j.jastp.2011.03.006.

Pedatella, N. M., and J. M. Forbes (2010), Evidence for stratosphere sudden warming ionosphere coupling due to vertically propagating tides, *Geophys. Res. Lett.*, *37*, L11104, doi:10.1029/2010GL043560.

Pedatella, N. M., and H.-L. Liu (2013), The influence of atmospheric tide and planetary wave variability during sudden stratosphere warmings on the low latitude ionosphere, *J. Geophys. Res. Space Physics*, *118*, 5333–5347, doi:10.1002/jgra.50492.

Roble, R. G. (1977), *The Upper Atmosphere and Magnetosphere*, pp. 57, National Academy of Science, Washington, D. C.

Russell, J. M., III, M. G. Mlynczak, L. L. Gordley, J. Tansock, and R. Esplin (1999), An overview of the SABER experiment and preliminary calibration results, *Proc. SPIE Int. Soc. Opt. Eng.*, *3756*, 277–288.

Shepherd, M. G., and G. G. Shepherd (2011), Stratospheric warming effects on thermospheric O(^{1}S) dayglow dynamics, *J. Geophys. Res.*, *116*, A11327, doi:10.1029/2011JA016762.

Solomon, S. C., and V. J. Abreu (1989), The 630 nm dayglow, *J. Geophys. Res.*, *94*, 6817–6824, doi:10.1029/JA094iA06p06817.

Sridharan, S., S. Sathishkumar, and S. Gurubaran (2009), Variabilities of mesospheric tides and equatorial electrojet strength during major stratospheric warming events, *Ann. Geophys.*, *27*, 4125–4130.

Vineeth, C., T. K. Pant, and R. Sridharan (2009), Equatorial counter electrojets and polar stratospheric sudden warmings—A classical example of high latitude-low latitude coupling?, *Ann. Geophys.*, *27*, 3147–3153, doi:10.5194/angeo-27-3147-2009.

Walterscheid, R., G. Sivjee, and R. G. Roble (2000), Mesospheric and lower thermospheric manifestations of a stratospheric warming event over Eureka, Canada (80°N), *Geophys. Res. Lett.*, *27*, 2897–2900, doi:10.1029/2000GL003768.

Witasse, O., J. Lilensten, C. Lathuillère, and P.-L. Blelly (1999), Modeling the OI 630.0 and 557.7 nm thermospheric dayglow during EISCAT-WINDII coordinated measurements, *J. Geophys. Res.*, *104*, 24,639–24,655, doi:10.1029/1999JA900260.

Yamazaki, Y., and A. D. Richmond (2013), A theory of ionospheric response to upward-propagating tides: Electrodynamic effects and tidal mixing effects, *J. Geophys. Res. Space Physics*, *118*, 5891–5905, doi:10.1002/jgra.50487.

Yue, X., W. S. Schreiner, J. Lei, C. Rocken, D. C. Hunt, Y.-H. Kuo, and W. Wan (2010), Global ionospheric response observed by COSMIC satellites during the January 2009 stratospheric sudden warming event, *J. Geophys. Res.*, *115*, A00G09, doi:10.1029/2010JA015466.

Zhang, S. P., and G. G. Shepherd (2004), Solar influence on the O(^{1}D) dayglow emission rate: Global-scale measurements by WINDII on UARS, *Geophys. Res. Lett.*, *31*, L07804, doi:10.1029/2004GL019447.

Zhang, S. P., and G. G. Shepherd (2005), On the response of the O(^{1}S) dayglow emission rate to the sun's energy input: An empirical model deduced from WINDII/UARS global measurements, *J. Geophys. Res.*, *110*, A03304, doi:10.1029/2004JA010887.

Laskar et al. Earth, Planets and Space 2014, 66:94
http://www.earth-planets-space.com/content/66/1/94

Earth, Planets and Space
a SpringerOpen Journal

FULL PAPER Open Access

Vertical coupling of atmospheres: dependence on strength of sudden stratospheric warming and solar activity

Fazlul I Laskar[1,2*], Duggirala Pallamraju[1] and Bhaskara Veenadhari[3]

Abstract

Comprehensive behavior of the low-latitude upper atmosphere during sudden stratospheric warming (SSW) events at varying levels of solar activity has been investigated. The equatorial electrojet (EEJ) strength and the total electron content (TEC) data from low latitudes over Indian longitudes during the mid-winter season in the years 2005 to 2013 are used in this study. Five major and three minor SSW events occurred in the observation duration, wherein the solar activity had varied from minimum (almost no sunspots) to mini-maximum (approximately 50 sunspots of the solar cycle 24). Spectral powers of the large-scale planetary wave (PW) features in the EEJ and the TEC have been found to be varying with solar activity and SSW strengths. Specially, the spectral powers of quasi-16-day wave variations during the three very strong SSW events in the years 2006, 2009, and 2013 were found to be very high in comparison with those of other years. For these major events, the amplitudes of the semi-diurnal tides and quasi-16-day waves were found to be highly correlated and were maximum around the peak of SSW, suggesting a strong interaction between the two waves. However, this correlation was poor and the quasi-16-day spectral power was low for the minor events. A strong coupling of atmospheres was noted during a relatively high solar activity epoch of 2013 SSW, which was, however, explained to be due to the occurrence of a strong SSW event. These results suggest that the vertical coupling of atmospheres is stronger during strong major SSW events and these events play an important role in enabling the coupling even during high solar activity.

Keywords: Sudden stratospheric warming; Planetary waves; Atmospheric tides; Total electron content; Sun-Earth interaction; Vertical coupling; Upper atmosphere; Ionosphere; Thermosphere

Background

The low-latitude upper atmosphere of the Earth is coupled vertically to the lower atmospheric and horizontally to the high-latitude dynamical processes. While the neutral motions are affected via waves in the atmosphere and incoming solar radiation, the plasma motions are driven by the electrodynamical processes. Since both plasma and neutral species share the same space, their motions are coupled to each other in the upper atmosphere. Waves generated in the lower atmosphere propagate to the upper atmosphere under favorable background conditions (Shiokawa et al. 2009) and influence it by altering the conductivities of the E-region, which, in turn, modulate the F-region processes, especially, over the low and equatorial latitudes, where the magnetic field lines are nearly horizontal.

Direct propagation of large-scale planetary wave (PW) (periods in the range of 2 to 30 days) oscillations which are mainly generated in the troposphere into the upper atmosphere is highly improbable (Pancheva and Mukhtarov 2012). However, it is believed that they can influence the upper atmosphere by modulating the shorter period gravity waves and tides (Lastovicka 2006). The gravity waves and tides with greater horizontal wavelengths are allowed to propagate to the upper atmosphere under suitable conditions, thereby enabling communication of the large-scale lower atmospheric waves into the upper atmosphere. During sudden stratospheric warming (SSW) events, the PW amplitudes get amplified and the stratospheric and

* Correspondence: fazlul84@gmail.com
[1]Space and Atmospheric Sciences Division, Physical Research Laboratory, Ahmedabad 380009, India
[2]Indian Institute of Technology, Gandhinagar 382424, India
Full list of author information is available at the end of the article

mesospheric zonal winds are also altered drastically rendering the conditions conducive for the propagation of the small-scale waves which are already modulated by the PWs (Liu et al. 2010; Yiğit and Medvedev 2012).

Even though the SSW is a northern hemispheric wintertime polar latitude phenomenon, the whole atmosphere of the Earth responds to these large-scale meteorological events (e.g., Fuller-Rowell et al. 2011). It is believed that the SSWs are produced by the wintertime vertical propagation of the tropospheric quasi-stationary PWs into the stratosphere and their interaction with the zonal mean flow, resulting in the dissipation of the waves in the stratosphere (Matsuno 1971). Due to this dissipation, energy and momentum are deposited in the stratosphere which modify the usual wintertime eastward zonal wind and enhance the stratospheric temperature. According to the World Meteorological Organization, if the stratospheric (at an altitude of 10-hPa pressure level) temperature at northern polar latitudes (poleward of 60° N) increases by more than 25 K within a week, then it is called an SSW event, and these temperature enhancements are considered as a good tracer of the planetary wave activity in the stratosphere. If in addition to the increase in temperature the usual wintertime eastward zonal mean zonal wind at 10 hPa and at 60° N reverses its direction, then the event is called major or else minor (Andrews et al. 1987). During SSW events, the interaction between enhanced planetary waves and tides and the interaction between tides and modified middle atmosphere modulate the tidal components, which register their signature in the upper atmospheric parameters (Jin et al. 2012; Pedatella and Liu 2013; Guharay et al. 2014). Also, nonlinear interaction between PWs and tides produces additional waves at the sum and the difference frequencies of the two original waves (Teitelbaum and Vial 1991) which fall mainly in the tidal domain.

By using datasets, such as the stratospheric wind, equatorial electrojet (EEJ) strength, total electron content (TEC), and multiwavelength dayglow intensities which originate from different altitudes of the atmosphere, it has been shown that the PW influence on the upper atmosphere is solar activity dependent (Laskar et al. 2013). That study motivated the present investigations using low-latitude datasets at varying levels of SSW strengths and of solar activity (minimum to maximum). Clear signatures of the interaction between enhanced PWs and tides during SSW and the resulting influence on the upper atmospheric EEJ strength and TEC values are presented to demonstrate the vertical coupling of atmospheres and its dependence on solar activity and planetary wave activity in the lower atmosphere.

Methods

To obtain information on the low-latitude coupled ionosphere-thermosphere system during SSW and at different levels of solar activity, the EEJ strength and TEC data are used in this study.

EEJ strength

The horizontal component of geomagnetic field (H) data is collected by magnetometers at an equatorial station, Tirunelveli (TIR) (8.7° N, 77.7° E; 0.1° N, magnetic latitude (MLAT)), and an off-equatorial station, Alibag (ABG) (18.6° N, 72.9° E; 10.3° N MLAT). The anomalies in H relative to its nighttime values at Alibag (ΔH_{ABG}) are subtracted from the corresponding values at Tirunelveli (ΔH_{TIR}), i.e., $\Delta H_{\mathrm{TIR}} - \Delta H_{\mathrm{ABG}}$, to obtain a measure on the EEJ strengths. The filled triangles in Figure 1 represent the locations from where magnetic measurements have been obtained.

TEC

The TEC data has been obtained from a southern hemispheric station, Diego Garcia (7.27° S, 72.4° E; 15.3° S MLAT), that is located approximately in the same longitude sector as that used for obtaining the EEJ strength. The filled circle in the map of Figure 1 represents the location of the Global Positioning System (GPS) receiver. The solid line in Figure 1 represents the geomagnetic equator (according to the IGRF-2010 magnetic field model), and the two dashed lines parallel to it are the ±15° latitudes, which represent the approximate locations of the crest regions of the equatorial ionization anomaly (EIA). One may note that the Diego Garcia station falls approximately under the southern crest of the EIA. The receiver independent exchange (RINEX) format International GNSS Service (IGS) (Dow et al. 2009) data are processed using open-source GPS ToolKit (GPSTk) (Harris and Mach 2007; Laskar et al. 2013). While calculating vertical TEC values, satellites with elevation angles greater than 50° are considered, which remove the dependence of TEC on ionospheric pierce point height and latitude, in addition to multipath effect in the low latitudes (Rama Rao et al. 2006; Bagiya et al. 2009).

High-latitude stratospheric temperature

The National Centers for Environmental Prediction (NCEP) and National Center for Atmospheric Research (NCAR) have cooperated in a project called reanalysis in which the temperature and wind are recovered from land surface, ship, rawinsonde, pilot balloon, aircraft, satellite, and other data (Kalnay et al. 1996). Daily averaged data at a 2.5° × 2.5° grid for the whole globe and for 17 pressure levels from the Earth's surface up to 10 hPa for several atmospheric parameters are made available. In this study, the stratospheric temperature at 10 hPa (approximately 30 km) from 90° N is used to obtain the temperature anomaly. From the NCEP/NCAR zonal mean zonal wind, it can be seen that three minor and

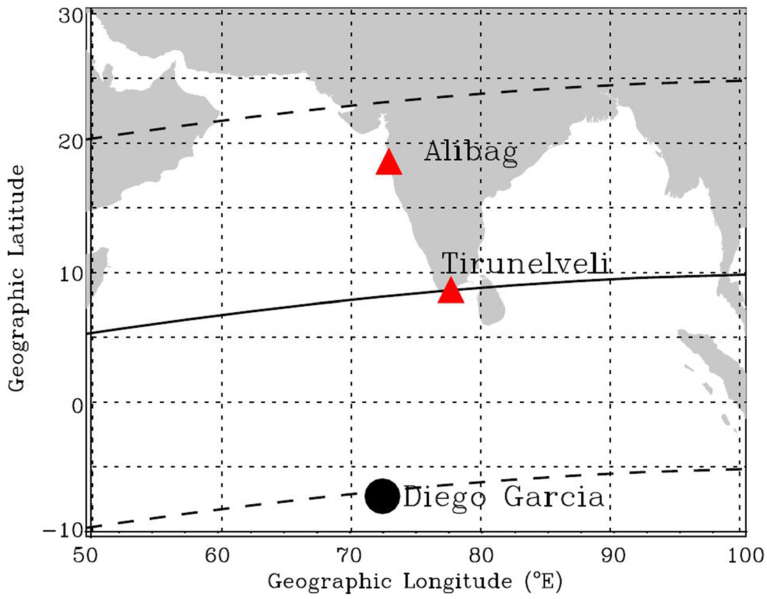

Figure 1 The geo-locations of the stations are depicted in the regional map in Indian longitudes. It may be noted that the GPS station (circle) and the EEJ derivation stations (triangles) are nearly at the same longitude sector. The dashed curves represent the ±15° latitudes, i.e., the approximate positions of the crest regions of the equatorial ionization anomaly.

five major warming events occurred during the years 2005 to 2013 (excluding those in the year 2008, wherein both major and minor events occurred one following the other). The nature of the SSW event and averaged sunspot number (<SSN>) during the observation period of January-February months in all the years are presented in Table 1. One can note that these events span solar activity levels with average SSN ranging from 0 to 51.

Analysis methodology

The EEJ strength and TEC data during the January-February months in the years 2005 to 2013 are used in this study. In order to investigate the interaction between local-time-dependent waves and large-scale PW-type waves during SSW events, the following approach has been adopted. For each day, data are binned in hourly intervals, and then the data of a particular bin of every day are arranged to make a time series of 60 data points (for the 60 days) as shown in the left side panel (a) in Figure 2 for the EEJ strength data in the year 2006. Lomb-Scargle periodograms (Lomb 1976; Scargle 1982; Torrence and Compo 1998) of each of the time series in the left panel are shown in the right panel (b) in Figure 2. The plots are placed one below the other according to bins that are arranged by local time. Such analysis has the advantage that it reveals the local-time dependence, if any, of waves (such as solar tides of different periodicities and planetary-scale waves). One can note the presence of periods in 12 to 16 days, which are above the 90% significance level, in these periodograms. Also, there is a systematic pattern in the PW-type periodicities of 12 to 16 days in the TEC and the EEJ, which is seen to be prominent throughout the daytime hours. Such method of determination of the dominant periods at different hours in the time series as shown in Figure 2b for 2006 has been carried out for all the years (2005 to 2013) in

Table 1 Some of the atmospheric and solar parameters during the years 2005 to 2013

	Year								
	2005	2006	2007	2008	2009	2010	2011	2012	2013
ΔT_{SSW}	40	60	40	60	60	40	35	30	45
T_{peak_SSW}	240	260	245	268	265	237	235	245	248
U_{east}	+10	−25	−8	−15	−35	−6	+25	+5	−12
SSW str.	Minor	Major	Major	Major	Major	Major	Minor	Minor	Major
<SSN>	30	10	14	3	1	16	24	46	51

ΔT_{SSW}, stratospheric temperature anomaly at 90° N; T_{peak_SSW}, peak stratospheric temperature during SSW at 90° N; U_{east}, peak eastward zonal mean stratospheric wind at 60° N during SSW; SSW str., SSW strength; <SSN>, average SSN.

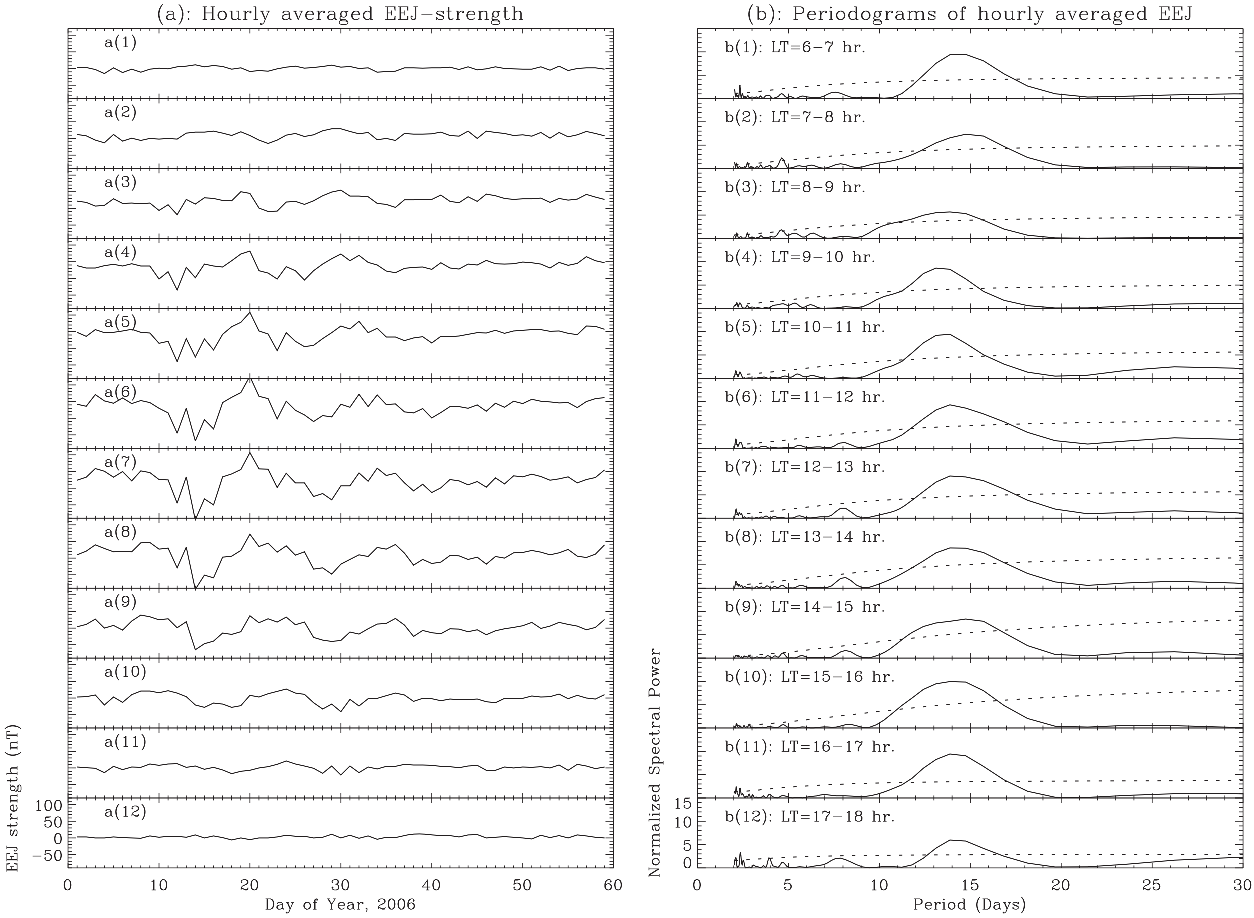

Figure 2 Values of EEJ strength and corresponding Lomb-Scargle periodograms for the year 2006. **(a)** Hourly binned daily values of EEJ strength and **(b)** their corresponding normalized Lomb-Scargle periodograms are presented. This type of binned daily values average out the gravity waves with periods less than 1 h. Moreover, they show periods that are dependent on local time (like solar tides). Also, as the larger scale planetary waves modulate these local-time dependent tidal waves, the periodogram spectral power is a direct measure of the interaction strength between tidal and planetary waves. Dashed lines in the right panel represent the 90% significance levels. Here, one can note a systematic variation of statistically significant periodicities with respect to local time for the wave periods between 11 and 20 days (i.e., the quasi-16-day periods are present here at all the local times).

both the observed parameters, namely the EEJ and the TEC. The details of these periods and their dependence on SSW strength and solar activity level are described in the next section. As both major and minor events occurred in the year 2008 one after the other in quick succession, the events in this year have not been considered in the current analysis. Moreover, the TEC data also do not exist for this year.

Results and discussion

The low-latitude ionospheric dynamics is governed dominantly by the dynamo electric field of the E-region of the ionosphere. The off-equatorial E-region electric field (E) maps over to the magnetic equator at the lower F-region altitudes. Under the influence of this E field and the magnetic field (B) of the Earth, the F-region plasma over the magnetic equator moves upward due to $E \times B$ drift. This plasma then diffuses along the magnetic field lines and accumulates at around ±15° latitudes off the magnetic equator, building up regions of enhanced densities (crests) in plasma, and this phenomenon is known as the EIA (Raghavarao et al. 1988). The strength and latitude coverage of the EIA crest depends on season and lower atmospheric forcings of tidal nature (Immel et al. 2006; Pallamraju et al. 2004, 2010). Waves propagating from the lower atmosphere perturb the E-region dynamo electric field which is mapped to the F-region and thereby contribute to the redistribution of plasma. The amplitudes of these tidal waves are modulated at the lower atmosphere by the large-scale PW-type waves that are enhanced during SSW events. In addition to the shorter period dominant tidal waves, the normal-mode-type PW oscillations of 2, 5, 10, 16, and 25 days are generally observed in the upper atmosphere (e.g., Salby 1984; Sassi et al. 2012; Laskar et al. 2013). The EEJ strength which originates from around 105-km altitude region in the equatorial latitudes has been shown to be strongly modulated by lunar 14 to 15 day lunitidal period (Park et al. 2012). Here, in this study, the presence of waves in the PW regime (2 to 30 days) can be seen in Figure 2. The most dominant waves that have been observed in all these durations of observations are of the quasi-16-day type (11.2 to 20 days; Salby 1984). In some local time bins, the presence of 5- to 6-, 9- to 10-, and 27-day periods is also observed to be above the 90% significance level. However, the dominant mode present here is of quasi-16-day-type PWs which originate mainly in the lower atmosphere and are very sensitive to the stratospheric and mesospheric mean zonal winds (Luo et al. 2000). So, the large-scale waves and periodicities that appear in Figure 2 are believed to be associated with both variabilities of tides and PWs from the lower atmosphere.

A similar analysis, as that carried out for EEJ in the year 2006 as shown in Figure 2, has been carried out for all the years and in both the EEJ strength and the TEC data. For brevity, these periodograms have been converted into contour plots and all the periodograms at different local times have been normalized with their respective 90% significance level values and are shown in Figure 3. The left (a) and right (b) panels show the periodogram contours for the EEJ strength and the TEC from Diego Garcia. Each column represents data for 8 years from 2005 to 2013, wherein the x-axis represents the periods in days and the y-axis is the local time. The color bar represents the relative spectral powers compared to the strongest power in the year 2009 - the year of strongest SSW event of the past decade. This is done in order to compare the inter-year variation in powers for a given periodicity. Here, all the periods greater than the relative power of approximately 0.6 (dark green) are above 90% significance level. From this figure, one can note that the relative powers of the periods in the quasi-16-day range are very prominent and are present in almost all the years presented here. The maxima of power at the quasi-16-day period range occur mostly at the same period range with respect to local time in the years 2006, 2007, and 2009 while for 2005, 2012, and 2013, one can note that the periods with maxima in power shift from shorter to longer periods from morning to evening. It is also notable that the periodicities in the EEJ and the TEC are, to a large extent, similar which is due to the fact that the low-latitude E-region electric field acts as a dominant driver for the plasma processes that eventually affect the F-region processes. Other than the quasi-16-day periods, one can see periodicities at 2, 5, 8 to 9, and 25 days in Figure 3. The 2- and 5-day waves are the normal mode oscillation of the lower atmosphere (Salby 1984). In addition to the Doppler-shifted 10-day normal mode oscillation origin, the 8- to 9-day waves have also been reported to be related with the quasi-periodic variations of solar wind high-speed streams and recurrent geomagnetic activity, especially for the year 2005 (Thayer et al. 2008). Thus, some of the wave activities seen in these upper atmospheric parameters are due to both solar and lower atmospheric origin.

The average spectral power of the variations within the quasi-16-day range (11.5 to 20 days) and 6 to 18 h local time in the contour plots shown in Figure 3 are produced in Figure 4 for both the EEJ strength and the TEC. The letters ‘m’ and ‘M’ just above the x-axis stand for ‘minor’ and ‘major’ SSW events, respectively, that occurred during those observation windows. The dashed line (‘+’ symbol) in Figure 4 shows the northern polar latitude (90° N) stratospheric temperature anomalies (ΔT) that occurred during the SSW events. The ΔT values are calculated by averaging the stratospheric temperature for a fairly stable duration prior to the occurrence of the SSW. In the absence of any index or parameter which represents the true strength of the SSW, this temperature anomaly is used as an indicator of the strength. It is expected that the ΔT values represent the stratospheric behavior in response to the SSW events. Strikingly, there are three maxima in both temperature anomaly and spectral powers of EEJ and TEC which occurred during the three strong major SSW years 2006, 2009, and 2013. Also, during the three minor warmings in the years 2005, 2011, and 2012, the spectral powers are comparatively low. These observations suggest that the strength of the SSW decides the spectral power of quasi-16-day waves in the upper atmospheric parameters. The quasi-16-day-type variations in the EEJ and ionospheric parameters are widely shown to be enhanced during SSW events (Pancheva et al. 2009). Notably, these three strong major events were the strongest of the major events in the last two decades. So, higher spectral power in these three major events implies that the stronger the SSW event, the stronger will be its effect on the low-latitude upper atmosphere. This happens because during major warmings the semi-diurnal tidal (both solar and lunar) and PW amplitudes are amplified and their combined action registers higher influence on the ionosphere (Stening et al. 1997; Pedatella and Liu 2013).

It can be noticed from Figure 3 that there are statistically significant quasi-16-day periods in all the years in addition to those in the three strong major warming years mentioned above. In spite of the fact that the SSWs in 2005, 2011, and 2012 were minor in nature, they showed appreciable amplitudes in the quasi-16-day power. Notably, these three minor events occurred during low solar activity epoch. Laskar et al. (2013) used

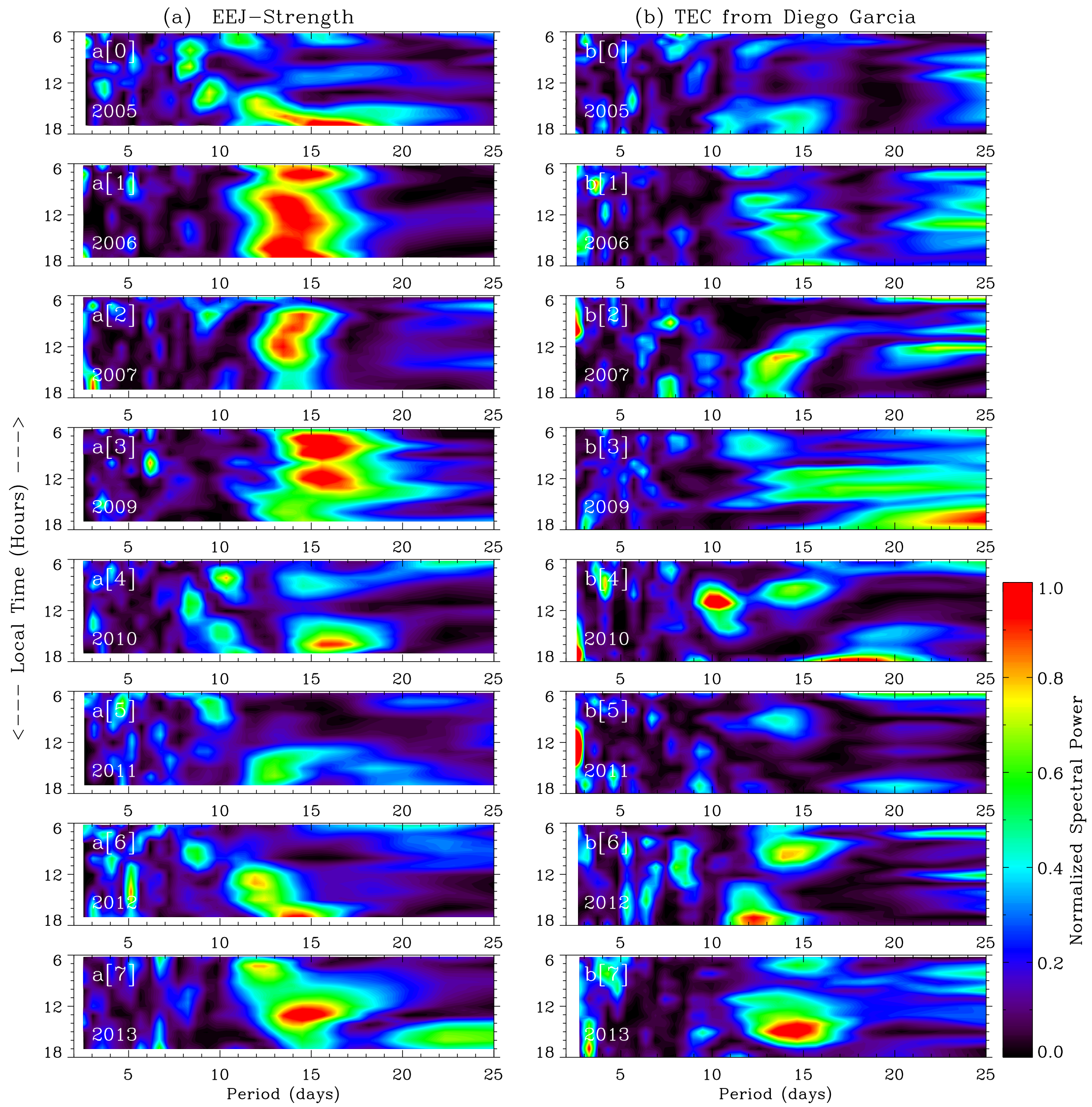

Figure 3 The contour plots of periodograms of EEJ and TEC in the years 2005 to 2013. Contour plot of the Lomb-Scargle periodograms corresponding to all the local times as shown in Figure 2b is presented in subplot a[1]. Similarly, periodograms of EEJ in the left panel **(a)** and TEC in the right panel **(b)** for the observation durations in the years 2005 to 2013 are shown. The spectral powers are normalized with respect to their respective 90% significance level values. The color bar represents the strength/relative power of the significant periods, and all the periods with relative power greater than approximately 0.6 (dark green) are above 90% significance level. It should be noted that during the major warming cases in 2006, 2009, and 2013, both the EEJ and the EIA crest region station, Diego Garcia, show strong quasi-16-day periodicities.

experimental observations to show that the coupling of lower and upper atmospheres is higher (lower) during low (high) solar activity. Such coupling in low solar activity is further enhanced when additional energy is available, such as that present during SSW events, which thus explains the appreciable amplitudes during these three minor events. Using numerical simulations, Pedatella and Liu (2013) showed that for the same level of SSW activity, the lower atmospheric influence on the upper atmosphere is greater during low solar activity period in comparison to that at high solar activity, wherein solar influences dominate. Further, in the present case, one can note that the major SSW event in 2013, which occurred in relatively higher solar activity (average SSN of 51), shows strong

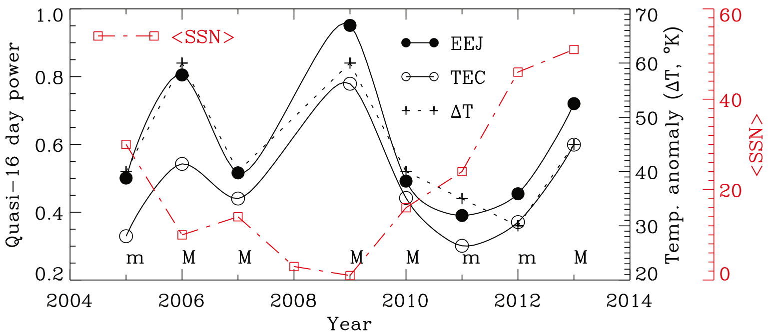

Figure 4 The mean normalized power of the quasi-16-day periodicities in EEJ strength and TEC. The power spectra as shown in Figure 3 are averaged between 11.5- and 20-day periods and for the whole day. The letters 'm' and 'M' represent 'minor' and 'major' SSW events, respectively, that occurred in the given year. The dashed curve shows the high-latitude stratospheric temperature anomaly (Δ*T*) on the peak of the SSW-related warming that represents the lower atmospheric behavior. One can note that the amplitudes have three peaks during the three strong major SSW events in the years 2006, 2009, and 2013 and three minima during the minor events in 2005, 2011, and 2012. It can be noted that there is a clear and systematic correspondence between the quasi-16-day amplitudes and the polar stratospheric temperature anomaly. The average SSN values are also shown with its axis at the right. It may also be noted that the relatively higher solar activity year 2013 showed a strong coupling due to increased lower atmospheric activity during strong SSW event.

amplitudes in the quasi-16-day periods. In our earlier study (Laskar et al. 2013), it was conjectured that even during high solar activity if there occurs a major SSW event, then it would provide additional energy which will significantly influence the upper atmosphere. In this work, the observation of the SSW event in 2013 is an experimental evidence to that conjecture. Support for this conjecture is also obtained from the published literature wherein the existence of perturbations in the ionosphere due to lower atmospheric forcings was reported during high solar activity in 2001 to 2004 and 2013, which actually occurred in simultaneity with major SSW events (e.g., Liu and Roble 2005; Pancheva et al. 2009; Fejer et al. 2010; Pedatella and Liu 2013; Goncharenko et al. 2013). These earlier reports have to be viewed in light of our conjecture that if the lower atmospheric forcing is stronger, as it happens during strong SSW events, then they can affect the upper atmosphere even during high solar activity periods. The current study demonstrates these features and places things in perspective with larger and independent datasets during low, moderate, and high solar activity epochs. The present study also reveals the plausible conditions in which an SSW event shows a greater effect on the upper atmosphere based on various waves and background dynamics as discussed below.

As mentioned above, the enhanced PWs and middle atmospheric dynamics during SSW modulate the tidal waves (mainly semi-diurnal) which further influence the ionosphere through the electrodynamical processes. To study the behavior of these waves, the relative variation in amplitudes of quasi-16-day and semi-diurnal waves had been looked into. Figure 5 shows the amplitudes of the semidiurnal (SD; thin continuous lines), an estimate of the SD envelope ($SD_{envelope}$; thick continuous lines), and quasi-16-day (dashed) periodic variations in EEJ strength during the years of the current study. These amplitudes are obtained using the wavelet-based spectral analysis technique (Torrence and Compo 1998; Zaourar et al. 2013). It is known from the wavelet theory that the amplitudes of the harmonic components, like tides and PWs, can be obtained from the absolute value of the wavelet transform of the time series with the Morlet function as mother wavelet. The Morlet mother wavelet is best suited for studies of sinusoidal-type geophysical waves. The details of wavelet-based spectral analysis can be found in Torrence and Compo (1998). Both the semi-diurnal and quasi-16-day amplitudes appearing in Figure 5 are derived from the wavelet transform of the hourly values of the EEJ strength data. Interestingly, one may note from Figure 5 that the amplitudes of both semi-diurnal tides and quasi-16-day amplitudes are high and broadly vary in a similar fashion (as if semi-diurnal tides are modulated by the quasi-16-day waves) around the peak of SSW event, especially for the three strong major SSW events in 2006, 2009, and 2013.

As semi-diurnal oscillations are of higher frequency than those of planetary-scale waves in order to enable quantification of the correlation between SD variations and quasi-16-day waves, an envelope of semi-diurnal amplitude, $SD_{envelope}$, values are derived. These $SD_{envelope}$ values are obtained by a two-point smoothing of the curve joining the maxima of the 3-day (72 h) smoothed semi-diurnal amplitudes. One can note from Figure 5 that $SD_{envelope}$ fairly follows the SD maximum amplitudes. The cross-correlation coefficients (*R*) between $SD_{envelope}$ and quasi-16-day amplitudes are also shown within the plots. One can note that for the three strong major SSW years 2006, 2009, and 2013, the correlation coefficient values are 0.78,

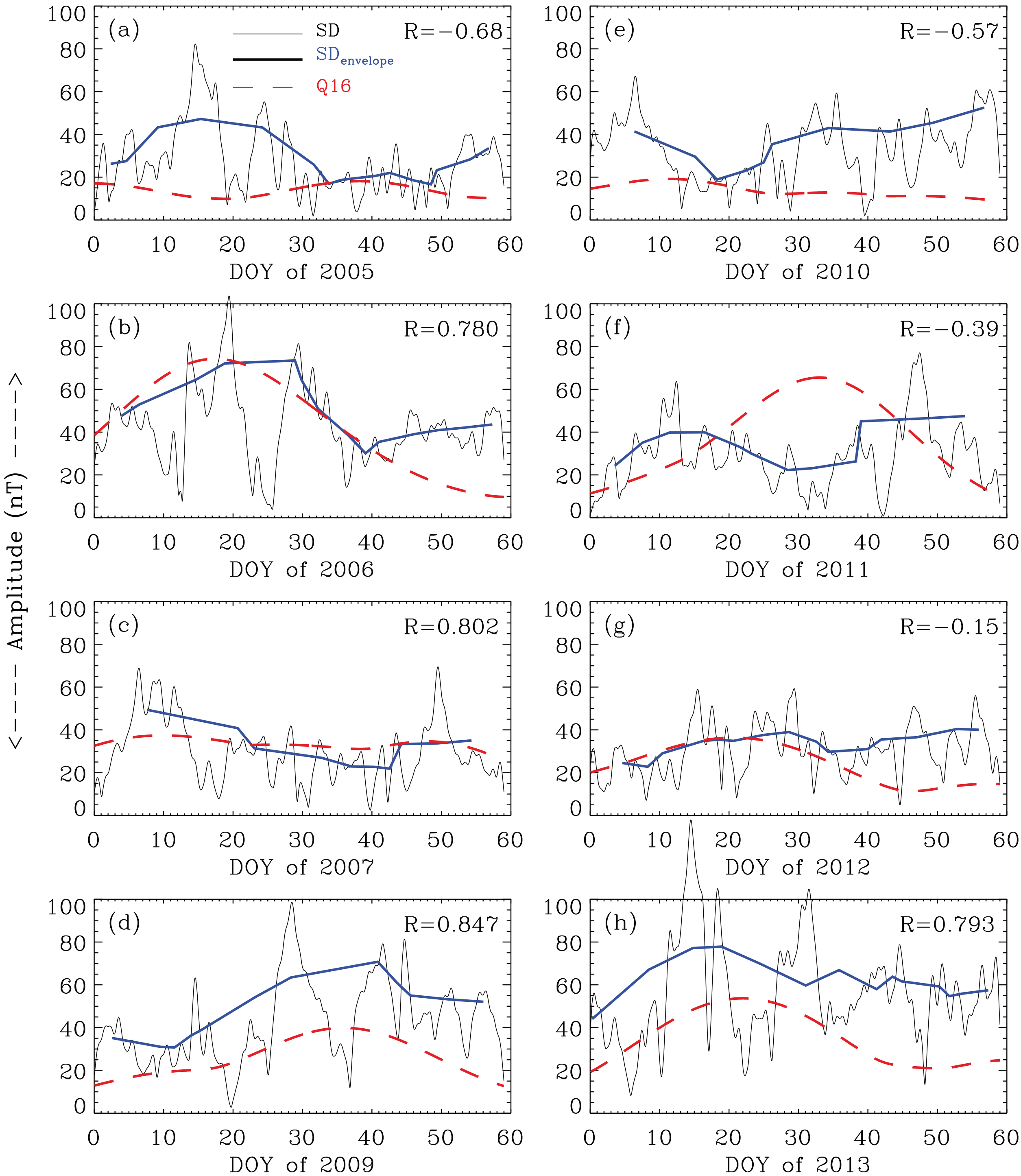

Figure 5 Amplitudes of SD, $SD_{envelope}$, and Q16 (a-h). The amplitudes of the semi-diurnal (SD; thin continuous lines), semi-diurnal envelope ($SD_{envelope}$; thick continuous lines), and quasi-16-day (Q16; dashed) periods in the EEJ strengths are shown along with the correlation coefficient (*R*) between $SD_{envelope}$ and quasi-16-day wave amplitudes. One can note that there is a good correlation between these two parameters for the three strong major warming years 2006, 2009, and 2013 (*R* values are 0.78, 0.85, and 0.79, respectively). This signifies that during the strong SSW events, the interaction between semi-diurnal and quasi-16-day waves is stronger.

0.85, and 0.79, respectively. For the less major and the minor events, the correlation coefficients are negative (except for 2007, which was a late winter SSW event), which may possibly be due to the interaction of tides with some other PWs or with middle atmospheric dynamics (Jin et al. 2012). From these results, the plausible conclusion that can be arrived at is that during the three strong major SSW events in 2006, 2009, and 2013, there were strong interactions between semi-diurnal tides and quasi-16-day waves. Further, recent modeling studies suggest that the middle atmospheric dynamics play a dominant role in coupling the lower atmosphere and upper atmosphere during SSW events (Jin et al. 2012; Pedatella and Liu 2013). This study thus provides experimental evidence to the conjecture proposed earlier and revealed new aspects of interactions on the vertical coupling of atmospheres. These new aspects call for a detailed modeling and simulation studies, which are beyond the scope of the present communication, and will be carried out in the future.

Conclusions

Using two independently measured upper atmospheric parameters, namely the EEJ and the TEC, the vertical coupling of atmospheres during SSW events at varying levels of solar activity has been investigated. Individual SSW events during the years 2005 to 2013 have been considered. There were three very strong events during 2006, 2009, and 2013 of which the first two occurred during the low solar activity epoch and the 2013 event occurred during the so-called maximum of the 24th solar cycle. The main findings of this work are summarized below:

1. The spectral powers of the quasi-16-day wave oscillations in the EEJ and the TEC (over the crest of the EIA) are found to vary in a similar fashion to the high-latitude stratospheric temperature anomaly. The quasi-16-day spectral powers were found to be strong during the three strong major warming cases in 2006, 2009, and 2013 and weaker during the minor warming events in 2005, 2011, and 2012, implying that the intenseness of the SSW event decides the strength of vertical coupling.
2. It is observed that for those major events for which the quasi-16-day amplitudes are high, the broad variations in the amplitudes of semi-diurnal tide and the quasi-16-day amplitudes are quite similar. To first order, this suggests that there occurs a strong interaction between semi-diurnal tides and quasi-16-day planetary waves for the strong major SSW events. This interaction has been found to be weaker for less major and minor events.
3. Even though the 2013 event occurred during relatively high solar activity epoch, the powers in the quasi-16-day period in both the EEJ and the TEC were significantly strong. This observation supports the Laskar et al. (2013) proposition that even during high solar activity if an SSW event occurs, then the upper atmosphere is influenced significantly by lower atmospheric forcings due to additional energy that becomes available for enabling the vertical coupling of atmospheres through the PWs and
middle atmospheric dynamics.

To conclude, the vertical coupling of atmospheres in terms of the strength of spectral amplitude is found to be dependent on the strength of SSW, solar activity, and interaction between tides and planetary waves.

Abbreviations
EEJ: equatorial electrojet; EIA: equatorial ionization anomaly; GPS: Global Positioning System; GNSS: Global Navigation Satellite System; IGRF: International Geomagnetic Reference Field; NCEP: National Centers for Environmental Prediction; PW: planetary wave; SD: semi-diurnal tides; SSN: sunspot number; SSW: sudden stratospheric warming; TEC: total electron content.

Competing interests
The authors declare that they have no competing interests.

Authors' contributions
FIL developed the data analysis methodology, interpreted the results, and drafted the manuscript. DP actively participated in the discussions on this work and provided time to time guidelines, suggestions, and improvements during the preparation of the results and the manuscript. BV collected and validated the EEJ datasets and provided comments to the manuscript. All authors have approved the final manuscript.

Acknowledgements
The RINEX format GPS observational and navigational data are obtained from the International GNSS Service (IGS) network available online at http://sopac.ucsd.edu/cgi-bin/dbDataBySite.cgi. We are grateful to NOAA/OAR/ESRL PSD, Boulder, CO, USA, for the NCEP/NCAR Reanalysis data on the website http://www.esrl.noaa.gov/psd/. The sunspot number and other geomagnetic indices data are obtained from NASA OMNIWeb. This work is supported by the Department of Space, Government of India.

Author details
[1]Space and Atmospheric Sciences Division, Physical Research Laboratory, Ahmedabad 380009, India. [2]Indian Institute of Technology, Gandhinagar 382424, India. [3]Indian Institute of Geomagnetism, Navi-Mumbai 410218, India.

Received: 30 April 2014 Accepted: 7 August 2014
Published: 18 August 2014

References
Andrews DG, Holton JR, Leovy CB (1987) Middle Atmosphere Dynamics. Academic, San Diego, p 489
Bagiya MS, Joshi HP, Iyer KN, Aggarwal M, Ravindran S, Pathan BM (2009) TEC variations during low solar activity period (2005–2007) near the equatorial ionospheric anomaly crest region in India. Ann Geophys 27:1047–1057. doi:10.5194/angeo-27-1047-2009
Dow J, Neilan R, Rizos C (2009) The International GNSS Service in a changing landscape of global navigation satellite systems. J Geod 83:191–198. doi:10.1007/s00190-008-0300-3
Fejer BG, Olson ME, Chau JL, Stolle C, Lühr H, Goncharenko LP, Yumoto K, Nagatsuma T (2010) Lunar-dependent equatorial ionospheric electrodynamic effects during sudden stratospheric warmings. J Geophys Res 115:A00G03. doi:10.1029/2010JA015273
Fuller-Rowell T, Akmaev R, Wu F, Fedrizzi M, Viereck RA, Wang H (2011) Did the January 2009 sudden stratospheric warming cool or warm the thermosphere? Geophys Res Lett 38:L18104. doi:10.1029/2011GL048985

Goncharenko L, Chau JL, Condor P, Coster A, Benkevitch L (2013) Ionospheric effects of sudden stratospheric warming during moderate-to-high solar activity: case study of January 2013. Geophys Res Lett 40:4982–4986. doi:10.1002/grl.50980
Guharay A, Batista P, Clemesha B (2014) On the variability of the seasonal scale oscillations over Cachoeira Paulista (22.7S, 45W). Brazil Earth Planets Sp 66(1):45. doi:10.1186/1880-5981-66-45
Harris R, Mach R (2007) The GPSTk: an open source GPS toolkit. GPS Solut 11:145–150. doi:10.1007/s10291-006-0043-7
Immel TJ, Sagawa E, England SL, Henderson SB, Hagan ME, Mende SB, Frey HU, Swenson CM, Paxton LJ (2006) Control of equatorial ionospheric morphology by atmospheric tides. Geophys Res Lett 33:L15108. doi:10.1029/2006GL026161
Jin H, Miyoshi Y, Pancheva D, Mukhtarov P, Fujiwara H, Shinagawa H (2012) Response of migrating tides to the stratospheric sudden warming in 2009 and their effects on the ionosphere studied by a whole atmosphere–ionosphere model GAIA with COSMIC and TIMED/SABER observations. J Geophys Res Space Physics 117:A10. doi:10.1029/2012JA017650
Kalnay E, Kanamitsu M, Kistler R, Collins W, Deaven D, Gandin L, Iredell M, Saha S, White G, Woollen J, Zhu Y, Chelliah M, Ebisuzaki W, Higgins W, Janowiak J, Mo KC, Ropelewski C, Wang J, Leetmaa A, Reynolds R, Jenne R, Joseph D (1996) The NCEP/NCAR 40-year reanalysis project. Bull Amer Meteorol Soc 77(3):437–471
Laskar FI, Pallamraju D, Lakshmi TV, Reddy MA, Pathan BM, Chakrabarti S (2013) Investigations on vertical coupling of atmospheric regions using combined multiwavelength optical dayglow, magnetic, and radio measurements. J Geophys Res Space Physics 118:4618–4627. doi:10.1002/jgra.50426
Lastovicka J (2006) Forcing of the ionosphere by waves from below. J Atmos Sol–Terr Phys 68:479–497
Liu H-L, Roble RG (2005) Dynamical coupling of the stratosphere and mesosphere in the 2002 Southern Hemisphere major stratospheric sudden warming. Geophys Res Lett 32:L13804. doi:10.1029/2005GL022939
Liu H-L, Wang W, Richmond AD, Roble RG (2010) Ionospheric variability due to planetary waves and tides for solar minimum conditions. J Geophys Res 115:A00G01. doi:10.1029/2009JA015188
Lomb NR (1976) Least-squares frequency analysis of unequally spaced data. Astrophys Space Sci 39:447–462. doi:10.1007/BF00648343
Luo Y, Manson AH, Meek CE, Meyer CK, Forbes JM (2000) The quasi 16-day oscillations in the mesosphere and lower thermosphere at Saskatoon (52°N, 107°W), 1980–1996. J Geophys Res 105:2125–2138. doi:10.1029/1999JD900979
Matsuno T (1971) A dynamical model of the stratospheric sudden warming. J Atmos Sci 28(8):1479–1494. doi:10.1175/1520-0469(1971)028<1479:ADMOTS>2.0.CO;2
Pallamraju D, Chakrabarti S, Valladares CE (2004) Magnetic storm-induced enhancement in neutral composition at low latitudes as inferred by $O(^1D)$ dayglow measurements from Chile. Ann Geophys 22(9):3241–3250. doi:10.5194/angeo-22-3241-2004
Pallamraju D, Das U, Chakrabarti S (2010) Short- and long-timescale thermospheric variability as observed from OI 630.0 nm dayglow emissions from low latitudes. J Geophys Res 115:A06312
Pancheva D, Mukhtarov P (2012) Planetary wave coupling of the atmosphere–ionosphere system during the Northern winter of 2008/2009. Adv Space Res 50(9):1189–1203
Pancheva D, Mukhtarov P, Andonov B, Mitchell NJ, Forbes JM (2009) Planetary waves observed by TIMED/SABER in coupling the stratosphere–mesosphere–lower thermosphere during the winter of 2003/2004: part 2—altitude and latitude planetary wave structure. J Atmos Sol–Terr Phys 71(1):75–87
Park J, Lühr H, Kunze M, Fejer BG, Min KW (2012) Effect of sudden stratospheric warming on lunar tidal modulation of the equatorial electrojet. J Geophys Res 117:A03306. doi:10.1029/2011JA017351
Pedatella NM, Liu H-L (2013) The influence of atmospheric tide and planetary wave variability during sudden stratosphere warmings on the low latitude ionosphere. J Geophys Res Space Physics 118:5333–5347. doi:10.1002/jgra.50492
Raghavarao R, Sridharan R, Sastri JH, Agashe VV, Rao BCN, Rao PB, Somayajulu VV (1988) The equatorial ionosphere. In: Liu CH, Belva E (ed) WITS handbook. World Ionosphere/Thermosphere Study, vol 1. SCOSTEP Secretariat, University of Illinois, Urbana, pp 48–93
Rama Rao PVS, Niranjan K, Prasad DSVVD, Gopi Krishna S, Uma G (2006) On the validity of the ionospheric pierce point (IPP) altitude of 350 km in the Indian equatorial and low-latitude sector. Ann Geophys 24(8):2159–2168. doi:10.5194/angeo-24-2159-2006
Salby ML (1984) Survey of planetary-scale travelling waves: the state of theory and observations. Rev Geophys 22(2):209–236. doi:10.1029/RG022i002p00209
Sassi F, Garcia R, Hoppel K (2012) Large-scale Rossby normal modes during some recent northern hemisphere winters. J Atmos Sci 69(3):820–839
Scargle JD (1982) Studies in astronomical time series analysis. II - statistical aspects of spectral analysis of unevenly spaced data. Astrophys J 263:835–853
Shiokawa K, Otsuka Y, Ogawa T (2009) Propagation characteristics of nighttime mesospheric and thermospheric waves observed by optical mesosphere thermosphere imagers at middle and low latitudes. Earth Planets Sp 61(4):479–491. doi:10.1186/BF03353165
Stening RJ, Forbes JM, Hagan ME, Richmond AD (1997) Experiments with lunar atmospheric tidal model. J Geophys Res 102:13465–13471. doi:10.1029/97JD00778
Teitelbaum H, Vial F (1991) On tidal variability induced by nonlinear interaction with planetary waves. J Geophys Res 96(A8):14169–14178. doi:10.1029/91JA01019
Thayer JP, Lei J, Forbes JM, Sutton EK, Nerem RS (2008) Thermospheric density oscillations due to periodic solar wind high-speed streams. J Geophys Res 113:A06307. doi:10.1029/2008JA013190
Torrence C, Compo GP (1998) A practical guide to wavelet analysis. Bull Am Meteorol Soc 79(1):61–78. doi:10.1175/1520-0477(1998)079<0061:APGTWA>2.0.CO;2
Yiğit E, Medvedev AS (2012) Gravity waves in the thermosphere during a sudden stratospheric warming. Geophys Res Lett 39:L21101. doi:10.1029/2012GL053812
Zaourar N, Hamoudi M, Mandea M, Balasis G, Holschneider M (2013) Wavelet-based multiscale analysis of geomagnetic disturbance. Earth Planets Sp 65(12):1525–1540. doi:10.5047/eps.2013.05.001

doi:10.1186/1880-5981-66-94
Cite this article as: Laskar et al.: **Vertical coupling of atmospheres: dependence on strength of sudden stratospheric warming and solar activity.** *Earth, Planets and Space* 2014 **66**:94.